



University of Naples “Federico II”

**Analytical, Numerical and Experimental Study of a
Novel Low-Cost Base Isolation System**

A Thesis Submitted in Partial Fulfillment of the Requirements
for the Degree of Doctor of Philosophy in

CONSTRUCTION ENGINEERING

by

Andrea Calabrese

March, 2013

ABSTRACT

The earthquakes of L'Aquila (2009) and Haiti (2010) showed, once again, the dramatic consequences of seismic events striking brittle, heavy and poorly constructed buildings. Worldwide, the high number of earthquake casualties still motivates structural engineers to search for effective seismic prevention technologies that can be adopted on a large scale. This work is oriented to introduce an innovative base isolation system: Recycled Rubber-Fiber Reinforced Bearings (RR-FRBs). These devices consist of several layers of recycled rubber, and are reinforced with sheets of composite materials. Compared to traditional rubber isolators, the weight and the cost are reduced by using fiber-reinforcements, no end-plates, and no bonding to support surfaces. The use of a flexible reinforcement, together with the absence of any constraint to the support surfaces, eliminates the presence of tensile stresses in the bearing under shear actions. This allows using a low quality rubber, as the one obtained from exhausted tyres or industrial leftovers. These materials are available everywhere in large quantities, they are inexpensive, and can be easily transformed with simple industrial processes. Consequently, RR-FRBs are a very low-cost technology. With the scope of assessing the use of RR-FRBs for seismic protection of buildings, this dissertation presents a comprehensive theoretical and experimental study. Firstly, closed-form expressions describing the compression and shear behavior of RR-FRBs are analytically obtained based on linear-elastic theory. These solutions are meant to be applied as design formulas for the devices. Finite Element Analyses (FEAs) are then performed, and the results are used as benchmark for the analytical expressions. A third phase of the research is dedicated to the experimental characterization of the recycled rubber. Based on derived material properties, analytical and FEAs results, prototypes of RR-FRBs are designed, manufactured and tested. The acquired knowledge of the behavior of the bearings is used to analyze a case study. Inelastic time-history analyses are performed on a prototype representing a common residential building typology. Numerical results show the high potential of such low-cost isolators in reducing the seismic damage to housing structures. It is hoped that the outcomes of this research could contribute to mitigate human life losses in developing countries located in earthquake-prone regions of the world.

ACKNOWLEDGEMENTS

Expressing gratitude is always a sad circumstance: it generally coincides with the end of a cycle, with leaving friends, experiences and changing life style. It is something that I would rather avoid but, in some cases as this, it is more than inevitable. There are so many people at which I will always be grateful.

My advisor, Prof. Serino, from University of Naples. He gave me different wonderful opportunities and encouragements over the last five years. Most of my latest experiences and successes are due to his guidance and commitment.

Prof. Kelly, from UCB. He has always been full of suggestions, enthusiasm and patience. He gave me lessons in different fields of knowledge and he is for me a life teacher, more than an incomparable expert in earthquake engineering. I am also grateful for how I was welcomed by his family and for the time I spent with them.

Dimitri, Tracy, Andreas, Vesna, Gerard. They have been wonderful colleagues at the field station in Richmond. Sharing some experiences with them has been a pleasure: they have been good references, friends and supporters. The environment they created at Berkeley was friendly and exciting, more than anything I could have asked for.

Dr. Levine BH and the BHGC. They took me under their wings. With them I spent time studying aerodynamics and the laws of flight. Ed Levin was the room of one of the best lesson set I received while in Berkeley. They taught me something that will mark the rest of my life, and I wish that I will be able to transmit to other people the knowledge I received.

My parents, Luigi and Rosa, my brother Armando, my sister-in-law Heidi, and my fiancée Francesca. There are no words for what they did. I probably have been critic at different times but, considering the starting point and the rest, the life path I had until this point has been a real adventure. Most of my achievements are due to them, to their continuous support and presence. Memorable will be the discussion about the stars.

A special thanks goes to my brother Armando as un-official advisor and mentor.

A good part of my gratitude is left for people not mentioned here, they all know the important part they played in supporting me for this endeavor.

TABLE OF CONTENTS

ABSTRACT	III
ACKNOWLEDGEMENTS	V
TABLE OF CONTENTS	VII
LIST OF FIGURES	XI
LIST OF TABLES	XXI
1. INTRODUCTION	1
1.1 MOTIVATION	1
1.2 OBJECTIVES AND SCOPE OF THE RESEARCH	1
1.3 OUTLINE OF THE WORK	3
2. BASE ISOLATION: A BRIEF INTRODUCTION	7
2.1 INTRODUCTION	7
2.2 PRINCIPLES OF BASE ISOLATION	7
2.3 BASE ISOLATION COMPONENTS	9
2.3.1 Rubber Bearings	9
2.3.2 Friction Pendulum System	12
2.3.3 Fiber Reinforced Bearings	13
3. FLEXIBLE REINFORCED BEARINGS UNDER COMPRESSION	16
3.1 INFINITELY LONG STRIP ISOLATORS	16
3.1.1 Equilibrium in Elastomeric Layer	16
3.1.2 Equilibrium in Reinforcing Sheet	18
3.1.3 Solution of Pressure and Effective Compressive Modulus	22
3.1.4 Flexible Reinforcement and Compressibility	23
3.2 CIRCULAR PAD	28
3.2.1 Deformation of Pad under Compression	28
3.2.2 Compression Stiffness and Pressure Distribution	35
3.3 RECTANGULAR PAD	39

3.3.1	Equilibrium in Elastomeric Layer	39
3.3.2	Equilibrium in Reinforcing Sheet.....	41
3.3.3	Approximate Boundary Conditions	42
3.3.4	Solution of Pressure	44
3.3.5	Effective Compressive Modulus	46
3.4	GENERAL SHAPE PAD	50
3.4.1	Equilibrium in Elastomeric Layer	50
3.4.2	Stress in the Reinforcement	52
3.4.3	Complete System of Equation.....	53
4.	FINITE ELEMENT ANALYSIS OF UNBONDED BEARINGS.....	55
4.1	INTRODUCTION	55
4.1.1	Material and Mechanical Properties of the Bearings	56
4.1.2	Contact Bodies, Boundary Conditions	58
4.2	INFINITELY LONG STRIP ISOLATORS	58
4.2.1	Geometrical Properties	58
4.2.2	Compression Results.....	60
4.2.3	Shear Results	67
4.3	CIRCULAR BEARINGS.....	72
4.3.1	Geometrical Properties	72
4.3.2	Compression Results.....	74
4.4	SQUARE BEARINGS.....	82
4.4.1	Geometrical Properties	82
4.4.2	Compression Results.....	84
5.	ULTIMATE DISPLACEMENT OF UNBONDED BEARINGS	89
5.1	INTRODUCTION	89
5.2	LIMIT DISPLACEMENT CRITERIA	90
5.2.1	Stability of Horizontal Displacement.....	90
5.2.2	No Contact with Horizontal Subgrade.....	91
6.	MATERIAL TESTING	95
6.1	INTRODUCTION	95
6.2	MECHANICAL TESTS ON RECYCLED RUBBER	97

6.2.1	Tensile Tests	97
6.2.2	Shear Tests	102
6.3	TENSILE TESTS ON FIBER REINFORCED POLYMERS.....	106
7	TESTS ON PROTOTYPES	111
7.1	INTRODUCTION.....	111
7.2	COMPRESSION TESTS.....	111
7.2.1	Experimental Setup.....	111
7.2.2	Test Specimens	113
7.2.3	Summary of Results	114
7.3	SHEAR TESTS	119
7.3.1	Bearings Design and Properties	119
7.3.2	Description of Test Setup and Protocol	120
7.3.3	Results of Horizontal Tests	122
8	SEISMIC ISOLATION FOR LOW-COST HOUSING: A CASE STUDY.....	129
8.1	INTRODUCTION.....	129
8.2	THE DEMONSTRATION BUILDING OF PASIR BADAK, INDONESIA.....	129
8.2.1	Description of the Building	129
8.2.2	Description of the Isolation System in Use.....	131
8.2.3	Site Specific Response Spectra	132
8.3	DESIGN AND NUMERICAL MODELLING OF BASE ISOLATION DEVICES FOR THE DEMONSTRATION BUILDING.....	133
8.3.1	Bilinear Hysteretic Behavior of Conventional Isolators	133
8.3.2	Lead-Rubber Bearings	134
8.3.3	Friction Pendulum System.....	135
8.3.4	Fiber Reinforced Rubber Bearings	139
8.4	TIME-HISTORY ANALYSES.....	146
8.4.1	Superstructure Model	146
8.4.2	Ground Motion Selection	147
8.5	ANALYTICAL PREDICTION OF PERFORMANCE OF THE DEMONSTRATION BUILDING	149
8.5.1	Time-History Responses	149
8.6	SUMMARY	155

9. CONCLUSIONS	157
9.1 SUMMARY OF WORK	157
9.2 SUMMARY OF RESULTS	158
9.3 RECOMMENDATIONS FOR FUTURE RESEARCH.....	163
9.4 CURRENT DEVELOPMENTS.....	164
REFERENCES	165
Appendix A: SHEAR TESTS ON RECYCLED RUBBER.....	171
Appendix B: COMPRESSION TESTS ON RR-FRBs	179
Appendix C: SHEAR TESTS ON RR-FRBs	187
Appendix D: INPUT GROUND MOTIONS FOR THE ANALYSES	197
Appendix E: TIME HISTORY ANALYSIS RESULTS	213

LIST OF FIGURES

Figure 1.1	Thesis flow chart.	5
Figure 2.1	Two-degrees of freedom isolated structure.	8
Figure 2.2	Schematic of Laminated Rubber Bearing.....	9
Figure 2.3	Hysteresis loops for a Lead Rubber Bearing (Courtesy of Prof. J.M.Kelly. University of California, Berkeley).....	11
Figure 2.4	Schematic representation of a Friction Pendulum System (FPS) bearing.....	13
Figure 2.5	Three-dimensional view of a Triple Friction Pendulum (TFP) bearing (from [Dao <i>et al.</i> , 2013.]).	13
Figure 2.6	Displaced configuration of a Fiber Reinforced Bearing (Courtesy of Prof. J.M.Kelly. University of California, Berkeley).....	14
Figure 3.1	Infinitely long rectangular pad showing dimensions.	17
Figure 3.2	Forces in reinforcing sheet bonded to layers of elastomer.....	19
Figure 3.3	Normalized force pattern in reinforcement.....	21
Figure 3.4	Displacement pattern for fiber reinforcement for various values of α	21
Figure 3.5	Variation of effective compression modulus with αb in infinitely long strip pad.....	23
Figure 3.6	Variation of normalized effective compression modulus with α and β , in an infinitely long strip pad.	27
Figure 3.7	Variation of normalized effective compression modulus with β for $\alpha = 0-3$27	
Figure 3.8	Coordinate system for a circular pad of radius R.....	28
Figure 3.9	Normalized effective modulus as a function of α and β37	
Figure 3.10	Normalized effective modulus as a function of α for different values of β38	
Figure 3.11	Normalized effective modulus as a function of α ($\beta = 0; \nu = 0; 1/3$)38	
Figure 3.12	Reference system for a rectangular pad showing dimensions.	39
Figure 3.13	Forces in reinforcing sheet bonded to rectangular layers of elastomer.	41
Figure 3.14	Variation of effective compressive modulus with αa in rectangular pad.....	48

Figure 3.15	Variation of effective compressive modulus with reinforcement stiffness in rectangular pad ($a/b = 0.5$)	48
Figure 3.16	Variation of effective compressive modulus with width/thickness in rectangular pad ($a/b = 0.5$)	49
Figure 3.17	Ratio of effective compressive modulus of rectangular pad to infinitely long strip pad ($a/b = 0$) versus aspect ratio.....	49
Figure 3.18	Constrained rubber pad and coordinate system.....	51
Figure 4.1	Integration points for element type 84 in MSC.Marc 2005 [MSC.Software 2004].	58
Figure 4.2	Strip type bearing showing reinforcements and dimensions.	59
Figure 4.3	Model mesh and layout of the reinforcement layers [el. type 143].	60
Figure 4.4	Von Mises stress contours at peak vertical force in a bearing of base $B = 250\text{mm}$ [SET2 ($t_f = 0.07\text{ mm}$)]	61
Figure 4.5	Von Mises stress contours at peak vertical force in a bearing of base $B = 500\text{mm}$ [SET2 ($t_f = 0.07\text{ mm}$)]	62
Figure 4.6	Tension contours in the fiber reinforcement ($B = 250\text{mm}$; $\sigma_y = 3.45\text{ MPa}$; SET2). 62	
Figure 4.7	Tension contours in the fiber reinforcement ($B = 500\text{mm}$; $\sigma_y = 3.45\text{ MPa}$; SET2). 63	
Figure 4.8	Vertical stiffness (FE analysis versus pressure solution).	65
Figure 4.9	Stress distributions in the reinforcement (FE analysis versus pressure solution) for $B=250\text{mm}$	66
Figure 4.10	Stress distributions in the reinforcement (FE analyses versus pressure solution) for $B=500\text{mm}$	66
Figure 4.11	Non-dimensional stress (FE/pressure solution) against non-dimensional length (x/B).....	67
Figure 4.12	Von Mises stress contours at peak horizontal force in a bearing of base $B=250\text{mm}$.68	
Figure 4.13	Von Mises stress contours at peak horizontal force in a bearing of base $B=500\text{mm}$.69	
Figure 4.14	Tension contours in the fiber reinforcement at maximum shear ($B=250\text{mm}$).....	70
Figure 4.15	Tension contours in the fiber reinforcement at maximum shear ($B=500\text{mm}$).....	70
Figure 4.16	Force-displacement curves for different base widths of the devices.....	71
Figure 4.17	Force-displacement/base curves for different base widths of the devices.....	71
Figure 4.18	Stress-strain curves for different base widths of the devices.....	72
Figure 4.19	Circular type bearing showing reinforcements and dimensions.....	73
Figure 4.20	Model mesh and layout of the reinforcement layers (elements 143).....	73

Figure 4.21	Von Mises stress contours at peak vertical force in a cross section of a rubber layer (left=core, $\Phi=250\text{mm}$ – SET1 $t_f=0.07\text{mm}$).	74
Figure 4.22	Von Mises stress contours at peak vertical force in a cross section of a rubber layer (left=core, $\Phi=500\text{mm}$ – SET1 $t_f=0.07\text{mm}$).	75
Figure 4.23	Von Mises stress contours at peak vertical force in a cross section of a rubber layer (left=core, $\Phi=250\text{mm}$ – SET2 $t_f=0.25\text{mm}$).	75
Figure 4.24	Von Mises stress contours at peak vertical force in a cross section of a rubber layer (left=core, $\Phi=500\text{mm}$ – SET2 $t_f=0.25\text{mm}$).	76
Figure 4.25	Tension contours in a fiber reinforcement ($\Phi=250\text{mm}$ – SET1 $t_f=0.07\text{mm}$ $\sigma_y = 3.45 \text{ MPa}$).	76
Figure 4.26	Tension contours in a fiber reinforcement ($\Phi=500\text{mm}$ – SET1 $t_f=0.07\text{mm}$ $\sigma_y = 3.45 \text{ MPa}$).	77
Figure 4.27	Tension contours in a fiber reinforcement ($\Phi=250\text{mm}$ – SET2 $t_f=0.25\text{mm}$ $\sigma_y = 3.45 \text{ MPa}$).	77
Figure 4.28	Tension contours in a fiber reinforcement ($\Phi=500\text{mm}$ – SET2 $t_f=0.25\text{mm}$ $\sigma_y = 3.45 \text{ MPa}$).	78
Figure 4.29	Vertical test results (FE analysis versus closed-form pressure solution). Gray lines are the solutions for SET1 while black lines are the solutions for SET2.	80
Figure 4.30	Vertical stiffness results.	80
Figure 4.31	Non-dimensional stiffness versus diameter.	81
Figure 4.32	K_{vFEM}/K_{vPS} as a function of the diameter.	81
Figure 4.33	Square type bearing showing reinforcements and dimensions.	82
Figure 4.34	Model mesh for a single pad (element type 84 in MSC.Marc 2005 [MSC.Software 2004]).	83
Figure 4.35	Vertical force–vertical displacement.	85
Figure 4.36	Vertical stiffness versus base.	86
Figure 4.37	K_{vFEM}/K_{vPS} as a function of the base.	86
Figure 4.38	K_{vFEM}/K_{vPS} as a function of the base-diameter for square and circular bearings.	87
Figure 5.1	Bonded bearing under compression and shear.	89
Figure 5.2	Normal and shear stress distributions on the top and bottom faces of the unbonded bearing in its deformed shape.	90
Figure 5.3	Unbonded bearing under shear load.	91
Figure 5.4	Schematic representation of the deformed bearing.	92
Figure 6.1	Tyre Derived Materials produced by Isolomma Srl (VI, Italy).	97

Figure 6.2	Experimental setup for tensile tests on rubber.....	98
Figure 6.3	Tensile test results on fiber of SBR specimens of different density [kg/m ³].	99
Figure 6.4	Tensile test results on grains of SBR specimens of different density [kg/m ³].	100
Figure 6.5	Tensile test results on big grains of EPDM specimens of different density [kg/m ³].	100
Figure 6.6	Tensile strength of recycled rubber.....	101
Figure 6.7	Ultimate strain of recycled rubber.	101
Figure 6.8	Machine for shear tests on rubber.....	103
Figure 6.9	Shear modulus from static tests.....	104
Figure 6.10	Shear modulus from dynamic tests.	105
Figure 6.11	Damping ratio from dynamic shear tests.	105
Figure 6.12	Production of FRP specimens for tensile tests.....	107
Figure 6.13	Universal testing machine used for tensile tests on FRP sheets.....	108
Figure 6.14	Tensile tests on fiber sheets.	108
Figure 7.1	Universal testing machine modified to accommodate the recycled rubber bearings.....	112
Figure 7.2	Load-patterns for vertical tests.	113
Figure 7.3	Vertical test results.....	115
Figure 7.4	Vertical test results.....	118
Figure 7.5	Sizes of the tested elastomeric bearings.....	119
Figure 7.6	RR-FRBs tested in shear.....	119
Figure 7.7	Instrumentation setup for 1D shaking table tests.....	121
Figure 7.8	Instrumentation setup for horizontal tests.....	121
Figure 7.9	Specimen 7LG(SG)250 at peak shear deformation.	123
Figure 7.10	Energy Dissipated per Cycle.	125
Figure 8.1	Photograph of the demonstration building of Pasir Badik (Courtesy of Prof. J.M.Kelly. University of California, Berkeley).....	130
Figure 8.2	Typical plan of the demonstration building (Courtesy of Prof. J.M.Kelly. University of California, Berkeley).	130
Figure 8.3	Elevations of the demonstration building (Courtesy of Prof. J.M.Kelly. University of California, Berkeley).	131
Figure 8.4	Vertical load – for the seismic load combination.....	131
Figure 8.5	Deformed configuration of isolation bearing with recessed plate connection.....	132

Figure 8.6	Site acceleration response spectra ($\xi=5\%$).....	133
Figure 8.7	Bilinear hysteretic model.	134
Figure 8.8	Hysteresis loops for an FPS Bearing [Almazan <i>et al.</i> 1998].	136
Figure 8.9	Bilinear model for FPS and LRB.	138
Figure 8.10	Indonesian building – FRBs distribution.	139
Figure 8.11	RR-FRB (B=240mm) at peak horizontal displacement.	141
Figure 8.12	RR-FRB (B=240mm) at ultimate horizontal displacement.	142
Figure 8.13	RR-FRB (B=240mm) horizontal load vs horizontal displacement. Large displacements analysis.....	142
Figure 8.14	RR-FRB (B=240mm) analysis step vs vertical displacement. Large displacements analysis.	143
Figure 8.15	FRB trilinear models and results by FEAs.....	143
Figure 8.16	Load displacement relation from FEAs.....	144
Figure 8.17	Deformed configuration under compression.....	144
Figure 8.18	Bulging of the rubber and stretching of the fiber layers under compression.....	145
Figure 8.19	Trilinear model for the FRB isolators.	145
Figure 8.20	Indonesian building-superstructure frame.....	147
Figure 8.21	MPE combination for the site.....	148
Figure 8.22	500yrs combination for the site.....	149
Figure 8.23	1th floor peak interstory-drift (500yrs events).....	152
Figure 8.24	4th floor peak interstory-drift (500yrs events).....	152
Figure 8.25	1th floor peak interstory-drift (MPE events).....	153
Figure 8.26	4th floor peak interstory-drift (MPE events).....	153
Figure 8.27	Shear force base isolation level (MPE events).....	155
Figure 9.1	Collapses of old buildings after two major Italian earthquakes.....	163
Figure A.1	Dynamic shear tests 1mm lateral displacement (10Hz).	172
Figure A.2	Dynamic shear tests 5mm lateral displacement (1Hz).	172
Figure A.3	Dynamic shear tests 10mm lateral displacement (1Hz).	173
Figure A.4	Rubber type 500 – dynamic shear test results (5mm lateral displacement).	173
Figure A.5	Rubber type 500 – dynamic shear test results (10mm lateral displacement).	174
Figure A.6	Rubber type 600 – dynamic shear test results (5mm lateral displacement).	174
Figure A.7	Rubber type 600 – dynamic shear test results (10mm lateral displacement).	175

Figure A.8	Rubber type B800 – dynamic shear test results (5mm lateral displacement).....	175
Figure A.9	Rubber type B800 – dynamic shear test results (10mm lateral displacement).....	176
Figure A.10	Rubber type G800 – dynamic shear test results (5mm lateral displacement).....	176
Figure A.11	Rubber type G800 – dynamic shear test results (10mm lateral displacement).....	177
Figure B.1	Vertical test results for rpad(BG)250.....	180
Figure B.2	Vertical test results for rpad(SG)250.....	180
Figure B.3	Vertical test results for rpad(BG)300.....	181
Figure B.4	Vertical test results for 1LS(BG)300.....	181
Figure B.5	Vertical test results for 1LC(BG)300.....	182
Figure B.6	Vertical test results for 3LC(BG)300.....	182
Figure B.7	Vertical test results for 4LC(SG)250.....	183
Figure B.8	Vertical test results for 3LG(BG)250.....	183
Figure B.9	Vertical test results for 3LG(SG)250.....	184
Figure B.10	Vertical test results for 4LG(SG)250.....	184
Figure B.11	Vertical test results for 7LG(SG)250.....	185
Figure C.1	Horizontal test results for 3LG(SG)250 with 1MPa vertical pressure (1st displacement sequence-12mm).....	188
Figure C.2	Horizontal test results for 3LG(SG)250 with 1MPa vertical pressure (2nd displacement sequence-12mm).....	188
Figure C.3	Horizontal test results for 3LG(SG)250 with 1MPa vertical pressure (3rd displacement sequence-12mm).....	189
Figure C.4	Horizontal test results for 3LG(SG)250 with 2MPa vertical pressure (12mm horizontal displacement).....	189
Figure C.5	Horizontal test results for 3LG(SG)250 with 1MPa vertical pressure (24mm horizontal displacement).....	190
Figure C.6	Horizontal test results for 3LG(SG)250 with 2MPa vertical pressure (24mm horizontal displacement).....	190
Figure C.7	Horizontal test results for 3LG(SG)250 with 1MPa vertical pressure (36mm horizontal displacement).....	191
Figure C.8	Horizontal test results for 3LG(SG)250 with 2MPa vertical pressure (36mm horizontal displacement).....	191
Figure C.9	Horizontal test results for 3LG(SG)250 with 3MPa vertical pressure (36mm horizontal displacement).....	192
Figure C.10	Horizontal test results for 3LG(SG)250 with 2MPa vertical pressure (48mm horizontal displacement).....	192

Figure C.11	Horizontal test results for 3LG(SG)250 with 3MPa vertical pressure (48mm horizontal displacement).	193
Figure C.12	Horizontal test results for 3LG(SG)250 with 3MPa vertical pressure (48mm horizontal displacement).	193
Figure C.13	Horizontal test results for 7LG(SG)250 with 1MPa vertical pressure (12mm horizontal displacement).	194
Figure C.14	Horizontal test results for 7LG(SG)250 with 2MPa vertical pressure (12mm horizontal displacement).	194
Figure C.15	Horizontal test results for 7LG(SG)250 with 1MPa vertical pressure (24mm horizontal displacement).	195
Figure C.16	Horizontal test results for 7LG(SG)250 with 2MPa vertical pressure (24mm horizontal displacement).	195
Figure C.17	Horizontal test results for 7LG(SG)250 with 2MPa vertical pressure (36mm horizontal displacement).	196
Figure D.1	MPE combination – record 000074xa, SF:0.53092	198
Figure D.2	MPE combination – record 000074ya, SF:0.45376	198
Figure D.3	MPE combination – record 000333xa, SF:1.4206	199
Figure D.4	MPE combination – record 000333ya, SF:1.0558	199
Figure D.5	MPE combination – record 001231xa, SF:2.0336	200
Figure D.6	MPE combination – record 001231ya, SF:1.4624	200
Figure D.7	MPE combination – record 001257xa, SF:1.1042	201
Figure D.8	MPE combination – record 001257ya, SF:1.3388	201
Figure D.9	MPE combination – record 004674xa, SF:1.0283	202
Figure D.10	MPE combination – record 004674ya, SF:0.96826	202
Figure D.11	MPE combination – record 006331xa, SF:6.2497	203
Figure D.12	MPE combination – record 006331ya, SF:8.3041	203
Figure D.13	MPE combination – record 006334xa, SF:0.77762	204
Figure D.14	MPE combination – record 006334ya, SF:0.45345	204
Figure D.15	500yrs combination – record 000074xa, SF:0.40891	205
Figure D.16	500yrs combination – record 000074ya, SF:0.34948	205
Figure D.17	500yrs combination – record 000333xa, SF:1.0942	206
Figure D.18	500yrs combination – record 000333ya, SF:0.81319	206
Figure D.19	500yrs combination – record 000600xa, SF:1.4652	207
Figure D.20	500yrs combination – record 000600ya, SF:2.3728	207

Figure D.21	500yrs combination – record 000625xa, SF:2.3013	208
Figure D.22	500yrs combination – record 000625ya, SF:3.1697.....	208
Figure D.23	500yrs combination – record 001231xa, SF:1.5663	209
Figure D.24	500yrs combination – record 001231ya, SF:1.1263.....	209
Figure D.25	500yrs combination – record 001257xa, SF:0.85044	210
Figure D.26	500yrs combination – record 001257ya, SF:1.0311.....	210
Figure D.27	500yrs combination – record 006331xa, SF:4.8135	211
Figure D.28	500yrs combination – record 006331ya, SF:6.3958.....	211
Figure E.1	Relative acceleration x-direction – event 74 MPE combination.....	214
Figure E.2	Relative acceleration x-direction – event 333 MPE combination.....	214
Figure E.3	Relative acceleration x-direction – event 1231 MPE combination.....	215
Figure E.4	Relative acceleration x-direction – event 1257 MPE combination.....	215
Figure E.5	Relative acceleration x-direction – event 4674 MPE combination.....	216
Figure E.6	Relative acceleration x-direction – event 6331 MPE combination.....	216
Figure E.7	Relative acceleration x-direction – event 6334 MPE combination.....	217
Figure E.8	Relative acceleration x-direction – event 74 500yrs combination.....	217
Figure E.9	Relative acceleration x-direction – event 333 500yrs combination.....	218
Figure E.10	Relative acceleration x-direction – event 600 500yrs combination.....	218
Figure E.11	Relative acceleration x-direction – event 625 500yrs combination.....	219
Figure E.12	Relative acceleration x-direction – event 1231 500yrs combination.....	219
Figure E.13	Relative acceleration x-direction – event 1257 500yrs combination.....	220
Figure E.14	Relative acceleration x-direction – event 6331 500yrs combination.....	220
Figure E.15	Relative acceleration x-direction – event 74 MPE combination.....	221
Figure E.16	Relative acceleration x-direction – event 333 MPE combination.....	221
Figure E.17	Relative acceleration x-direction – event 1231 MPE combination.....	222
Figure E.18	Relative acceleration x-direction – event 1257 MPE combination.....	222
Figure E.19	Relative acceleration x-direction – event 4674 MPE combination.....	223
Figure E.20	Relative displacement x-direction – event 6331 MPE combination.....	223
Figure E.21	Relative acceleration x-direction – event 6334 MPE combination.....	224
Figure E.22	Relative acceleration x-direction – event 74 500yrs combination.....	224
Figure E.23	Relative acceleration x-direction – event 333 500yrs combination.....	225

Figure E.24	Relative acceleration x-direction – event 600 500yrs combination.	225
Figure E.25	Relative acceleration x-direction – event 625 500yrs combination.	226
Figure E.26	Relative acceleration x-direction – event 1231 500yrs combination.	226
Figure E.27	Relative acceleration x-direction – event 1257 500yrs combination.	227
Figure E.28	Relative acceleration x-direction – event 6331 500yrs combination.	227

LIST OF TABLES

Table 4.1	Geometrical properties of the long strip bearings.	59
Table 4.2	Model characteristics and pressure solution results (long strip bearings).	63
Table 4.3	Ultimate performances of the bearings (SET1) under horizontal load.	72
Table 4.4	Geometrical properties of the circular bearings.	73
Table 4.5	Model characteristics and pressure solution results (circular bearings).	79
Table 4.6	Geometrical properties of the square bearings.	83
Table 4.7	Model characteristics and pressure solution results (square bearings).	85
Table 6.1	Specimens for tensile tests.	98
Table 6.2	Tensile tests results.	102
Table 6.3	Specimens for shear tests.	103
Table 6.4	Shear tests program.	103
Table 6.5	Fiber specimens for tensile tests.	107
Table 6.6	Tensile test results.	109
Table 7.1	MTS 810 characteristics.	111
Table 7.2	Fiber-reinforced test bearings.	114
Table 7.3	Vertical test results for 2-3MPa vertical pressure.	116
Table 7.4	Vertical test results for 3-4MPa vertical pressure.	116
Table 7.5	Vertical test results for 4-5MPa vertical pressure.	117
Table 7.6	Displacement-controlled tests for Recycled Rubber Fiber Reinforced Bearings.	120
Table 7.7	Shear test results.	124
Table 8.1	Properties of LRB for the analyses ($K_1 = 10K_2$)	135
Table 8.2	Properties of FPS for the analyses ($K_1 = 100K_2$)	138
Table 8.3	Properties of RR-FRBs for the analyses.	146
Table 8.4	Average interstory-drift.	151

1.INTRODUCTION

1.1 MOTIVATION

Many large urban areas, especially in developing countries, are extremely vulnerable to seismic events. Every day new housing buildings need to be constructed in nations with a significant population growth. Moreover, old existing buildings are generally vulnerable in case of an earthquake. Only to provide an example, cities such as Istanbul, Tehran, and Lima have thousands of buildings that were designed only for gravity loads, with no specific provisions for lateral loading. In historic downtowns, masonry buildings in the range of two to six stories are very common. Most of these structures have been constructed prior to the introduction of modern seismic codes. Some of them are valuable buildings and cannot be demolished and replaced. Retrofitting them by conventional methods would be costly and highly disruptive.

Based on these considerations, it is deemed that the introduction of a low-cost seismic isolation system can have a very high impact on the society. In fact, technology that can be easily produced by a relatively simple manufacturing process would stimulate base isolation applications for new constructions, as well as for the retrofitting of existing buildings.

1.2 OBJECTIVES AND SCOPE OF THE RESEARCH

Seismic isolation technology is currently applied mainly to computer centers, chip fabrication factories, emergency operation centers, and hospitals. The isolators used in these applications are expensive, large and heavy. In some cases an individual device can weight more than one ton. To significantly extend to housing, schools, and commercial buildings this valuable earthquake-resistant strategy, it is necessary to reduce the isolators' cost and weight. The primary weight in an isolator is due to the reinforcing steel plates, which are used to provide vertical stiffness. A typical rubber isolator has two large endplates (thickness around 20 mm), and several thin reinforcing plates (thickness around 2 mm). The high cost of producing conventional devices results from the labour involved in preparing them. In fact, the steel plates need to be bonded to the rubber layers with a vulcanization process. The steel plates are cut, sandblasted, acid cleaned, and then coated with a bonding compound. Next, the compounded rubber sheets with the interleaved

steel plates are put into a mold and heated under pressure for several hours to complete the manufacturing process [Gent 2001].

The main concept behind the research work herein presented is that the weight and the cost of an isolator can be diminished by eliminating the steel reinforcing plates and replacing them with fiber reinforcement. The novel idea is that a further substantial cost reduction is possible by using a recycled rubber compound as the one obtained by exhausted tyres or industrial leftovers. An innovative technology is therefore presented in this dissertation.

Different are the scopes of this work.

- To introduce RR-FRBs as a cost-effective alternative to conventional existing devices.
- To provide practical analytical tools for the study of RR-FRBs' mechanics.
- To assess the performances and the characteristics of RR-FRBs by means of Finite Element Analyses (FEAs), also for a comparison with the results of the developed analytical models.
- To determine recycled-rubber material properties with a campaign of laboratory tests.
- To conduct experimental analyses on real-scale RR-FRBs prototypes in order to determine the optimal configuration in terms of rubber compound and composite materials used for reinforcement.
- To assess the suitability of the proposed technology to decrease the seismic demand on a residential building.

The above objectives are achieved by:

- a) reviewing characteristics of existing rubber devices and comparing them versus the innovative ones;
- b) deriving closed-form solutions for the compression and shear behavior of flexible reinforced rubber bearings. The obtained solutions are based on principles of mechanics of solids, and represent a generalization of the classical theory currently used to describe the steel-reinforced isolators;
- c) performing advanced numerical analyses of rubber bearings with flexible reinforcement. The simulations are carried out with the general-purpose finite element program MSC.Marc 2005 [MSC.Software 2004];
- d) implementing an experimental campaign for tensile and shear tests of several recycled rubber compounds. The different rubber mixtures vary in density, chemical formulations of rubber aggregates (from tyres: SBR - Styrene Butadiene

- Rubber; from industrial leftovers: EPDM - Ethylene Propylene Diene Monomer), and physical configurations of the rubber particles (fiber, grains);
- e) evaluating the possibility of substituting the epoxy resin of Fiber Reinforced Polymers (FRPs) with a polyurethane matrix, as this is a common binder for recycled rubber;
 - f) implementing a testing program on bearing prototypes. Specimens are realized with different combinations of dimensions, rubber mixtures, number of layers, reinforcing materials (Carbon and Glass FRPs);
 - g) carrying out time history analyses of a building isolated with traditional and innovative bearings to compare the seismic demand on the superstructure for the different cases.

1.3 OUTLINE OF THE WORK

The report is organized into nine Chapters, whose contents are briefly herein described. A graphical representation of the structure of the thesis is reported in the flow chart of Figure 1.1.

The first Chapter illustrates the objective and scope of the study. It gives the general background motivation for a comprehensive study on RR-FRBs and illustrates the methodology developed in the research.

Chapter 2 presents a synthetic overview of base isolations concepts. Traditional devices characteristics are described, together with the innovative features of the proposed bearings.

Aiming to describe the behavior of FRBs in compression, in Chapter 3 simplified analytical models are proposed. The framework of the theoretical models is the well-known pressure solution proposed by Kelly in several works (*e.g.*, [Kelly 1999], [Kelly and Takhirov 2002]). In these works, solutions are given for pads of strip and square shape in compression. In the Chapter an extension of the formulations is proposed for circular bearings and for pads of generic shape. It is also shown how each formulation can be derived starting from the generic shape case. Theoretical solutions for strip shape and square bearings are re-arranged in order to propose consistent formulations and similarities in the results with different shapes models.

The FEAs of Chapter 4 are used as benchmark of the theoretical formulations for bearings of different shapes and dimensions both under compression and shear.

The theoretical solution for shear is presented in Chapter 5. In this section design formulas for determining FRBs' dimensions are also provided.

Chapter 6 presents the results of an extensive experimental campaign on rubber and FRPs. Tests were performed to characterize the behavior of recycled rubber in tension and shear. Moreover, also fiber reinforcement were tested especially to investigate

the possibility of substituting the, commonly used, epoxy matrix with a polyurethane binder.

The manufacture of real RR-FRBs prototypes and their testing is described in Chapter 7, wherein the behavior of bearings with different reinforcements, rubber types and geometries is analyzed in compression and shear.

A case study of a residential building application for seismic isolation is illustrated in Chapter 8. The building, already described in a previous PEER report by Taniwangsa and Kelly [1996], is used as benchmark in this research. The performances of the building with different base-isolation configurations are investigated. The comparison is made between the structural demand reductions obtained by Laminated Rubber Bearings (LRBs), Friction Pendulum System (FPS) and RR-FRBs. The numerical assessment indicates a very satisfactory performance of the proposed bearings.

Finally, Chapter 9 summarizes the most important results for the research. Conclusions are presented, as well as considerations and suggestions for further research and future developments.

Parts of this original research have been already published in scientific works. The formulations proposed in the Chapter 3 have been presented in [Calabrese *et al.* 2012], while the content of Chapters 3, 4 and 5 of the thesis has been published as a Pacific Earthquake Engineering Research (PEER) Report by Kelly and Calabrese [2012].

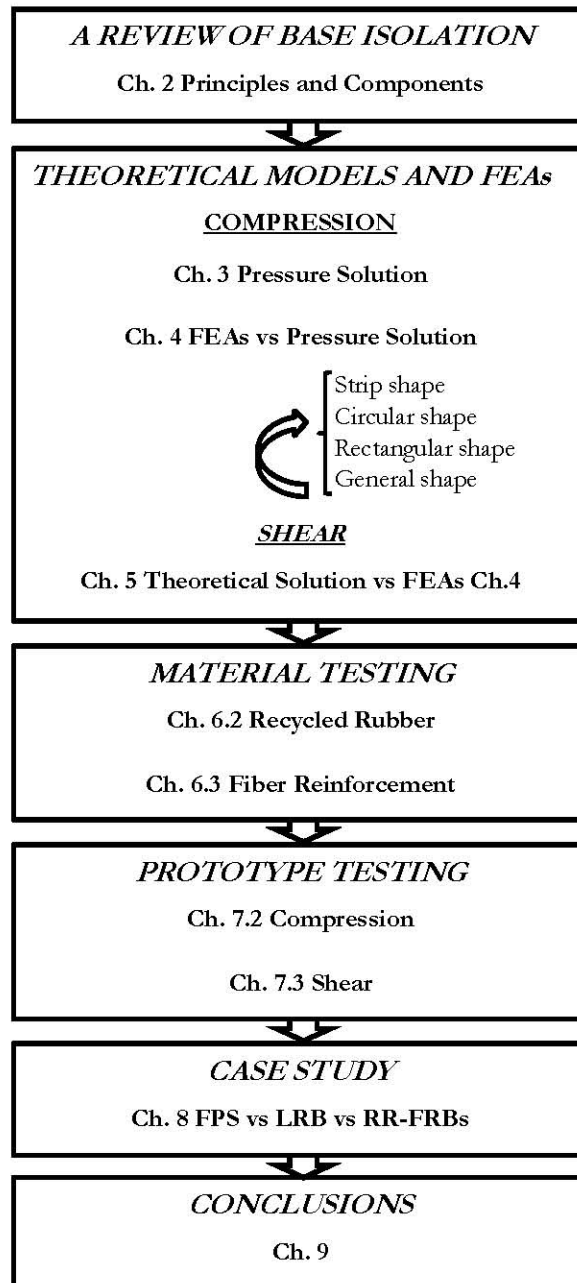


Figure 1.1

Thesis flow chart.

2.BASE ISOLATION: A BRIEF INTRODUCTION

2.1 INTRODUCTION

As an engineered application, base isolation is a relatively recent achievement. In fact, even if the possibility of decoupling the motion of the upper structure from the ground motion was supposed by different ancient civilizations, the first modern and scientific applications of the technology were realized only about fifty years ago [Kelly 1997]. In this Chapter are briefly covered the main concepts related to the seismic protection of the structures by base isolation. Basics theoretical principles are reported, together with a description of the devices commonly in use.

2.2 PRINCIPLES OF BASE ISOLATION

A detailed discussion of base isolation theory is given in several well consolidated references, (e.g.,[Naeim and Kelly 1999]). For this reason, in this paragraph only a few concepts are recalled. It is also noted that, despite wide variation in details, base isolation techniques basically follow two approaches.

The first approach consists in the introduction of an isolation layer with low horizontal stiffness. This layer is commonly placed between the structure and the foundation. The effect of a low horizontal stiffness at the isolation level is the decoupling of the building response from the horizontal components of the ground motion. As result, an isolated structure has a first dynamic mode involving only deformation at the isolators level, the structure above being rigid. The higher modes do not participate in the motion as they are orthogonal to the first mode and to the ground motion. An implication of this dynamic behavior is that the energy content at high frequencies of seismic events cannot be transmitted into the structure. For the concept expressed, base isolation is not based on energy dissipation, but rather on energy deflection. Generally, the effects of base isolation are described by analyzing the dynamic behavior of a two-degrees of freedom system, as the one represented in Figure 2.1. The mass of the superstructure of the system is m , and the mass above the isolation level is m_b . The stiffness of the structure is k_s , and its damping is c_s . The stiffness and the damping of the isolation layer are k_b and c_b . Assuming that $m < m_b$ but of the same order of magnitude, in the hypothesis of

$$\omega_b^2 / \omega_s^2 = O(10^{-2}) \quad (2.1)$$

where

$$\omega_b^2 = \frac{k_b}{m + m_b}, \quad \omega_s^2 = \frac{k_s}{m} \quad (2.2)$$

and considering a system with low damping, the uncoupled modal equations of motion can be derived. From the equations of motion, base isolation displacement and interstory-drift can be easily obtained [Naeim and Kelly 1999].

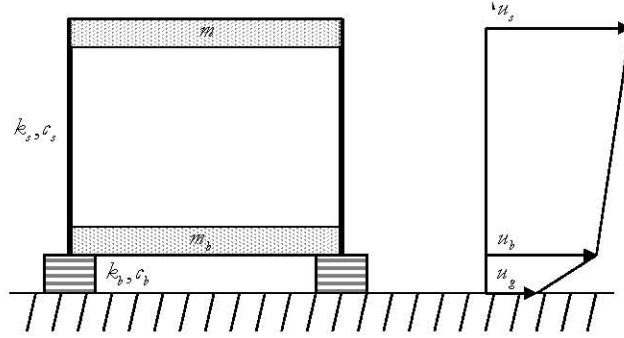


Figure 2.1 Two-degrees of freedom isolated structure.

In the previous assumptions it is demonstrated that, for a typical design spectrum, the isolation system can be designed for a relative base displacement of $S_D(\omega_b, \beta_b)$ and the building for a base shear coefficient of $S_A(\omega_b, \beta_b)$, where

$$\beta_b = \frac{c_b}{2\omega_b(m + m_b)} \quad (2.3)$$

When compared to the fixed base case, for a constant velocity spectrum, the reduction in base shear is equal to the frequencies ratio ω_b / ω_s . Moreover, it is also demonstrated that the first frequency of the two-degrees of freedom system is almost equal to ω_b .

It is important to mention that base isolation works for linear systems also if they are undamped. Damping is needed only to control a possible resonance at the isolation frequency and to reduce the horizontal displacements of the isolators. Moreover, it is analytically and experimentally demonstrated that when additional damping is added to the isolation system, the increased energy dissipation does not always lead to a decreased response of the structure. On the contrary, high energy dissipation at the isolation level

induces acceleration in the higher modes of the system. An high level of damping is not only unnecessary for base isolation, but also detrimental [Kelly 1999].

The second approach commonly used for base isolation consists in limiting the shear force transmitted to the structure across the isolation interface. This is done using sliders with a low level of friction. However, friction must be significantly high to sustain wind loading and small earthquakes without sliding. In this type of isolation system, the sliding displacements can be controlled by using a concave sliding surface or by laminated rubber bearings.

2.3 BASE ISOLATION COMPONENTS

A variety of seismic isolation bearings have been developed and implemented over the years. Most common bearings can be classified into two typologies: (a) elastomeric and (b) sliding. For both categories, this section briefly illustrates the main characteristics of the devices.

2.3.1 Rubber Bearings

A rubber bearing consists of a rubber block reinforced with many thin steel shims and two thick steel endplates (Figure 2.2).

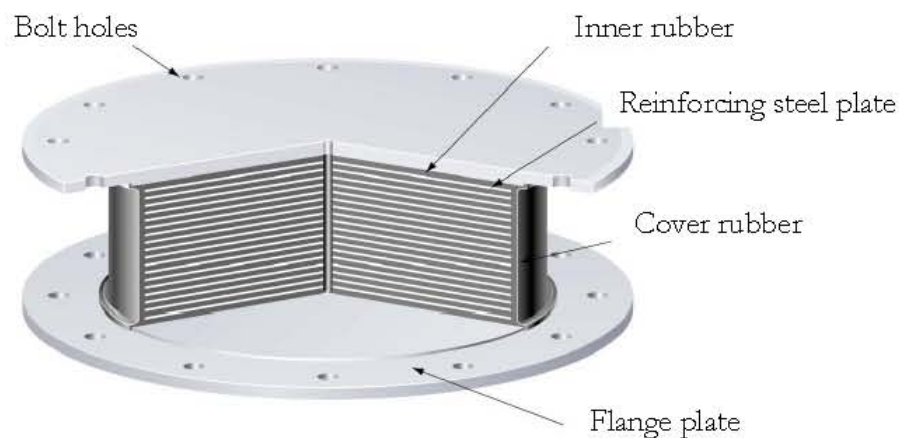


Figure 2.2 Schematic of Laminated Rubber Bearing.

These devices have a large field of applications. They are used in mechanical and automotive engineering for vibration control and in civil engineering for seismic isolation, vibration control and for the realization of expansion joints. Their invention is due to the famous engineer Eugène Freyssinet (1879-1962) that obtained a patent in 1954 for the

technology [Freyssinet 1954]. The essential characteristic of the elastomeric isolators is the very large ratio of the vertical stiffness relative to the horizontal stiffness. This feature is given by the reinforcing plates. Such plates prevent lateral bulging of the rubber, but allow the rubber to shear freely. The steel reinforcement also provides enhanced resistance of the isolator to bending moments, usually referred to as the “tilting stiffness”. This important design quantity makes the isolator stable also for large vertical loads [Simo and Kelly 1984]. Commonly the layers of rubber have thickness in the range of 3 to 10 mm and the steel plates of 2 to 5 mm. A rubber cover is provided to protect the internal rubber layers and steel plates from environmental degradation [Lake and Lindley 1967]. A characteristic of these isolators is the shape factor S , defined as the ratio of the loaded area over the free area. For circular isolators the usual shape factors value are in the range of 30 to 40, with maximum values of 45. In Japan are generally used devices with larger shape factors than in other countries [Pan *et al.* 2005]. This is primary done for the purpose of avoiding buckling in large deformations, and to ensure large vertical stiffness in order to minimize overturning effects. The second shape factor, S_2 , for a circular bearing is generally around 5. For a circular device, S_2 is the ratio of the diameter over the total thickness of the elastomer.

The key parameters in the design of laminated-rubber bearings are the gravity load carrying capacity, the lateral stiffness and the maximum achievable lateral displacement. For the carrying capacity, the vertical loads induced by the displacement of the structure need to be considered. The stiffness of the bearings directly influences the natural period of the structure. The maximum lateral displacement is limited by the overall stability of the device or the allowable strain in the elastomer. The horizontal stiffness and buckling of the steel reinforced isolator is modeled by an equivalent beam theory. This model assumes that a bearing with many discrete pads can be idealized as a continuous composite beam. The plane sections normal to the undeformed axis are considered to remain plane but not normal to the deformed axis, given the very low shear stiffness of the rubber and the flexural rigidity of the steel reinforcement.

The main drawbacks of this technology are its high production cost and the large weight of the devices. The latter is due to metallic shims and end plates. The high cost results from the labor involved in preparing the steel plates and the assembly of the rubber sheets and steel plates for vulcanization bonding in a mold. The steel plates are cut, sandblasted, acid cleaned, and then coated with a bonding compound. Next, the compounded rubber sheets with the interleaved steel plates are put into a mold and heated under pressure for several hours to complete the manufacturing process.

Manufacturers offer different types of rubber in terms of shear modulus, usually from 0.35 to 1 MPa. The design maximum shear strain is set to about 250% to 300%. The

dependency of vertical and lateral stiffness on creep, aging, vertical stress, shear strain, temperature, load history, frequency of loading cycles is verified by test series (*e.g.*, [Kelly and Quiroz 1990]). For rubber bearings are used natural or synthetic elastomers. The rubber and consequently the bearings can be categorized as: (a) low-damping; and (b) high-damping.

Low-damping natural rubber bearings exhibits nearly linear shear stress-strain behavior up to, approximately, 150% shear strain. For these devices the energy dissipation is proportional to the velocity, therefore they can be modelled by equivalent viscous damping. The damping ratio for bearings used in bridge engineering is commonly in the order of 5% to 10% of the critical at 100% shear strain. Given their quasi elastic force-displacement relationship, the devices are usually assumed to have recentering capacity and almost constant stiffness. Typically, supplemental damping devices are used in parallel with low-damping natural rubber bearings to limit the displacements.

Modern high-damping rubber bearings can produce damping up to 25% of critical at 300% shear strain [Pan *et al.* 2005]. This is obtained using special dissipative rubber compounds. However, high-damping rubber is more susceptible to property changes during cyclic loading and to aging effects. Different models to capture the by directional behavior of high damping laminated rubber bearings have been proposed (*e.g.*, [Grant *et al.* 2005]).

Another common rubber device is known as Lead-Rubber Bearing (LRB). This system was first introduced and used in New Zealand in the late 1970s [Robinson 1977] [Robinson 1982]. A common force displacement loop for LRBs is depicted in Figure 2.3.

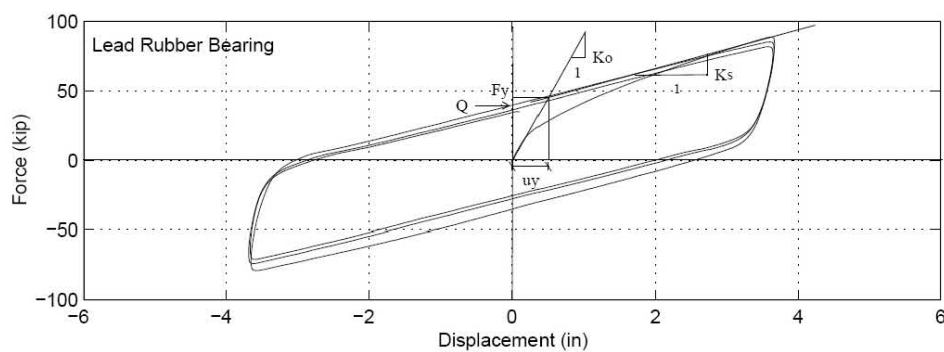


Figure 2.3 Hysteresis loops for a Lead Rubber Bearing (Courtesy of Prof. J.M.Kelly, University of California, Berkeley).

The construction process of lead-rubber bearings differs from rubber bearings only by a lead-plug that is press-fit into a central hole in the bearing. The plastic shear deformation of the lead plug dissipates energy, enhancing the dissipation capabilities of the device. In fact, lead behaves approximately as an elasto-plastic solid and yields in shear at a stress of about 10MPa. As shown in Figure 2.3, the energy dissipation mechanism is primary hysteretic. In Section 8.3 a bilinear model for LRBs is discussed and used for the preliminary design of a structure with different isolator configurations.

2.3.2 Friction Pendulum System

The Friction Pendulum System (FPS) is a friction-type sliding device. It consists of a single articulated slider moving on a concave surface. Figure 2.4 is a sectional view of a FPS bearing. The system uses gravity as restoring force. An high initial lateral stiffness before sliding has to be provided to resist wind loads. The main characteristic of a FPS is that the isolated period is only dependent on the curvature of the surface, and it is not affected by the weight of the superstructure. The initial stiffness significantly decreases once sliding is initiated. However, in order to reduce initial lateral stiffness values, that may promote higher modes vibration, FPSs can also be mounted on top of rubber bearings. The coefficient of friction depends primary on the vertical pressure and sliding velocities. It decreases with vertical pressure while the dependence on sliding velocities is less significant and tends to stabilize for velocities not smaller than 0.1m/s [Pan *et al.* 2005]. The single pendulum bearing maintains constant friction, lateral stiffness, and dynamic period for all levels of earthquake motion and displacements. A bilinear model for FPS bearings is discussed in Section 8.3 for the study of a prototype building isolated with different devices. A larger displacement capacity for these devices can be achieved by increasing the concave surface dimensions, but this causes a substantial cost increase. To reduce the cost and the dimensions of FPSs, evolutions of the technology have been proposed and validated. For instance, the double friction pendulum system introduced by Constantinou [2004] consists of a combination of two friction pendulum systems. More recently other sliding surfaces have been added to the system, the result is the Triple Friction Pendulum (TFP). A 3D view of a TFP bearing is shown in Figure 2.5. In the triple pendulum bearing, the three pendulum mechanisms are sequentially activated as the earthquake motions become stronger. Small earthquakes and high frequency ground motions are absorbed by the inner pendulum. For stronger earthquakes, both the bearing friction and period increase, resulting in lower bearing displacements and lower structure base shears. For the extreme events, both the bearing friction and lateral stiffness increase, reducing the bearing displacement. This behavior is obtained by using different radii of the sliding surfaces and different coefficients of friction. For a severe event, the plan dimensions of a triple pendulum bearing can be up to 40% of an equivalent single

surface device. Different models have proposed and experimentally validated to describe the nonlinearities and the kinematic of TFP bearings (e.g., [Becker and Mahin 2012]).

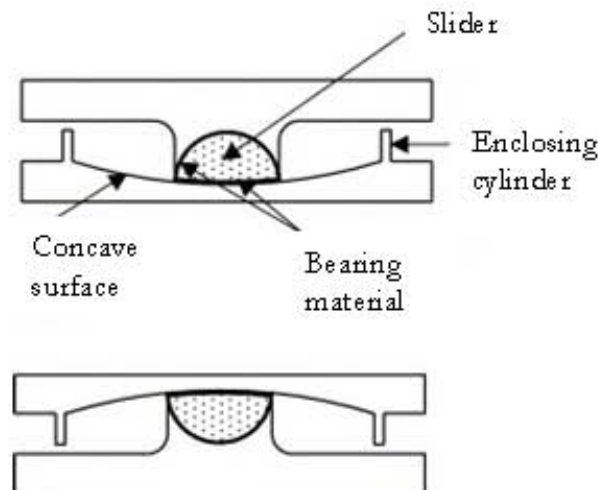


Figure 2.4 Schematic representation of a Friction Pendulum System (FPS) bearing

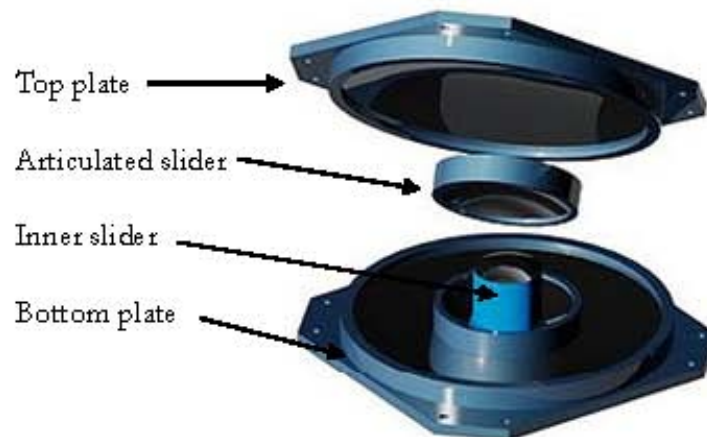


Figure 2.5 Three-dimensional view of a Triple Friction Pendulum (TFP) bearing (from [Dao *et al.*, 2013.]).

2.3.3 Fiber Reinforced Bearings

A Fiber Reinforced Bearing (FRB) in its displaced configuration is shown in Figure 2.6.

A FRB is a rubber device where the traditionally used steel reinforcements are replaced by fiber layers. These devices have been used mainly as bridge expansion joints. Studies on this technology started soon after World War II as a consequence of the need for a new generation of bridge bearings. In fact, the widespread use of bridges with long frames or curved and skewed structures increased the demand of structural devices leading to the development of more performing structural bearings [Caltrans 1994]. The experimental behavior of FRBs is been investigated by Kelly and Takhirov [2002]. A conclusion of the experimental campaign was the need of further studies to assess the possibility of using FRBs as seismic devices for base isolation of residential buildings in less developed countries. In fact, the main advantages of this technology are a lower weight and a lower cost when compared to more common rubber isolators. These two characteristic are very advantageous in order to promote seismic isolation applications on large scale.

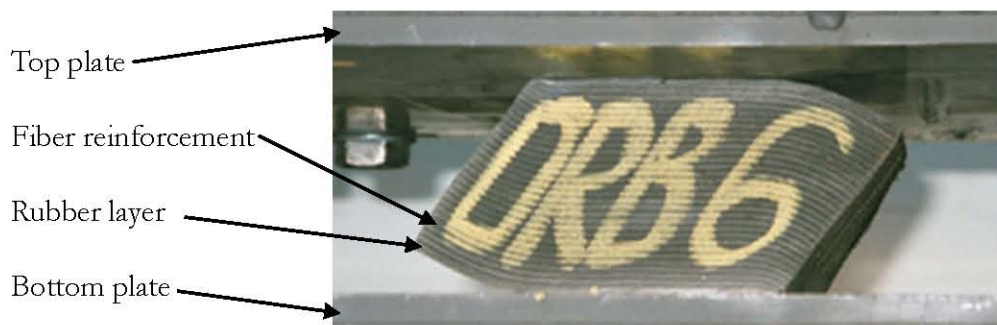


Figure 2.6 Displaced configuration of a Fiber Reinforced Bearing (Courtesy of Prof. J.M.Kelly. University of California, Berkeley).

For FRBs, the weight reduction is possible by using composite fiber materials for the reinforcement layers. These materials have an elastic stiffness that is of the same order of the steel one, but they have a much lighter weight. The cost saving is due to a less labor-intensive manufacturing process (compared to the one needed to produce traditional rubber bearings) which is allowed by the use of fibers. Another benefit of using fiber reinforcement is the possibility to build isolators in long rectangular strips, whereby individual isolators can be cut to the required size. In fact, all isolators are currently manufactured as either circular or square in the mistaken belief that if the isolation system for a building is to be isotropic, it needs to be made of symmetrically shaped isolators. Moreover, in some cases, rectangular isolators in the form of long strips would have distinct advantages over square or circular isolators. For example, when isolation is applied to buildings with structural walls, additional wall beams have to be used to carry

the load from isolator to isolator. With rectangular shaped devices, it could be possible to build the structural walls directly on top of the bearings, avoiding the use of connection beams. Moreover, thanks to the fiber reinforcement, FRBs could be easily cut to the required shapes and dimensions. In this way rectangular bearings could be obtained by long rectangular strips, and this is another significant economic advantage for the industrial production of these devices.

In FRBs, the fiber reinforcement is made up of many individual fibers grouped in strands and coiled into a cord of sub millimeter diameter. The cords are more flexible in tension than the individual fibers; therefore, they can stretch when the bearing is loaded by the weight of a building. On the other hand, they are completely flexible in bending, so the assumption made when modeling steel reinforced isolators that plane sections remain plane no longer holds. In order to predict the vertical stiffness, the stress distribution in the reinforcing layers and the deformation under loading of FRBs, the extensional flexibility of the fiber reinforcement needs to be incorporated into the theoretical solutions.

In this work the use of recycled rubber for a further reduction of the production costs of FRBs is proposed and investigated. Analytical models for the description of FRBs in compression (Chapter 3) and shear (Chapter 5) are numerically (Chapter 4 and Chapter 8) and experimentally validated (Chapter 6 and Chapter 7).

3.FLEXIBLE REINFORCED BEARINGS UNDER COMPRESSION

In this Chapter, the behavior of Fiber Reinforced Bearings under compression is described. A simplified solution is given to determine the vertical stiffness, the stress in the reinforcing layers and the deformation in the elastomer. The theoretical solution includes compressibility of the rubber and stretching of the reinforcing layers. A solution is derived for strip, circular and rectangular isolators. It is also shown a theoretical formulation for pads of generic shape, from which all the other cases can be derived. The results of the theoretical models are compared to Finite Element Analyses in Chapter 4.

3.1 INFINITELY LONG STRIP ISOLATORS

3.1.1 Equilibrium in Elastomeric Layer

A layer of elastomer in an infinitely long, rectangular isolator is shown in Figure 3.1. The elastomeric layer has a width of $2b$ and a thickness of t . The top and bottom surfaces of the layer are perfectly bonded to flexible reinforcements that are modeled as an equivalent sheet with a thickness of t_f . A coordinate system (x, y, z) is established by locating the origin at the center of the layer and the y coordinate direction is attached to the infinitely long side. Under the compression load P in the z direction, the deformation of the elastomer is in a plane strain state so that the displacement component in the y direction vanishes. The displacement components of the elastomer in the x and z coordinate directions, denoted as u and w , respectively, are assumed to have the form

$$u(x, z) = u_0(x) \left(1 - \frac{4z^2}{t^2} \right) + u_1(x) \quad (3.1)$$

$$w(x, z) = w(z) \quad (3.2)$$

In Equation (3.1), the term of u_0 represents the kinematic assumption that vertical lines in the elastomer become parabolic after deformation; the horizontal deformation is supplemented by additional displacement u_1 , which is constant through

the thickness and is intended to accommodate the stretch of the reinforcement. Equation (3.2) represents the assumption that horizontal planes in the elastomer remain planar after deformation. The elastomer is assumed to have linearly elastic behavior with incompressibility. The assumption of incompressibility means that the summation of normal strain components is negligible and produces a constraint on displacements in the form

$$u_{,x} + w_{,z} = 0 \quad (3.3)$$

where the commas imply partial differentiation with respect to the indicated coordinate.

Substitution of Equations (3.1) and (3.2) into the above equation gives

$$u_{0,x} \left(1 - \frac{4z^2}{t^2} \right) + u_{1,x} + w_{,z} = 0 \quad (3.4)$$

Integration through the thickness of the elastomer from $z = -t/2$ to $z = t/2$ leads to

$$u_{0,x} + \frac{3}{2} u_{1,x} = \frac{3}{2} \varepsilon_c \quad (3.5)$$

in which ε_c is the nominal compression strain defined as

$$\varepsilon_c = - \frac{w\left(\frac{t}{2}\right) - w\left(-\frac{t}{2}\right)}{t} \quad (3.6)$$

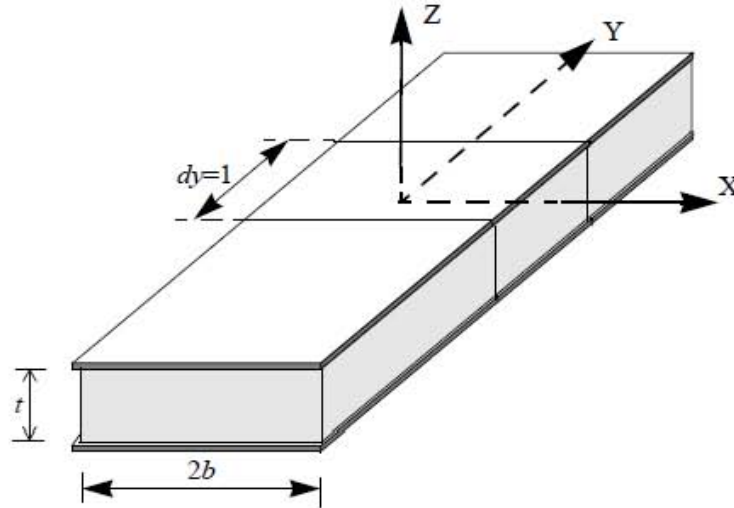


Figure 3.1 Infinitely long rectangular pad showing dimensions.

The stress state in the elastomer is assumed to be dominated by the internal pressure p , such that the normal stress components τ_{xx} and τ_{zz} are assumed as

$$\tau_{xx} \approx \tau_{zz} \approx -p \quad (3.7)$$

Under these stress assumptions, the equilibrium equation of the elastomer in the x direction

$$\tau_{xx,x} + \tau_{xz,z} = 0 \quad (3.8)$$

is reduced to

$$-p_{,x} + \tau_{xz,z} = 0 \quad (3.9)$$

The assumption of linearly elastic behavior for the elastomer means that

$$\tau_{xz} = G(u_{,z} + w_{,x}) \quad (3.10)$$

with G being the shear modulus of the elastomer. Using the displacement assumptions in Equations (3.1) and (3.2), the above equation becomes

$$\tau_{xz} = -8Gn_0 \frac{z}{t^2} \quad (3.11)$$

which gives, from Equation (3.9),

$$p_{,x} = -\frac{8G}{t^2} n_0 \quad (3.12)$$

Differentiating the above equation with respect to x and then combining the result with Equation (3.5) to eliminate the term of $n_{0,x}$, we have

$$p_{,xx} = \frac{12G}{t^2} (u_{1,x} - \varepsilon_e) \quad (3.13)$$

3.1.2 Equilibrium in Reinforcing Sheet

The deformation of the elastomeric layers bonded to the top and bottom surfaces of the reinforcing sheet generates the bonding shear stresses σ_{xz} on the surfaces of the reinforcing sheet, as shown in Figure 3.2.

In an infinitesimal width of the reinforcing sheet, dx , the internal normal force per unit length in the x direction, F , is related to these bonding shear stresses through the equilibrium equation

$$dF_{,x} + \left(\sigma_{xz} \Big|_{z=-\frac{t}{2}} - \sigma_{xz} \Big|_{z=\frac{t}{2}} \right) = 0 \quad (3.14)$$

The shear stresses acting on the top and bottom surfaces of the reinforcing sheet can be derived from Equation (3.11)

$$\sigma_{xz}\Big|_{z=\frac{t}{2}} = \frac{8G}{2t}u_0, \quad \sigma_{xz}\Big|_{z=-\frac{t}{2}} = -\frac{8G}{2t}u_0 \quad (3.15)$$

Substitution of these into Equation (3.14) gives

$$F_{,xx} = -\frac{8G}{t}u_0 \quad (3.16)$$

The displacement in the reinforcement is related to the internal normal forces through the linearly elastic strain-stress relation such that

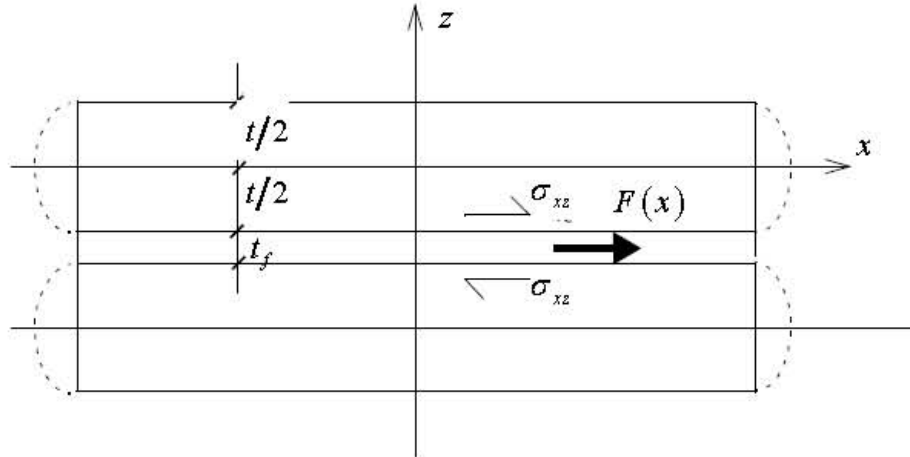


Figure 3.2 Forces in reinforcing sheet bonded to layers of elastomer.

$$\varepsilon_f = u_{1,x} = \frac{F}{E_f t_f} \quad (3.17)$$

where E_f is the elastic modulus of the reinforcement, and F is the internal normal force per unit length in the y direction. Combined with Equation (3.16) gives

$$u_{1,xx} = -\frac{8G}{E_f t_f t}u_0 \quad (3.18)$$

The complete system of equations is

$$p_{,xx} = -\frac{8Gu_0}{t^2} \quad (3.19)$$

$$u_{0,x} + \frac{3}{2}u_{1,x} = \frac{3\Delta}{2t} \quad (3.20)$$

$$u_{1,\infty} = -\frac{8G}{E_f t_f t} u_o \quad (3.21)$$

with boundary conditions or symmetric conditions as follows

$$u_0(0) = 0 \quad (3.22)$$

$$u_1(0) = 0 \quad (3.23)$$

$$\tau_{\infty}(\pm b) = 0 \quad (3.24)$$

$$F(\pm b) = 0 \quad (3.25)$$

Combining Equation (3.20) and Equation (3.21) to eliminate u_o , gives

$$u_{1,\infty} = -\frac{12G}{E_f t_f t} u_{1,x} = -\frac{12G}{E_f t_f t} \frac{\Delta}{t} \quad (3.26)$$

We define

$$\alpha = \sqrt{\frac{12Gb^2}{E_f t_f t}} \quad (3.27)$$

leading to

$$\frac{2}{3}u_1 = A + B \cosh \alpha x/b + C \sinh \alpha x/b + \frac{\Delta}{t}x \quad (3.28)$$

Symmetry suggests that $A=0$, $B=0$, giving

$$u_1 = C \sinh \alpha x/b + \frac{\Delta}{t}x \quad (3.29)$$

From Equation (3.17) we have

$$F = E_f t_f u_{1,x} = E_f t_f \left(\frac{\alpha}{b} C \cosh \alpha x/b + \frac{\Delta}{t} \right) \quad (3.30)$$

which with $F=0$ on $x=\pm b$ leads to

$$F(x) = \frac{\Delta}{t} E_f t_f \left(1 - \frac{\cosh \alpha x/b}{\cosh \alpha} \right) \quad (3.31)$$

The force and the displacement patterns for the reinforcement and the force in the reinforcement for various values of α are shown in Figure 3.3 and Figure 3.4. As the

reinforcement becomes more flexible, the displacement tends to be almost linear in x and the force is almost constant.

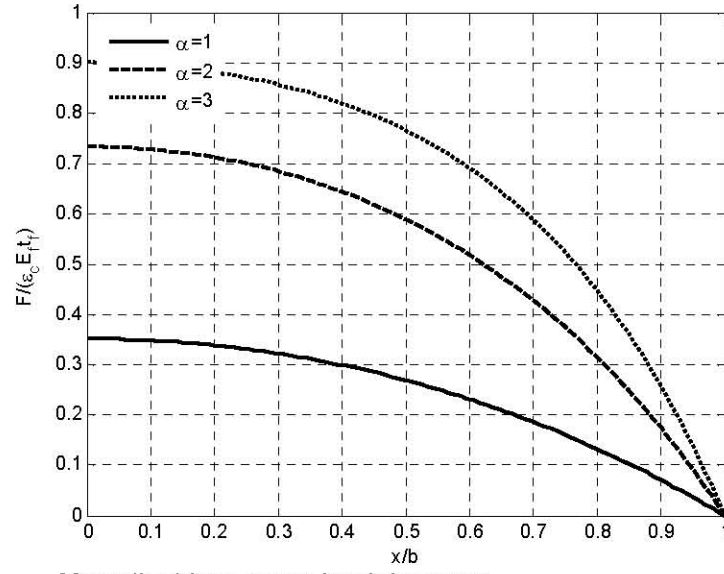


Figure 3.3

Normalized force pattern in reinforcement.

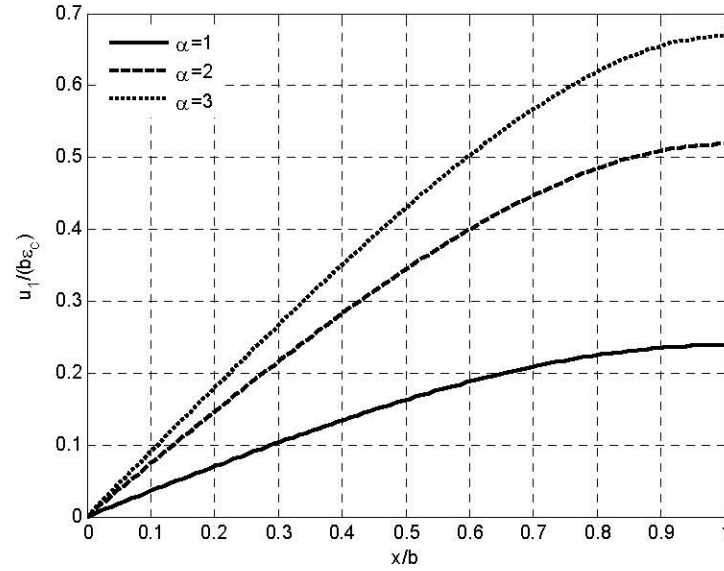


Figure 3.4

Displacement pattern for fiber reinforcement for various values of α .

3.1.3 Solution of Pressure and Effective Compressive Modulus

Equation (3.30) with $F=0$ on $\varkappa=\pm b$ leads to

$$u_1(\varkappa) = \frac{\Delta}{t} \left(\varkappa - \frac{b \sinh \alpha \varkappa / b}{\alpha \cosh \alpha} \right) \quad (3.32)$$

$$u_0(\varkappa) = \frac{3}{2} \frac{\Delta}{t} \frac{b \sinh \alpha \varkappa / b}{\alpha \cosh \alpha} \quad (3.33)$$

Also, using Equation (3.13) and the boundary condition $\tau_{\infty} = 0$ at $\varkappa = \pm b$ gives

$$p = \frac{\Delta E_f t_f}{t} \left(1 - \frac{\cosh \alpha \varkappa / b}{\cosh \alpha} \right) \quad (3.34)$$

The load per unit length of the strip, P , is given by

$$\begin{aligned} P &= \frac{E_f t_f}{t} 2 \int_0^b \left(1 - \frac{\cosh \alpha \varkappa / b}{\cosh \alpha} \right) d\varkappa \frac{\Delta}{t} = \\ &= \frac{2 E_f t_f}{\alpha t} b \left(\alpha - \tanh \alpha \right) \frac{\Delta}{t} \end{aligned} \quad (3.35)$$

This result can be interpreted as an effective compression modulus, E_e , given by

$$E_e = \frac{P}{A} \frac{t}{\Delta} = \frac{E_f t_f}{t} \left(1 - \frac{\tanh \alpha}{\alpha} \right) \quad (3.36)$$

We note that when $\alpha \rightarrow 0$, i.e., $E_f \rightarrow \infty$, we have $E_e \rightarrow 4GS^2$ as for rigid reinforced bearing. The formula also shows that $E_e < 4GS^2$ for all finite values of E_f .

The effect of the elasticity of the reinforcement on the various quantities of interest can be illustrated by a few examples. We normalize the compression modulus, E_e , by dividing by $4GS^2$, giving from Equation (3.36)

$$\frac{E_e}{4GS^2} = \frac{3}{\alpha^2} \left(1 - \frac{\tanh \alpha}{\alpha} \right) \quad (3.37)$$

which is shown in Figure 3.5 for $0 \leq \alpha \leq 5$; note how the stiffness decreases with decreasing E_f .

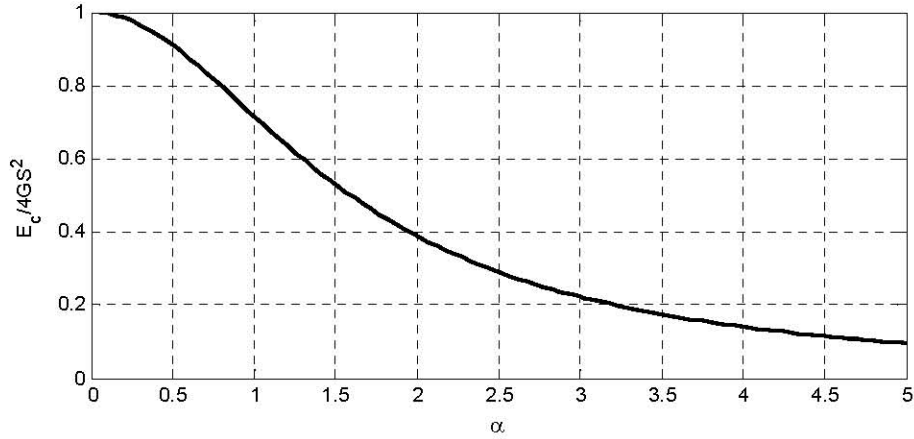


Figure 3.5 Variation of effective compression modulus with αb in infinitely long strip pad.

3.1.4 Flexible Reinforcement and Compressibility

In cases of large shape factors, to estimate E_c including compressibility in a manner consistent with the assumptions of the previous analysis, the equation of incompressibility is replaced by

$$\varepsilon_{xx} + \varepsilon_{yy} = -\frac{p}{K} \quad (3.38)$$

where K is the bulk modulus. Integration through the thickness leads to

$$\frac{2}{3}u_{0,x} + u_{1,x} + \frac{p}{K} = \varepsilon_c \quad (3.39)$$

This is then supplemented by the same equation of stress equilibrium and by the equation for the forces in the reinforcement. The system of equation for the combined effects of reinforcement flexibility and compressibility is now

$$p_{,x} = -\frac{8Gu_0}{t^2} \quad (3.40)$$

$$u_{1,xx} = -\frac{8Gu_0}{E_f t_f t} \quad (3.41)$$

$$\frac{2}{3}u_{0,x} + u_{1,x} + \frac{p}{K} = \varepsilon_c \quad (3.42)$$

Two dimensionless parameters, $\alpha = \sqrt{12Gb^2/E_f t_f t}$ and $\beta = \sqrt{12Gb^2/Kt^2}$, determine the comparative significance of flexibility in the reinforcement and compressibility in the elastomer.

In terms of α and β , Equation 3.40 and Equation 3.41 become

$$\left(\frac{p}{K}\right)_{,x} = \frac{2}{3}\beta^2 u_0 b^2 \quad (3.43)$$

$$u_{1,\infty} = -\frac{2}{3}\alpha^2 u_0 / b^2 \quad (3.44)$$

Differentiation of Equation 3.42 once and substitution of p and u_1 from Equations 3.43 and 3.44 gives

$$u_{0,\infty} - \frac{(\alpha^2 + \beta^2)}{b^2} u_0 = 0 \quad (3.45)$$

from which we have

$$u_0 = A \cosh \lambda x / b + B \sinh \lambda x / b \quad (3.46)$$

where

$$\lambda^2 = \alpha^2 + \beta^2 \quad (3.47)$$

In turn, using Equation 3.40 and Equation 3.41 gives solution for p and u_1 in the forms

$$u_1 = -\frac{2}{3}\frac{\alpha^2}{\lambda^2} A \cosh \lambda x / b + -\frac{2}{3}\frac{\alpha^2}{\lambda^2} B \sinh \lambda x / b + C_1 x + D \quad (3.48)$$

and

$$\frac{p}{K} = -\frac{2}{3}\frac{\beta^2}{\lambda b} A \sinh \lambda x / b + -\frac{2}{3}\frac{\beta^2}{\lambda b} B \cosh \lambda x / b + C_2 \quad (3.49)$$

The constants of integration are, of course, not independent of each other but are related through the basic equations. Substitution of three solutions into Equation 3.49 gives

$$\begin{aligned} & \frac{2}{3}\frac{\lambda}{b} (A \sinh \lambda x / b + B \cosh \lambda x / b) + \\ & -\frac{2}{3}\frac{\alpha^2}{\lambda b} (A \sinh \lambda x / b + B \cosh \lambda x / b) - \\ & + C_1 - \frac{2}{3}\frac{\beta^2}{\lambda} (A \sinh \lambda x / b + B \cosh \lambda x / b) + C_2 = \varepsilon_e \end{aligned} \quad (3.50)$$

The coefficients of $\sinh \beta x / b$ and $\cosh \beta x / b$ vanish and the result is $C_1 + C_2 = \varepsilon_e$.

For the particular problem of compression of the strip it is convenient to use the symmetry of the solutions. Thus u_0 and u_1 are anti-symmetric and p is symmetric on $-b \leq x \leq +b$. It follows that $A=0$ and $D=0$ giving

$$u_0 = B \sinh \lambda x / b \quad (3.51)$$

$$u_1 = -\frac{2}{3} \frac{\alpha^2}{\lambda^2} B \sin \lambda x / b + C_1 x \quad (3.52)$$

$$\frac{p}{K} = -\frac{2}{3} \frac{\beta^2}{\lambda b} B \cosh \lambda x / b + \varepsilon_c - C_1 \quad (3.53)$$

The boundary conditions for B and C_1 are that the pressure p at the edges $x = \pm b$ is zero and that the stress in the reinforcement $E_f u_{1,x}$ also vanishes at the edges. Thus

$$-\frac{2}{3} \frac{\alpha^2}{\lambda b} B \cos \lambda + C_1 = 0 \quad (3.54)$$

$$-\frac{2}{3} \frac{\beta^2}{\lambda b} B \cosh \lambda - C_1 = -\varepsilon_c \quad (3.55)$$

giving

$$B = \frac{3}{2} \frac{\lambda}{\alpha^2 + \beta^2} b \frac{1}{\cosh \lambda} \varepsilon_c \quad (3.56)$$

$$C_1 = \frac{\alpha^2}{\alpha^2 + \beta^2} \varepsilon_c \quad (3.57)$$

and the solution becomes

$$u_0 = \frac{3}{2} b \frac{\sinh \lambda x / b}{\alpha \cosh \lambda} \varepsilon_c \quad (3.58)$$

$$u_1 = b \frac{\alpha^2}{\alpha^2 + \beta^2} \left(\frac{x}{b} - \frac{\sinh \lambda x / b}{\lambda \cosh \lambda} \right) \varepsilon_c \quad (3.59)$$

and

$$\frac{p}{K} = \frac{\beta^2}{\alpha^2 + \beta^2} \left(1 - \frac{\cosh \lambda x / b}{\cosh \lambda} \right) \varepsilon_c \quad (3.60)$$

Integration of p from Equation 3.60 gives

$$E_c = K \frac{\beta^2}{\alpha^2 + \beta^2} \left(1 - \frac{\tanh \lambda}{\lambda} \right) \quad (3.61)$$

If the effect of compressibility is negligible, then $\beta \rightarrow 0$ and $\lambda = \alpha$, resulting in

$$K\beta^2 = \frac{12Gb^2}{t^2} \quad (3.62)$$

giving

$$E_e = \frac{E_f t_f}{t} \left(1 - \frac{\tanh \alpha}{\alpha} \right) \quad (3.63)$$

which is the same as the result in the previous section. On the other hand, if the flexibility of the reinforcement is negligible, then $\alpha \rightarrow 0$ and $\lambda \rightarrow \beta$, giving

$$E_e = K \left(1 - \frac{\tanh \beta}{\beta} \right) \quad (3.64)$$

If the compression modulus is normalized by $4GS^2$, then from Equation 3.63 it comes

$$\frac{E_e}{4GS^2} = \frac{3}{\alpha^2 + \beta^2} \left(1 - \frac{\tanh(\alpha^2 + \beta^2)^{1/2}}{(\alpha^2 + \beta^2)^{1/2}} \right) \quad (3.65)$$

which demonstrates that the vertical stiffness is reduced by both compressibility in the elastomer and flexibility in the reinforcement. Figure 3.6 shows the variation of normalized effective compression modulus with α and β , while Figure 3.7 shows the variation of normalized effective compression modulus with β for various values of α , from $\alpha = 0$ to $\alpha = 3$.

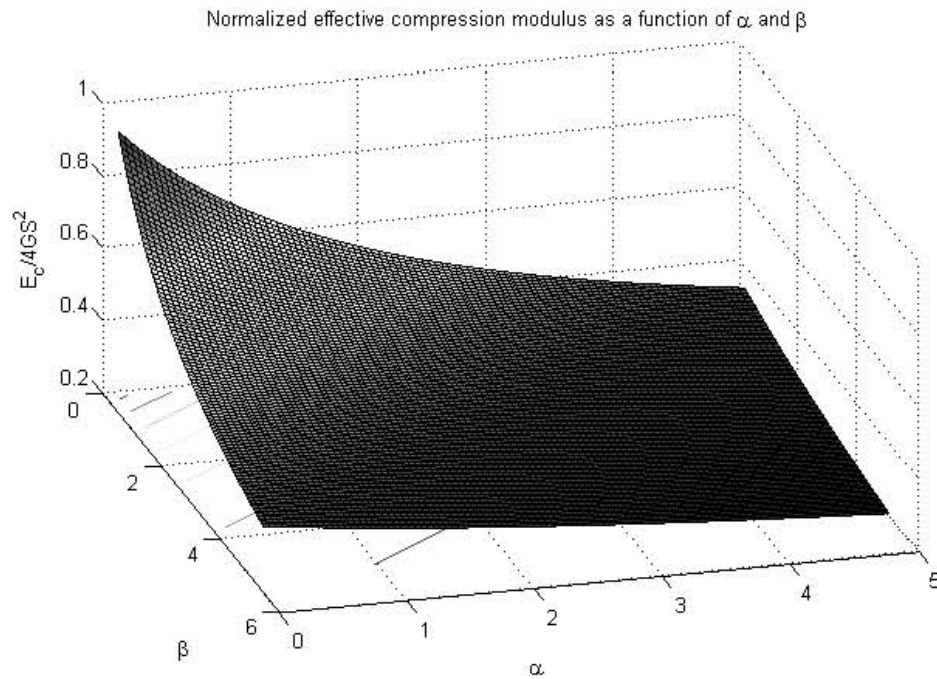


Figure 3.6 Variation of normalized effective compression modulus with α and β , in an infinitely long strip pad.

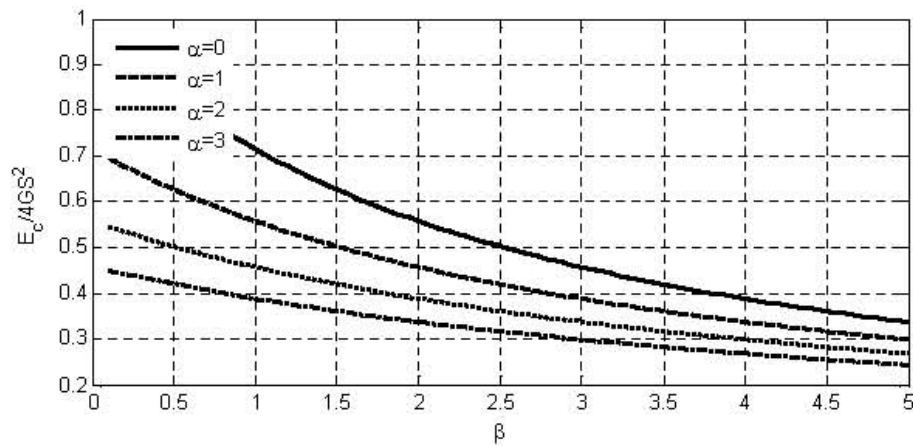


Figure 3.7 Variation of normalized effective compression modulus with β for $\alpha = 0-3$.

3.2 CIRCULAR PAD

3.2.1 Deformation of Pad under Compression

The circular pad shown in Figure 3.8 has a radius of R and a thickness of t , in which we locate a cylindrical coordinate system, (r, θ, z) , in the middle surface of the pad. The displacements of the elastomer along the r and z directions, denoted as u_r , are assumed to have the forms

$$\begin{aligned} u_r(r, z) &= u_0(r) \left(1 - \frac{4z^2}{t^2} \right) + u_1(r) \\ w(r, z) &= w(z) \end{aligned} \quad (3.66)$$

In the first equation, the term of u_0 represents the kinematic assumption of quadratically varied deformation of the vertical lines in the elastomer and is supplemented by additional displacement u_1 to accommodate the stretch of the reinforcement. The second equation represents the assumption that horizontal plane remain planar after deformation in the elastomer.

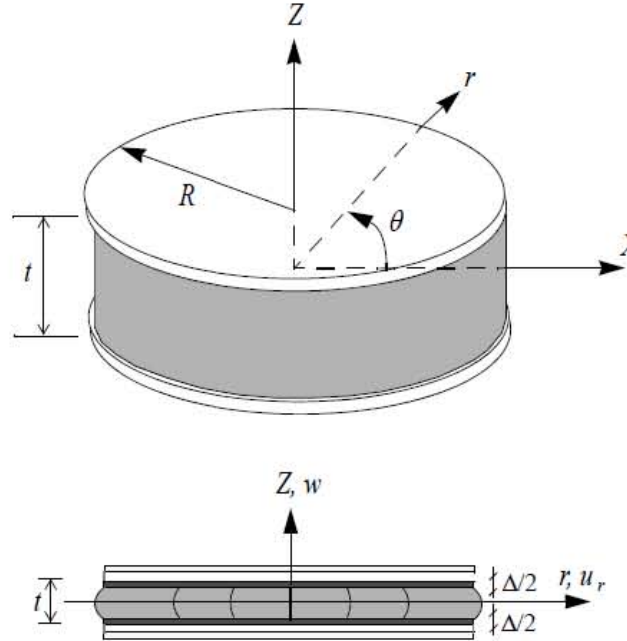


Figure 3.8 Coordinate system for a circular pad of radius R .

If the assumption of incompressibility were to be made, further constraint on the three components of strain, $\varepsilon_r, \varepsilon_\theta, \varepsilon_z$, in the form $\varepsilon_r + \varepsilon_\theta + \varepsilon_z = 0$ would be needed; but when the material is assumed to be compressible with bulk modulus K , this constraint is replaced by

$$\varepsilon_r + \varepsilon_\theta + \varepsilon_z = -\frac{p}{K} \quad (3.67)$$

where p is the pressure in the elastomer. The three normal strains are given by

$$\begin{aligned} \varepsilon_r &= \frac{du_r}{dr} = \frac{du_0}{dr} \left(1 - \frac{4z^2}{t^2} \right) \frac{du_1}{dr} \\ \varepsilon_\theta &= \frac{1}{r} u_r = \frac{1}{r} \left(1 - \frac{4z^2}{t^2} \right) \frac{1}{r} u_1 \\ \varepsilon_z &= \frac{dw}{dz} \end{aligned} \quad (3.68)$$

leading to

$$\left(\frac{du_0}{dr} + \frac{1}{r} u_0 \right) \left(1 - \frac{4z^2}{t^2} \right) + \frac{du_1}{dr} + \frac{1}{r} u_1 + \frac{dw}{dz} = -\frac{p}{K} \quad (3.69)$$

which, when integrated through the thickness with respect to z , leads to

$$\left(\frac{du_0}{dr} + \frac{1}{r} u_0 \right) + \frac{3}{2} \left(\frac{du_1}{dr} + \frac{1}{r} u_1 \right) = \frac{3\Delta}{2t} - \frac{3p}{2K} \quad (3.70)$$

The stress state is assumed to be dominated by the internal pressure, p , such that the normal stress components, $\sigma_r, \sigma_\theta, \sigma_z$, differ from $-p$ only by terms of order $(t^2/R^2)p$, i.e.,

$$\sigma_r \approx \sigma_\theta \approx \sigma_z \approx -p \quad (3.71)$$

The shear stress component, τ_{rz} , which is generated by the constraints at the top and bottom of the pad, is assumed to be of order $(t/R)p$. The equation of stress equilibrium in the rubber along the radial direction

$$\frac{d\sigma_r}{dr} + \frac{d\tau_{rz}}{dz} + \frac{\sigma_r - \sigma_\theta}{r} = 0 \quad (3.72)$$

reduces to

$$\frac{d\tau_{rz}}{dz} = \frac{dp}{dr} \quad (3.73)$$

The assumption of elastic behavior means that

$$\tau_{rz} = G\gamma_{rz} \quad (3.74)$$

in which G is the shear modulus of the rubber and γ_{rz} is the shear strain with

$$\gamma_{rz} = -\frac{8z}{t^2}u_0 \quad (3.75)$$

These give

$$\frac{dp}{dr} = -\frac{8Gu_0}{t^2} \quad (3.76)$$

The internal forces per unit length in the reinforcing sheet are denoted by N_r in the radial r direction and N_θ in the tangential direction. If the sheet is made of fiber reinforcement, the individual fibers are replaced by an equivalent sheet of reinforcement of thickness t_f . As shown in Figure 3.2, the internal forces of the equivalent reinforcing sheet are related to the shear stresses on the top and bottom of the pad through the equilibrium equation

$$\frac{dN_r}{dr} + \frac{N_r - N_\theta}{r} - \tau_{rz}\Big|_{z=\frac{t}{2}} + \tau_{rz}\Big|_{z=-\frac{t}{2}} = 0 \quad (3.77)$$

From Equations (3.74) and (3.75) it results

$$\tau_{rz}\Big|_{z=\frac{t}{2}} = -\frac{8Gu_0}{2t}; \tau_{rz}\Big|_{z=-\frac{t}{2}} = \frac{8Gu_0}{2t} \quad (3.78)$$

giving

$$\frac{dN_r}{dr} + \frac{N_r - N_\theta}{r} = -\frac{8Gu_0}{t} \quad (3.79)$$

The extensional strains in the reinforcement are

$$\varepsilon_r^f = \frac{du_1}{dr}; \varepsilon_\theta^f = \frac{1}{r}u_1 \quad (3.80)$$

which are related to the internal forces through the elastic modulus E_f and Poisson's ratio ν of the equivalent sheet and its thickness t_f such that

$$\varepsilon_r^f = \frac{N_r - \nu N_\theta}{E_f t_f}; \varepsilon_\theta^f = \frac{-\nu N_r + N_\theta}{E_f t_f} \quad (3.81)$$

and by inversion

$$N_r = \frac{E_f t_f}{1-\nu^2} (\varepsilon_r^f + \nu \varepsilon_\theta^f); N_\theta = \frac{E_f t_f}{1-\nu^2} (\nu \varepsilon_r^f + \varepsilon_\theta^f) \quad (3.82)$$

Substitution of these relationships into the equation of equilibrium for the reinforcement, Equation (3.79), gives

$$u_0 = -\frac{E_f t_f}{8(1-\nu^2)G} \left[\frac{d^2 u_1}{dr^2} + \nu \frac{d}{dr} \left(\frac{u_1}{r} \right) - \right. \\ \left. + (1-\nu) \frac{1}{r} \frac{du_1}{dr} - (1-\nu) \frac{u_1}{r^2} \right] \quad (3.83)$$

which reduces to

$$u_0 = -\frac{3R^2}{2\alpha^2} \left(\frac{d^2 u_1}{dr^2} + \frac{1}{r} \frac{du_1}{dr} - \frac{u_1}{r^2} \right) = -\frac{3R^2}{2\alpha^2} \left(\frac{d}{dr} \left(\frac{du_1}{dr} + \frac{1}{r} u_1 \right) \right) \quad (3.84)$$

in which a non-dimensional parameter α can be defined as

$$\alpha^2 = \frac{12(1-\nu^2)GR^2}{E_f t_f} \quad (3.85)$$

A second non-dimensional parameter β is defined as

$$\beta^2 = \frac{12GR^2}{Kt^2} \quad (3.86)$$

in terms of which the equilibrium equation of the elastomer can be written as

$$\frac{d(p/K)}{dr} = -\frac{2\beta^2 u_0}{3R^2} \quad (3.87)$$

It is convenient at this point to collect together the three equations for the three unknown functions u_0 , u_1 and p in the form,

$$\frac{d(p/K)}{dr} = -\frac{2\beta^2 u_0}{3R^2} \quad (3.88)$$

$$\frac{d}{dr} \left(\frac{du_1}{dr} + \frac{1}{r} u_1 \right) = -\frac{2\alpha^2 u_0}{3R^2} \quad (3.89)$$

$$\frac{2}{3} \left(\frac{du_0}{dr} + \frac{1}{r} u_0 \right) + \left(\frac{du_1}{dr} + \frac{1}{r} u_1 \right) = \frac{\Delta}{t} - \frac{p}{K} \quad (3.90)$$

Differentiation of the third equation and substitution of p and u_1 from the first and second equation leads to

$$\frac{2}{3} \left(\frac{du_0}{dr} + \frac{1}{r} u_0 \right) - \frac{\alpha^2 + \beta^2}{R^2} u_0 = 0 \quad (3.91)$$

It is now clear that two apparently unrelated effects of stretching of the reinforcement and compressibility of the elastomer affect the solution in the same way: the parameter α solely determines the effect of stretching and β that of compressibility. At this point it is convenient to define another parameter λ through

$$\lambda^2 = \alpha^2 + \beta^2 \quad (3.92)$$

The solution of Equation (3.91) is

$$u_0(r) = \mathcal{A} I_1(\lambda(r/R)) + B K_1(\lambda(r/R)) \quad (3.93)$$

where \mathcal{A} and B are constants of integration and I_n, K_n are modified Bessel functions of the first and second kind of order n . In turn, substitution of this into the first two equations provides the solutions for p and u_1 in the forms

$$p/K = -\frac{2\beta^2}{3\lambda R} \left(\frac{\mathcal{A} I_0(\lambda(r/R))}{-B K_0(\lambda(r/R))} \right) + C_1 \quad (3.94)$$

and

$$u_1(r) = -\frac{2\alpha^2}{3\lambda^2} \left(\frac{\mathcal{A} I_1(\lambda(r/R))}{+B K_1(\lambda(r/R))} \right) + \frac{C_2}{2} r + \frac{D}{r}. \quad (3.95)$$

The constants of integration \mathcal{A} , B , C_1 , C_2 , and D are not independent but are related through the compressibility constraint equation. Substitution of the three solutions into Equation (3.70) gives

$$\begin{aligned} & \frac{2}{3} \left[\frac{1}{r} \frac{d}{dr} \left(\mathcal{A} r I_1(\lambda(r/R)) + B r K_1(\lambda(r/R)) \right) \right] + \\ & - \frac{2\alpha^2}{3\lambda^2} \left[\frac{1}{r} \frac{d}{dr} \left(\mathcal{A} r I_1(\lambda(r/R)) \right) \right] - \\ & + \left[\frac{1}{r} \frac{d}{dr} \left(\frac{C_2 r^2}{2} + D \right) \right] + \\ & - \frac{2\beta^2}{3\lambda R} \left[\frac{\mathcal{A} I_0(\lambda(r/R))}{+B K_0(\lambda(r/R))} \right] - \\ & + C_1 = \epsilon_i \end{aligned} \quad (3.96)$$

The first expression becomes

$$\begin{aligned}
& \frac{2}{3} \left[\frac{1}{r} \frac{d}{dr} \left(\mathcal{A} r I_1 \left(\lambda r / R \right) + B r K_1 \left(\lambda r / R \right) \right) \right] = \\
& \frac{2\mathcal{A}}{3r} \left[I_1 \left(\lambda r / R \right) + \frac{r\lambda}{R} I_0 \left(\lambda r / R \right) + \right. \\
& \quad \left. - r \left(\frac{R}{\lambda r} \right) I_1 \left(\lambda r / R \right) \right] - \\
& + \frac{2B}{3r} \left[K_1 \left(\lambda r / R \right) + \frac{r\lambda}{R} K_0 \left(\lambda r / R \right) \cdot \right. \\
& \quad \left. \cdot \left(-r \left(\frac{R}{\lambda r} \right) K_1 \left(\lambda r / R \right) \right) \right] \\
& = \frac{2}{3} \mathcal{A} \frac{\lambda}{R} I_0 \left(\lambda r / R \right) + \frac{2}{3} B \frac{\lambda}{R} K_0 \left(\lambda r / R \right)
\end{aligned} \tag{3.97}$$

The second term becomes by the same process

$$-\frac{2\alpha^2}{3\lambda^2} \left[\mathcal{A} \frac{\lambda}{R} I_0 \left(\lambda r / R \right) + B \frac{\lambda}{R} K_0 \left(\lambda r / R \right) \right] + C_1 + 0 \tag{3.98}$$

which with

$$p/K = -\frac{2\beta^2}{3\lambda R} \left(\mathcal{A} I_0 \left(\lambda(r/R) \right) + B K_0 \left(\lambda(r/R) \right) \right) + C_1 \tag{3.99}$$

leads to the result that the terms multiplied by \mathcal{A} and B both vanish, D drops out, and we find

$$C_1 + C_2 = \varepsilon_c \tag{3.100}$$

If the pad is annular, $a \leq r \leq b$, then there are four boundary conditions for the four constants \mathcal{A} , B , C_1 , and D namely,

$$\begin{aligned}
N_r(a) &= 0 & N_r(b) &= 0 \\
p(a) &= 0 & p(b) &= 0
\end{aligned} \tag{3.101}$$

If the pad is a complete circle of radius R , i.e., $0 \leq r \leq R$, we have $N_r(R) = 0$ and $p(R) = 0$, and boundedness of u_1 and p at $r = 0$. In fact, by the assumption of radial symmetry, $u_1(0) = 0$.

Since $K_1(x) \rightarrow \ln \frac{1(2)}{x}$ as $x \rightarrow 0$, we must have $B = 0$ and $D = 0$. With these simplifications the solutions for the complete circular pad become

$$u_0(r) = \mathcal{A} I_1 \left(\lambda(r/R) \right) \tag{3.102}$$

$$p/K = -\frac{2\beta^2}{3\lambda R} \left(\mathcal{A}I_0(\lambda(r/R)) \right) + C_1 \quad (3.103)$$

$$u_1(r) = -\frac{2\alpha^2}{3\lambda^2} \left(\mathcal{A}I_1(\lambda(r/R)) \right) + \frac{\varepsilon_c - C_1}{2} r \quad (3.104)$$

The condition that the pressure is zero at the boundary $r=R$ means that

$C_1 = \frac{2\beta^2}{3\lambda R} \mathcal{A}I_0(\lambda)$; thus the pressure is given by

$$p/K = \frac{2\beta^2}{3\lambda R} \mathcal{A} \left(I_0(\lambda) - I_0(\lambda(r/R)) \right) \quad (3.105)$$

The remaining constant of integration must be determined from the requirement that the radial stress in the reinforcement is zero at the edge, $r=R$. From Equation (3.81) it comes

$$\begin{aligned} \varepsilon_r^f &= -\frac{2\alpha^2}{3\lambda R} \mathcal{A} \left[\frac{I_0(\lambda(r/R))}{\lambda(r/R)} + \frac{1}{\lambda(r/R)} I_1(\lambda(r/R)) \right] + \frac{1}{2}(\varepsilon_c - C_1) \\ \varepsilon_\theta^f &= -\frac{2\alpha^2}{3\lambda R} \mathcal{A} \left[\frac{1}{\lambda(r/R)} I_1(\lambda(r/R)) \right] + \frac{1}{2}(\varepsilon_c - C_1) \end{aligned} \quad (3.106)$$

thus

$$\begin{aligned} N_r(r) &= \frac{E_f t_f}{1-\nu^2} \left\{ -\frac{2\alpha^2}{3\lambda R} \mathcal{A} \left[\frac{I_0(\lambda(r/R))}{\lambda(r/R)} + \frac{1-\nu}{\lambda(r/R)} I_1(\lambda(r/R)) \right] - \right. \\ &\quad \left. + (1+\nu) \frac{1}{2}(\varepsilon_c - C_1) \right\} \\ N_\theta(r) &= \frac{E_f t_f}{1-\nu^2} \left\{ -\frac{2\alpha^2}{3\lambda R} \mathcal{A} \left[\frac{\nu I_0(\lambda(r/R))}{\alpha R} + \frac{1-\nu}{\alpha R} I_1(\lambda(r/R)) \right] - \right. \\ &\quad \left. + (1+\nu) \frac{1}{2}(\varepsilon_c - C_1) \right\} \end{aligned} \quad (3.107)$$

The requirement that $N_r(R) = 0$ means

$$\begin{aligned} &-\frac{2\alpha^2}{3\lambda R} \mathcal{A} \left[I_0(\lambda) - \frac{1-\nu}{\lambda} I_1(\lambda) \right] + \\ &-\frac{2\beta^2}{3\lambda R} \frac{1+\nu}{2} \mathcal{A}I_0(\lambda) = -(1+\nu) \frac{1}{2} \varepsilon_c \end{aligned} \quad (3.108)$$

leading to

$$A = \frac{\varepsilon_c(1+\nu)}{2} \left\{ \frac{1}{\frac{2\alpha^2}{3\lambda R} \left[I_0(\lambda) - \frac{1-\nu}{\lambda} I_1(\lambda) \right] - \frac{2\beta^2}{3\lambda R} \frac{1+\nu}{2} I_0(\lambda)} \right\} \quad (3.109)$$

$$u_1(r) = \frac{\Delta}{2t} \left\{ r - \frac{(1+\nu)I_1(\alpha r)}{\alpha \left[I_0(\alpha r) - \frac{1-\nu}{\alpha r} I_1(\alpha r) \right]} \right\} \quad (3.110)$$

$$N_r(r) = \frac{E_f t_f}{2(1-\nu)} \frac{\Delta}{t} \left[1 - \frac{I_0(\alpha r) - \frac{1-\nu}{\alpha r} I_1(\alpha r)}{I_0(\alpha R) - \frac{1-\nu}{\alpha R} I_1(\alpha R)} \right] \quad (3.111)$$

$$N_\theta(r) = \frac{E_f t_f}{2(1-\nu)} \frac{\Delta}{t} \left[1 - \frac{\nu I_0(\alpha r) + \frac{1-\nu}{\alpha r} I_1(\alpha r)}{I_0(\alpha R) - \frac{1-\nu}{\alpha R} I_1(\alpha R)} \right] \quad (3.112)$$

3.2.2 Compression Stiffness and Pressure Distribution

The vertical stiffness of a rubber bearing is given by the formula

$$K_V = \frac{E_c A}{t_r} \quad (3.113)$$

where A is the area of the bearing, t_r is the total thickness of rubber in the bearing, and E_c is the instantaneous compression modulus of the rubber-steel composite under the specified level of vertical load. The value of E_c for a single rubber layer is controlled by the shape factor, S , defined as $S = \text{the loaded area/free area}$, a dimensionless measure of the aspect ratio of the single layer of the elastomer. For a circular pad of radius R and thickness t ,

$$S = R/2t \quad (3.114)$$

To determine the compression modulus, E_c , p is integrated over the area to determine the resultant normal load, P ; E_c is then given by

$$E_c = P / \mathcal{A} \varepsilon_c \quad (3.115)$$

where $\mathcal{A} = \pi R^2$ is the area of the pad and $\varepsilon_c = \Delta/t$ is the compression strain.

The total axial load P is

$$P = 2\pi \int_0^R p(r) r dr \quad (3.116)$$

where $p(r)$ from Equation (3.103) can be written as

$$p = \frac{8GR}{\lambda t^2} \mathcal{A} \left(I_0(\lambda) - I_0(\lambda(r/R)) \right) \quad (3.117)$$

which with Equation (3.104) becomes

$$P = \pi \frac{8GR^3 \mathcal{A}}{\lambda t^2} \left[I_0(\lambda) - \frac{2}{\lambda} I_1(\lambda) \right] \quad (3.118)$$

which, when \mathcal{A} is substituted from Equation (3.98), becomes

$$P = \pi R^2 \frac{8G}{\lambda t^2} \frac{\left[I_0(\lambda) - \frac{2}{\lambda} I_1(\lambda) \right]}{\frac{2\alpha^2}{3\lambda R} \left[\frac{I_0(\lambda)}{-\frac{1-\nu}{\lambda} I_1(\lambda)} \right] + \frac{2\beta^2}{3\lambda R} \frac{1+\nu}{2} I_0(\lambda)} \cdot \frac{\varepsilon_c (1+\nu)}{2} \quad (3.119)$$

Using Equation (3.115), one finally has

$$E_c = 24GS^2 (1+\nu) \cdot \frac{\left[I_0(\lambda) - \frac{2}{\lambda} I_1(\lambda) \right]}{\alpha^2 \left[I_0(\lambda) - \frac{1-\nu}{\lambda} I_1(\lambda) \right] + \beta^2 \frac{1+\nu}{2} I_0(\lambda)} \quad (3.120)$$

In order to confirm the accuracy of this result it is useful to examine number of special cases. For the limit case of $K \rightarrow \infty$ and $\beta \rightarrow \infty$ in which $\lambda = \alpha$ and the compression modulus is

$$E_c = 24GS^2 (1+\nu) \frac{\left[I_0(\alpha) - \frac{2}{\alpha} I_1(\alpha) \right]}{\alpha^2 \left[I_0(\alpha) - \frac{1-\alpha}{\alpha} I_1(\alpha) \right]} \quad (3.121)$$

and if $\alpha \rightarrow \infty$, this reduces to $6GS^2$ independent of ν as it should. For the other special case where $E_f \rightarrow \infty$, $\alpha^2 \rightarrow \infty$, and ν drops out, $\lambda = \beta$, and the compression modulus becomes

$$E_c = 48GS^2 \frac{\left[I_0(\beta) - \frac{2}{\beta} I_1(\beta) \right]}{\beta^2 I_0(\beta)} \quad (3.122)$$

In the case where $\beta \rightarrow 0$, E_c tends to $6GS^2$ as before.

Figure 3.9 is a three-dimensional plot of the normalized effective modulus as a function of α and β . Plots of the full equation for varying α and for several values of β are shown in Figure 3.10. Figure 3.11 is a plot of the normalized effective modulus as a function of α for $\beta = 0$ and $\nu = 0, 1/3$.

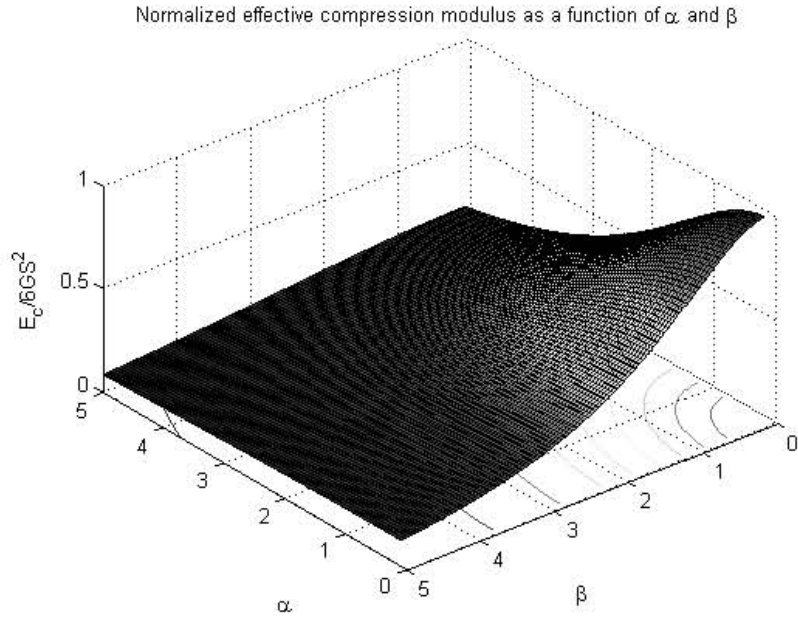


Figure 3.9 Normalized effective modulus as a function of α and β .

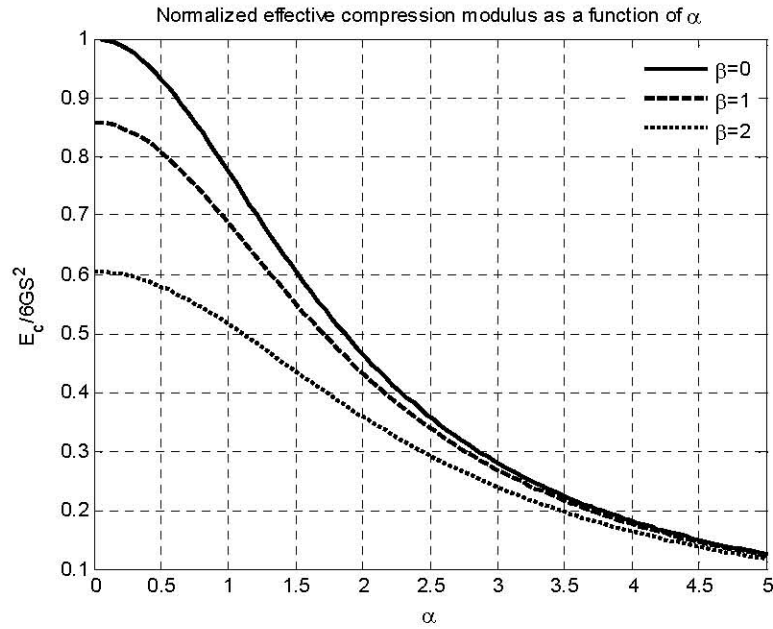


Figure 3.10 Normalized effective modulus as a function of α for different values of β .

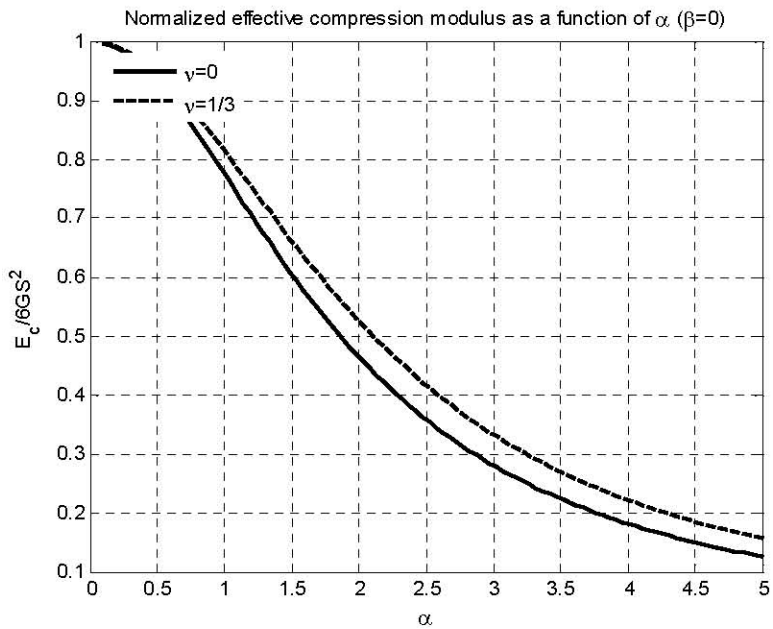


Figure 3.11 Normalized effective modulus as a function of α ($\beta=0; \nu=0; 1/3$).

3.3 RECTANGULAR PAD

3.3.1 Equilibrium in Elastomeric Layer

A layer of elastomer in a rectangular isolator is shown in Figure 3.12. The elastomeric layer has a thickness of t . Its side length parallel to the x axis is $2a$ and to the y axis is $2b$. Top and bottom surfaces of the elastomeric layer are perfectly bonded to flexible reinforcements that were modeled as an equivalent sheet of thickness t_f . Let u , v , and w denote the displacements of the elastomer in the x , y , and z coordinate directions, respectively. In addition, u_1 and v_1 denote the displacements of the reinforcement in the x and y directions. Under the compression load P in the z direction, the displacements of the elastomer are assumed to have the form

$$\begin{cases} u(x, y, z) = u_0(x, y) \left(1 - \frac{4z^2}{t^2} \right) + u_1(x, y) \\ v(x, y, z) = v_0(x, y) \left(1 - \frac{4z^2}{t^2} \right) + v_1(x, y) \\ w(x, y, z) = w(z) \end{cases} \quad (3.123)$$

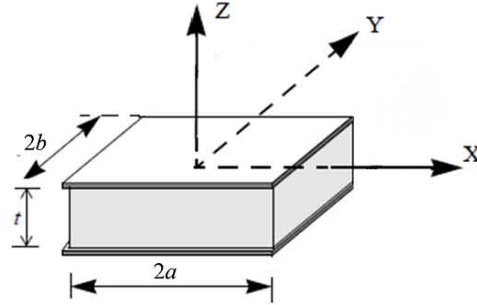


Figure 3.12 Reference system for a rectangular pad showing dimensions.

In Equation (3.123), the terms of u_0 and v_0 represent the kinematic assumption of quadratically varied displacements and are supplemented by additional displacements u_1 and v_1 , respectively, which are constant through the thickness and are intended to accommodate the stretch of the reinforcement. The elastomer is assumed to have linearly elastic behavior with incompressibility. The assumption of incompressibility produces a constraint on displacements in the form

$$u_{,x} + v_{,y} + w_{,z} = 0 \quad (3.124)$$

where the commas imply partial differentiation with respect to the indicated coordinate. Substituting Equation (3.123) into the above equation and then taking integration through the thickness from $z = -t/2$ to $z = t/2$ leads to

$$\frac{2}{3}(u_{0,x} + v_{0,y}) + u_{1,x} + v_{1,y} = \varepsilon_c \quad (3.125)$$

in which $\varepsilon_c = [w(-t/2) - w(t/2)]/t$ is the nominal compression strain. The stress state in the elastomer is assumed to be dominated by the internal pressure, p , such that the stress components of the elastomer are [Kelly 1997]

$$\begin{aligned} \sigma_{xx} &\approx \sigma_{yy} \approx \sigma_{zz} \approx -p \\ \sigma_{xy} &\approx 0 \end{aligned} \quad (3.126)$$

The equilibrium equations in the x and y directions for the stresses of the elastomer are then reduced to

$$\begin{aligned} -p_{,x} + \sigma_{xz,z} &= 0 \\ -p_{,y} + \sigma_{yz,z} &= 0 \end{aligned} \quad (3.127)$$

Using the displacement assumptions in Equation (3.123), the shear stress components of the elastomer become

$$\begin{aligned} \sigma_{xz} &= -\frac{8G}{t^2} u_0 z \\ \sigma_{yz} &= -\frac{8G}{t^2} v_0 z \end{aligned} \quad (3.128)$$

with G being the shear modulus of the elastomer. Substitution of these into the equilibrium equations of Equation (3.127) leads to

$$\begin{aligned} p_{,x} &= -\frac{8G}{t^2} u_0 \\ p_{,y} &= -\frac{8G}{t^2} v_0 \end{aligned} \quad (3.129)$$

Differentiating Equation (3.129) with respect to x and y , respectively, and then adding it up yields

$$p_{,xx} + p_{,yy} = -\frac{8G}{t^2} (u_{0,x} + v_{0,y}) \quad (3.130)$$

3.3.2 Equilibrium in Reinforcing Sheet

The internal forces acting in an infinitesimal dx by dy area of the reinforcing sheet are shown in Figure 3.13, where N_{xx} and N_{yy} are the normal forces per unit length in the x and y directions, respectively, and N_{xy} is the in-plane shear force per unit length. These internal forces are related to the shear stresses, σ_{xz} and σ_{yz} , on the surfaces of the reinforcing sheet bonded to the top and bottom layers of elastomer through two equilibrium equations in the x and y directions

$$dN_{xx}dy + dN_{xy}dx + (\sigma_{xz}|_{z=-t/2} - \sigma_{xz}|_{z=t/2})dx dy = 0 \quad (3.131)$$

$$dN_{yy}dy + dN_{xy}dx + (\sigma_{yz}|_{z=-t/2} - \sigma_{yz}|_{z=t/2})dx dy = 0 \quad (3.132)$$

Substituting Equation (3.128) into the above equations, and then combining the results with the equilibrium equations of the elastomeric layer in Equation (3.129) to eliminate u_0 and v_0 , leads to

$$\begin{aligned} N_{xx,x} + N_{xy,y} &= p_{,x} \\ N_{yy,y} + N_{xy,x} &= p_{,y} \end{aligned} \quad (3.133)$$

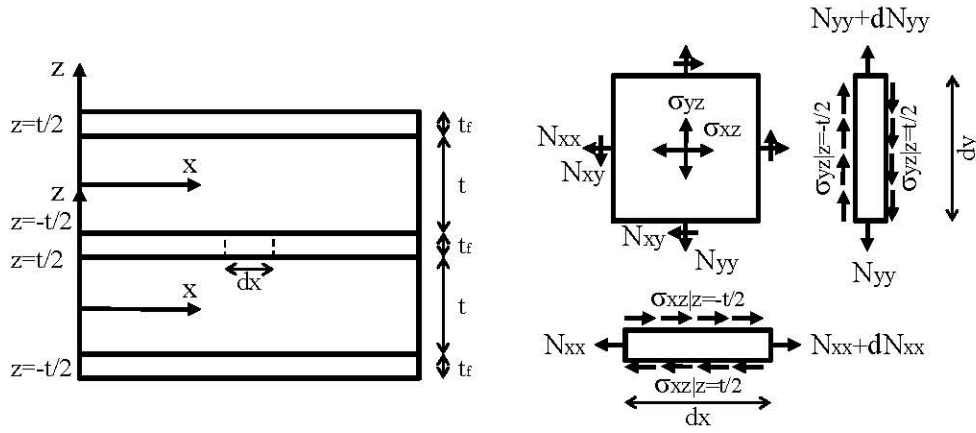


Figure 3.13 Forces in reinforcing sheet bonded to rectangular layers of elastomer.

The displacements in the reinforcement are related to the internal normal forces through the linearly elastic strain-stress relation such that

$$\begin{aligned} N_{xx} &= \frac{E_f t_f}{1-\nu^2} (u_{1,x} + \nu v_{1,y}) \\ N_{yy} &= \frac{E_f t_f}{1-\nu^2} (v_{1,y} + \nu u_{1,x}) \end{aligned} \quad (3.134)$$

where E_f and ν are the elastic modulus and Poisson's ratio of the reinforcement. The in-plane shear force has the following relation with the displacements

$$N_{xy} = \frac{E_f t_f}{2(1+\nu)} (u_{1,y} + v_{1,x}) \quad (3.135)$$

Substitution of Equations (3.134) and (3.135) into Equation (3.133) leads to

$$u_{1,xx} + \nu v_{1,xx} + \frac{1-\nu}{2} (u_{1,yy} + v_{1,xy}) = \frac{(1-\nu^2)t}{E_f t_f} p_{,x} \quad (3.136)$$

$$v_{1,yy} + \nu u_{1,yy} + \frac{1-\nu}{2} (u_{1,xy} + v_{1,xx}) = \frac{(1-\nu^2)t}{E_f t_f} p_{,y} \quad (3.137)$$

differentiating Equations (3.136) and (3.137) with respect to x and y , respectively, and adding them yields

$$q_{,xx} + q_{,yy} = \frac{(1-\nu^2)t}{E_f t_f} (p_{,xx} + p_{,yy}) \quad (3.138)$$

in which, for clarification, the term q is used to denote

$$q = u_{1,x} + v_{1,y} \quad (3.139)$$

Combining Equation (3.125) with Equation (3.130) to eliminate the terms of u_0 and v_0 and using the definition of q in Equation (3.139), gives

$$q = \varepsilon_e + \frac{t^2}{12G} (p_{,xx} + p_{,yy}) \quad (3.140)$$

Substitution of this into Equation (3.138) leads to

$$p_{,xxxx} + 2p_{,xxyy} + p_{,yyyy} - \alpha^2 (p_{,xx} + p_{,yy}) = 0 \quad (3.141)$$

3.3.3 Approximate Boundary Conditions

In Equation (3.126), the in-plane shear stress of the elastomer, σ_{xy} , is assumed to be negligible

$$\sigma_{xy} = G(u_{,y} + v_{,x}) \approx 0 \quad (3.142)$$

Substituting the displacement assumptions in Equation (3.123) into the above equation and taking integration through the thickness of the elastomeric layer leads to

$$\frac{2}{3}(u_{0,y} + v_{0,x}) + (u_{1,y} + v_{1,x}) \approx 0 \quad (3.143)$$

The last term, $u_{1,y} + v_{1,x}$, is the in-plane shear strain of the reinforcement, which is of the second order and the in-plane shear force of the reinforcement, N_{xy} , is negligible.

Therefore, we can assume

$$\begin{aligned} N_{xy,x}(a, y) &= 0 \\ N_{xy,y}(x, b) &= 0 \end{aligned} \quad (3.144)$$

which gives, from Equation (3.133),

$$\begin{aligned} N_{xx,x}(x, b) &\approx p_{,x}(x, b) \\ N_{yy,y}(a, y) &\approx p_{,y}(a, y) \end{aligned} \quad (3.145)$$

Another equation relating the pressure of the elastomer with the internal normal forces of the reinforcement is established by adding Equation (3.134), which gives

$$q = \frac{1-\nu}{E_f t_f} (N_{xx} + N_{yy}) \quad (3.146)$$

and combining this with Equation (3.140) to eliminate q leads to

$$\frac{t^2}{12G}(p_{,xx} + p_{,yy}) = \frac{1-\nu}{E_f t_f} (N_{xx} + N_{yy}) - \epsilon_e \quad (3.147)$$

According to the assumption of pressure dominance given in Equation (3.126), the stress boundary conditions of the elastomeric layer give

$$\begin{aligned} p(\pm a, y) &= 0 \\ p(x, \pm b) &= 0 \end{aligned} \quad (3.148)$$

The stress boundary conditions of the reinforcement give

$$\begin{aligned} N_{xx}(\pm a, y) &= 0 \\ N_{yy}(x, \pm b) &= 0 \end{aligned} \quad (3.149)$$

The boundary condition $p(x, \pm b) = 0$ means $p_{,x}(x, \pm b) = 0$ which, when substituted into Equation (3.144), gives $N_{yy}(\pm a, y)$ being constant. From the boundary condition $N_{yy}(x, \pm b) = 0$ it is known that $N_{yy}(\pm a, \pm b) = 0$, thus

$$N_{yy}(\pm a, y) = 0 \quad (3.150)$$

Bringing this into Equation (3.147) and using the boundary condition $N_{yy}(\pm a, y) = 0$ from $p(x, \pm b) = 0$ lead to

$$p_{,xx}(\pm a, y) = -\frac{12G}{t^2} \varepsilon_e \quad (3.151)$$

The boundary condition $p(x, \pm b) = 0$ gives $N_{yy}(\pm a, y)$ being constant. From the boundary condition $N_{yy}(x, \pm b)$, it is known that $N_{yy}(\pm a, \pm b) = 0$, thus

$$N_{xx}(x, \pm b) = 0 \quad (3.152)$$

Bringing this into Equation (3.147) and using the boundary condition $N_{yy}(x, \pm b) = 0$ and $p_{,xx}(x, \pm b) = 0$ from $p(x, \pm b) = 0$ leads to

$$p_{,yy}(x, \pm b) = -\frac{12G}{t^2} \varepsilon_e \quad (3.153)$$

Note that N_{xy} is not neglected when we derive the governing equation of the pressure in Equation (3.141). To solve for the pressure in this governing equation, we use the approximate boundary conditions of the pressure in Equations (3.151) and (3.153), which are derived by assuming that the derivatives of N_{xy} at the edges are negligible and stem from the assumption that the stress field of the elastomer is dominated by the pressure.

3.3.4 Solution of Pressure

To solve for the pressure, $p(x, y)$ is decomposed into two pressure components $p_1(x, y)$ and $p_2(x, y)$

$$p(x, y) = p_1(x, y) + p_2(x, y) \quad (3.154)$$

The boundary conditions for the pressure in Equations (3.148), (3.151), and (3.153) are split into two sets. Each pressure component satisfies a different set of boundary conditions. The first set of boundary conditions is

$$\begin{aligned} p_1(\pm a, y) &= 0; \quad p_{1,xx}(\pm a, y) = 0; \\ p_1(x, \pm b) &= 0; \quad p_{1,yy}(x, \pm b) = -\frac{12G}{t^2} \varepsilon_e \end{aligned} \quad (3.155)$$

and the second set of boundary conditions is

$$\begin{aligned} p_2(\pm a, y) &= 0; p_{2,\infty}(\pm a, y) = -\frac{12G}{t^2} \varepsilon_c; \\ p_2(x, \pm b) &= 0; p_{2,y}(x, \pm b) = 0 \end{aligned} \quad (3.156)$$

Adding the boundary conditions in Equation (3.156) yields the same boundary conditions defined in Equation (3.148). These pressure components are solved from the same governing equation in Equation (3.141), that is

$$p_{1,\infty\infty} + 2p_{1,\infty y} + p_{1,yy} - \alpha^2(p_{1,\infty} + p_{1,y}) = 0 \quad (3.157)$$

$$p_{2,\infty\infty} + 2p_{2,\infty y} + p_{2,yy} - \alpha^2(p_{2,\infty} + p_{2,y}) = 0 \quad (3.158)$$

Because the compression loading is symmetric with respect to the x axis and y axis, the pressure components are even functions of x and y . The first pressure component can be assumed to be a cosine series of y

$$p_1(x, y) = \sum_{n=1}^{\infty} f_1^{(n)}(y) \cos \gamma_n x \quad (3.159)$$

where the amplitude $f_1^{(n)}$ is an even function of y and

$$\bar{\gamma}_n = \left(n - \frac{1}{2}\right) \frac{\pi}{b} \quad (3.160)$$

Substituting Equation (3.159) into Equation (3.157) and using boundary conditions at $x = \pm a$ in Equation (3.155), $f_1^{(n)}$ is solved to have the form [Tsai and Kelly 2001]

$$f_1^{(n)}(y) = \varepsilon_c \frac{24G}{\pi \alpha^2 t^2} \frac{(-1)^{n-1}}{(n-1/2)} \left(\frac{\cosh \gamma_n y}{\cosh \gamma_n b} - \frac{\cosh \beta_n y}{\cosh \beta_n b} \right) \quad (3.161)$$

with

$$\beta_n = \sqrt{\gamma_n^2 + \alpha^2} \quad (3.162)$$

The second pressure component can be assumed to be a cosine series of y

$$p_2(x, y) = \sum_{n=1}^{\infty} f_2^{(n)}(x) \cos \bar{\gamma}_n y \quad (3.163)$$

where the amplitude $f_2^{(n)}$ is an even function of x and

$$\bar{\gamma}_n = \left(n - \frac{1}{2}\right) \frac{\pi}{b} \quad (3.164)$$

Substituting Equation (3.163) into Equation (3.158) and using boundary conditions at $x = \pm a$ in Equation (3.153), $f_2^{(n)}$ is solved to have the form [Tsai and Kelly 2001]

$$f_2^{(n)}(x) = \varepsilon_c \frac{24G}{\pi \alpha^2 t^2} \frac{(-1)^{n-1}}{(n-1/2)} \left(\frac{\cosh \bar{\gamma}_n x}{\cosh \bar{\gamma}_n a} - \frac{\cosh \bar{\beta}_n y}{\cosh \bar{\beta}_n a} \right) \quad (3.165)$$

with

$$\bar{\beta}_n = \sqrt{\bar{\gamma}_n^2 + \alpha^2} \quad (3.166)$$

Substitution of $p_1(x, y)$ in Equation (3.159) and $p_2(x, y)$ in Equation (3.163) into Equation (3.154) gives the solution of the pressure $p(x, y)$

$$p(x, y) = \varepsilon_c \frac{24GS^2}{\pi(\alpha a)^2} \left(1 + \frac{a}{b} \right)^2 \sum_{n=1}^{\infty} \frac{(-1)^{n-1}}{(n-1/2)} \cdot \left[\left(\frac{\cosh \gamma_n y}{\cosh \gamma_n b} - \frac{\cosh \beta_n y}{\cosh \beta_n ab} \right) \cosh \gamma_n x - \left(\frac{\cosh \gamma_n x}{\cosh \gamma_n a} - \frac{\cosh \beta_n x}{\cosh \beta_n a} \right) \right] \quad (3.167)$$

in which S is the shape factor of the rectangular layer of the elastomer defined as

$$S = \frac{ab}{(a+b)t} \quad (3.168)$$

3.3.5 Effective Compressive Modulus

The compression stiffness of a rectangular isolator is given by $K_c = E_c A / t_r$, where $A = 4ab$ is the area of the isolator, t_r total thickness of the elastomer in the isolator, and E_c effective compressive modulus for a single bonded layer of elastomer, defined as $E_c = P / (A \varepsilon_c)$. Using the assumption in Equation (3.126), the resultant compression load P has the form

$$P = \int_{-b-a}^b \int_{-b-a}^a \sigma_{xx} dx dy \approx \int_{-b-a}^b \int_{-b-a}^a p(x, y) dx dy \quad (3.169)$$

Bringing the pressure solution $p(x, y)$ in Equation (3.167), the effective compressive modulus becomes

$$E_c = \frac{24GS^2}{\pi^2(\alpha a)^2} \left(1 + \frac{a}{b} \right)^2 \sum_{n=1}^{\infty} \frac{1}{(n-1/2)^2} \cdot \left(\frac{\tanh \gamma_n b}{\gamma_n b} - \frac{\tanh \beta_n b}{\beta_n b} + \frac{\tanh \bar{\gamma}_n a}{\bar{\gamma}_n a} - \frac{\tanh \bar{\beta}_n a}{\bar{\beta}_n a} \right) \quad (3.170)$$

When the aspect ratio a/b tends to zero, Equation (3.170) is reduced to

$$E_e|_{a/b=0} = \frac{12GS^2}{(\alpha a)^2} \left(1 + \frac{\tanh \alpha a}{\alpha a} \right) \quad (3.171)$$

which is the effective compressive modulus of the infinitely long strip isolator. When a tends to zero, Equation (3.170) becomes

$$E_e|_{\alpha=0} = \frac{12GS^2}{\pi^4} \left(1 + \frac{a}{b} \right)^2 \sum_{n=1}^{\infty} \frac{1}{(n-1/2)^4} \cdot \left[\frac{\tanh \gamma_n b}{\gamma_n b} - \frac{1}{\cosh^2 \gamma_n b} + \frac{b^2}{a^2} \left(\frac{\tanh \bar{\gamma}_n a}{\bar{\gamma}_n a} - \frac{1}{\cosh^2 \bar{\gamma}_n a} \right) \right] \quad (3.172)$$

which is the effective compressive modulus of the rectangular elastomer with the rigid reinforcement. From Equation (3.170), it is known that the ratio $E_e/(GS^2)$ is a function of αa and the aspect ratio a/b . The variation of $E_e/(GS^2)$ with αa is plotted in Figure 3.14, which shows that the effective compressive modulus decreases with increasing αa .

To have an high compressive modulus, the value of αa must be small. Figure 3.14 also reveals that a larger value of a/b produces a larger value of the effective compressive modulus. For clarification, the in-plane stiffness of the reinforcement is defined as $k_f = E_f t_f / (1 - \nu^2)$, from which Equation (3.121) becomes

$$\alpha a = \frac{a}{t} \sqrt{12 \frac{Gt}{k_f}} \quad (3.173)$$

Substituting the shape factor S in Equation (3.168) and αa in Equation (3.173) into Equation (3.170), the normalized effective compression modulus E_e/G can be expressed as a function of the ratios a/b , a/t and $k_f = Gt$. When a/t tends to infinity, Equation (3.170) becomes

$$E_e|_{a/t=\infty} = \frac{2}{\pi^2} \frac{k_f}{t} \sum_{n=1}^{\infty} \frac{1}{(n-1/2)^4} \left(\frac{\tanh \gamma_n b}{\gamma_n b} + \frac{\tanh \bar{\gamma}_n a}{\bar{\gamma}_n a} \right) \quad (3.174)$$

The curves of E_e/G versus k_f/Gt are plotted in Figure 3.15 for $a/b = 0.5$ and several a/t values, which shows that the effective compressive modulus increases with an increase in the reinforcement stiffness until reaching the asymptotic value in Equation (3.172). The curve of the smaller shape factor reaches a plateau at the smaller value of

k_f/Gt . The curves of E_c/G versus a/t are plotted in Figure 3.16 for $a/b = 0.5$ and several k_f/Gt values, which shows that the effective compressive modulus increases with increasing shape factor until reaching the asymptotic value as in Equation (3.174). The curve of the smaller value of k_f/Gt reaches a plateau at a smaller shape factor.

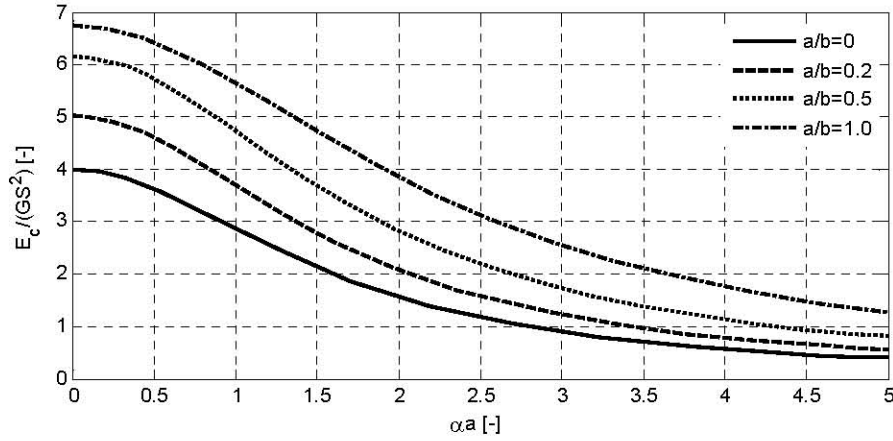


Figure 3.14 Variation of effective compressive modulus with αa in rectangular pad.

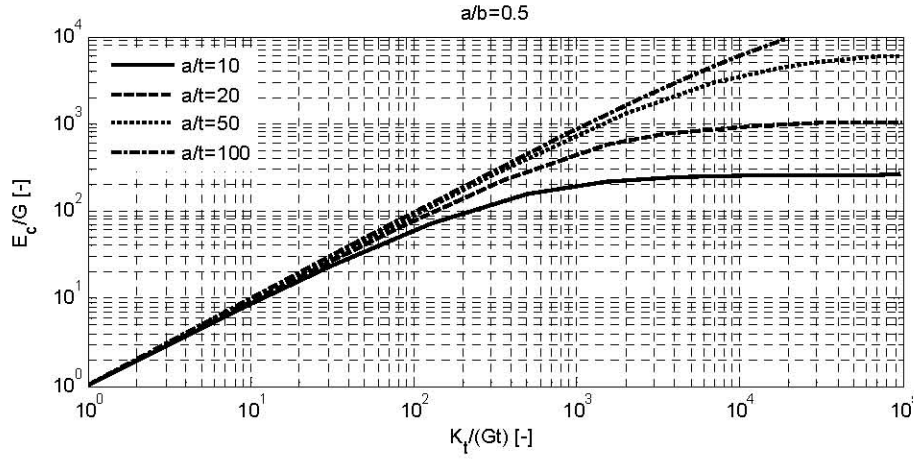


Figure 3.15 Variation of effective compressive modulus with reinforcement stiffness in rectangular pad ($a/b = 0.5$).

To study the variation of the effective compressive modulus with the aspect ratio a/b , the ratio of the compressive modulus between the rectangular layers ($a/b > 0$) in

Equation (3.170) and the infinitely long strip layer ($a/b=0$) in Equation (3.171) is plotted in Figure 3.17, which reveals that the effective compressive modulus varies almost linearly with the aspect ratio a/b .

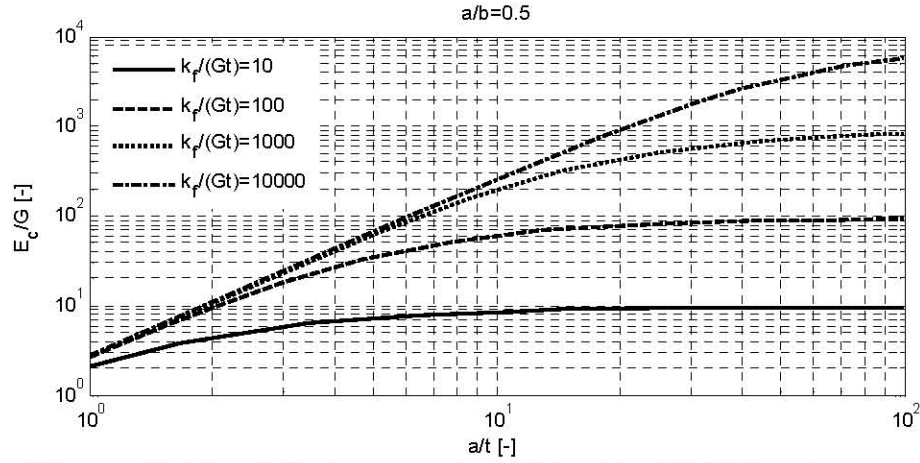


Figure 3.16 Variation of effective compressive modulus with width/thickness in rectangular pad ($a/b=0.5$).

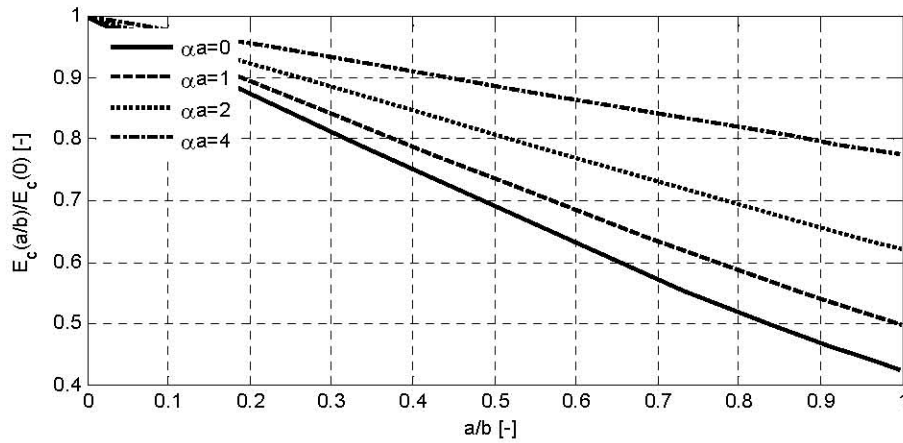


Figure 3.17 Ratio of effective compressive modulus of rectangular pad to infinitely long strip pad ($a/b=0$) versus aspect ratio.

Utilizing the regression analysis on the data calculated from the exact formula in Equation (3.170), an approximate formula for the effective compressive modulus of rectangular reinforced layers is established [Tsai and Kelly 2001]

$$E_e = \frac{12GS^2}{(\alpha a)^2} \left(1 - \frac{\tanh \alpha a}{\alpha a} \right) \cdot \left\{ 1 + \frac{a}{b} \left[\frac{-0.59 + 0.026\alpha a + 0.074(\alpha a)^2}{-0.022(\alpha a)^3 + 0.0019(\alpha a)^4} + \right] \right\} \quad (3.175)$$

Because the range of the αa values used in the regression analysis is between 0 and 5, the effective compressive modulus in Equation (3.175) is only applicable to the range of $0 \leq \alpha a \leq 5$. The maximum error is smaller than 4% in this range.

3.4 GENERAL SHAPE PAD

3.4.1 Equilibrium in Elastomeric Layer

Consider a layer of elastomer in an arbitrarily shaped pad of thickness t and locate a rectangular Cartesian coordinate system (x, y, z) in the middle surface of the pad as shown in Figure 3.18. The displacements of the elastomer along the coordinate directions are

$$\begin{cases} u(x, y, z) = u_0(x, y) \left(1 - 4z^2/t^2 \right) + u_1(x, y) \\ v(x, y, z) = v_0(x, y) \left(1 - 4z^2/t^2 \right) + v_1(x, y) \\ w(x, y, z) = w(z) \end{cases} \quad (3.176)$$

Remembering that

$$\varepsilon_{xx} + \varepsilon_{yy} + \varepsilon_{zz} = -\frac{p}{K} \quad (3.177)$$

where K is the bulk modulus and

$$\varepsilon_{xx} = u_{0,x} \left(1 - \frac{4z^2}{t^2} \right) + u_{1,x} \quad (3.178)$$

$$\varepsilon_{yy} = v_{0,y} \left(1 - \frac{4z^2}{t^2} \right) + v_{1,y} \quad (3.179)$$

$$\varepsilon_{zz} = w'_{,z} \quad (3.180)$$

in which the commas imply a partial differentiation with respect to the indicated coordinate. Substituting in Equation (3.177), Equation (3.178), Equation (3.179), and Equation (3.180), we have

$$u_{0,x} \left(1 - \frac{4z^2}{t^2} \right) + u_{1,x} + v_{0,y} \left(1 - \frac{4z^2}{t^2} \right) + v_{1,y} + w'_{,z} = -\frac{p}{K} \quad (3.181)$$

When integrated through the thickness this gives

$$u_{o,x} + v_{o,y} + \frac{3}{2}(u_{1,x} + v_{1,y}) = \frac{3}{2}\left(\frac{\Delta}{t} - \frac{p}{K}\right) \quad (3.182)$$

where, Δ , is the change of thickness of the pad (positive in compression).

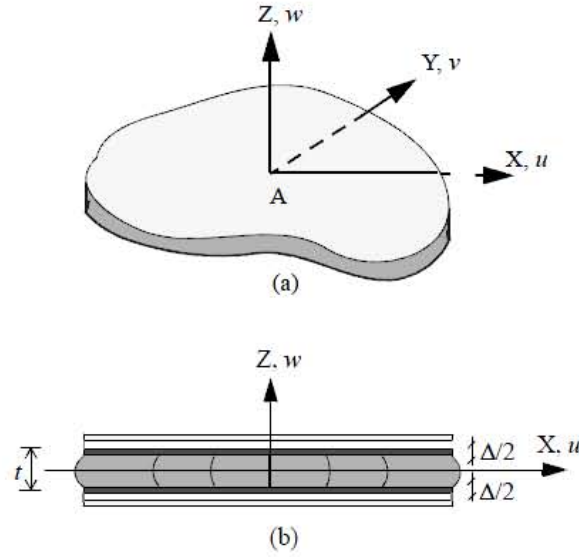


Figure 3.18 Constrained rubber pad and coordinate system.

Assuming that the stress state is dominated by the internal pressure, p , the equations of equilibrium for the stresses

$$\begin{aligned} \tau_{xx,x} + \tau_{xy,y} + \tau_{xz,z} &= 0 \\ \tau_{xy,x} + \tau_{yy,y} + \tau_{yz,z} &= 0 \\ \tau_{xz,x} + \tau_{yz,y} + \tau_{zz,z} &= 0 \end{aligned} \quad (3.183)$$

reduce under this assumption to

$$\begin{aligned} \tau_{xz,z} &= -\tau_{xx,x} = p_{,x} \\ \tau_{yz,z} &= -\tau_{yy,y} = p_{,y} \end{aligned} \quad (3.184)$$

Assuming that the material is linear elastic, the shear stresses τ_{xz} and τ_{yz} are related to the shear strains, γ_{xz} and γ_{yz} , by

$$\begin{aligned} \tau_{xz} &= G\gamma_{xz} \\ \tau_{yz} &= G\gamma_{yz} \end{aligned} \quad (3.185)$$

with G being the shear modulus of the material; thus,

$$\begin{aligned}\tau_{xx} &= -G u_0 \frac{8z}{t^2} \\ \tau_{yy} &= -G v_0 \frac{8z}{t^2}\end{aligned}\tag{3.186}$$

The equilibrium equations now become

$$\begin{aligned}\tau_{xx,x} &= \frac{8G u_0}{t^2} = -p_{,x} \\ \tau_{yy,y} &= \frac{8G v_0}{t^2} = -p_{,y}\end{aligned}\tag{3.187}$$

3.4.2 Stress in the Reinforcement

The individual fibers are replaced by an equivalent sheet of reinforcement of thickness t_f . The internal state of stress in the reinforcing layer is denoted by the force field $\underline{F} = t_f \underline{\sigma}^f$. Equilibrium requires that

$$F_{xx,x} + F_{xy,y} + X = 0\tag{3.188}$$

$$F_{yx,x} + F_{yy,y} + Y = 0\tag{3.189}$$

where

$$X = -\tau_{xx}\Big|_{z=+\frac{t}{2}} + \tau_{xx}\Big|_{z=-\frac{t}{2}}\tag{3.190}$$

$$Y = -\tau_{yy}\Big|_{z=+\frac{t}{2}} + \tau_{yy}\Big|_{z=-\frac{t}{2}}.\tag{3.191}$$

From Equation (3.186) we have

$$\tau_{xx}\Big|_{z=+\frac{t}{2}} = -\frac{8G u_0}{2t} \quad \tau_{xx}\Big|_{z=-\frac{t}{2}} = +\frac{8G u_0 t}{2t}\tag{3.192}$$

and

$$\tau_{yy}\Big|_{z=+\frac{t}{2}} = -\frac{8G v_0}{2t} \quad \tau_{yy}\Big|_{z=-\frac{t}{2}} = +\frac{8G v_0 t}{2t}\tag{3.193}$$

from which

$$X = \frac{8G u_0}{t}; \quad Y = \frac{8G v_0}{t}\tag{3.194}$$

Remembering that

$$\sigma_{xx}^f = \frac{F_{xx}}{t_f} = \frac{E_f}{1-\nu^2} (\varepsilon_{xx}^f + \nu \varepsilon_{yy}^f) \quad (3.195)$$

$$\sigma_{yy}^f = \frac{F_{yy}}{t_f} = \frac{E_f}{1-\nu^2} (\varepsilon_{yy}^f + \nu \varepsilon_{xx}^f) \quad (3.196)$$

$$\sigma_{xy}^f = \frac{F_{xy}}{t_f} = \frac{E_f}{2(1+\nu)} \gamma_{xy}^f \quad (3.197)$$

where

$$\varepsilon_{xx}^f = u_{1,x}, \quad \varepsilon_{yy}^f = v_{1,y}, \quad \gamma_{xy}^f = u_{1,y} + v_{1,x} \quad (3.198)$$

it can be derived that,

$$F_{xx} = \frac{t_f E_f}{1-\nu^2} [u_{1,x} + \nu v_{1,y}] \quad (3.199)$$

$$F_{yy} = \frac{t_f E_f}{1-\nu^2} [v_{1,y} + \nu u_{1,x}] \quad (3.200)$$

$$F_{xy} = \frac{t_f E_f}{2(1+\nu)} [u_{1,y} + v_{1,x}] \quad (3.201)$$

3.4.3 Complete System of Equation

Substituting these relations in Equation (3.188) and Equation (3.189) gives

$$\frac{t_f E_f}{1-\nu^2} \left[u_{1,xx} + \nu v_{1,xx} + \frac{1}{2} \frac{1-\nu^2}{1+\nu} (u_{1,yy} + v_{1,xy}) \right] + \frac{8Gu_0}{t} = 0 \quad (3.202)$$

$$\frac{t_f E_f}{1-\nu^2} \left[v_{1,yy} + \nu u_{1,yy} + \frac{1}{2} \frac{1-\nu^2}{1+\nu} (u_{1,xy} + v_{1,xx}) \right] + \frac{8Gv_0}{t} = 0 \quad (3.203)$$

A complete system of five equations in five unknowns is derived

$$\tau_{xx,x} = \frac{8Gu_0}{t^2} = -p_{,x} \quad (3.204)$$

$$\tau_{yy,y} = \frac{8Gv_0}{t^2} = -p_{,y} \quad (3.205)$$

$$\frac{t_f E_f}{1-\nu^2} \left[u_{1,xx} + \nu v_{1,xx} + \frac{1}{2} \frac{1-\nu^2}{1+\nu} (u_{1,yy} + v_{1,xy}) \right] + \frac{8Gu_0}{t} = 0 \quad (3.206)$$

$$\frac{t_f E_f}{1 - \nu^2} \left[v_{1,y} + \nu u_{1,xy} + \frac{1}{2} \frac{1 - \nu^2}{1 + \nu} (u_{1,xx} + v_{1,xy}) \right] + \frac{8Gv_0}{t} = 0 \quad (3.207)$$

$$u_{o,x} + v_{o,y} + \frac{3}{2} (u_{1,x} + v_{1,y}) = \frac{3}{2} \left(\frac{\Delta}{t} - \frac{p}{K} \right) \quad (3.208)$$

The unknowns are u_o, v_o, u_1, v_1, p . Considering the infinitely long rectangular pad of Figure 3.1 for which $u_o = 0$ and $v_o = 0$, the complete system of equations, in accordance with Section 3.1 reduces to

$$p_{,x} = -\frac{8Gu_0}{t^2} \quad (3.209)$$

$$u_{1,xx} = -\frac{8Gu_0}{E_f t_f t} \quad (3.210)$$

$$u_{o,x} + \frac{3}{2} u_{1,x} = \frac{3}{2} \left(\frac{\Delta}{t} - \frac{p}{K} \right) \quad (3.211)$$

4.FINITE ELEMENT ANALYSIS OF UNBONDED BEARINGS

4.1 INTRODUCTION

Many studies of the global behavior of steel reinforced rubber bearings by means of FE analyses have been conducted. Seky *et al.* [1987] investigated qualitatively the principal strain distributions in an elastomeric bearing denoting the rubber-steel interface as the most likely failure region. This result was confirmed by means of experimental campaigns [Kelly 1991]. Takayama *et al.* [1994] analyzed the principal strain and stress distributions for different values of the mean vertical pressure, Simo and Kelly [1984] considered the stability of multilayer elastomeric bearings within the framework of two-dimensional finite elasticity through a finite element formulation which is capable of accounting for very general boundary conditions. Only few studies, however, have been conducted on the finite element analysis of FRBs. In this Chapter the load-displacement behavior and stress state of strip-shaped, square and circular FRBs are analyzed using extensive Finite Element Analyses (FEAs). Results of FEAs are compared to the theoretical solutions derived in Chapter 3. A series of FEAs was conducted using the general-purpose finite element program MSC.Marc 2005 [MSC.Software 2004].

Modelling the ultimate behavior of FRB is challenging for finite element codes because the problem involves a lot of settings such as the change of contact conditions, sliding, large strain (elastomeric behavior) and near-incompressibility of the rubber. Furthermore, the problem requires robust contact and self-contact capabilities because the bearing deforms enough to fold over upon itself. Use of traditional finite elements that have not been tailored for incompressibility analysis will produce extremely poor solutions due to ill-conditioning resulting from division by very small numbers. More importantly, the pathological behavior called volumetric mesh-locking is very likely to occur. The so-called mixed methods used in modern finite element treatments of incompressible and nearly-incompressible materials are based on the Hellinger-Reissner and Hu-Washizu variational principles [MSC Software 2000]. In mixed methods, both the stress and strains are treated as unknowns.

The results of the analyses presented in this report are based on the widely popular mixed method proposed by Herrmann [1965]. A restricted case of the general

Hellinger-Reissner variational principle is used to derive the stiffness equations. The software used to run the analyses is expressly designed to study elastomeric materials: they can be represented with popular material laws as Mooney-Rivlin and Boyce-Arruda, and a built-in curve fitting used that computes coefficients from stress-strain data. Moreover specialized element types automatically address numerical issues to get accurate solutions to large strain problems. The FE analyses consisted of two-dimensional models under the plane strain assumption for strip-type bearings and three-dimensional models for the other considered geometries.

4.1.1 Material and Mechanical Properties of the Bearings

For the two-dimensional models, the fiber reinforcement is modeled using a rebar element: it is a tension element of a linear elastic isotropic material with Young's modulus $E=14000 \text{ MPa}$, and thickness $t_f = 0.07 \text{ mm}$ (SsET1) and $G=0.7 \text{ MPa}$ (SET1). For the three-dimensional models, the reinforcing shim are modeled as four nodes thin shells (*i.e.*, no flexural rigidity) of constant thickness with Young's modulus $E=14000 \text{ MPa}$ and Poisson's ratio equal to zero.

The rubber is modeled by a single-parameter Mooney-Rivlin material (*i.e.*, Neo-Hookean) with strain energy function that is described by the shear modulus $G=0.7 \text{ MPa}$, and the bulk modulus $\kappa=2000 \text{ MPa}$.

In incompressible Mooney-Rivlin solids, the strain energy density function, \mathcal{W} , is a linear combination of two invariants of the left Cauchy-Green deformation tensor

$$\mathcal{W} = C_1(\bar{I}_1 - 3) + C_2(\bar{I}_2 - 3) \quad (4.1)$$

In Equation (4.1), C_1 and C_2 are empirically determined material constants, and \bar{I}_1 and \bar{I}_2 are the first and the second invariant of the deviatoric component of the left Cauchy-Green deformation tensor

$$\bar{I}_1 = J^{-2/3} I_1, I_1 = \lambda_1^2 + \lambda_2^2 + \lambda_3^2; J = \det(F) \quad (4.2)$$

$$\bar{I}_2 = J^{-4/3} I_2, I_2 = \lambda_1^2 \lambda_2^2 + \lambda_2^2 \lambda_3^2 + \lambda_3^2 \lambda_1^2 \quad (4.3)$$

where F is the deformation gradient. For an incompressible material, $J = 1$.

The constants C_1 , C_2 are determined by fitting the predicted stress from the above equations to experimental data. For a special case of uniaxial tension of an incompressible Mooney-Rivlin material, the stress-strain equation can be expressed as

$$\sigma = 2 \left((1 + \varepsilon) - (1 + \varepsilon)^{-2} \right) \left(c_1 + c_2 (1 + \varepsilon)^{-1} \right) \quad (4.4)$$

The initial shear modulus is

$$G = 2(C_1 + C_2) \quad (4.5)$$

If the material is incompressible, the initial tensile modulus E is calculated by

$$E = 6(C_1 + C_2) \quad (4.6)$$

As mentioned above, the two-dimensional analysis is carried out under the plane strain assumption. In the plane models the rubber is modeled by the use of four-node, isoparametric, quadrilateral elements (element type 80 in Marc). The element uses bilinear interpolation functions, and the strains tend to be constant throughout the element. Hence, the use of a fine mesh is required. The pressure field is constant in this element. The stiffness of this element is formed using four-point Gaussian integration. This element is designed to be used for incompressible elasticity only. It can be used for either small strain behavior or large strain behavior using the Mooney or Ogden models. For the three-dimensional models, the rubber is described by eight-node, isoparametric, three-dimensional brick elements with trilinear interpolation (element type 84 in Marc). The element is based on the following type of displacement assumption and mapping from the (x, y, z) space into a cube in the

$$X = a_0 + a_1\xi + a_2\eta + a_3\zeta + a_4\xi\eta + a_5\xi\zeta + a_6\eta\zeta + a_7\xi\eta\zeta \quad (4.7)$$

$$Y = b_0 + b_1\xi + b_2\eta + b_3\zeta + b_4\xi\eta + b_5\xi\zeta + b_6\eta\zeta + b_7\xi\eta\zeta \quad (4.8)$$

Either the coordinate or function can be expressed in terms of the nodal quantities by the integration functions

$$X = \sum_{i=1}^8 X_i \Phi_i \quad (4.9)$$

$$\begin{aligned} \Phi_1 &= \frac{1}{8}(1-\xi)(1-\eta)(1-\zeta) & \Phi_2 &= \frac{1}{8}(1+\xi)(1-\eta)(1-\zeta) \\ \Phi_3 &= \frac{1}{8}(1+\xi)(1+\eta)(1-\zeta) & \Phi_4 &= \frac{1}{8}(1-\xi)(1+\eta)(1-\zeta) \\ \Phi_5 &= \frac{1}{8}(1-\xi)(1-\eta)(1+\zeta) & \Phi_6 &= \frac{1}{8}(1+\xi)(1-\eta)(1+\zeta) \\ \Phi_7 &= \frac{1}{8}(1+\xi)(1+\eta)(1+\zeta) & \Phi_8 &= \frac{1}{8}(1-\xi)(1+\eta)(1+\zeta) \end{aligned} \quad (4.10)$$

These elements use eight-point Gaussian integration as shown in Figure 4.1. Element 84 has one extra node with a single degree of freedom (pressure). This element uses a mixed formulation for incompressible analysis.

Large strain theory was employed for all the analyses. The kinematics of deformation is described following the Updated Lagrangian formulation (*i.e.*, the Lagrangian frame of reference is redefined at the last completed iteration of the current increment). Furthermore, a full Newton-Raphson solution method is used. Analysis of

elastomeric bearings includes both nonlinear material and nonlinear geometric effects, since the bearings can undergo high shear strains during an earthquake

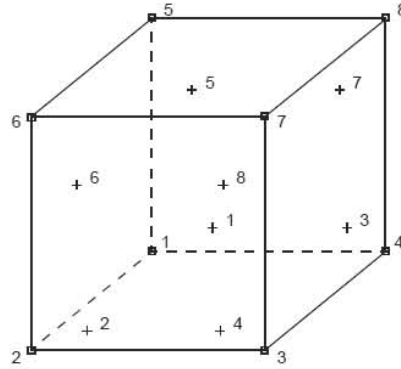


Figure 4.1 Integration points for element type 84 in MSC.Marc 2005 [MSC.Software 2004].

4.1.2 Contact Bodies, Boundary Conditions

The top and bottom support surfaces are modeled as rigid lines/surfaces. The contact between the rubber and the support surfaces is modeled by Coulomb friction with $\mu = 0.9$ for shear tests and $\mu = 0$ for compression tests. The MSC.Marc 2005 has a CONTACT option that detects deformable body to deformable body or deformable body to rigid body contact as can occur under compression and large shear strains where the elastomer can contact the reinforcing shims [MSC.Software 2004].

4.2 INFINITELY LONG STRIP ISOLATORS

4.2.1 Geometrical Properties

Finite element models of FRBs with different shape factors are defined ($S = B/2tr = 43.48; 39.13; 34.78; 26.09; 21.74; 43.48$). The different values of the shape factor are obtained by increasing the values of the base of the device ($B = 250; 300; 350; 400; 450; 500\text{mm}$). The longitudinal dimension of the bearings is 750mm. As shown in Figure 4.2, each device is made of twenty-eight rubber layers with twenty-nine interleaf fiber sheets. Each rubber layer is 5.75mm thick ($= t_r$), and each fiber sheet is 0.07mm thick ($= t_f$) for the first set (SET1) and 0.25mm thick for the second set (SET2). The geometrical characteristics are reported in Table 4.1, and the finite element discretization is shown in Figure 4.3. It consists of square four-node elements with side length of 2mm and is denser at the contact interface.

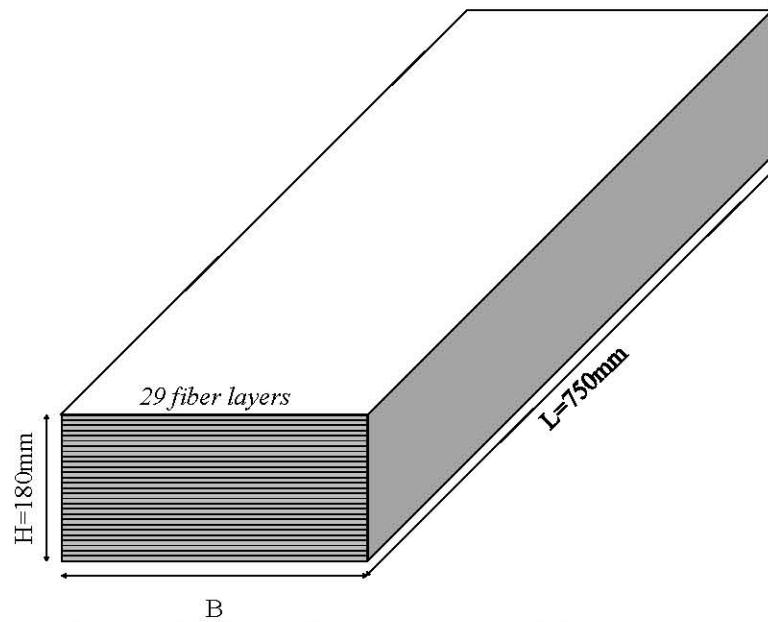


Figure 4.2 Strip type bearing showing reinforcements and dimensions.

Table 4.1 Geometrical properties of the long strip bearings.

	B	H	t_r	t_f	S
	[mm]	[mm]	[mm]	[mm]	[-]
Name	500				43.48
	450			0.07	39.13
	400			(SET1)	34.78
	350	180	5.75		30.43
	300			0.25	26.09
				(SET2)	
	250				21.74

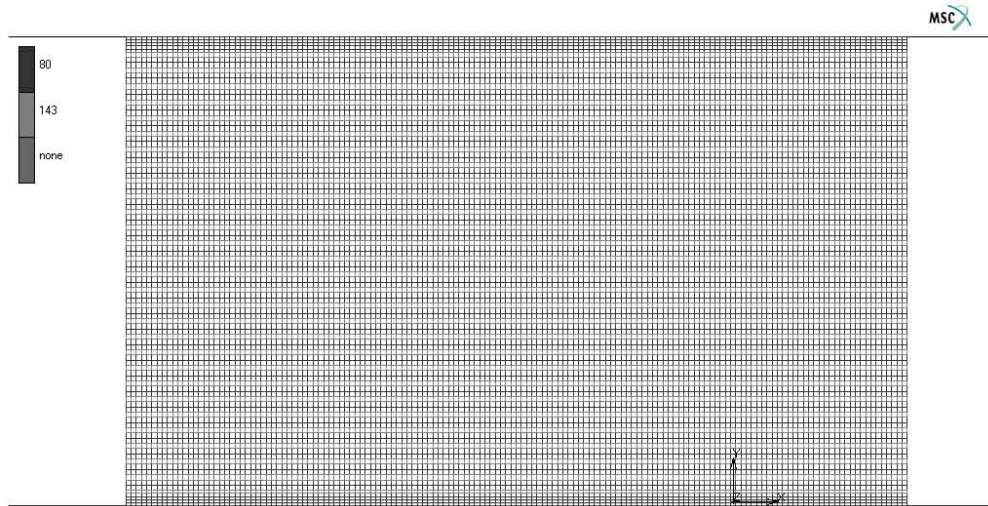


Figure 4.3 Model mesh and layout of the reinforcement layers [el. type 143].

4.2.2 Compression Results

For design purposes, it is particularly important to predict the vertical stiffness and the collapse condition of FRBs under compression. Under compression, collapse of the bearing can occur for global failure due to buckling of the device, local ruptures of the reinforcement or detachment of the rubber from the fiber sheets. Therefore, an accurate knowledge of the global characteristics of the device and of the stress distributions at the rubber-fiber interfaces and in the fiber reinforcement is necessary.

Approximate analytical solutions for a pad confined by rigid and flexible reinforcements subjected to axial loads have been proposed (*e.g.*, [Kelly 2002]). Among these, the pressure solution, previously reported (Chapter 3) for strip-type bearings, seems to be particularly suited to provide a simple formulation of the vertical stiffness and to describe the stress state in elastomeric bearings. The goal of this section is to verify the validity of the results provided by the pressure solution by comparing them with results from FE analyses.

Figure 4.4 and Figure 4.5 are the contour maps of the equivalent stress obtained from analysis with MSC.Marc 2005 for bearings 250 and 500 ($t_f = 0.07 \text{ mm}$) under pure compression. The contours show a stress concentration in the core of the bearings. For a given compressive force P (average pressure $= P/A = 3.45 \text{ MPa}$) in the considered range of bases, the maximum equivalent stress in the core of the bearing is unaffected by the change of the dimension of the device. Therefore, the stress in the core of the bearing is

the same when the base dimension is modified. However, as expected, a new arrangement of stress distribution along the base length can be observed when the dimensions are changed. As a result, for bigger bearings as we move towards the free edges, the stress drops less aggressively than for smaller ones.

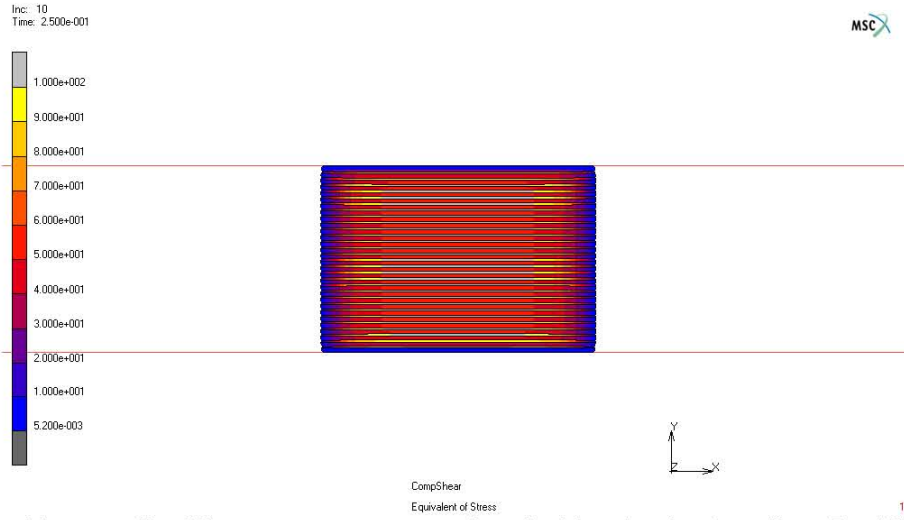


Figure 4.4 Von Mises stress contours at peak vertical force in a bearing of base $B = 250\text{mm}$ [SET2 ($t_f = 0.07\text{ mm}$)].

Figure 4.6 and Figure 4.7 show the stress contours in the fiber layers. Note that due to the frictional restraint of the supports, the fiber layers closest to the supports are in compression. In the vertical direction the force displacement behavior is linear in the considered range of load.

The results from FE analyses can be compared to the pressure solution results. Recalling a result of Chapter 2, the vertical stiffness of the bearing, K_V , and the tensile stress in the reinforcement, $\sigma_f(x)$, can be written as

$$K_V = (E_c A) / t_r \quad (4.11)$$

$$\sigma_f(x) = \varepsilon_c E_f \left(1 - \frac{\cosh \alpha x}{\cosh \alpha b} \right) \quad (4.12)$$

where

$$\alpha^2 = 12G / E_f t_f t \quad (4.13)$$

and

$$E_t = 4G \frac{b^2}{t^2} \left(1 - \frac{2}{5} \alpha^2 b^2 \right) \quad (4.14)$$

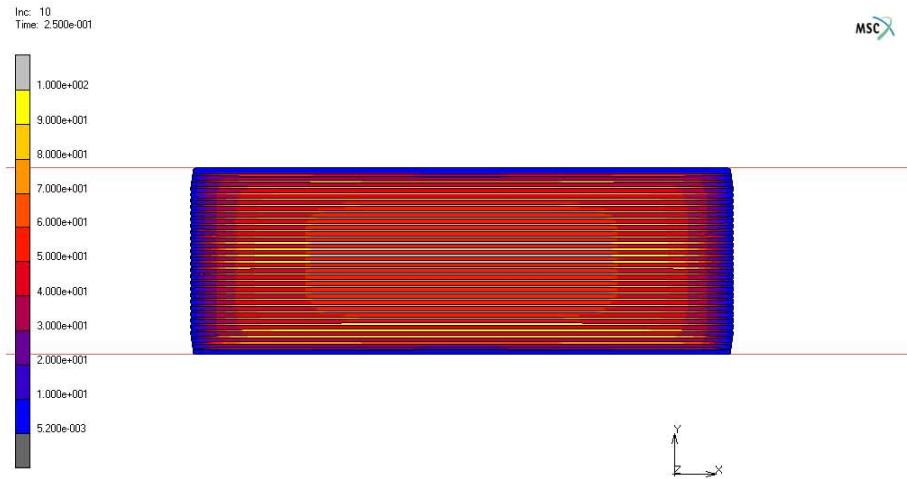


Figure 4.5 Von Mises stress contours at peak vertical force in a bearing of base B = 500mm [SET2 ($t_f = 0.07 \text{ mm}$)].

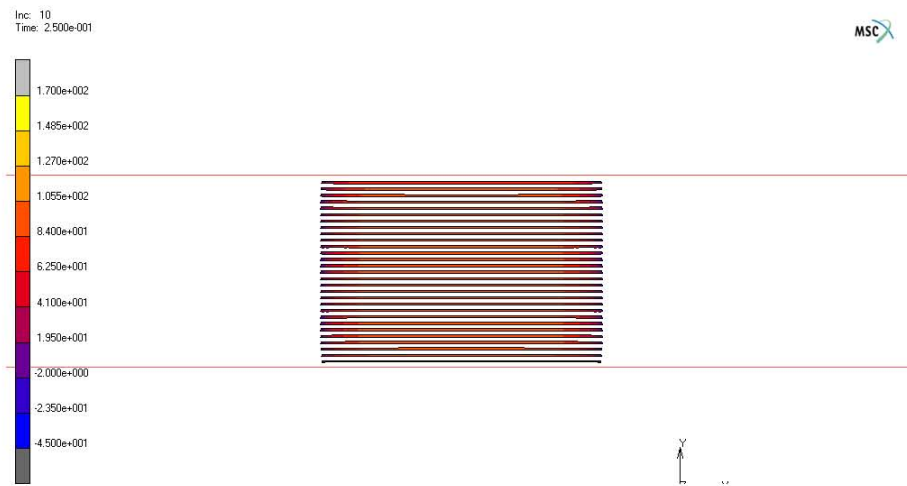


Figure 4.6 Tension contours in the fiber reinforcement (B = 250mm; $\sigma_y = 3.45 \text{ MPa}$; SET2).

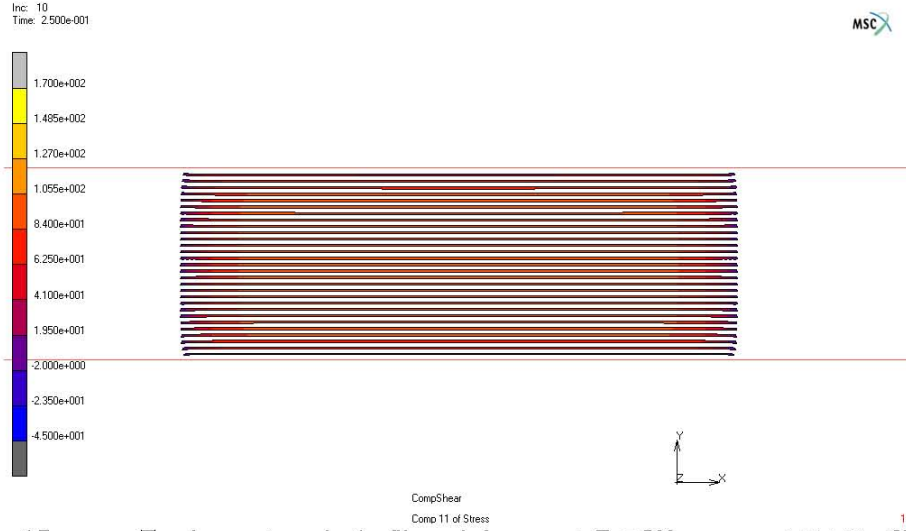


Figure 4.7 Tension contours in the fiber reinforcement ($B = 500\text{mm}$; $\sigma_v = 3.45\text{ MPa}$; SET2).

The previous formulae refer to the hypothesis of incompressibility of the rubber. Taking the compressibility into account, it gives

$$E_c = K \frac{\beta^2}{\alpha^2 + \beta^2} \left(1 - \frac{\tanh \lambda}{\lambda} \right) \quad (4.15)$$

where K is the bulk modulus of the elastomer,

$$\beta = \sqrt{\frac{12G}{K}} S^2 \quad (4.16)$$

$$\lambda = \sqrt{\alpha^2 + \beta^2} \quad (4.17)$$

Table 4.2 summarizes the model characteristics and the results of the pressure solution. The values reported in the Table 4.2 are plotted in Figure 4.8. For the considered range of bases (eq. shape factors), the vertical stiffness is linear with respect to the shape factor. Figure 4.8 is a plot of the vertical stiffness as a function of the shape factor for the twelve bearings of different geometries and reinforcement configurations.

Table 4.2 Model characteristics and pressure solution results (long strip bearings).

		Geometrical and Mechanical Properties					
B	[mm]	250	300	350	400	450	500
H	[mm]				180		
L	[mm]				750		
t_f	[mm]			0.07 (SET1)			
				0.25 (SET2)			

SET 1 (K=2000MPa)							
β	[-]	1.27	1.53	1.78	2.04	2.29	2.55
λ	[-]	4.76	5.72	6.67	7.62	8.58	9.53
E_c	[MPa]	113.10	118.11	121.69	124.37	126.45	128.12
K_v	[N/mm]	119160	149319	179481	209643	239806	269969
SET 2							
β	[-]	1.31	1.58	1.83	2.10	2.36	2.63
λ	[-]	2.79	3.35	3.91	4.47	5.03	5.59
E_c	[MPa]	284.90	310.41	329.02	343.08	354.05	362.83
K_v	[N/mm]	309229	404302	499954	595796	691700	787625

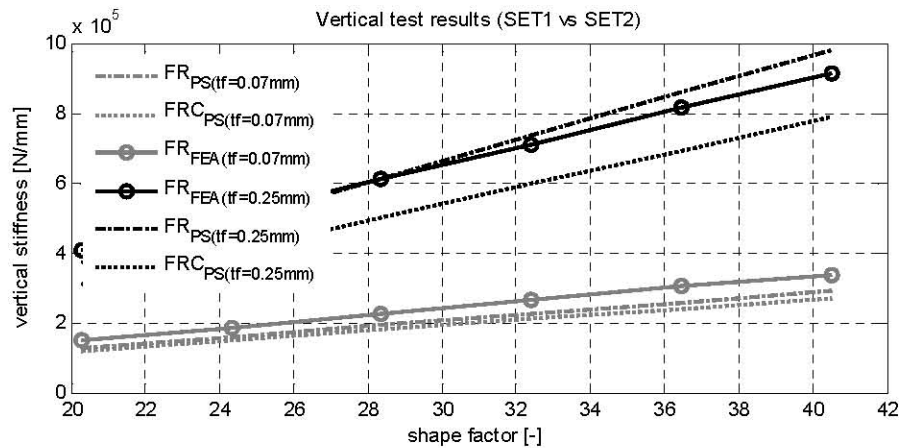


Figure 4.8 Vertical stiffness (FE analysis versus pressure solution).

In Figure 4.8, the gray and the black lines refer to SET1 and SET2, respectively. The continuous lines (FR_{FEA}) are plots of the FE analysis results, FR_{PS} and FRC_{PS} are the theoretical vertical stiffness results of FRBs for incompressible and compressible material respectively. It can be observed how there is a significant agreement between the performed FE analyses and the results of the Pressure Solution. However, the FE analyses give higher values of vertical stiffness. This could be addressed to a stiffening contribution of the quadratic mesh.

Figure 4.9 and Figure 4.10 show the plot of tensile stress as a function of the dimensionless length of the device, x/B , for the mid-height fiber layer—where the stresses are the largest—for $B=250\text{mm}$ and $B=500\text{mm}$, respectively. The gray lines refer to $t_f=0.07\text{ mm}$ (SET1) while the black lines refer to $t_f=0.25\text{ mm}$ (SET2). In each Figure the solid lines represent the pressure solution results and the dashed lines

represent the FE analyses results. The pressure solution and the FE analyses curves have the same trend.

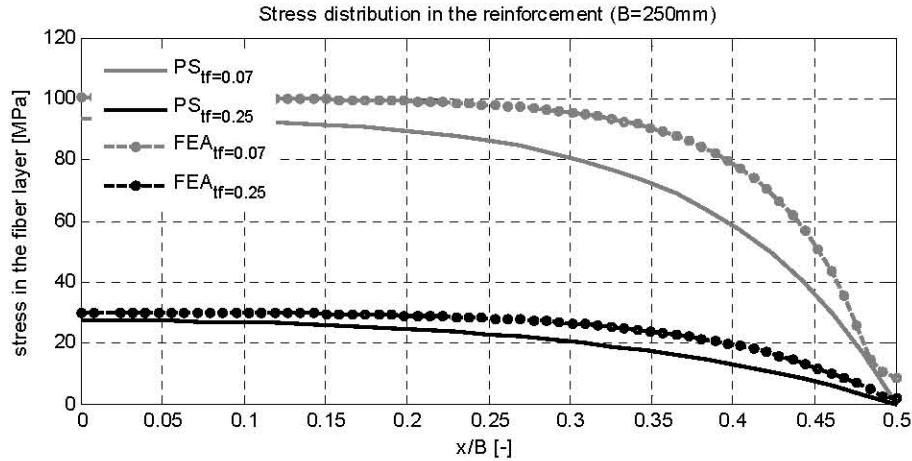


Figure 4.9 Stress distributions in the reinforcement (FE analysis versus pressure solution) for B=250mm.

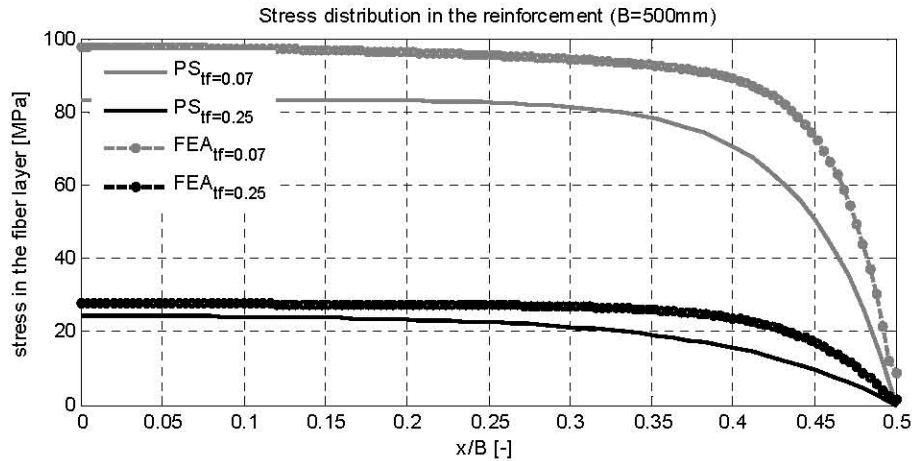


Figure 4.10 Stress distributions in the reinforcement (FE analyses versus pressure solution) for B=500mm.

However, it is noted that, for the considered values of shape factor, the pressure solution gives higher values of vertical stiffness than the FE analyses. The results also show that the pressure solution loses accuracy as the shape factor increases. This is in agreement with other research findings. Kelly and Takhirov suggest that the loss of accuracy is due mainly to the assumption of incompressibility of the material, and that the results

presented there can be considered valid only for low values of the shape factor ($S < 5$) [Kelly and Takhirov 2002].

The pressure solution results (dashed lines) show a good agreement with the output of the FE analyses. In Figure 4.11 the ratio between the stresses derived by the FE models and the stresses derived by the pressure solution is plotted against the dimensionless length x/B . The pressure solution gives accurate results for the description of the stress of the fiber in the bearing's core. Towards the free edges of the bearings, for a length of approximately the 10% of the base, the FE and the pressure solution results are different. This difference is very low for bearings with lower shape factors, but it is significant as the shape factor increases.

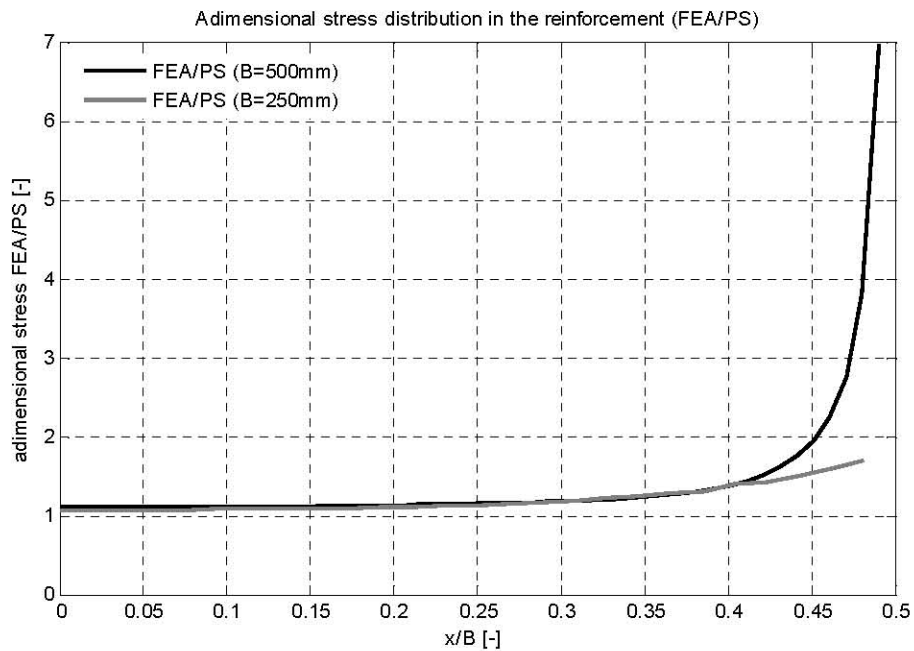


Figure 4.11 Non-dimensional stress (FE/pressure solution) against non-dimensional length (x/B).

4.2.3 Shear Results

In order to investigate the ultimate behavior of the bearings, in the second part of the analyses, a constant vertical load is applied, and then the horizontal displacement is increased. Figure 4.12 and Figure 4.13 are Von Mises stress contour maps for $B=250\text{mm}$

and $B=500\text{mm}$ [SET1, ($t_f = 0.07\text{ mm}$)], respectively, at a displacement that corresponds to the peak force in the load-displacement curve.

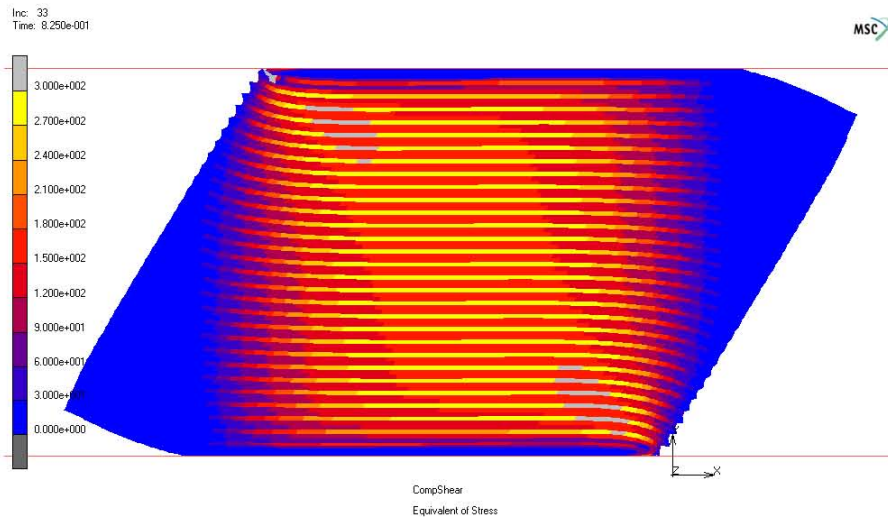


Figure 4.12 Von Mises stress contours at peak horizontal force in a bearing of base $B=250\text{mm}$.

The aforementioned Figures clearly show the favorable response of an isolator that is not bonded to the top and bottom supports. This is due to the elimination of tension in the elastomer. In a bonded bearing under the simultaneous action of shear and compression, the presence of an unbalanced moment at both top and bottom surfaces produces a distribution of tensile stresses in the triangular region outside the overlap between top and bottom. The compression load is carried through the overlap area, and the triangular regions created by the shear displacement provide the tensile stresses to balance the moment. These tensile stresses must be sustained by the elastomer and also by the bonding between the elastomer and the steel reinforcement plates. It is important to recall that the provision of these bonding requirements is the main reason for the high cost of current designs of isolator bearings for buildings and bridges. With the elimination of these tensile stresses, the bonding requirements for this type of bearings are reduced.

For bearings $B=250\text{mm}$ and $B=500\text{mm}$ (SET1), a concentration of stress in the cores is evident. The stress at peak horizontal force is twice the one due to compressive load. For different geometries, the maximum value of stress is the same. Changing shape factor has the only effect of changing the distribution of the stress in the bearing. Figure

4.14 and Figure 4.15 are the stress contours in the reinforcement at peak horizontal force for which the previous considerations are still valid.

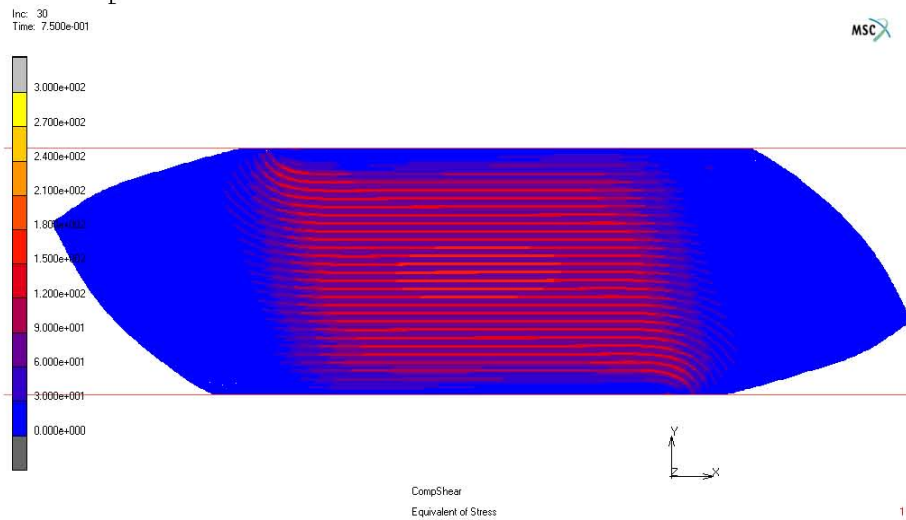


Figure 4.13 Von Mises stress contours at peak horizontal force in a bearing of base $B=500\text{mm}$.

Figure 4.16 plots the horizontal load as a function of the horizontal displacement for the six bearings of SET1 under a vertical pressure of 3.45MPa . The maximum horizontal displacement of the 500mm bearing is approximately the double of the one corresponding to 250mm bearing, while the peak force is the quadruple. Figure 4.17 shows the horizontal load versus the dimensionless horizontal displacement. The peak lateral displacement that the bearings exhibit is approximately equal to half the base. Figure 4.18 is a plot of the shear stress versus shear strain curves. These curves are straight lines up to the value of the lateral load for which roll-off starts to occur.

A progressive reduction of the lateral tangent stiffness is then observed with further increase of the lateral load. From the obtained results it can be stated that the numerical models can accurately reproduce the response of the devices at large deformations but, the distortion of the mesh makes the analyses grossly inaccurate. Moreover, some analyses also fail due to individual mesh elements turning inside out and pre-specified convergence criteria not being satisfied. This problem could be solved by employing remeshing, but the program has no algorithm that can be used to automatically remesh the rebar elements. Therefore, the ultimate theoretical displacement cannot be easily verified because of the very large distortion in the mesh. The values describing the ultimate behavior for the bearings SET1 are summarized in Table 4.3.

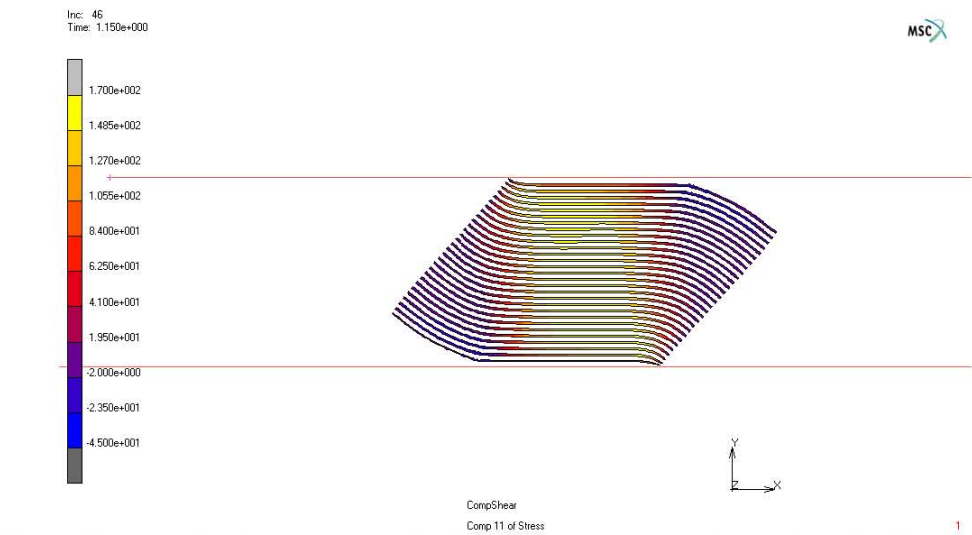


Figure 4.14 Tension contours in the fiber reinforcement at maximum shear ($B=250\text{mm}$).

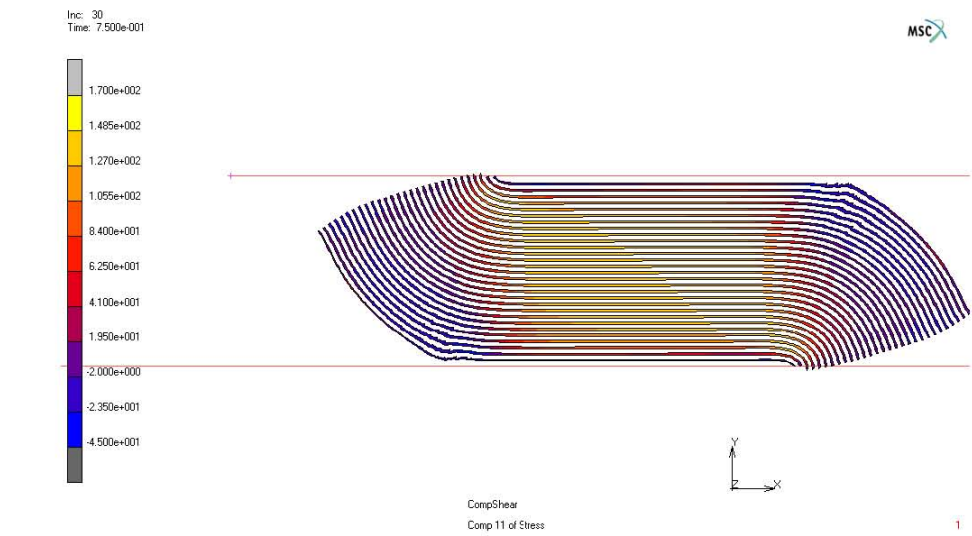


Figure 4.15 Tension contours in the fiber reinforcement at maximum shear ($B=500\text{mm}$).

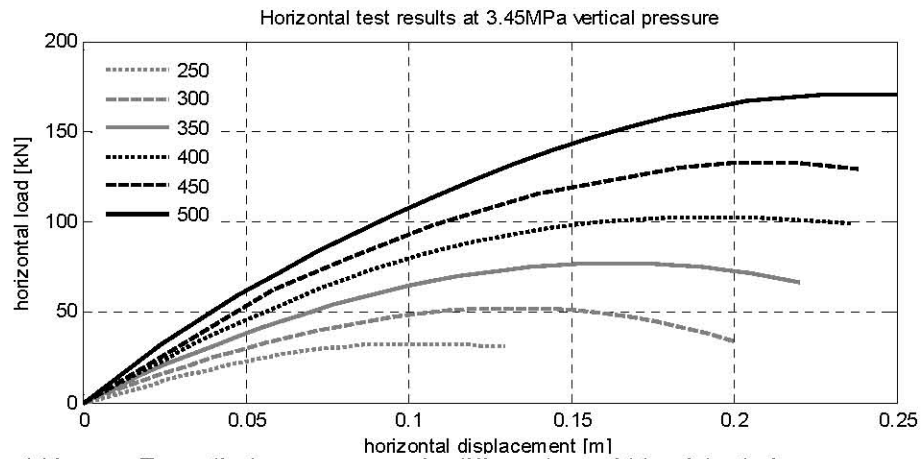


Figure 4.16 Force-displacement curves for different base widths of the devices.

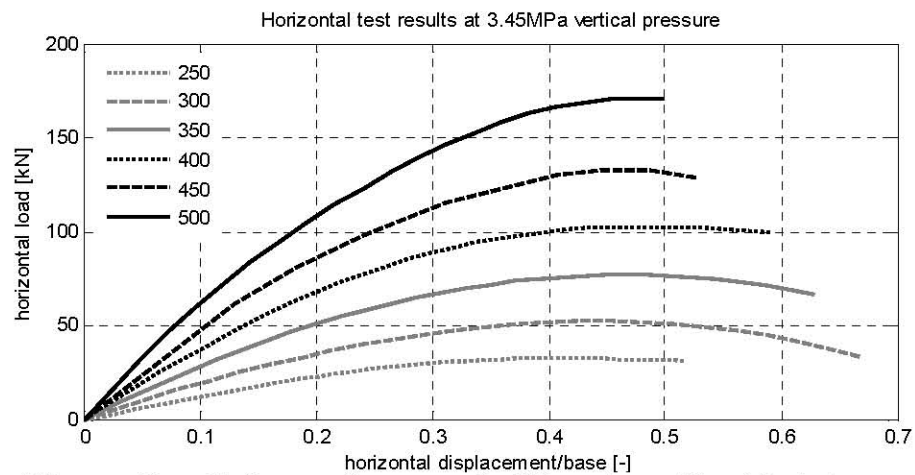


Figure 4.17 Force-displacement/base curves for different base widths of the devices.

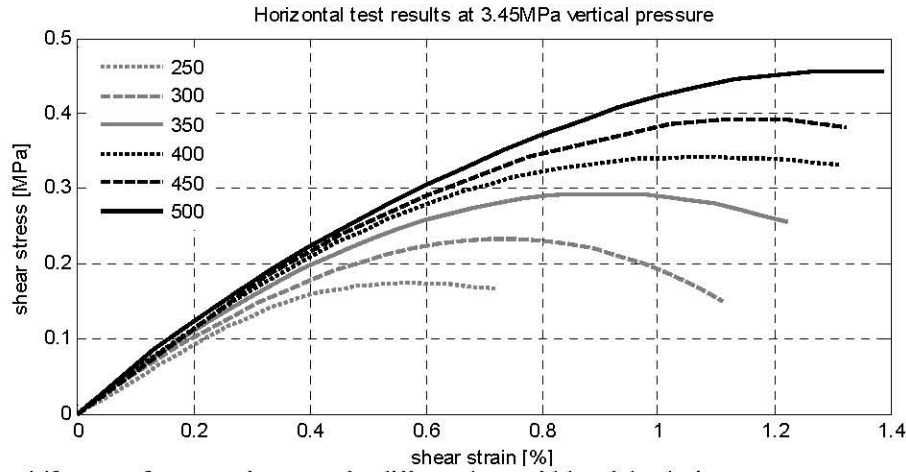


Figure 4.18 Stress-strain curves for different base widths of the devices.

Table 4.3

Ultimate performances of the bearings (SET1) under horizontal load.

B	S	$F_{h,u}$	τ_u	Δ_u	Δ_u/B	γ_u
[mm]	[-]	[kN]	[MPa]	[mm]	[-]	[%]
500	43.48	170.5	0.45	204	0.4	1.1
450	39.13	139.9	0.41	195	0.4	1.1
400	34.78	104.1	0.35	190	0.5	1.1
350	26.09	77.17	0.29	167	0.5	0.9
300	21.74	52.13	0.23	136	0.5	0.8
250	43.48	32.92	0.18	104	0.4	0.6

4.3 CIRCULAR BEARINGS

4.3.1 Geometrical Properties

Finite element models of FRBs with different shape factors are defined ($S = \Phi/4t = 10.13; 12.17; 14.18; 16.21; 18.23; 20.26$). The different values of the shape factor are obtained by increasing the values of the diameter of the device ($\Phi = 250; 300; 350; 400; 450; 500\text{mm}$). As shown in Figure 4.19, each device is made of twenty-nine fiber layers with twenty-eight interleaf rubber sheets. Each rubber layer is 5.75mm thick ($= t_r$), and each fiber sheet is 0.07mm thick ($= t_f$) for SET1 and 0.25mm thick for SET2. The geometrical characteristics are shown in Table 4.4. The FE discretization is shown in Figure 4.20, consisting of 8 + 1-node hexahedron elements with side length of $\sim 2\text{mm}$.

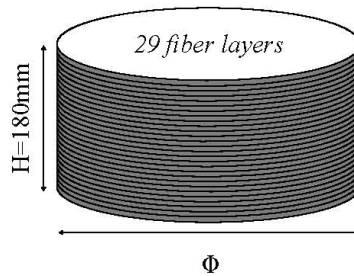


Figure 4.19 Circular type bearing showing reinforcements and dimensions.

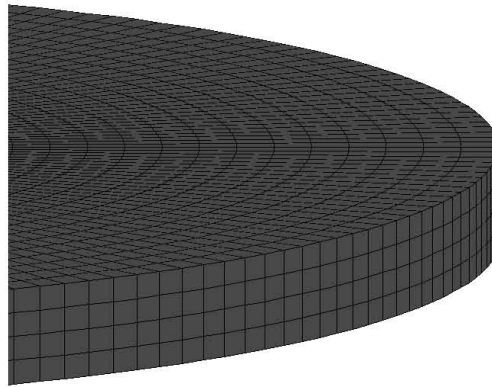


Figure 4.20 Model mesh and layout of the reinforcement layers (elements 143).

Table 4.4 Geometrical properties of the circular bearings.

	Φ	H	t_r	t_f	S
	[mm]	[mm]	[mm]	[mm]	[-]
Name	500				20.26
	450				18.23
	400			0.07 (SET1)	16.21
	350	180	5.75	0.25 (SET2)	14.18
	300				12.17
	250				10.13

4.3.2 Compression Results

The goal of this section is to verify the validity of the results provided by the pressure solution by comparing them with results from FE analyses. The contour maps of the equivalent stress in cross sections of a rubber layer obtained from analysis with MSC.Marc 2005 for bearings 250mm and 500mm, ($t_f = 0.07mm$) and ($t_f = 0.25mm$) under pure compression (peak vertical force = average pressure = $P/A = 3.45MPa$) are plotted from Figure 4.21 to Figure 4.24. The plots show the results on half of the bearing. From Figure 4.25 to Figure 4.28 the stress contours in the fiber layers are shown. In the vertical direction the force displacement behavior is linear in the considered range of load. The results from FE analyses can be compared to the results of the pressure solution.

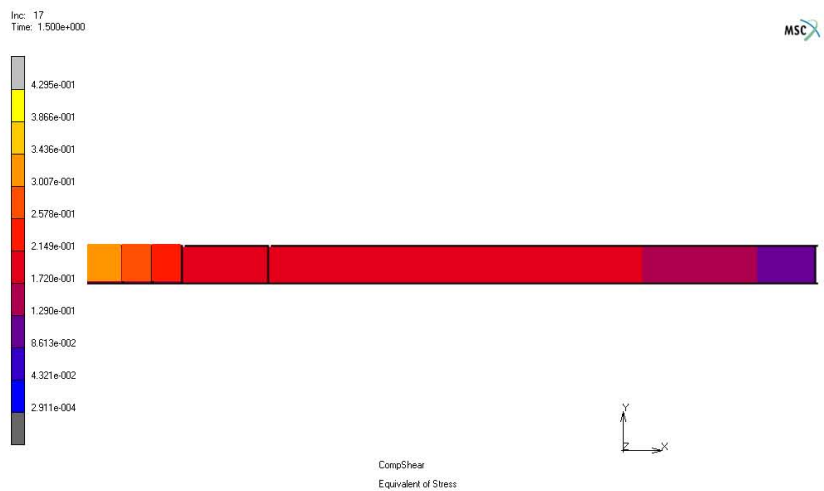


Figure 4.21 Von Mises stress contours at peak vertical force in a cross section of a rubber layer (left=core, $\Phi=250mm$ – SET1 $t_f=0.07mm$).

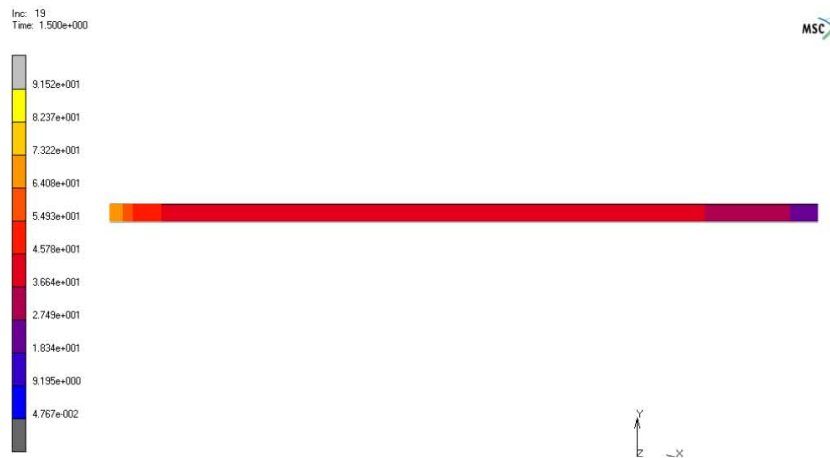


Figure 4.22 Von Mises stress contours at peak vertical force in a cross section of a rubber layer (left=core, $\Phi=500\text{mm}$ - SET1 $t_f=0.07\text{mm}$).

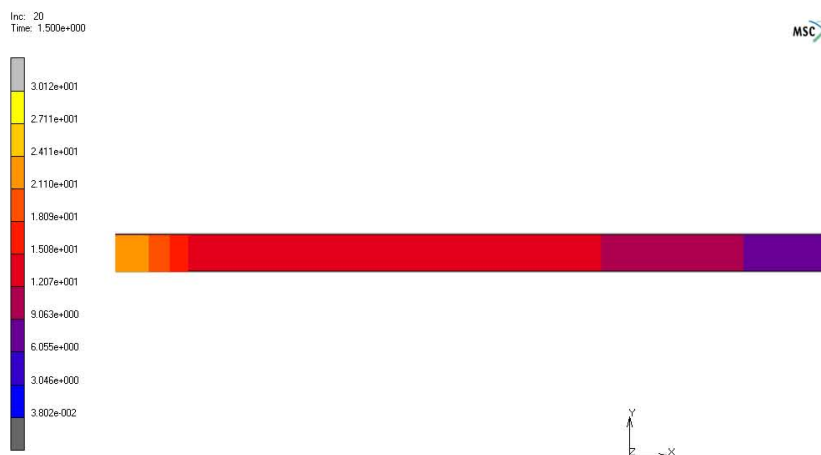


Figure 4.23 Von Mises stress contours at peak vertical force in a cross section of a rubber layer (left=core, $\Phi=250\text{mm}$ - SET2 $t_f=0.25\text{mm}$).

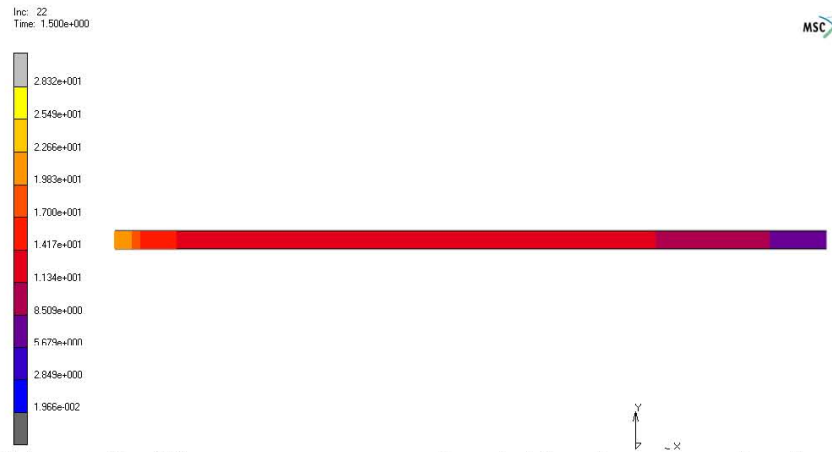


Figure 4.24

Von Mises stress contours at peak vertical force in a cross section of a rubber layer (left=core, $\Phi=500\text{mm}$ - SET2 tf =0.25mm).

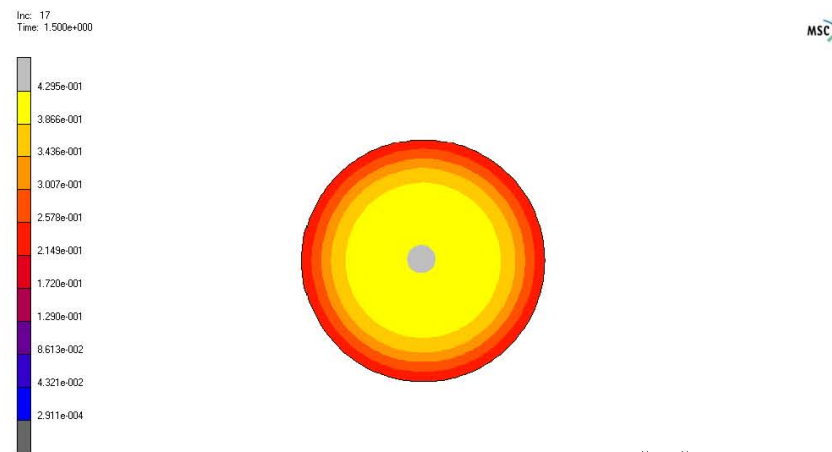


Figure 4.25

Tension contours in a fiber reinforcement ($\Phi=250\text{mm}$ - SET1 tf =0.07mm $\sigma_y = 3.45\text{ MPa}$).

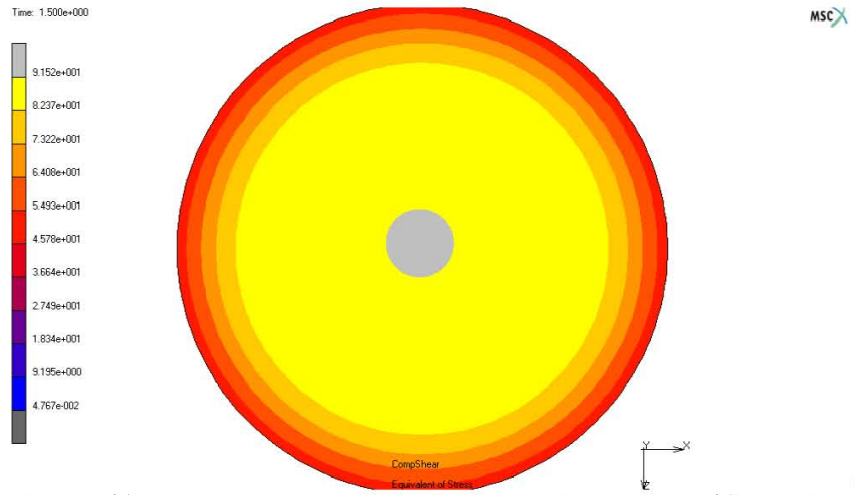


Figure 4.26

Tension contours in a fiber reinforcement ($\Phi=500\text{mm}$ – SE/T1 $t_f=0.07\text{mm}$
 $\sigma_y = 3.45 \text{ MPa}$).

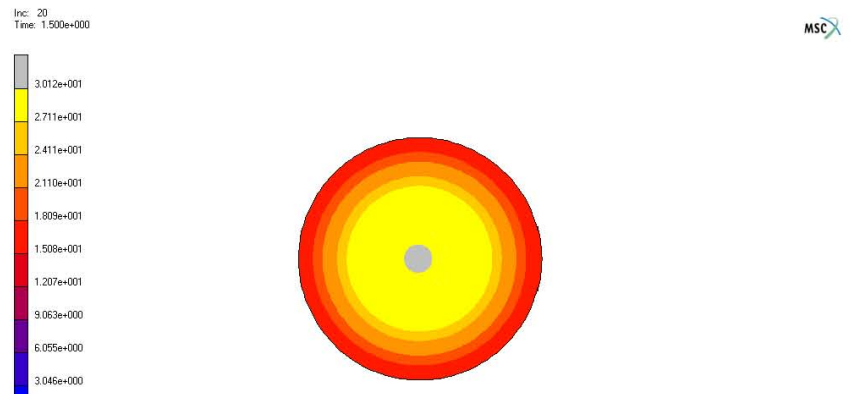


Figure 4.27

Tension contours in a fiber reinforcement ($\Phi=250\text{mm}$ – SE/T2 $t_f=0.25\text{mm}$
 $\sigma_y = 3.45 \text{ MPa}$).

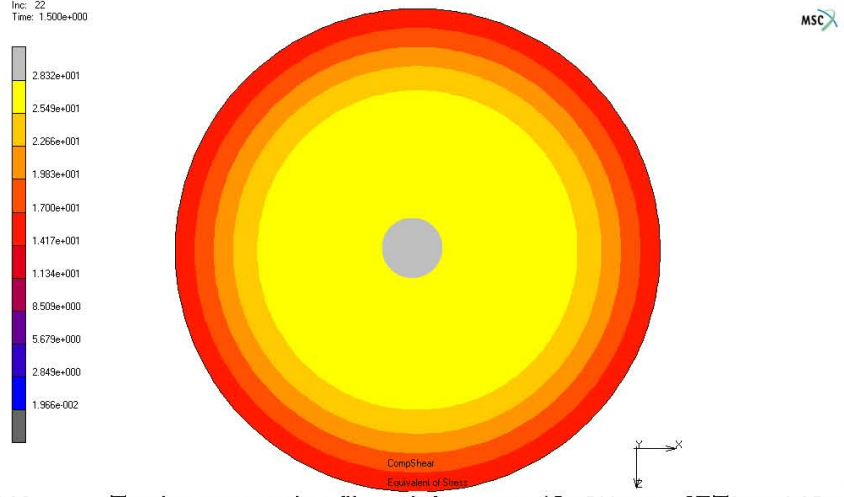


Figure 4.28 Tension contours in a fiber reinforcement ($\Phi=500\text{mm}$ – SET2 tf =0.25mm $\sigma_p = 3.45\text{MPa}$).

Recalling Chapter 3, the vertical stiffness of the bearing, K_V , can be written as

$$K_V = (E_c A) / t_r \quad (4.18)$$

For circular bearings

$$E_c = 24GS^2(1+\nu) \cdot \frac{\left[I_0(\lambda) - \frac{2}{\lambda} I_1(\lambda) \right]}{\alpha^2 \left[I_0(\lambda) - \frac{1-\nu}{\lambda} I_1(\lambda) \right] + \beta^2 \frac{1+\nu}{2} I_0(\lambda)} \quad (4.19)$$

in which I_0 and I_1 are modified Bessel functions of the first and second kind of order n , $S = \Phi/4t_r$, and

$$\alpha^2 = \frac{12(1-\nu^2)GR^2}{E_f t_f t} \quad (4.20)$$

$$\beta^2 = \frac{12GR^2}{Kt^2} \quad (4.21)$$

$$\lambda^2 = \alpha^2 + \beta^2 \quad (4.22)$$

Table 4.5 summarizes the model characteristics and the results of the pressure solution. Figure 4.29 is a plot of the load displacement relations for the twelve bearings of different geometry/reinforcement. The values reported in Table 4.5 are plotted in Figure 4.30

where the vertical stiffness is a function of the shape factor for the twelve bearings of different geometry/reinforcement. The gray curves refer to SET1 bearings and the black curves to SET2. Continuous lines describe the pressure solution results for flexible reinforcement and the dashed lines refer to flexible reinforcement and compressibility.

Continuous marked lines are the FE analyses results. The gray and the black lines refer to SET1 and SET2, respectively. The PS and PS+C lines are the theoretical vertical stiffness results of FRBs for incompressible and compressible materials, respectively. As can be seen from the plots, the FE analyses results and pressure solution outputs are in good agreement. It is noted that the FE analyses gives higher values of vertical stiffness because of a stiffening contribution of the hexahedric mesh.

Table 4.5 Model characteristics and pressure solution results (circular bearings).

Geometrical and Mechanical Properties							
Φ	[mm]	250	300	350	400	450	500
H	[mm]				180		
t_f	[mm]			0.07 (SET1)			
				0.25 (SET2)			
n layers	[-]			29			
t_r	[mm]			6.37 (SET 1)			
				6.17 (SET 2)			
E_f	[MPa]			14000			
ν	[-]			0			
G	[MPa]			0.70			
Compression Stiffness with Flexible Reinforcement							
SET 1							
E_c	[MPa]	50.04	52.51	54.25	55.55	56.54	57.33
K_v	[N/mm]	14218.00	21485.00	30216.00	40406.00	52055.00	65162.00
SET 2							
E_c	[MPa]	142.04	158.64	171.00	180.39	187.73	193.56
K_v	[N/mm]	40362.00	64914.00	95235.00	131220.00	172830.00	220000.00
Flexible Reinforcement and Compressibility							
SET 1 (K=2000MPa)							
E_c	[MPa]	48.56	50.92	52.58	53.82	54.77	55.53
K_v	[N/mm]	13799.00	20835.00	29286.00	39151.00	50428.00	63116.00
SET 2							
E_c	[MPa]	130.42	144.51	154.93	162.85	169.03	173.96
K_v	[N/mm]	37059.00	59130.00	86287.00	118460.00	155620.00	197730.00

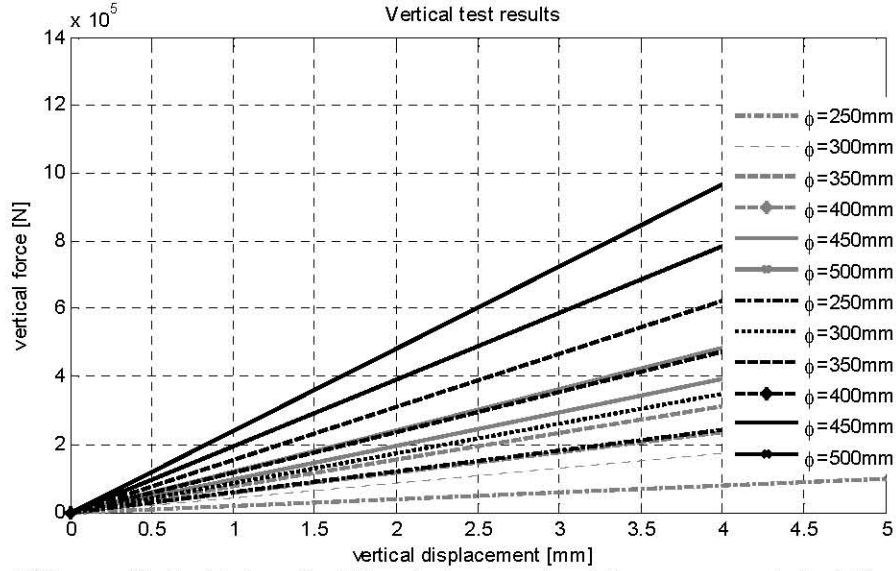


Figure 4.29 Vertical test results (FE analysis versus closed-form pressure solution). Gray lines are the solutions for SET1 while black lines are the solutions for SET2.

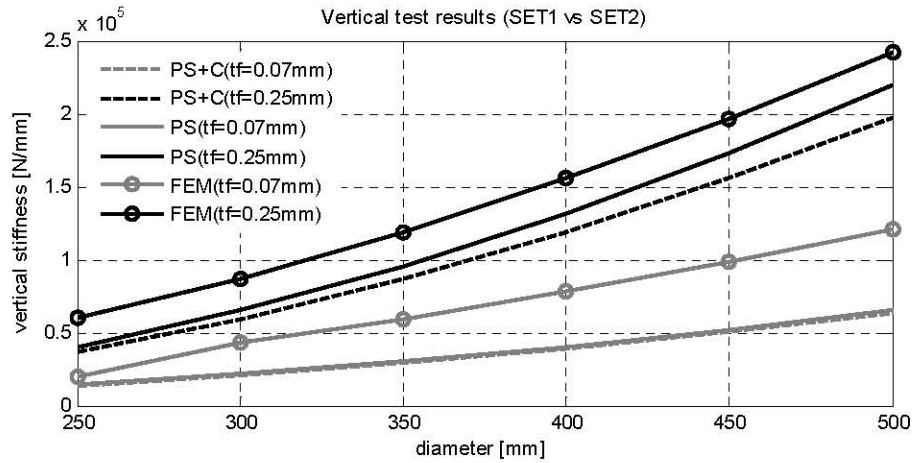


Figure 4.30 Vertical stiffness results.

Figure 4.31 is the plot of non-dimensional stiffness $K_{\nu 0.25}/K_{\nu 0.07}$ as a function of the diameter, Φ . The solid line represents the pressure solution result and the dashed line represents the FE analysis outputs. The FE analyses and pressure solution outputs

are in good agreement (see Figure 4.32), although the FE analyses give higher values of vertical stiffness because of a stiffening contribution of the hexahedral mesh. For $t_f = 0.25$ mm, it is evident that the ratio between the different solutions increases with increasing the nominal dimension of the device: the compressibility of the rubber is the main quota of the deformation so that it cannot be neglected [Chahoub and Kelly 1986] [Chahoub and Kelly 1990].

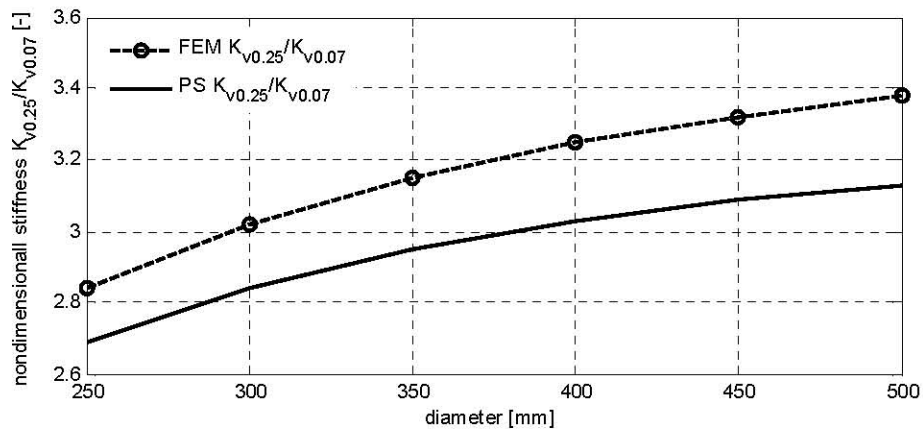


Figure 4.31 Non-dimensional stiffness versus diameter.

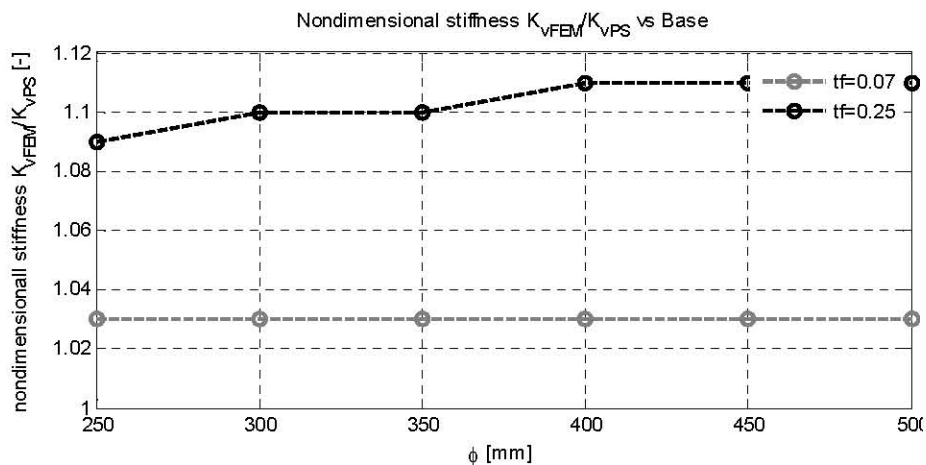


Figure 4.32 K_{vFEM}/K_{vPS} as a function of the diameter.

4.4 SQUARE BEARINGS

4.4.1 Geometrical Properties

Finite element models of square type FRBs with different shape factors are defined ($S=B/4t_r=10.87; 13.04; 15.22; 17.39; 19.57; 21.74$). The different values of the shape factor are obtained by increasing the values of the base of the device ($B = 250; 300; 350; 400; 450; 500\text{mm}$) keeping a constant height. As shown in Figure 4.33, each device is made of twenty-eight rubber layers with twenty-nine interleaf fiber sheets. Each rubber layer is $\sim 5.7\text{mm}$ thick ($=t_r$), and each fiber sheet is 0.07mm thick ($=t_f$) for SET1 and 0.25mm thick for SET2. Figure 4.33 shows a cross section of the model of the square-type FRB investigated in this study. The geometrical characteristics are shown in Table 4.6.

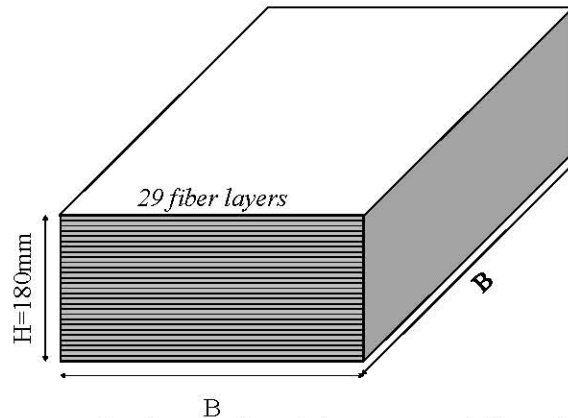


Figure 4.33 Square type bearing showing reinforcements and dimensions.

The finite element discretization is shown in Figure 4.34. As assumed in the pressure solution, also the FE models assume that there is no friction between the rubber and the top and bottom surfaces, and that the bearings are loaded in pure compression only. As a consequence, each layer of the bearing can deform evenly under compression, and it is sufficient to model only a single layer of the device to fully describe the behavior of the bearing [Koh and Kelly 1989]. For the specific load condition, the model is doubly-symmetric: the symmetry with respect two orthogonal planes is therefore applied as boundary condition. The three-dimensional meshes consist of eight-node, isoparametric, three-dimensional brick elements with trilinear interpolation (element type 84 in MSC.Marc 2005 [MSC.Software 2004]). Four layers of elements were used through

the thickness, and the size of the mesh along the base was chosen to have a ratio of distortion approximately equal to one.

Table 4.6 Geometrical properties of the square bearings.

B	H	t_r	t_f	S
[mm]	[mm]	[mm]	[mm]	[-]
500				21.74
450				19.57
400			0.07 (SET1)	17.39
350	180	5.75	0.25 (SET2)	15.22
300				13.04
250				10.87

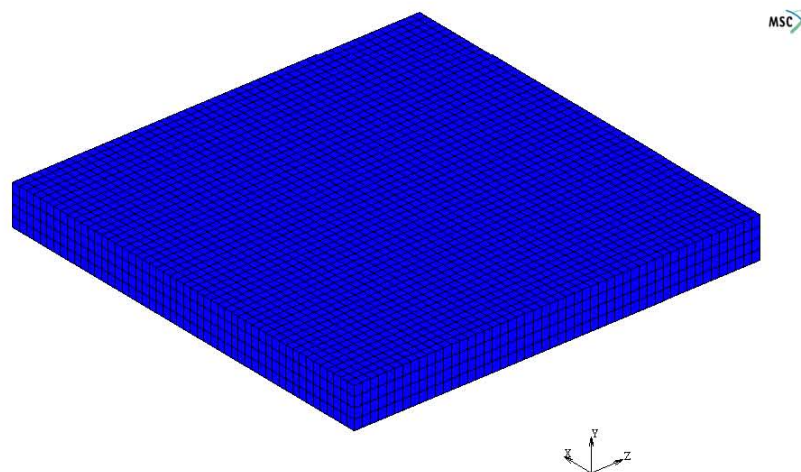


Figure 4.34 Model mesh for a single pad (element type 84 in MSC.Marc 2005 [MSC.Software 2004]).

4.4.2 Compression Results

The results from FE analyses can be compared to the results of the pressure solution. Recalling Chapter 3, the vertical stiffness of the bearing, K_V , can be written as

$$K_V = (E_c A) / t_r \quad (4.23)$$

For a square bearing

$$E_c = \frac{96GS^2}{\pi^2 (\alpha a)^2} \sum_{n=1}^{\infty} \frac{2}{(n-1/2)^2} \left(\frac{\tanh \gamma_n a}{\gamma_n a} - \frac{\tanh \beta_n a}{\beta_n a} \right) \quad (4.24)$$

$$\alpha = \sqrt{\frac{12G(1-\nu^2)}{E_f t_f t}} \quad (4.25)$$

$$\gamma_n = \left(n - \frac{1}{2} \right) \frac{\pi}{a} \quad (4.26)$$

$$\beta_n = \sqrt{\gamma_n^2 + \alpha^2} \quad (4.27)$$

It is again recalled that the previous formulae refer to the hypothesis of incompressibility of the rubber. Table 4.7 summarizes the models characteristics and the pressure solution results for square type bearings. The values reported in the Table 4.7 are plotted in Figure 4.35 and Figure 4.36. For the considered range of bases (eq. shape factors), the vertical stiffness is linear with respect to the shape factor. Figure 4.35 is a plot of the vertical test results. Figure 4.36 is a plot of the vertical stiffness as a function of the base (eq. shape factor) for the twelve bearings of different geometry/reinforcement. The gray lines refer to $t_f = 0.07$ mm (SET1) while the black lines refer to $t_f = 0.25$ mm (SET2). In each Figure the solid lines represent the pressure solution results, and the lines with markers represent the results obtained with the numerical models.

Figure 4.37 is a plot of the non-dimensional vertical stiffness (FE model/pressure solution) as a function of the base. Figure 4.38 is a plot of the non-dimensional vertical stiffness (FE model/pressure solution) as a function of the base/diameter for the square and the circular bearings.

Table 4.7

Model characteristics and pressure solution results (square bearings).

Geometrical and Mechanical Properties							
B	[mm]	250	300	350	400	450	500
H	[mm]	180					
t _f	[mm]	0.07 (SET1)					
		0.25 (SET2)					
n layers	[-]	29					
t _c	[mm]	6.37 (SET 1)					
		6.17 (SET 2)					
E _f	[MPa]	14000					
G	[MPa]	0.70					
Compression Stiffness with Flexible Reinforcement							
SET 1							
α	[-]	0.02					
E _{c (n=9)}	[MPa]	120.60	126.19	130.19	133.19	135.52	137.39
SET 2							
α	[-]	0.04					
E _{c (n=9)}	[MPa]	340.49	376.57	403.26	423.59	439.49	452.25

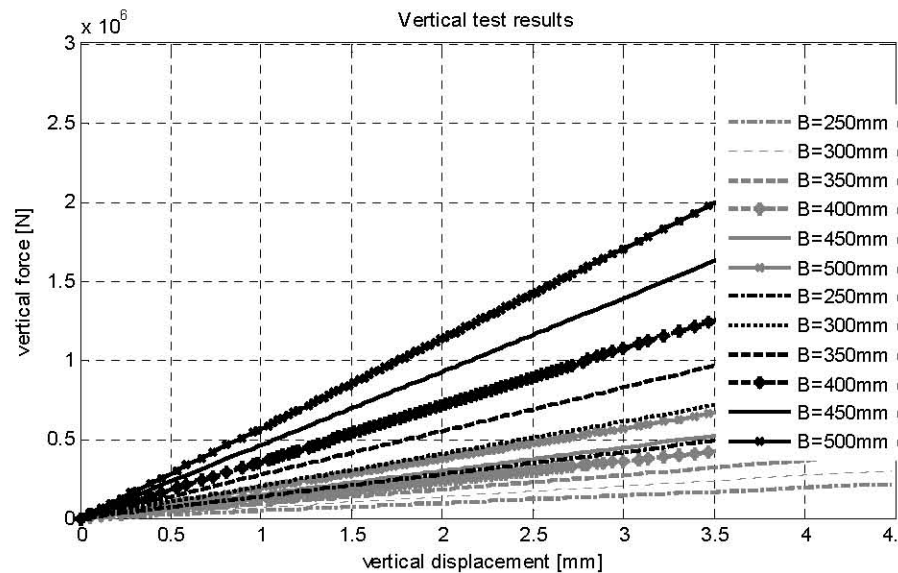


Figure 4.35

Vertical force–vertical displacement.

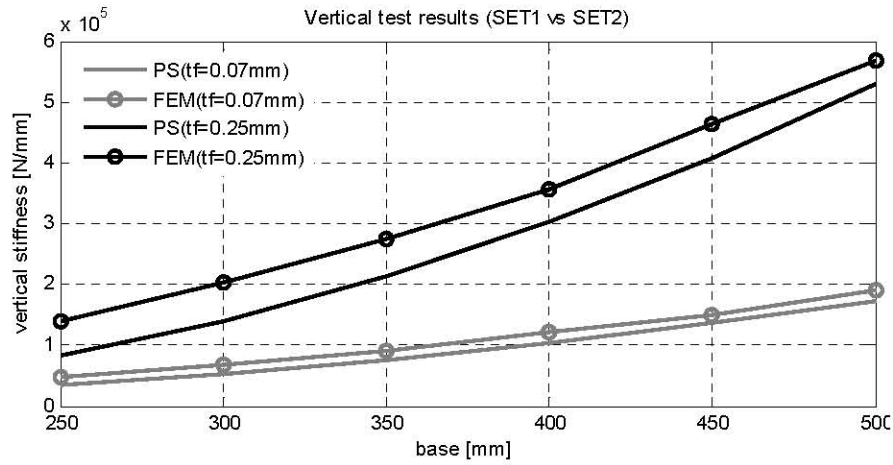


Figure 4.36 Vertical stiffness versus base.

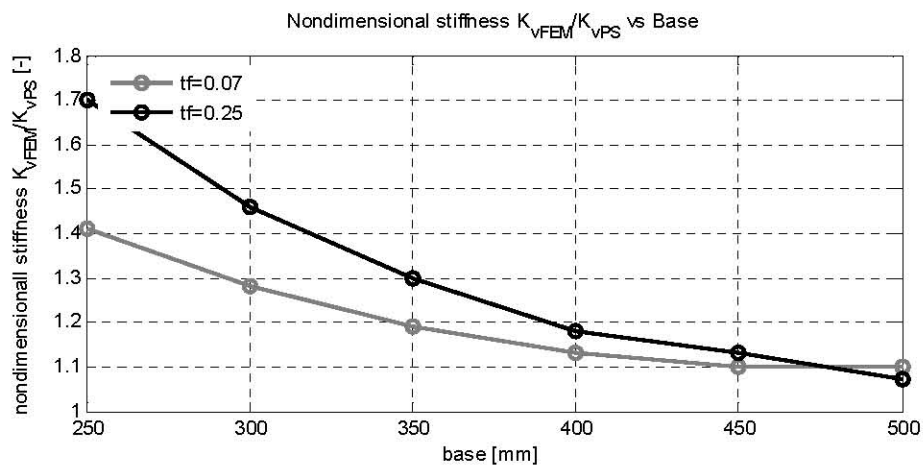


Figure 4.37 K_{vFEM}/K_{vPS} as a function of the base.

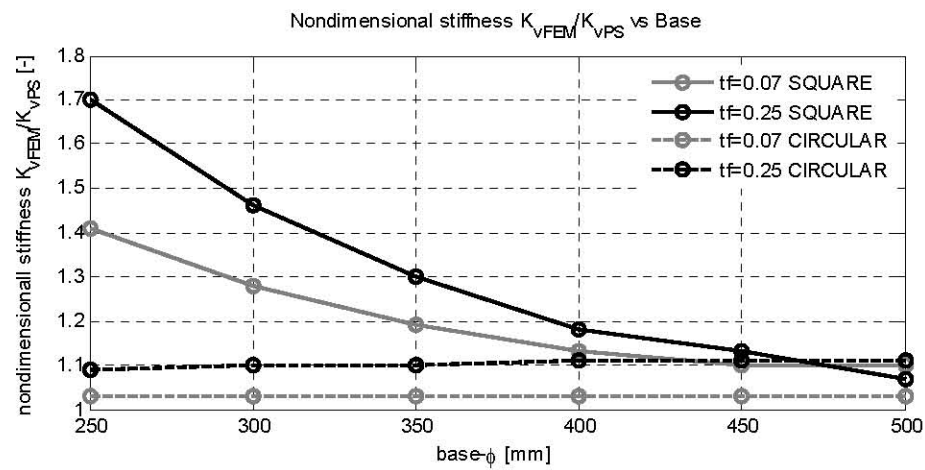


Figure 4.38 K_{vFEM}/K_{vPS} as a function of the base-diameter for square and circular bearings.

5. ULTIMATE DISPLACEMENT OF UNBONDED BEARINGS

5.1 INTRODUCTION

The most important aspects of FRBs are that they do not have thick end plates, they are not bonded to the top and bottom support surfaces, and their reinforcements are flexible. These features at first sight might seem to be deficiencies of their design, but they have the advantage of eliminating the presence of tensile stresses in the bearing by allowing it to roll off the supports. This reduces the costly stringent bonding requirements that are typical for conventional bearings. The FRBs can deform without damage if displacements of seismic magnitude are applied because the top and bottom surfaces can roll off the support surfaces and no tension stresses are produced. The unbalanced moments are resisted by the vertical load through offset of the force resultants on the top and bottom surfaces. In conventional bonded bearings, the compression is carried through the overlap region between top and bottom surfaces, and the unbalanced moment is carried by tension stresses in the regions outside the overlap Figure 5.1. In unbonded FRB, the moment created by the offset of the resultant compressive loads, P , balances the moment created by the shear, V , as shown in Figure 5.2.

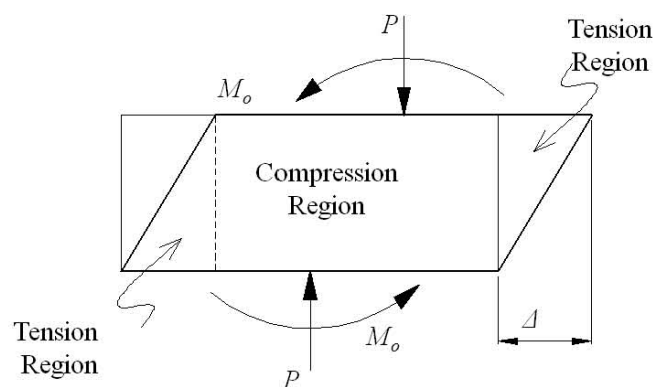


Figure 5.1 Bonded bearing under compression and shear.

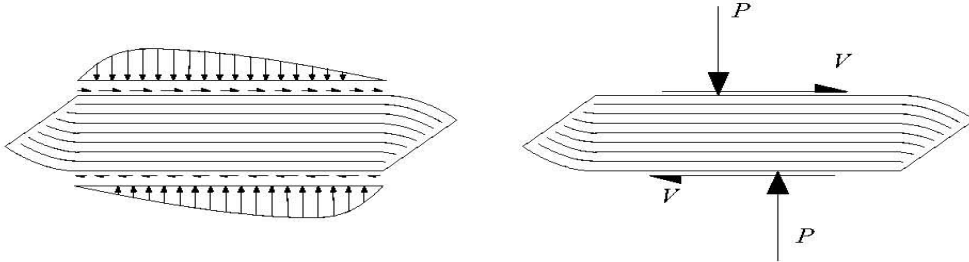


Figure 5.2 Normal and shear stress distributions on the top and bottom faces of the unbonded bearing in its deformed shape.

5.2 LIMIT DISPLACEMENT CRITERIA

In this section two limiting displacement criteria are introduced:

- overall stability;
- no contact with horizontal subgrade.

The overall stability represents the displacement at which the peak value of horizontal force is reached in the horizontal load-displacement path. After the peak is reached, the bearing can be displaced further. Experimental results [Kelly 1999] demonstrated that the roll-off response is limited by the fact that the lateral free edges of the bearing rotate from the vertical towards the horizontal with increasing shear displacement. The limit of this process is reached when the originally vertical surfaces at each side of the bearing come in contact with the horizontal surfaces at both top and bottom. Further horizontal displacements beyond this point can only be achieved by slipping. The friction coefficient between rubber and other surfaces can often take very large values, possibly as high as one. For this reason, slip can produce damage to the bearing through tearing of the surfaces and heat generated by the sliding motion.

5.2.1 Stability of Horizontal Displacement

The basic assumption for the behavior of these bearings under horizontal displacement is that the areas of the roll-off are free of stress and that the area below the contact region has constant shear stress, as shown in Figure 5.3. The basic hypothesis for the analysis of these bearings is that the regions that have rolled off the rigid supports are free of stress, and that the volume under the contact area has constant shear stress. Under these assumptions, the active area that produces the force of resistance F to displacement Δ is $B - \Delta$, and thus the force (per unit width of the bearing) is $F = G\gamma(B - \Delta)$, but $\gamma = \Delta / t_r$, thus $F = G(B - \Delta)\Delta / t_r$. Consequently, the force displacement curve has zero slope when

$$\frac{dF}{d\Delta} = \frac{G}{t_r}(B - 2\Delta) = 0, \text{ i.e., when } \Delta = B/2 \quad (5.1)$$

This implies that the bearing remains stable (positive tangential force-displacement relationship) as long as the displacement is less than half the length in the direction of the applied load. As a result of the limiting displacement analysis, it is possible to establish a simple design criterion for this type of bearing [Kelly *et al.* 2012]. The key is to determine a maximum required design displacement that would normally depend on the site, the isolation period, and damping. Indicating with Δ such displacement, then the requirement for positive incremental horizontal stiffness is that the width B of the bearing in the direction of the displacement is at least twice the displacement, i.e. $B \geq 2\Delta$.

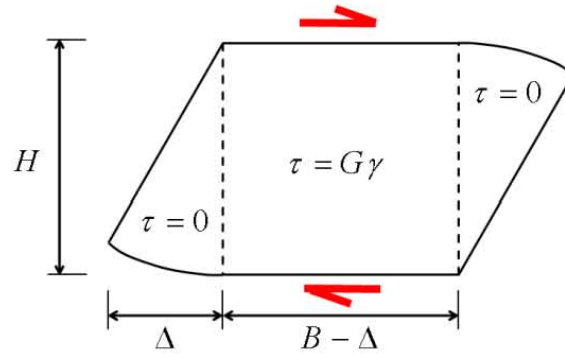


Figure 5.3 Unbonded bearing under shear load.

5.2.2 No Contact with Horizontal Subgrade

In FRBs, the fiber sheets are much more flexible compared to the steel reinforcing in current designs of building isolators. Under horizontal load this flexibility allows the unbonded surfaces to roll off the loading surfaces. Thus the maximum displacement for a bearing of this type can be specified as the point where the vertical free edges become parallel to an horizontal plane. In a normal case, where the bearing thickness is small in comparison to the in-plane dimension in the direction of loading, this can be estimated by studying only the deformation of one side and neglecting the interaction between the deformations at each end.

The basic assumptions used to predict the limiting shear deformation are:

- the material is incompressible;
- the plates are completely flexible;
- the free surfaces of the roll-off portions are stress free.

The first two points are reasonable hypotheses for the elastomeric and for the reinforcement of these bearings. The third assumption means that the displacement when the vertical surface touches the horizontal support is equal to the length of the curved arc of the free surface.

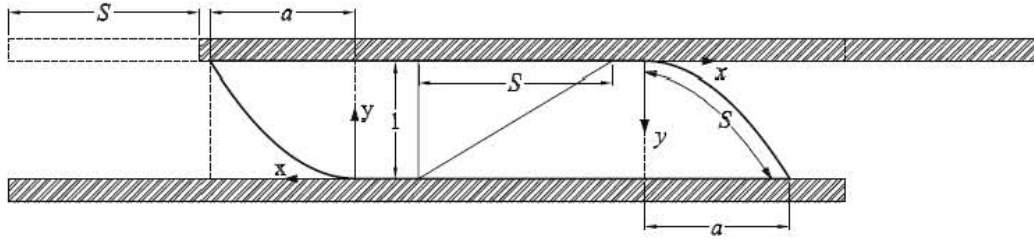


Figure 5.4 Schematic representation of the deformed bearing.

The geometry assumed in the derivation is shown in Figure 5.4. The thickness of the bearing is one, and the horizontal projection of the curved free surface is a . If S is a parabolic arc, then in the coordinate system x, y shown in the Figure, the curved surface is given by

$$y = \frac{x^2}{a^2}; \quad x = ay^{1/2} \quad (5.2)$$

The area of the region enclosed by the curved arc of length S is

$$A = \int_0^1 dy \int_0^{ay^{1/2}} dx = \int_0^1 ay^{1/2} dy = \frac{2}{3}a \quad (5.3)$$

The requirement of incompressibility means that the volume before and after deformation is preserved, thus

$$\frac{1}{2}S = \frac{2}{3}a, \quad \text{or} \quad a = \frac{3}{4}S \quad (5.4)$$

The length of the curved arc, S , is then given by

$$dS = (dx^2 + dy^2)^{1/2} \quad (5.5)$$

where

$$dy = \frac{2x dx}{a^2} \quad (5.6)$$

and

$$S = \int_0^a \left(1 + \frac{4x^2}{a^4} \right)^{1/2} dx \quad (5.7)$$

Using the change of variable $u = 2x / a^2$ and $du = 2 / a^2 dx$, it gives

$$S = \frac{a^2}{2} \int_0^{2/a} (1 + u^2)^{1/2} du \quad (5.8)$$

Let $u = \sinh(t)$, then

$$S = \frac{a^2}{2} \int_0^{\operatorname{arcsinh}(2/a)} \cosh(t)^2 dt \quad (5.9)$$

Since $\cosh(t)^2 = 1 / 2 (\cosh(2t) + 1)$, this leads to

$$S = \frac{a^2}{4} [\sinh(t) \cosh(t) + t]_0^{\operatorname{arcsinh}(2/a)} \quad (5.10)$$

and substituting $\cosh(t) = (1 + \sinh(t)^2)^{1/2}$, S can be expressed as

$$S = \frac{a^2}{4} \left[\frac{2}{a} \left(1 + \frac{4}{a^2} \right)^{1/2} + \operatorname{arcsinh} \left(\frac{2}{a} \right) \right] \quad (5.11)$$

The incompressibility condition requires that $S = 4a / 3$. This leads to an equation for a in the form

$$\operatorname{arcsinh} \left(\frac{2}{a} \right) = \frac{16}{3a} - \frac{2}{a} \left(1 + \frac{4}{a^2} \right)^{1/2} \quad (5.12)$$

Replacing $2 / a$ with t and inverting the equation leads to a transcendental formula for t , where

$$t = \sinh \left[\left(\frac{8}{3} - (1 + t^2)^{1/2} \right) t \right] \quad (5.13)$$

which after solving for t gives a and in turn S . The solution to an high degree of accuracy is $t = 1.60$, $a = 1.25$ and $S = 1.67$. This is the overall shear strain. The conclusion is that in broad terms these bearings can experience a displacement equal to the thickness of the rubber before they run the risk of damage by sliding.

The shear tests conducted in MSC.Marc 2005 [MSC.Software 2004] for the different bearings (Section 4.2.3) show that the peak horizontal displacement is approximately half of the base length. The theoretical model, which is used to determine the peak horizontal displacement, gives good results even when compared to the FE analyses with non-zero vertical load. It is noted that for a fixed axial load, the shear load

goes through a maximum as the shear deflection is further increased. The displacement at which this maximum occurs decreases with increasing axial load. Therefore, it can be concluded that further FE analyses are necessary to precisely evaluate the influence of the vertical load on the horizontal behavior of the bearings. Moreover, this study was conducted considering the shape factor, S , as the only variable. Analytical results showed that although shape factor is an important geometrical parameter that characterizes the mechanics of the bearings, there are other parameters — such as the slenderness of the bearing — that should be taken into account to fully describe the global behavior of the device.

6.MATERIAL TESTING

6.1 INTRODUCTION

As demonstrated by Kelly [1999], low-cost rubber bearings can be produced using natural rubber and fiber reinforcements.

For seismic isolators, reinforcements with Fiber Reinforced Polymers (FRP) seem to be particularly suitable: they offer excellent corrosion resistance, high stiffness to weight ratio, good fatigue properties, non-magnetic properties, ease of transportation and handling. Moreover, they need low energy consumption during fabrication [Micelli and Nanni 2003].

For a further reduction of the production costs of FRBs, in the following it is investigated the possibility of replacing natural rubber with a Tyre Derived Material (TDM). TDMs involve the reuse of materials available everywhere, leading to environmental friendly products. In this Chapter experimental tests conducted at Department of Structural Engineering – University of Naples are introduced and the mechanical behavior of a tyre derived rubber like material is discussed.

TDMs deserve special interest because the reuse of tyres is one of the most important topics in recycling and Environmental Engineering. According to the European Tyre and Rubber Manufacturers Association [ETRMA 2011], in 2006, the European Union generated approximately 3213 million tons of scrap tyres.

The 30% of these scrap tyres is used as Tyre-Derived Fuel, the 27.5% is used as recycling materials in Civil Engineering works, almost the 20% is disposed to landfill or is illegally dumped and the remaining quota is traded or sold abroad.

Also, the energy recovered from exhausted tyres by waste to energy plants is a quarter of the energy needed for their production and the process itself raises obvious pollution concerns.

Moreover, tyres are not desired at landfills. This is due to their large volume and 75% void space, which quickly consume areas and, trapping methylene gasses, makes tyres bubble to the surface damaging landfill liners that are generally installed to help keep landfills contained from polluting local surface and ground water. In response to these problems researchs on uses of scrap tyres have created many new markets and innovative applications [Makarov and Drozdovski 1991].

The US Army Corps for Engineers used tyres to protect marshland on Gaillard Island, Alabama, from wave action, enabling the plants to establish their root system. The US Environmental Protection Agency has conducted research projects on scrap tyres including rubberized asphalts and protection systems against erosion of bridge piers. The US Department of Energy has conducted research on innovative scrap tyre uses. They investigated the development of methods for treating rubber from scrap tyres in order to use it as automotive seals and gaskets, sealants, adhesives. Recycled rubber is also used to make absorptive sound barriers, playground surfaces, and for athletic and recreational applications.

The drawback is that the rubber treated with these processes requires much more energy than the polymers it replaces.

Different kinds of materials can be obtained by recycling used tyres. For the scope of producing low-cost seismic isolators, it is evident that a material of simple and versatile production technologies can be very appealing. The production process of the TDM considered in this work as valuable material for making low-cost isolators, comprises the following phases:

- a) tyres are shuddered into chips, mostly 50mm in size using a rotary shear shedder with two counter-rotating shafts;
- b) tyre chips enter a granulator and are reduced to a size smaller than 10mm while most of the steel cords are liberated by a combination of shaking screens and wind shifters;
- c) the rubber granules are selected to fit the desired design mix;
- d) polyurethane binder is added to the rubber granules mix until the mixture becomes an homogenous compound;
- e) pads of required size and shape are obtained by hot pressing or cold forging of the compound.

For hot pressing the compound is first leveled by a roller and then it is pressed. For binding optimization, hot steam is used and pressure is applied until the polymerization of the binder is complete. Cold forging requires the mixture to be pressured in dies. Figure 6.1 shows the final product forged in different shapes.

The industrial process previously described seemed particular feasible for the production of low-cost devices because it involves easy to implement technologies. Moreover, it requires low energy consumption and low labor demand. It is also noted that by changing rubber inert, binders, temperature, applied pressure, it is possible to produce materials with different mechanical characteristics. The elastomers used in the process are tyre derived as the Styrene Butadiene Rubber (SBR) or industrial leftovers as

the Ethylene-Propylene Diene Monomer (EPDM), a rubber used for the production of a wide variety of seals.

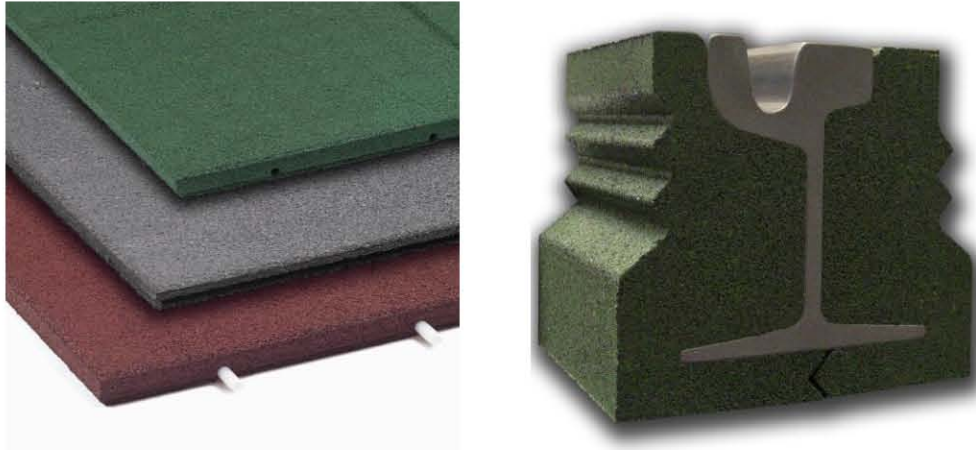


Figure 6.1 Tyre Derived Materials produced by Isolgomma Srl (VI, Italy).

6.2 MECHANICAL TESTS ON RECYCLED RUBBER

The physical properties of recycled rubber components are greatly influenced by the technologies used in their manufacture.

6.2.1 Tensile Tests

A set of tensile tests was performed aiming to determine the tensile strength of the proposed material.

ASTM D412 [ASTM D412 2006] describes the procedures to evaluate the uniaxial properties of rubber. According to the standard, since the experiment is intended to fail the specimen, dumbbell shaped samples should be used to prevent failure of the rubber in the clamps. Specific size requirements are described in order to compare the mechanical behavior of different samples.

Since it is particularly difficult to manufacture a TDM in a dumbbell shape, and there is also no need to refer to an absolute specific size requirement, tests are performed on straight specimens. The specimens characteristics are listed in Table 6.1. The length of all the tested specimens is $l_{tot}=350\text{mm}$. The width and the thickness are 20mm. Since specimen clamps give an indeterminate state of stress and strain in the region surrounding the clamps (due to gripping), the specimen straining, L/L_0 , is measured on the specimen, away from the extremities where a pure tension strain state is occurring ($L_0=100\text{mm}$).

In the tests, a non-contacting strain measuring device was used to achieve this. The load, P , is measured by a load cell. Figure 6.2. shows the complete experimental test system.

Table 6.1 collects information on the tested samples. It were considered TDMs made of fiber of SBR, grains of SBR, and large grains of EPDM with densities in the range $400 - 900 \text{ kg/m}^3$.

Table 6.1 Specimens for tensile tests.

Rubber Type	No.	Density	Length	Width	Height	Area
{}	{}	[kg/m^3]	[mm]	[mm]	[mm]	[mm^2]
Fiber of SBR	4	400	350	20	20	400
	4	600				
	4	700				
	4	900				
Grains of SBR	4	600				
	4	700				
	4	900				
Big grains of EPDM	4	600				
	4	700				
	4	900				



Figure 6.2 Experimental setup for tensile tests on rubber

The tests were carried out using displacement control. The test pieces were stretched at a constant rate of velocity until failure. The rate of displacement is $500 \pm 50 \text{ mm/min}$. From Figure 6.3 to Figure 6.5 the tensile tests results are presented.

The measured quantities are reported in Table 6.2.

Rubber for seismic isolators has a tensile strength higher than 15MPa [UNI 6065 2001]. Needless to say that the tensile strength of the Isolgamma Srl (VI, Italy) TDM is low when compared to natural rubber. Nevertheless its strength depends on the density of the compound. It is higher for higher densities and it is a function of the inert shapes. Fiber type rubber has higher strength and ultimate deformation than samples of the same density but with different inert shape. Also, for what concerns the ultimate deformation, this is lower than that of natural rubber (generally considered higher than 300% [UNI 6065 2001]).

For the TDM, the ultimate deformation is in the range 0.4-1%. This is some orders of magnitude lower than that of natural rubber and it is clear enough that no conventional devices could be produced using this low-cost material. In fact a visual inspection of the tested samples clarified that the polyurethane binder fails at the grains interface, without any failure surface dividing the grains.

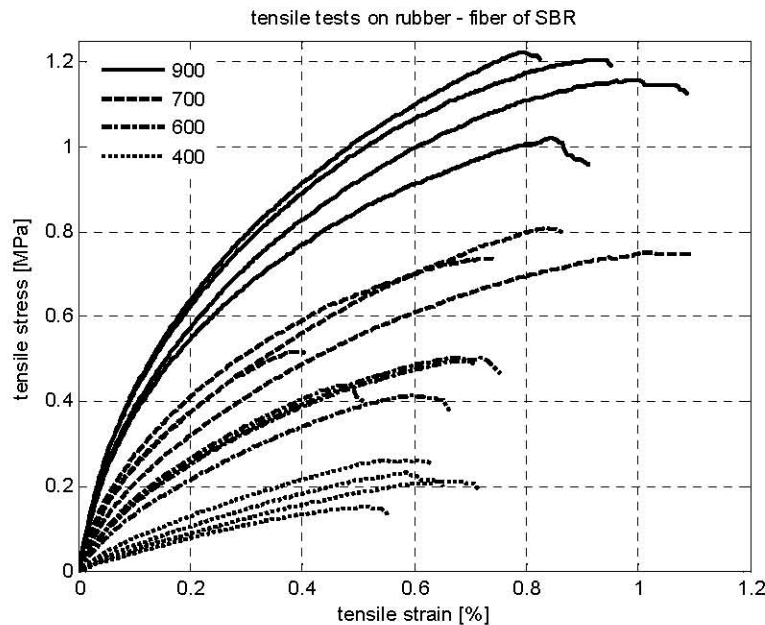


Figure 6.3

Tensile test results on fiber of SBR specimens of different density [kg/m^3].

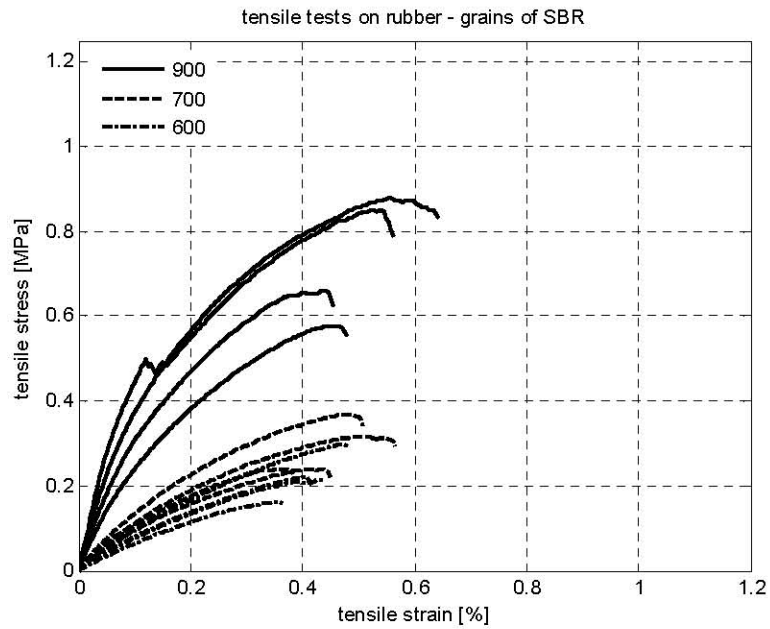


Figure 6.4 Tensile test results on grains of SBR specimens of different density [kg/m^3].

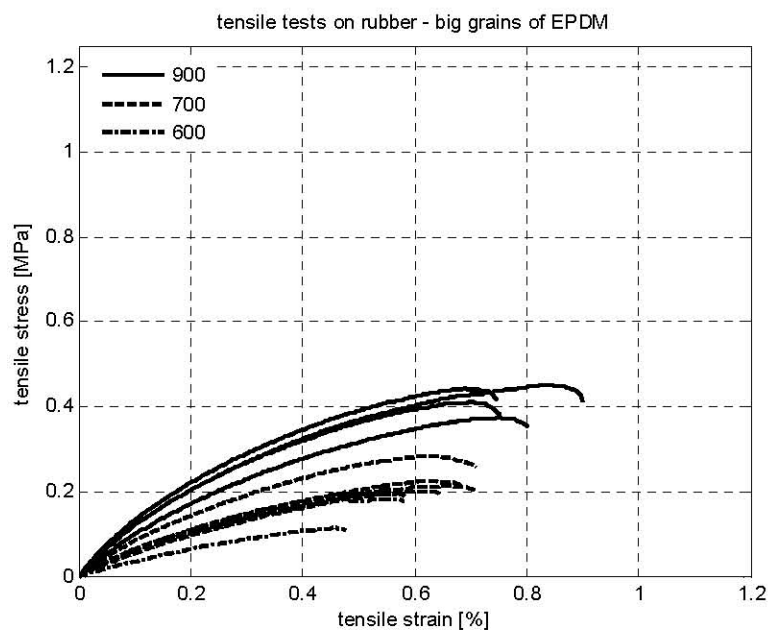


Figure 6.5 Tensile test results on big grains of EPDM specimens of different density [kg/m^3].

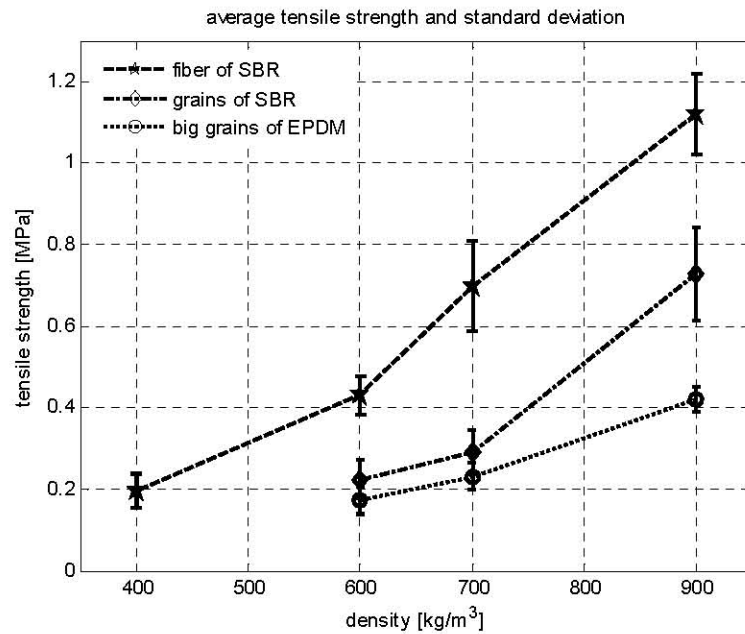


Figure 6.6 Tensile strength of recycled rubber.

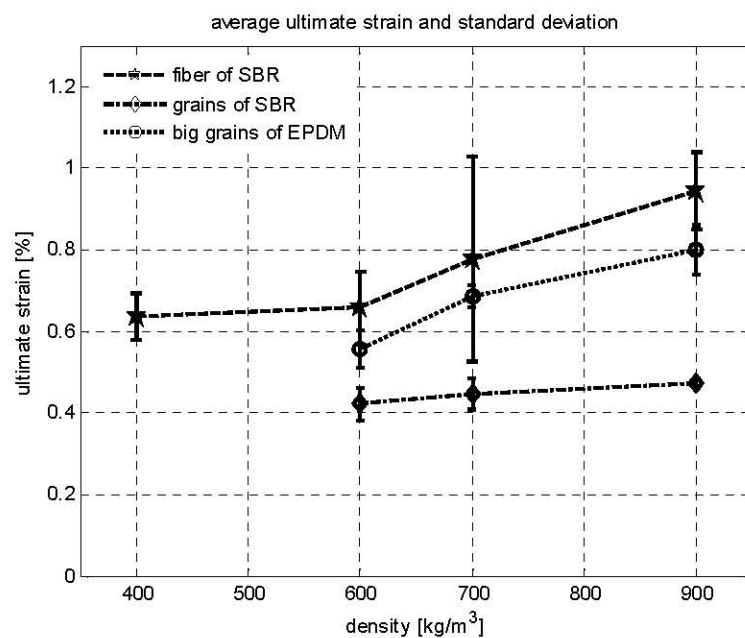


Figure 6.7 Ultimate strain of recycled rubber.

Table 6.2 Tensile tests results.

Rubber Type	No.	Density	Avg. tensile stress	Avg. ultimate strain
[-]	[-]	[kg/m ³]	[MPa]	[%]
Fiber of SBR	4	400	1.12	0.95
	4	600	0.70	0.78
	4	700	0.43	0,66
	4	900	0.19	0,64
Grains of SBR	4	600	0.73	0.47
	4	700	0.29	0.45
	4	900	0.22	0.42
Big grains of EPDM	4	600	0.73	0.80
	4	700	0.29	0,69
	4	900	0.22	0.56

None of the grains was broken. For fiber type compounds few fibers per section broke. As a matter of fact, this phenomenon gives higher strength and ultimate deformation capacities to the mixture with respect to the one containing grains.

6.2.2 Shear Tests

In order to implement hyper elastic material models, and to understand the mechanical behavior of recycled rubber materials, shear tests on recycled rubber were carried out at Tun Abdul Razak Research Centre (TARRC) in Brickendonbury, Hertford, UK. Samples were tested with the classical dual up simple shear tests commonly used in tyre industry. Figure 6.8 shows the complete test setup.

This test procedure does not allow for the measurement of compressibility and it is not failure oriented [Brown 2006]. The purpose of the experiment is to obtain information in order to correctly model the behavior of the material in the working range of strain and stresses. Rubber test pieces were supplied by Isolgomma Srl (VI, Italy). Specimens with different densities and compounds were tested.

Table 6.3 summarizes types and dimensions of the samples used for shear tests. Samples were loaded in compression and then sheared. The test program is presented in Table 6.4. From Figure 6.9 to Figure 6.11 shear tests results are presented. The hysteresis plots from the tests constitute Appendix A.

As expected, it is clear from the tests that higher density specimens have higher shear stiffness.

Table 6.3 Specimens for shear tests.

Sample No.	Density	Aggregates	Planar Dimensions	Thickness
[-]	[-]	[-]	[mm x mm]	[mm]
500	1	500	90x50	20
		80% SBR fibers 20% EPDM grains		
600	1	600		
		95% SBR fibers 5% EPDM grains		
B800	1	800	90x50	20
		80% SBR fibers 20% EPDM grains		
G800	1	800	90x50	20
		50% SBR fibers 50% EPDM grains		

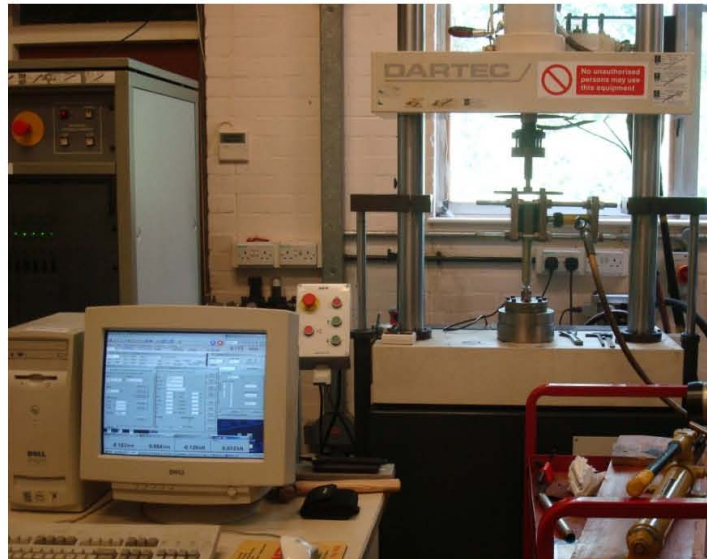


Figure 6.8 Machine for shear tests on rubber.

Table 6.4 Shear tests program.

STATIC TESTS				
Vertical Load	Vertical Stress	Shear strain amplitude based on initial rubber thickness	Deformation Rate	
[kN]	[MPa]	[%]	[mm/min]	
0.75	0.16	33; 64; 100	8	
DYNAMIC TESTS				
Vertical Load	Vertical Stress	Shear strain amplitude based on initial rubber thickness	Frequencies	Number of Cycles
[kN]	[MPa]	[%]	[Hz]	[-]
2.5	0.55	5; 25; 50; 75	0.1; 0.2; 1; 10	3

The material shows very little degradation: following cycles are almost coincident. The shear stiffness varies with the frequency and the amplitude of the applied displacement. Shear test results underlined that this material behaves almost like natural rubber. In fact, it exhibits a secant shear modulus in the range 0.4-1.1MPa for a deformation of 100% (Figure 6.9).

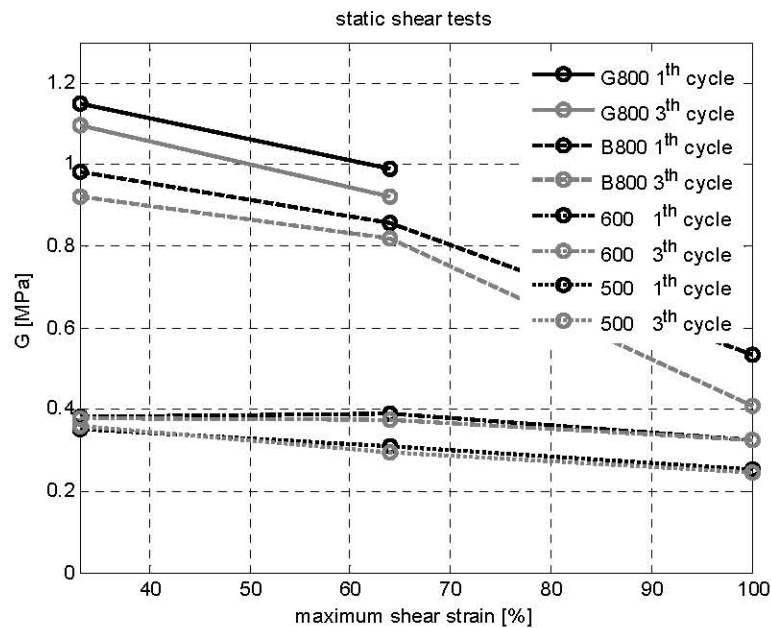


Figure 6.9 Shear modulus from static tests.

Moreover, only by changing the density of the rubber aggregates, it is possible to change the shear stiffness and the damping properties of this low cost material.

The most interesting characteristic that this TDM exhibits in shear is that, when the vertical load increases, the shear stiffness is modified significantly due to high interlocking of the rubber grains. This characteristic of the rubber is of extreme interest for seismic isolation: a Recycled Rubber-Fiber Reinforced Bearing will have an horizontal stiffness related to the applied vertical load. In other words, when the applied vertical load on an isolator increases, its horizontal stiffness will increase thus leading to a virtually zero eccentricity system and an unchanged period of isolation.

Damping is computed knowing the Energy Dissipated per Cycle (EDC). Results are shown in Figure 6.11. The frictional behavior of the grains gives high damping characteristics to the material.

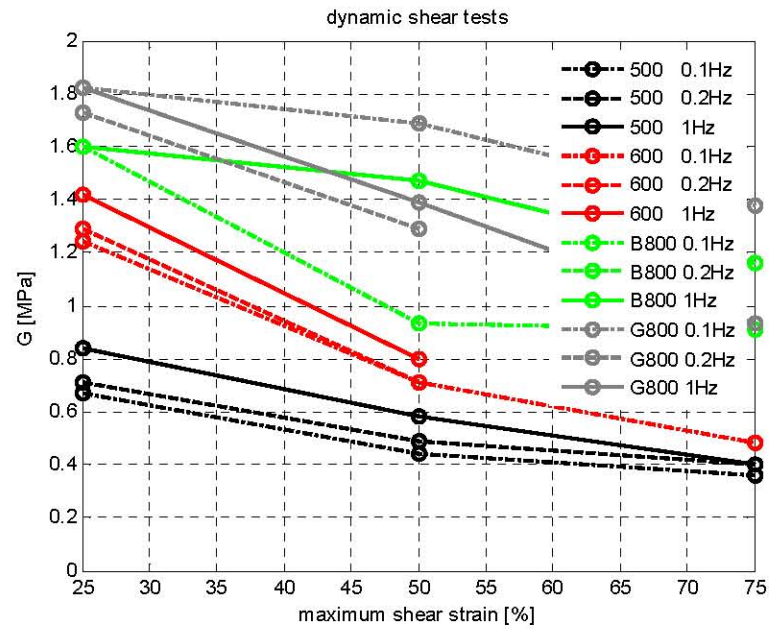


Figure 6.10 Shear modulus from dynamic tests.

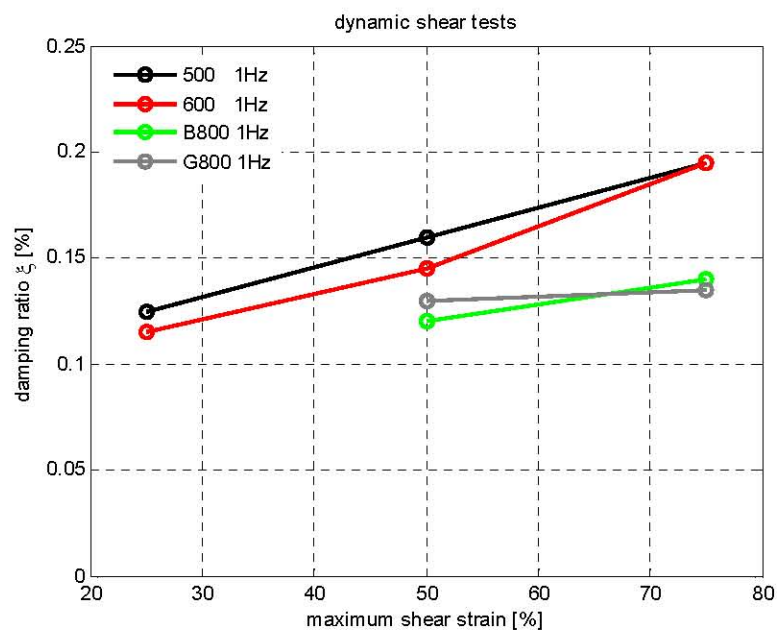


Figure 6.11 Damping ratio from dynamic shear tests.

6.3 TENSILE TESTS ON FIBER REINFORCED POLYMERS

For seismic isolators, reinforcements with Fiber Reinforced Polymers (FRP) seem to be particularly suitable. As reported before, they offer excellent corrosion resistance, high stiffness to weight ratio, good fatigue properties, non-magnetic properties, ease of transportation and handling, low energy consumption during fabrication [Micelli and Nanni 2003].

Conventionally, FRP sheets are made of aramid, carbon, or glass fibers. For carbon fibers it is generally used an epoxy matrix. Since the main idea behind the production of RR-FRBs is that of bonding fibers layers and rubber pads using a polyurethane binder (the same used to make the TDM), an experimental investigation was carried out to determine the influence of the polyurethane resin on the tensile strength, the elastic modulus and the ultimate strain of FRP sheets where the conventional epoxy resin is substituted by a polyurethane matrix. A particular protocol was used in order to address the followings issues:

- a) anchorage defect/sheet slip;
- b) failure outside the test length because of misalignment.

The gripping systems were sand blasted steel plates clamped on the FRP pieces using of an epoxy adhesive paste as in Figure 6.12.

The tensile tests were carried out by gripping the plates in the wedge grips of the testing machine. Tests were performed under displacement control, using a universal testing machine. The specimens were aligned with the grip axis. An electronic extensimeter with 51mm gauge length (0.025mm) accuracy was mounted at the center of gauge length to measure the displacements.

Strain gauges were also attached in order to compare the strain data with extensometer readings. The load, displacement, and strain data were recorded by a data acquisition system.

In this testing configuration, tensile stresses are applied to the specimens' end. None of the specimens failed outside the test length because of excessive gripping loads. Samples with different matrices and same geometrical dimensions were tested.

All FRP sheets were of equal thickness, as confirmed by accurate measurements, therefore the mean value of the derived cross section area was considered as representative of the set.

In Table 6.5, the geometries and other relevant properties of the samples are presented. The results of tensile tests show an elastic behavior of the sheets up to failure, Figure 6.14. This is a typical behavior of FRP composites. All specimens failed through rupture of the fibers.

Table 6.5 Fiber specimens for tensile tests.

Fiber Type	Matrix Type	No.	Nominal Thickness	Width	Free Test-Length
[-]	[-]	[-]	[mm]	[mm]	[mm]
Glass	polyurethane	1	0.16	25	250
Carbon	polyurethane	5			
Carbon	polyepoxide	1			



Figure 6.12 Production of FRP specimens for tensile tests.

Table 6.6 reports tensile tests results. It is clear from the tests that good tensile strength can be obtained using a polyurethane matrix.

Anyway, results differ significantly from the traditional epoxy matrix behavior. This mainly due to the fact that all the polyurethane impregnated samples were hand manufactured. The misalignment of the fiber strands produced differences in the tensile result.

Tensile tests confirmed that it is possible to produce carbon fiber reinforcements were the conventional epoxy matrix is substituted by a polyurethane one: tensile strength and ultimate deformation of the two materials are comparable.

It is important to mention that this results concern only the mechanical behavior of the new fiber material. Other studies are needed to investigate durability, corrosion resistance and carbon strands performance when immersed in a polyurethane adhesive.



Figure 6.13 Universal testing machine used for tensile tests on FRP sheets.

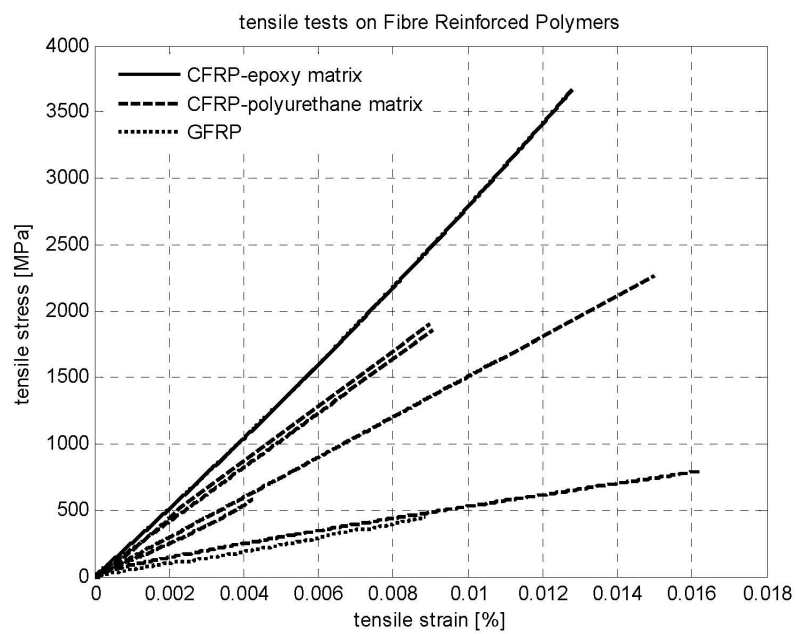


Figure 6.14 Tensile tests on fiber sheets.

Table 6.6

Tensile test results.

Fiber Type	Matrix Type	No.	σ	E	ϵ_u
[-]	[-]	[-]	[MPa]	[MPa]	[%]
Glass	polyurethane	1	447	50459	9
Carbon	polyurethane	5	1479	150652	11
Carbon	polyepoxide	1	3666	286659	13

7. TESTS ON PROTOTYPES

7.1 INTRODUCTION

Several samples of Recycled Rubber-Fiber Reinforced Bearings (RR-FRBs) were manufactured and tested in compression and shear to verify if the approach was practical.

All bearings were made by Isolgomma Srl (VI, Italy). All specimens were of square shape. However a variety of dimensions was adopted. The experimental research was conducted to study the behavior of the bearings in compression and shear at various level of vertical pre-load.

7.2 COMPRESSION TESTS

7.2.1 Experimental Setup

The bearings were tested at the Department of Structural Engineering (DIST) of the University of Naples Federico II. For compression tests it was used a universal testing machine MTS 810. The machine is suitable to perform tests both in compression and in tension. It includes an axial hydraulic actuator with a maximum capacity of 500kN and a stroke of 150mm. Both displacement control and force control procedures can be followed. The vertical load is applied through the upper loading plates that distributes the force from the vertical actuator to the test bearings. Table 7.1 shows the universal testing machine characteristics.

Table 7.1 MTS 810 characteristics.

Axial Hydraulic Actuator Capacity	Stroke	Hydraulic Grip System	Data Acquisition
[kN]	[mm]	[MPa]	
500	150	70	16 bit at 5KHz max.

The data acquisition and the control of the hydraulic actuator for the testing machine are performed by a software running on a personal computer. The typical data sampling was 25 points per seconds, and it could be changed according to the loading rate and duration of the test. The applied vertical load was averaged from two load cells. The relative vertical displacement between the end plates of the specimen was averaged

from four Linear Variable Displacement Transducers (LVDTs) located at the four corners of the plates as in Figure 7.1.

The average vertical stiffness of the bearings was obtained from compression tests carried out under load control. Vertical tests were carried out under load control. The loading histories of the vertical tests are presented in Figure 7.2.

The loading steps reported in the Figure are needed to accommodate the viscous response of the devices.

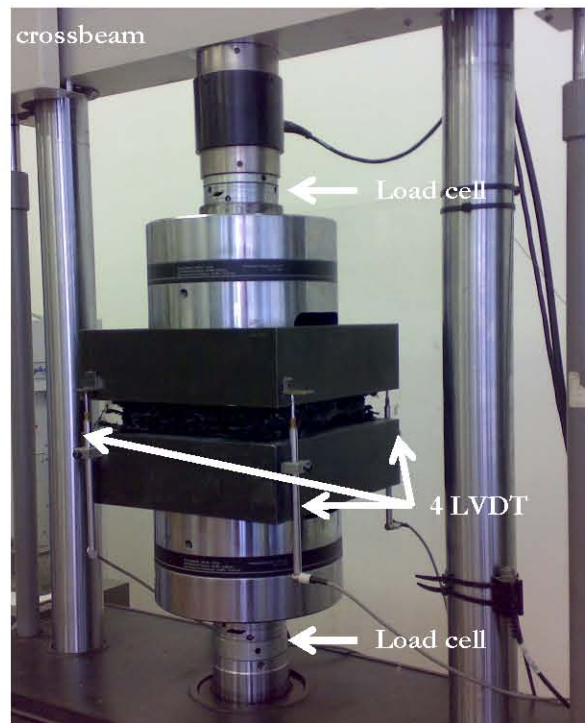


Figure 7.1

Universal testing machine modified to accommodate the recycled rubber bearings.

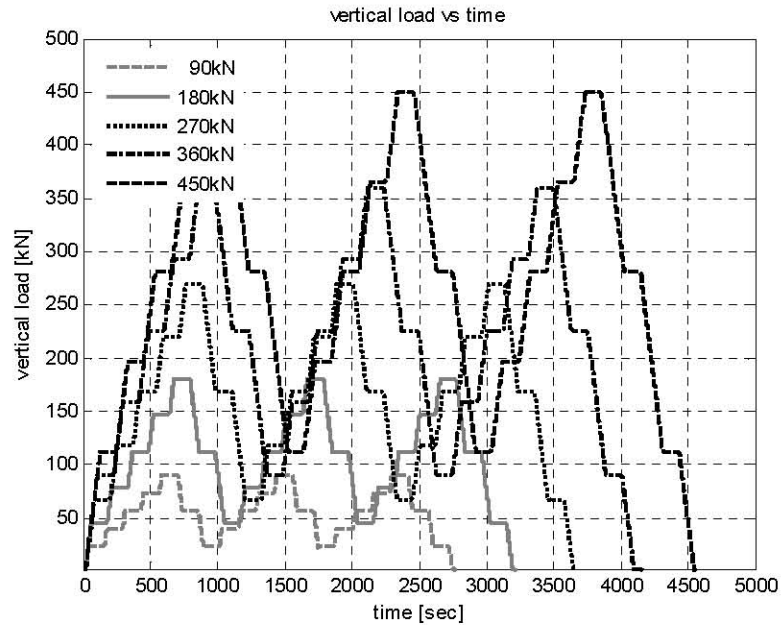



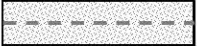









Figure 7.2 Load-patterns for vertical tests.

7.2.2 Test Specimens

Eleven specimens with different reinforcing layers and configurations were tested. The prototypes are of square shape with slightly different in-plane dimensions, but with a constant total height. All the specimens had no rubber cover. Table 7.2 reports the characteristics of the tested devices.

The total thickness of rubber was 60mm, a constant for all the testes RR-FRBs. The rubber in use was of the two types (SG600 and B800). The SG600 was made of Small Grains (SG) of SBR in a density of 600kg/m³. The B800 was produced using Big grains of SBR in a density of 800kg/m³. The performances of this two materials are discussed in the previous Chapter.

Table 7.2 Fiber-reinforced test bearings.

Bearing Designation	Cross-section of the Bearing	Rubber Type	Reinforcing Type	(No. of Reinforcing Layers)	Total Height	Width	Depth
					[mm]	[mm]	[mm]
rpad(BG)250		B800	-	0	60	250	250
rpad(SG)250		SG600	-	0	60	250	250
rpad(BG)300		B800	-	0	60	300	300
1LS(BG)300		B800	Steel shim	1	60	300	300
1LC(BG)300		B800	CFRP	1	60	300	300
3LC(BG)300		B800	CFRP	3	60	300	300
4LC(SG)250		SG600	CFRP	4	60	250	250
3LG(BG)250		B800	GFRP	3	60	250	250
3LG(SG)250		SG600	GFRP	3	60	250	250
4LG(SG)250		SG600	GFRP	4	60	250	250
7LG(SG)250		SG600	GFRP	7	60	250	250

7.2.3 Summary of Results

The compressive force – displacement curves for all the bearings at different levels of vertical pressure are presented in Appendix B.

Figure 7.3 shows the results at peak vertical pressure for the different bearings.

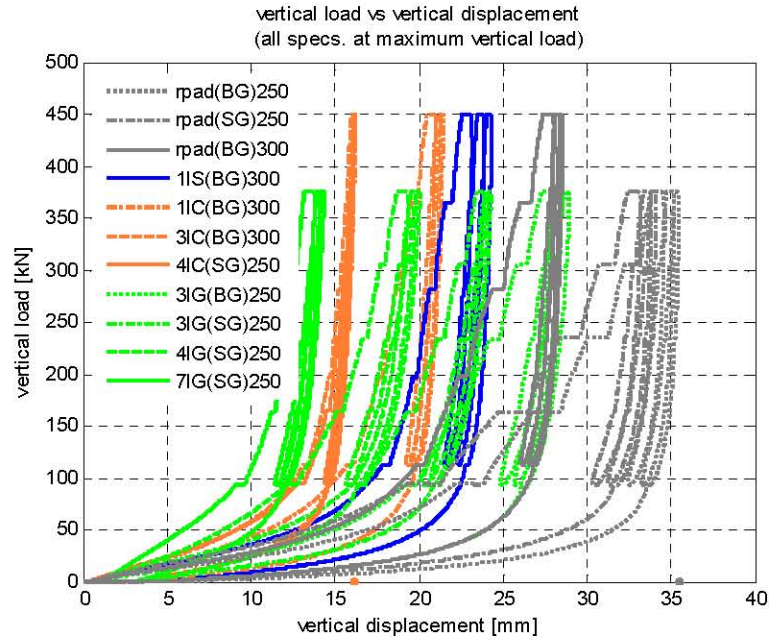


Figure 7.3 Vertical test results.

For steel and fiber reinforced bearings, the resulting vertical compressive stress-strain curves is highly nonlinear with significant run-in before the full vertical stiffness was developed. The nonlinear response is primarily due to the nonlinear behavior of the elastomer in compression [Robert 1988]. The initial run-in response was detected for Natural Rubber Fiber Reinforced Bearings (NR-FRB) where it depends on issues related to workmanship and initial lack of straightness in the fiber layers [Kelly 2008]. To reduce the initial run-in effect an orthogonal in plane tension should be applied to the bi-directional fabric prior to being bonded to the elastomeric layers. In other words, prestressing is required.

The procedure consents to reduce the initial run-in the load deflection response [Toopchi-Nezhad *et al.* 2009].

For the reported tests, no particular precautions were used. Moreover, the initial run-in was of little concern as the bearings developed adequate vertical stiffness under the expected vertical load. Vertical test results are shown in Tables 7.3 - 7.5.

Since the dimensions of the bearings are different, it is useful to tabulate the vertical stiffness in terms of the effective compression modulus, E_t , as defined by Equation 7.1.

$$E_c = \frac{P}{A\epsilon_c} \quad (7.1)$$

Table 7.3 Vertical test results for 2-3MPa vertical pressure.

Specimen	Area	Load Step		Pressure	Secant Stiffness	Compression Modulus	Vertical Frequency
	[m ²]	[kN]		[MPa]	[N/mm]	[MPa]	[Hz]
rpap(BG)250	0.063	125	188	2-3	23271	22	6
rpap(SG)250	0.063	125	188	2-3	20627	20	6
rpap(BG)300	0.090	180	270	2-3	55624	37	8
1LS(BG)300	0.090	180	270	2-3	81893	55	10
1LC(BG)300	0.090	180	270	2-3	84112	56	10
3LC(BG)300	0.090	180	270	2-3	124706	83	12
4LC(SG)250	0.063	125	188	2-3	57287	55	10
3LG(BG)250	0.063	125	188	2-3	56155	54	9
3LG(SG)250	0.063	125	188	2-3	23148	22	6
4LG(SG)250	0.063	125	188	2-3	41118	39	8
7LG(SG)250	0.063	125	188	2-3	57870	56	10

Table 7.4 Vertical test results for 3-4MPa vertical pressure.

Specimen	Area	Load Step		Pressure	Secant Stiffness	Compression Modulus	Vertical Frequency
	[m ²]	[kN]		[MPa]	[N/mm]	[MPa]	[Hz]
rpap(BG)250	0.063	188	250	3-4	18032	17	5
rpap(SG)250	0.063	188	250	3-4	18997	18	5
rpap(BG)300	0.090	270	360	3-4	55046	37	7
1LS(BG)300	0.090	270	360	3-4	78125	52	8
1LC(BG)300	0.090	270	360	3-4	91743	61	9
3LC(BG)300	0.090	270	360	3-4	178926	119	12
4LC(SG)250	0.063	188	250	3-4	102796	99	11
3LG(BG)250	0.063	188	250	3-4	41391	40	7
3LG(SG)250	0.063	188	250	3-4	23020	22	5
4LG(SG)250	0.063	188	250	3-4	82237	79	10
7LG(SG)250	0.063	188	250	3-4	105932	102	11

Table 7.5 Vertical test results for 4-5MPa vertical pressure.

Specimen	Area	Load Step		Pressure	Secant Stiffness	Compression Modulus	Vertical Frequency
	[m ²]	[kN]		[MPa]	[N/mm]	[MPa]	[Hz]
rpap(BG)250	0.063	250	313	4-5	121927	117	10
rpap(SG)250	0.063	250	313	4-5	34511	33	6
rpap(BG)300	0.090	360	450	4-5	62112	41	6
1LS(BG)300	0.090	360	450	4-5	85551	57	7
1LC(BG)300	0.090	360	450	4-5	90000	60	7
3LC(BG)300	0.090	360	450	4-5	250000	167	12
4LC(SG)250	0.063	250	313	4-5	163613	157	12
3LG(BG)250	0.063	250	313	4-5	19832	19	4
3LG(SG)250	0.063	250	313	4-5	54348	52	7
4LG(SG)250	0.063	250	313	4-5	68681	66	8
7LG(SG)250	0.063	250	313	4-5	115101	110	10

The fact that at the same pressures the E_c value for rpap(BG)300 is higher than for rpap(BG)250 is due to a larger influence of free ends in the larger pad. This effect it is also evident when the behavior of bearings with a similar reinforcement and different in plane dimensions is analyzed.

It is also evident for all the specimens a systematic increase in stiffness and E_c with increasing pressure. The behavior is not linear with the pressure: as the compression increases, the fiber sheets tend to straighten out the fiber strands, thus increasing the effective fiber stiffness.

Given the vertical stiffness, K_v , of the bearing under vertical pressure p , the vertical frequency, f_v , can be calculated as

$$f_v = \frac{1}{2\pi} \sqrt{\frac{K_v g}{pA}} \quad (7.2)$$

where A is the plan area of the specimen and g is the acceleration of gravity.

According to the results in Tables 7.3-7.5, the bearings have vertical frequencies in the range 4-12 Hz.

It must be noted that the bearings were not designed for a specific application. Rubber layers were bonded to different reinforcing sheets to evaluate the capability of different reinforcing materials in changing the vertical stiffness of the prototype devices.

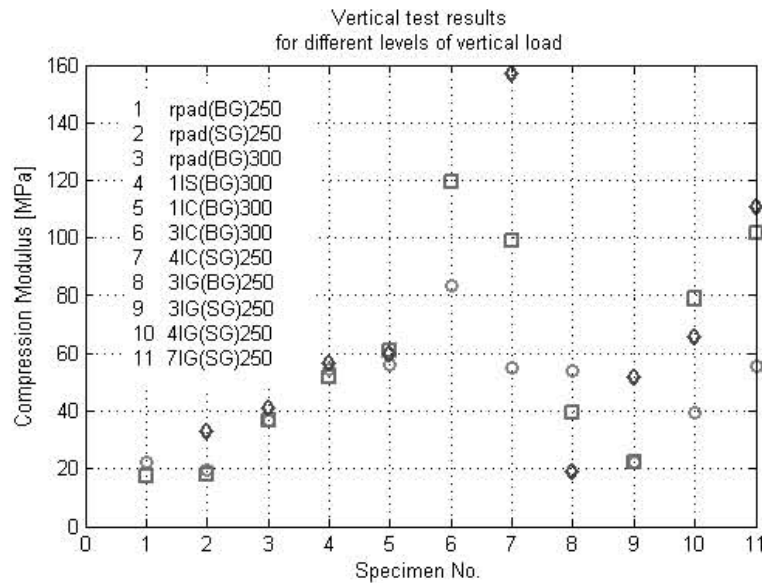


Figure 7.4 Vertical test results.

Carbon reinforced bearings performed better than glass reinforced ones. Glass sheets appeared to be made of a very poor quality material with actual fibers constituting only 20-25%. The rest were holes and the layers were clearly inadequate for these applications. Even if the elastic modulus of glass FRP strands is lower than carbon FRP, by using glass reinforced sheets composites with an high areal density, sufficient vertical stiffness and strength could be provided with an accessible price for low-cost applications.

The introduction of reinforcing layers is always effective in increasing the vertical stiffness of elastomeric devices. From Figure B.1 to Figure B.3 the load displacement relations for unreinforced rubber blocks are shown.

From the tests, it resulted that when high vertical loads are applied, the unreinforced blocks are highly damaged after loading. In fact the curves show large energy dissipation, and damage was visible after testing. Moreover, FRBs perform better than Steel Reinforced Bearings (SRBs) (Figure B.4 and Figure B.5). This is most likely due to a better adhesion of the fiber layers to the rubber surface. Since using a fiber reinforcement it results a lower rubber deformation, the TDM is not damaged after testing and a purely elastic behavior can be obtained (Appendix B).

A steel reinforced square isolator with the same geometry of 3LC(BG)300, ignoring compressibility effects, would have an effective compression modulus E_c of 108MPa ($G=1.1\text{MPa}$).

7.3 SHEAR TESTS

7.3.1 Bearings Design and Properties

Shear tests were conducted on 3LG(SG)250 and 7LG(SG)250 specimens. It is recalled that the bearings have the same plan dimensions of 250 by 250mm, with a total rubber thickness of 60mm, as shown in Figure 7.5.

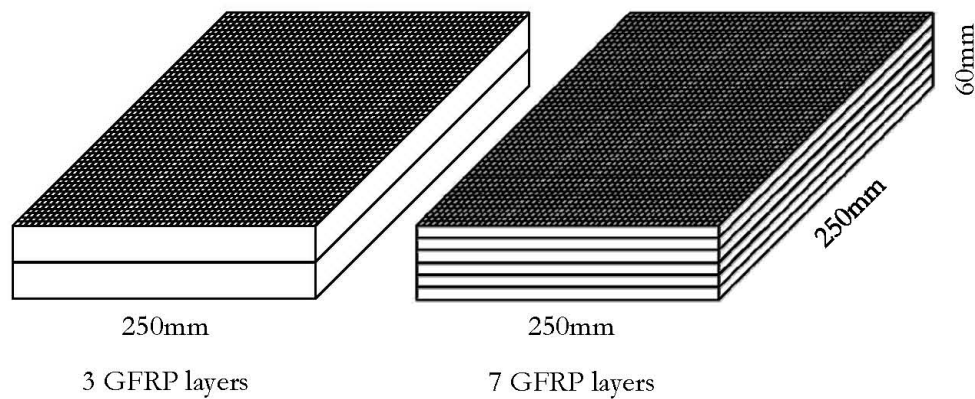


Figure 7.5 Sizes of the tested elastomeric bearings.

Figure 7.6 is a photograph of the tested devices. The bearings have the same total rubber thickness, fiber-layers thickness, no cover and footprint dimensions, but differ in the number of rubber layers and shims, and therefore in their total height.



Figure 7.6 RR-FRBs tested in shear.

The recycled rubber used for their manufacture is composed of 50% SBR fibers and 50% EPDM grains, with a density of 800kg/m^3 (G800).

7.3.2 Description of Test Setup and Protocol

The isolators were not bonded on top and bottom. A constant vertical load and fully reversed cycles of horizontal displacements were applied. By carrying out the tests, the force–displacement loops were obtained and, consequently, the effective horizontal stiffness, the effective shear modulus and the viscous damping.

To test the response of the bearings to loading conditions that would result from earthquake shaking, four cyclic signals with various amplitudes ranging from 20% up to 80% shear strain were used. Table 7.6 shows the test protocol.

Table 7.6 **Displacement-controlled tests for Recycled Rubber Fiber Reinforced Bearings.**

Test No.	Specimen	Shear Displacement	Shear Deformation	Speed	Frequency	Vertical Pressure	Vertical Load
[-]	[-]	[mm]	[%]	[mm/s]	[Hz]	[MPa]	[kN]
1	3LG(SG)250	12	20	0.5	0.04	1	62.5
2	3LG(SG)250	12	20	0.5	0.04	1	62.5
3	3LG(SG)250	12	20	0.5	0.04	1	62.5
4	3LG(SG)250	12	20	0.5	0.04	2	125.0
5	3LG(SG)250	24	40	0.5	0.02	1	62.5
6	3LG(SG)250	24	40	0.5	0.02	2	125.0
7	3LG(SG)250	36	60	1.0	0.03	1	62.5
8	3LG(SG)250	36	60	1.0	0.03	2	125.0
9	3LG(SG)250	36	60	1.0	0.03	3	187.5
10	3LG(SG)250	48	80	1.0	0.02	2	125.0
11	3LG(SG)250	48	80	1.0	0.02	3	187.5
12	3LG(SG)250	48	80	1.0	0.02	3	187.5
13	7LG(SG)250	12	20	0.5	0.04	1	62.5
14	7LG(SG)250	12	20	0.5	0.04	2	125.0
15	7LG(SG)250	24	40	0.5	0.02	1	62.5
16	7LG(SG)250	24	40	0.5	0.02	2	125.0
17	7LG(SG)250	36	60	1.0	0.03	2	125.0

Horizontal tests have been performed at the Mechanical Engineering Department of the University of Naples Federico II. The tests apparatus is shown in Figure 7.8. The same equipment can be used as a 1D shaking table machine as in Figure 7.7.

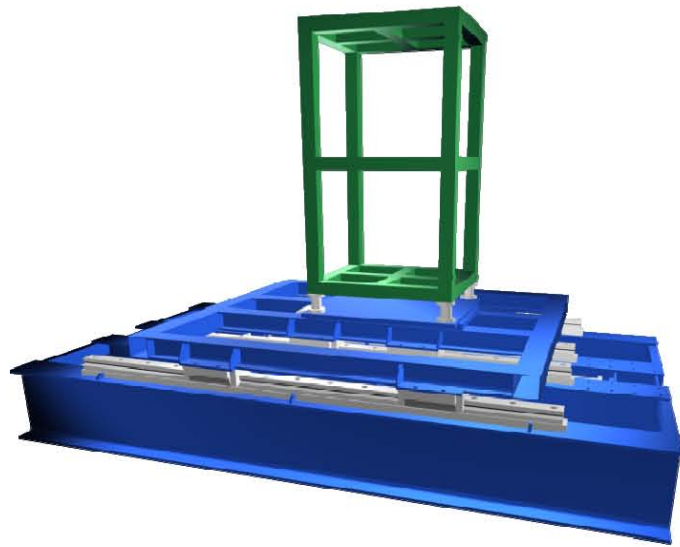


Figure 7.7 Instrumentation setup for 1D shaking table tests.

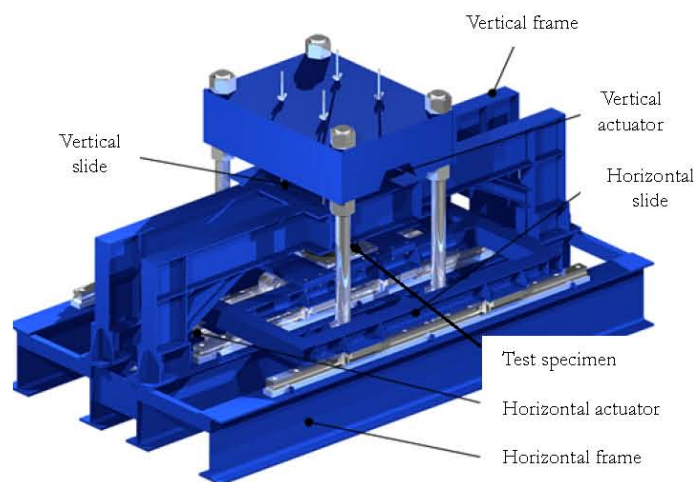


Figure 7.8 Instrumentation setup for horizontal tests.

The machine has two hydraulic actuators, one in the horizontal direction and the other in the vertical direction. In the apparatus, the vertical load is transferred by an horizontal plate, the lateral displacement is applied to the basement of the machine which can slide freely on roller bearings. The maximum force of the vertical actuator is 190kN. The horizontal actuator has a maximum stroke of 200mm and a maximum force of 50kN with a maximum speed of 2.2m/s. The bearing is located between two rigid steel plates with no bonding or fastening at its contact surfaces. Lateral displacements are imposed with an horizontal hydraulic actuator attached to the lower plate. A load cell is used to measure the lateral loads corresponding to the different lateral displacements imposed on the bearing. Two LVDTs are used to measure the relative vertical displacements between the lower and upper plates. All tests are conducted at room temperature and the data was sampled at 250 Hz.

The data acquisition and control of the hydraulic actuators are performed by a software package on a personal computer.

The horizontal tests are performed with different shear strain amplitudes of 20%, 40%, 60%, 80%. The displacement is imposed at a speed of 0.5mm/s and three cycles are applied for each of the shear strain amplitudes.

7.3.3 Results of Horizontal Tests

Some results of the horizontal tests performed on isolator specimens are shown in Appendix C as horizontal force versus displacement curves. As shown in the Figures, by increasing the number of cycles of loading, the value of horizontal stiffness marginally decreases in all tests. This stress softening is not associated with the Mullins effect which occurs in filled rubbers. In filled rubber, the Mullins effect reflects a breakdown of weak bonds between rubber molecules and filler particles [Gent 2001]. In recycled rubber compounds, the breakdown occurs at the interface between the binder and the granules, determining a softening of the TDM.

The horizontal stiffness, K_H , for conventional seismic isolation bearings is given by Equation 7.3

$$K_h = \frac{GA}{t_r} \quad (7.3)$$

where G is the shear modulus, A is the plan area of the bearing, and t_r is the total thickness of the rubber.

The applicability of this formula is very limited for the bearings in this study. The bearings are not bonded to the top and bottom support surfaces and have flexible reinforcements. Consequently, when they are sheared, fiber layers bend, and the bearing rolls off the top and bottom surfaces at opposite corners, as in Figure 7.9.

During the roll off, the shear area reduces, producing a decrease in stiffness. In this work, the shear strain for an unbounded bearing has the same definition as that for a bonded bearing (relative horizontal displacement of the supporting surfaces divided by the total height of the rubber). It is neglected the fact that the corners of the unbounded bearing roll off and that the bearing can actually slip. This effect become more evident for taller devices.

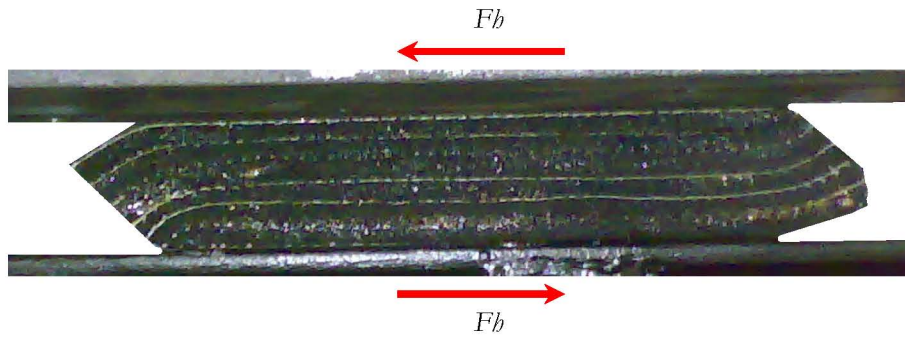


Figure 7.9 Specimen 7LG(SG)250 at peak shear deformation.

The two properties of interest are the effective lateral stiffness and EDC of the bearings at various amplitudes of vertical loads and lateral displacements.

Generally, the effective lateral stiffness is calculated based on the peak-to-peak lateral response in each cycle of the test. Since in some of the tests, the bearings slide on the horizontal surfaces, in order to compare the performances of the different bearings, the stiffness is herein computed as a secant value at a displacement $\Delta(F_{b,\max})$, as in Equation 7.4.

$$k_{b,\Delta} = \frac{F_{(b,\max)}}{\Delta(F_{b,\max})} \quad (7.4)$$

in which $\Delta(F_{b,\max})$ is the displacement where the maximum shear force is recorded

Table 7.7 shows the shear test results as effective shear modulus and EDC.

The values of effective shear stiffness of all fibers reinforced isolators are almost equal for several shear strain amplitudes, a given vertical load and the same frequency of shear loading. The shear modulus is lightly affected by the number of reinforcing layers. In Figure 7.10 the variations of the average EDC versus shear strain amplitude is compared for all prototypes. For a certain shear strain amplitude and frequency of shear loading (excluding the sliding cases) the EDC increases with the vertical load.

Table 7.7 Shear test results.

Test No.	Specimen	Shear Displacement	Shear Deformation	Vertical Pressure	Frequency	EDC	$K_{b,F \max}$
[-]	[-]	[mm]	[%]	[MPa]	[Hz]	[kN-mm]	[N/mm]
1	3LG(SG)250	12	20	1	0.04	200.6	2067
2	3LG(SG)250	12	20	1	0.04	187.6	1620
3	3LG(SG)250	12	20	1	0.04	180.1	1612
4	3LG(SG)250	12	20	2	0.04	244.6	2068
5	3LG(SG)250	24	40	1	0.02	629.6	1422
6	3LG(SG)250	24	40	2	0.02	804.5	1640
7	3LG(SG)250	36	60	1	0.03	1835.4	1339
8	3LG(SG)250	36	60	2	0.03	1639.7	1429
9	3LG(SG)250	36	60	3	0.03	1915.8	1617
10	3LG(SG)250	48	80	2	0.02	2433.6	1485
11	3LG(SG)250	48	80	3	0.02	3141.8	1449
12	3LG(SG)250	48	80	3	0.02	3074.3	1175
13	7LG(SG)250	12	20	1	0.04	179.5	1941
14	7LG(SG)250	12	20	2	0.04	242.7	2271
15	7LG(SG)250	24	40	1	0.02	1142.8	1851
16	7LG(SG)250	24	40	2	0.02	767.6	2542
17	7LG(SG)250	36	60	2	0.03	2346.4	1846

When a fiber reinforced isolator is subjected to shear loading, bending of the reinforcements causes a planar cross section not to remain plane, which is in contrast to the behavior of common steel reinforced isolators [Kelly 1999]. The interfacial slip of single fibers against each other in the threads produce a significant amount of frictional damping in reinforcement fibers.

Differently from Fiber Reinforced Natural Rubber Isolators, in Recycled Rubber Bearings a significant amount of dissipation is due to the friction between elastomeric grains. The natural rubber fiber reinforced specimens tested by Kelly had an equivalent viscous damping ratio around 15% at 100% shear, and 14% at 150% shear [Kelly 1999].

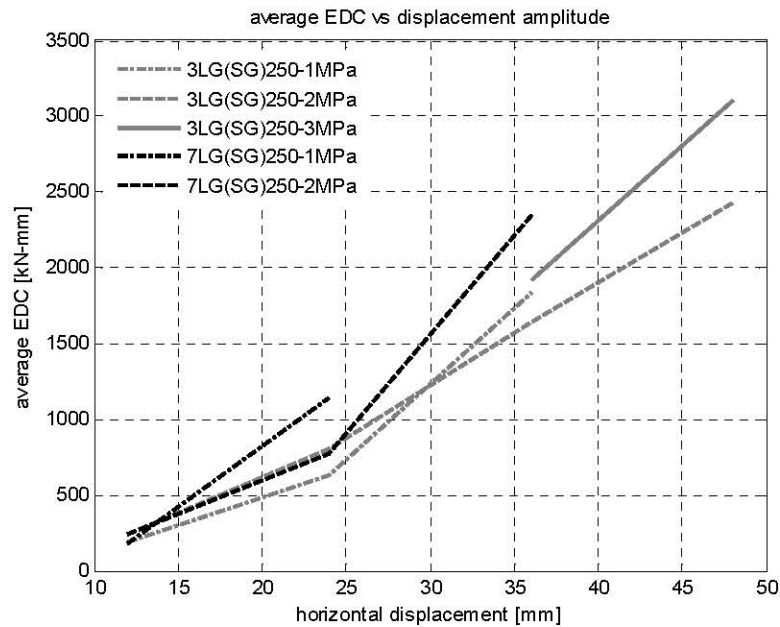


Figure 7.10 Energy Dissipated per Cycle.

In the horizontal tests of this research, even at large shear strains, plane cross sections of isolators remain almost plane. Only small regions at the edges become curved. The results of the tests show that the energy dissipation and the equivalent viscous damping of the fiber reinforced isolator specimens are almost equal to those of the rubber specimens tested at TARRC (Figure 6.11). Recycled rubber isolators showed an equivalent viscous damping of 12% at 20% shear, 13% at 40% shear, 15% at 60% shear.

Therefore, the energy dissipation, in the fiber layers, due to frictional damping is negligible. Since for the tested bearings the roll-off portion was small, the absence of frictional damping in the fibers is probably caused by the insignificant warping of the plane cross-sections and absence of interfacial slip of single fibers against each other in the threads.

Variations of vertical pressure in the range of 1–2MPa cause variations of horizontal stiffness and effective shear modulus of around 14%. In traditional devices, with increasing the vertical load, the effective horizontal stiffness and effective shear modulus decrease. Conversely, in RR-FRBs the horizontal stiffness increases with the vertical load. In fact the vertical load compacts the material and closes the internal voids. This results in an higher stiffness. Moreover, when the bearings do not slide, increasing the vertical load increases the energy dissipation and damping.

The experimental results show that the roll-off response is limited by the fact that the free edge of the bearing rotates from the vertical towards the horizontal with increasing shear displacement, and the limit of this process is reached when the originally vertical surfaces at each side come in contact with the horizontal surfaces at both top and bottom. Further horizontal displacement beyond this point can only be achieved by slipping. The friction factor between rubber and other surfaces can assume very large values, possibly as high as 1 and slip can produce damage to the bearing through tearing of the rubber, distortion of the reinforcing layers, and heat generated by the sliding motion [Konstantinidis *et al* 2008].

At each level of imposed lateral displacement, the larger load-resisting capacity and damping are observed during the first cycles (Appendix C). For the following cycles, at each level of displacement amplitude, the bearings exhibited stable hysteresis loops. All the bearings maintained positive incremental load-resisting capacity throughout the lateral response and exhibited stable deformations.

In fiber reinforced specimens, by increasing the shape factor from 8.3 to 25, the value of effective compression modulus in the range of pressure 2-3MPa increases by about 150%. The shape factor of elastomeric layers has some effect also on the effective shear modulus: for a shear deformation of 60%, with a vertical pressure of 2MPa, the variation is around 30%. The polyurethane binder used to glue the fiber layers, fills the voids in the elastomer and increases the stiffness of the devices.

Results of tests at three different pressures, same velocity rate, and different shear strain levels are shown in Appendix C. The tests confirmed that the EDC is fairly rate-independent and that damping is predominantly hysteretic, not viscous. There is generally an increase in the EDC with increasing vertical load for all the bearings, as can be seen in Table 7.7.

The value of Q , defined in Figure C.1, increases with increasing peak shear strain, but is not dependent on the loading rate.

Since none of the bearings was forced further beyond the peak resisting force, no damage was observed. For the bearings, the ultimate seismic shear strain should be the strain at which the vertical face become horizontal.

For 3LG(SG)250 and 7LG(SG)250 slip was observed under low vertical loading (1MPa). The measured horizontal force not exceeded 0.35 times the compressive load. The ratio of the horizontal force to the vertical force is an indication of the frictional resistance of the contact interfaces between the rubber bearing and the supports. At the initiation of sliding and during sliding, this ratio is referred to as the static and kinetic coefficient of friction. The peak for the test, with no sliding, was 0.70.

Caltrans guidelines [Caltrans 1994] address the importance of the frictional properties of the contact interface in seismic analyses and the difficulty in assigning a parameter that quantifies this resistance. Based on several test reports, the use of a Coulomb friction model with a friction coefficient of 0.40 for concrete to rubber and 0.35 for steel to rubber is suggested. This is the half of what was recorded during the tests.

The validity of a Coulomb friction model to describe the mechanical behavior of steel-to-rubber interface is questionable. While this model appears to work for rough hard surfaces like concrete to steel, it may not be appropriate for the interface of a hard material in contact with a soft material [Persson 2001].

It is observed that stiffness values estimated by Equation (7.3) slightly deviate from the experimentally determined values because of a little reduction in effective shear area due to contained roll-off effects.

8. SEISMIC ISOLATION FOR LOW-COST HOUSING: A CASE STUDY

8.1 INTRODUCTION

A project called *Use of Rubber-Based Bearings for Earthquake Protection of Small Buildings* was sponsored by the United Nations. It included the construction of demonstration buildings in different countries as prototypes for the implementation of base isolation for the seismic protection of public housing in developing countries. Taniwangsa and Kelly [1996] describe the studies carried out as part of the project for the design and construction of a building in Indonesia.

In this Chapter a study is conducted to assess the possibility of applying RR-FRBs to the demonstration building therein illustrated. This is done by comparing the performances of the building isolated with three different technologies, namely Lead-Rubber Bearings (LRBs), Friction Pendulum Systems (FPSs), and Recycled Rubber - Fiber Reinforced Bearings (RR-FRBs).

8.2 THE DEMONSTRATION BUILDING OF PASIR BADAQ, INDONESIA

8.2.1 Description of the Building

The base isolated building is a four-story, eight-apartment housing block constructed as a prototype near the city of Pelabuhan Ratu in Southwest Java, Indonesia. Figure 8.1 shows a photograph of the building. The superstructure consists of reinforced concrete frames with infilled masonry panels separated from the structural frames by seismic gaps.

The construction of the building was completed in 1984. The building is 7.5m by 18.0m and the height is 12.8m. It is supported by 16 High Damping Natural Rubber elastomeric bearings (HDNR). The building has a floor slab and beam assemblage to accommodate the isolation system. The isolators are placed between the superstructure and the foundation. Jacking points at the ground floor level were provided at several locations.

The building was designed so that it would exhibit a strong column, weak beam failure mechanism. The outer columns are 300x600mm, the inner columns are 300x300mm. The ground floor beams are 300x700mm while the first floor beams are 300x600mm. A 130mm concrete slab was cast together with the beam to have a rigid diaphragm.



Figure 8.1 Photograph of the demonstration building of Pasir Badik (Courtesy of Prof. J.M.Kelly, University of California, Berkeley).

The masonry infills are 140mm thick and are built with concrete block with an hollow area equal to the 65% of the cross section.

Figure 8.2 and Figure 8.3 show plan and elevations of the demonstration building.

The column loads for the seismic combination at the base isolation level are reported in Figure 8.4.

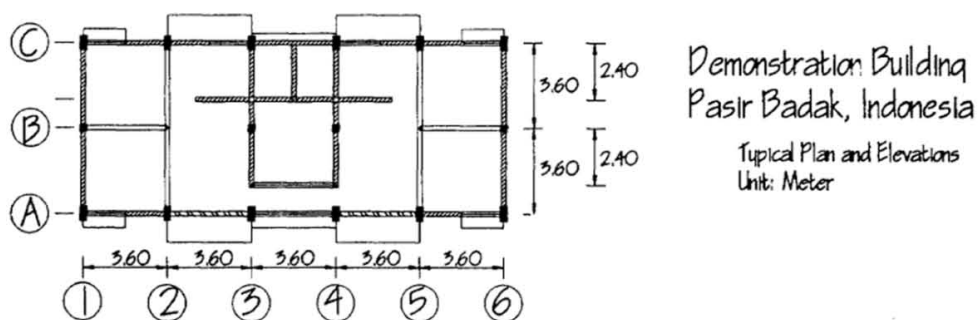


Figure 8.2 Typical plan of the demonstration building (Courtesy of Prof. J.M.Kelly, University of California, Berkeley).

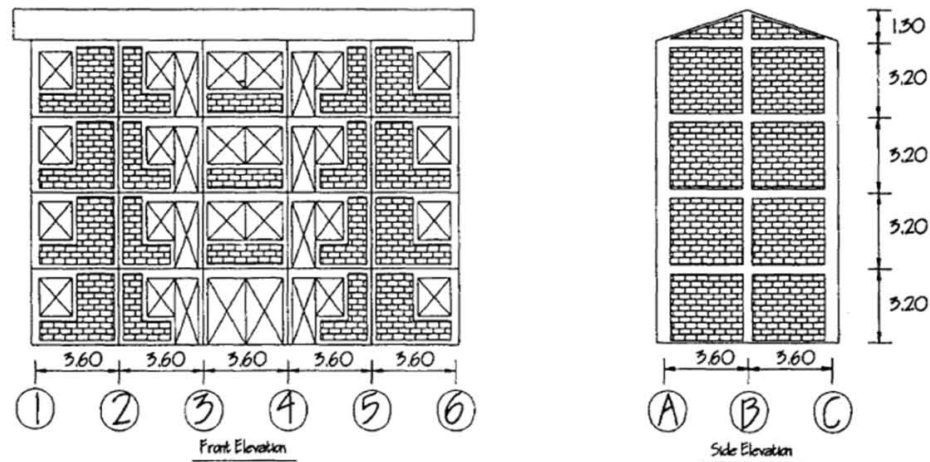


Figure 8.3 Elevations of the demonstration building (Courtesy of Prof. J.M.Kelly, University of California, Berkeley).

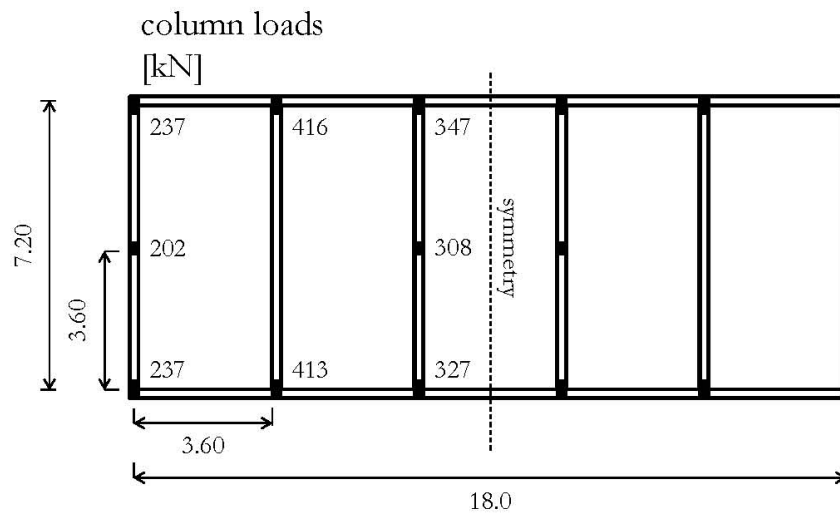


Figure 8.4 Vertical load – for the seismic load combination.

8.2.2 Description of the Isolation System in Use

The isolation system consisted of 16 high damping natural rubber bearings connected to the structure using recess plates.

Rubber bearings with light loads tend to have a small diameter, Φ , and a large total rubber thickness. This leads to unstable devices.

Since the building has some lightly loaded columns, in order to overcome the instability problems, for few devices it was used an HDNR compound with a shear modulus of 0.4MPa. For the other devices it was used an hard compound with a shear modulus of about 0.8MPa. All bearings are 330mm in diameter and 176.5mm high.

The connections were made using a pair of plates that confine the bearing in place. One plate is attached to the foundation and the other is attached to the upper structure.

Figure 8.5 shows the device in the deformed configuration. The end plates were designed thinner than those used in conventional devices in order to have a cost effective isolator.

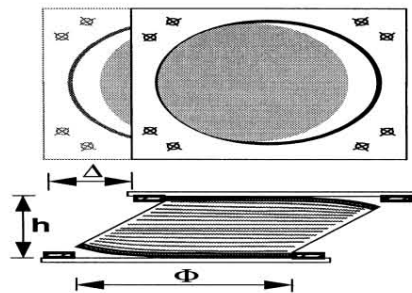


Figure 8.5 Deformed configuration of isolation bearing with recessed plate connection.

The isolation system was designed to have a period of isolation of 2 seconds and 10% of critical damping.

The design displacement for the isolation system was 101mm and the Maximum Probable Earthquake (MPE) displacement was 184mm.

8.2.3 Site Specific Response Spectra

The building is located in Pasir Badak, in the southern part of West Java, Indonesia. The main area of the site is basically flat and level on a stable slope. Some borehole tests indicated the proximity of the bedrock to the ground surface over most parts of the site. The surface layer appeared to be only 0.5m to 1.0m thick. The bedrock strength was in the range of 5 to 10MPa, therefore, a direct footing on the bedrock was proposed to provide adequate support for the building. The site design spectra were derived for 20, 200 and 500 years return period. Figure 8.6 shows the site spectra for 5% damping. The spectral value corresponding to the 200 years return period earthquake, at 2 seconds is 0.118g. This spectral value corresponds to 5% damping and should be reduced by a factor of 0.83 for 10% damping, which is the proposed damping value for the isolation system [Taniwangsa and Kelly 1996]. The MPE corresponds to an earthquake having a return period of 1000 years and a Peak Ground Acceleration (PGA) of 0.32g.

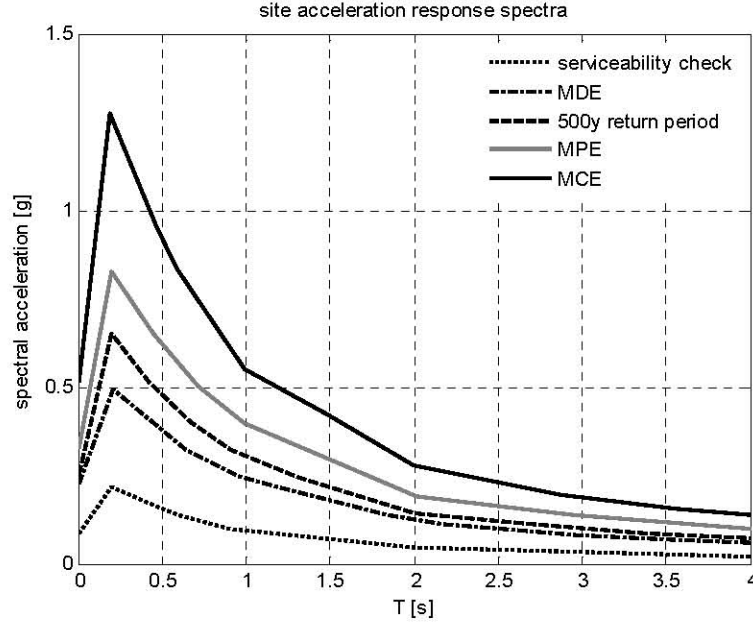


Figure 8.6 Site acceleration response spectra ($\xi=5\%$).

8.3 DESIGN AND NUMERICAL MODELLING OF BASE ISOLATION DEVICES FOR THE DEMONSTRATION BUILDING

8.3.1 Bilinear Hysteretic Behavior of Conventional Isolators

The conventional devices considered in this study are the Lead-Rubber Bearings and the Friction Pendulum System, both of which are usually represented by bilinear models (e.g., [Jerrams *et al.* 2001]).

The bilinear model (Figure 8.7) can be fully characterized by three parameters:

- the characteristic strength \mathcal{Q} ;
- the second stiffness K_2 ;
- the yield displacement D_y .

With these parameters, the effective stiffness, K_{eff} , the initial stiffness, K_1 , and the effective damping, β_{eff} , can be derived.

$$K_{eff} = K_2 + \frac{\mathcal{Q}}{D} \quad (8.1)$$

$$K_1 = K_2 + \frac{Q}{D_y} \quad (8.2)$$

$$\beta_{eff} = \frac{2Q(D - D_y)}{\pi K_{eff} D^2} \quad (8.3)$$

For LRBs, the ratio K_1/K_2 is generally taken to be around 10, while for FPSs a ratio of 100 is generally considered.

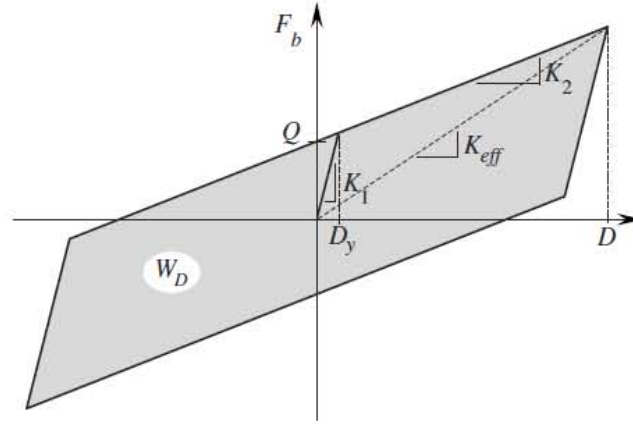


Figure 8.7 Bilinear hysteretic model.

Since K_{eff} and β_{eff} are function of the unknown D , an iterative procedure is needed to compute the three characteristic parameters.

The energy dissipated per cycle, W_D , is a function of Q, D and D_y , as expressed in the following formula

$$W_D = 4Q(D - D_y) \quad (8.4)$$

8.3.2 Lead-Rubber Bearings

For the scope of this work, the isolation system is designed at the MPE hazard level. A linear 10% damped system with 2s period has a maximum displacement of 19cm at the MPE hazard level and a displacement of 14cm at the 500yrs return period event.

Given the carried load W and the period T , the effective stiffness is

$$K_{eff} = \left(\frac{2\pi}{T} \right)^2 \frac{W}{g} \quad (8.5)$$

and the energy dissipated per cycle

$$W_D = 2\pi\beta_{eff}K_{eff}D^2 \quad (8.6)$$

From these two quantities, assuming the yield displacement equal to zero, a first estimate of the characteristic strength can be derived

$$Q = \frac{W_D}{4(D - D_y)} \quad (8.7)$$

from which, the second stiffness of the isolation system is given as

$$K_2 = K_{eff} - \frac{Q}{D} \quad (8.8)$$

and the yield displacement is

$$D_y = \frac{Q}{K_1 - K_2} \quad (8.9)$$

where

$$K_1 = 10K_2 \quad (8.10)$$

Table 8.1 Properties of LRB for the analyses ($K_1 = 10K_2$).

K_{eff}	312.8	[kN/m]
T	2	[s]
W_d	15.7	[kJ]
β_{eff}	20	[%]
D	0.2	[m]
Q	20.8	[kN]
D_y	11.1	[mm]
K_2	208.8	[kN/m]
K_1	2087.9	[kN/m]

8.3.3 Friction Pendulum System

A Friction Pendulum System (FPS) is a sliding device that utilizes a spherical surface to provide a restoring force and friction to dissipate energy [Zayas *et al.* 1987].

For an FPS isolator, the resisting force, F , is given by (e.g., [Almazan *et al.* 1998])

$$F = \frac{W}{R}D + \mu W(\text{sgn } D') \quad (8.11)$$

Where W is the load on the isolator, D is the horizontal displacement, μ is the friction coefficient and R is the radius of curvature of the dish.

The first term is the restoring force due to the rise of the mass, providing an horizontal stiffness K_b equal to

$$K_b = \frac{W}{R} \quad (8.12)$$

This gives a period of the isolated structure, T , as

$$T = 2\pi\sqrt{R/g} \quad (8.13)$$

that is independent of the carried mass.

For a given period, T , inverting this equation, the radius can be calculated

$$R = \frac{gT^2}{(2\pi)^2} \approx 10T^2 \quad (8.14)$$

Typical hysteresis loops for an FPS bearing are shown in Figure 8.8

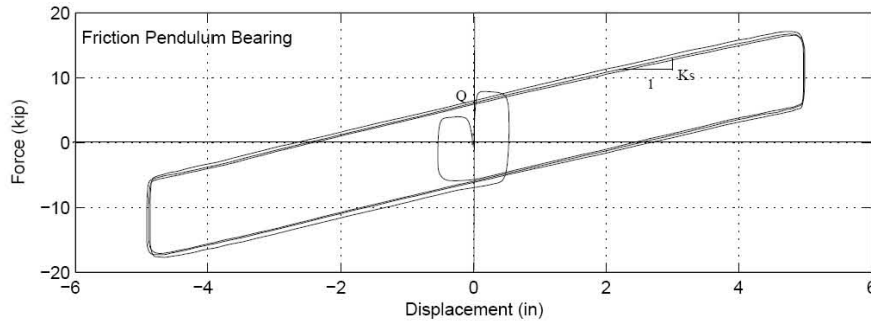


Figure 8.8 Hysteresis loops for an FPS Bearing [Almazan *et al.* 1998].

FPS bearings exhibit a linear restoring force, an high stiffness before sliding, and energy dissipation due friction during sliding. The equivalent (peak to peak) stiffness is given by

$$K_{eff} = \frac{W}{R} + \mu \frac{W}{D} \quad (8.15)$$

The damping produced by friction can be estimated as

$$\beta_{\text{eff}} = \frac{\text{Area of hysteresis loop}}{4\pi K_{\text{eff}} D^2} \quad (8.16)$$

Since the area of the loop is $4\mu WD$, thus

$$\beta = \frac{4\mu WD}{2\pi \left(\frac{W}{R} D + \mu W \right) D} = \frac{2}{\pi} \frac{\mu}{\left(\frac{D}{R} + \mu \right)} \quad (8.17)$$

The upward displacement of the system, δ_v , is given by

$$\delta_v = R \left[1 - \cos \left(\arcsin \left(\frac{D}{R} \right) \right) \right] \approx \frac{1}{2} \frac{D^2}{R} \quad (8.18)$$

FPSs are extremely simple to model, since they are essentially a one-parameter system where everything is controlled by the radius of the concave surface.

In practice, FPSs can be modeled by a bilinear model based on the three parameters, K_1 , K_2 , and Q , as shown in Figure 8.7. The characteristic strength, Q , is given by the friction coefficient of the sliding surface and the load carried by the bearing. The second slope, K_2 , is easy to determine for any type of isolation system, while the elastic stiffness, K_1 , can be estimated as a multiple of K_2 .

The value of K_1 has no influence on the effective stiffness, but has a strong influence on the damping. In fact, systems with the same Q and K_2 values (eq. systems with the same effective period at all values of D and the same hysteresis loop) with different values of K_1 can have a very different pattern of damping values depending only on the initial stiffness. In particular, for small displacements, if K_1 is large, the damping can be really high. On the other hand, if D is large, K_1 has no influence on the damping.

In the case study, FPSs are modeled in order to have a period of the base isolated building of 2s ($R=1\text{m}$). A friction coefficient $\mu=0.04$ is considered. This gives, for the design displacement of 0.2m, an effective stiffness of 378kN/m which is the same considered for LRB bearings. For, $D=0.14\text{m}$ the resultant damping is $\beta=0.15$. The initial stiffness K_1 is chosen to be equal to $100K_2$.

The resulting load displacement relations for the FPS and LRB are shown in Figure 8.9.

The eccentricity of the FPS base isolation layer is 0.016m. Modeling the vertical behavior of the bearings and the variability of the vertical force on the device could improve the accuracy in determining the forces transmitted by the bearings into the substructure.

Table 8.2 Properties of FPS for the analyses ($K_1 = 100K_2$).

K_{eff}	312.8	[kN/m]
T	2	[s]
W_d	15.7	[kJ]
β_{eff}	20	[%]
D	0.2	[m]
\mathcal{Q}	19.7	[kN]
D_y	0.9	[mm]
K_2	214.1	[kN/m]
K_1	21408.8	[kN/m]

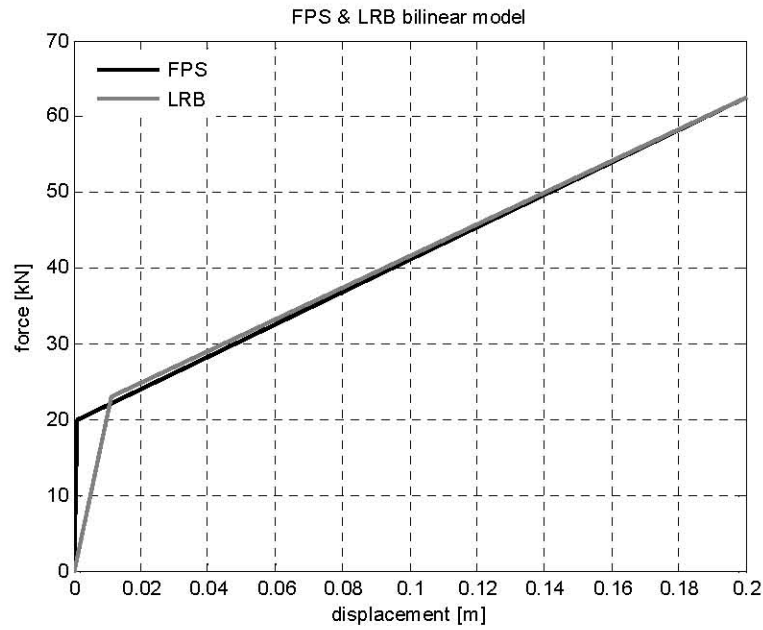


Figure 8.9 Bilinear model for FPS and LRB.

Anyway, tri-directional testing of a rigid-block frame shows that the vertical ground motion component has a small effect on the response of a structure isolated with FPSs (*e.g.*, [Mosqueda *et al.* 2004]). Therefore, only a 2D excitation is used in this work.

8.3.4 Fiber Reinforced Rubber Bearings

For the Indonesian building the resultant column loads, in the seismic load combination, are those of Figure 8.4. As done for the other isolation systems, FRBs are designed to have a period of isolation of 2s at target displacement. The design vertical pressure for the devices is set equal to 3.45MPa. The shear modulus of the rubber, G , is considered as 1.4MPa. Given this data, the geometry of the FRBs can be easily derived. In fact, the vertical pressure and the loads for each column give the base dimensions of the bearings, while the total thickness of the rubber can be computed solving a simple one-unknown equation obtained computing the secant stiffness at target displacement for each bearing (See Section 5.2). For the case study, the derived total thickness of the rubber, t_r , is 200mm.

The design base dimensions of the FRBs for the building are reported in Figure 8.10. It is recalled that the possibility of adopting devices of different sizes is one of the advantages of using FRBs as seismic isolators. In fact, each bearing could be easily obtained by cutting a larger pad. This could allow to have dimensions proportional to the applied vertical load. The result would be a zero eccentricity isolation system. For the case study, measures are rounded to the centimeters, this gives an eccentricity of the FRB base isolation layer of only 8mm. This result is one of the advantage of using FRBs.

In fact, having so many different dimensions would be impractical using conventional devices, as it would result in an unacceptable cost of the isolation system.

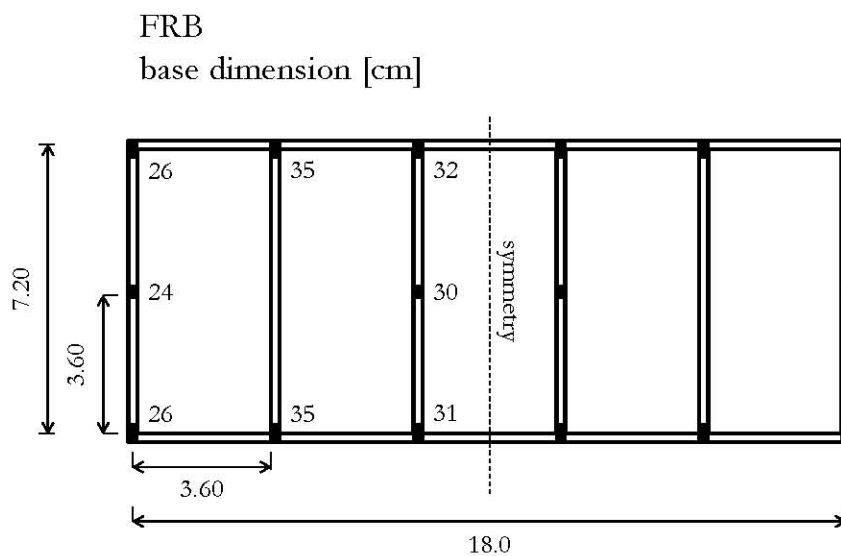


Figure 8.10 Indonesian building – FRBs distribution.

Since FRBs are not anchored to the structure, their frictional behavior has to be carefully investigated in order to define the performances of this new typology of bearings. Results of FEAs showed that assuming a friction coefficient $\mu = 0.7$, which was experimentally verified by different authors (*e.g.*, [Konstantinidis *et al.* 2003] [Russo and Pauletta 2013]), the bearings were capable of transferring the shear force from the device to the superstructure and substructure. Numerical analyses were carried out to simulate the behavior of the bearings designed for the building. The analyses showed no slipping at the contact interface and the ability for each device to deform in shear and to reach its ultimate horizontal behavior (see definition in Chapter 5).

A set of large displacement analyses was performed also. They showed the behavior of FRBs when displaced in their unstable range. For the description of the phenomenon are considered in this section the outputs of large displacement analyses on a bearing of base, B , equal to 240mm. The peak horizontal load is achieved in a deformed configuration as that of Figure 8.11. This deformed configuration is indicated with a red marker in the force-displacement plot of Figure 8.13. Once the peak displacement value is reached, the horizontal displacement can further be increased, but the deformed configuration will be unstable. At this point, the force-displacement relation shows a clear softening pattern.

Figure 8.13 illustrates the loss of lateral load resistance with negative values of the lateral load. This effectively means that, in the negative forces half-plane, a resistance has to be imposed to control the rotation of the originally vertical surfaces. In fact, for large deformations, the overturning moment generated by the applied vertical load overtakes the resistance provided by the device.

However, the unstable roll out of the bearing is limited by the touching of the originally vertical surfaces with the horizontal support. This condition is depicted in Figure 8.12. The displacement value corresponding to this configuration is defined “ultimate displacement”. This condition is indicated in Figure 8.13 with a green marker. Continuing to displace the isolator will result in a very steep hardening branch. This is due to the indentation of the reinforcing layers on the horizontal plates. In fact, at this point the edges of reinforcing and rubber layers, after a rotation of 90° , have reached the horizontal supports. It is also important to note that, in this range, the device could be progressively damaged with a delamination of the layers. Such degradation is due to the friction generated by the horizontal movement, and this tends to tear apart the strata.

For the time-history analyses, the horizontal behavior of the bearings is described using a trilinear model with hardening (Figure 8.19). The numerical values for the model are reported in Table 8.3. Trilinear relations have been used to describe the back-bone curve of the force displacement relations depicted in Figure 8.15. In fact, it is considered

that this model is capable of describing the devices for the scope of having first outcomes on the behavior of a RR-FRBs isolated building.

This assumption is validated by the observation that the energy dissipation of a non-linear element depends mainly on the global envelope of the force displacement curves.

It is also recognized that other constitutive relations could be used to describe the nonlinear behavior described above but, in this phase, a simplified model can be considered satisfactory.

Another effect of the roll-out of the isolator is the vertical displacement of the upper loading plate.

This effect is showed in Figure 8.14 where the vertical displacement is plotted against the analysis steps.

The vertical behavior of the bearings is simplified in the analyses using a compressive stiffness equal to that of the bearings undeformed in shear (Figures 8.16 - 8.18).

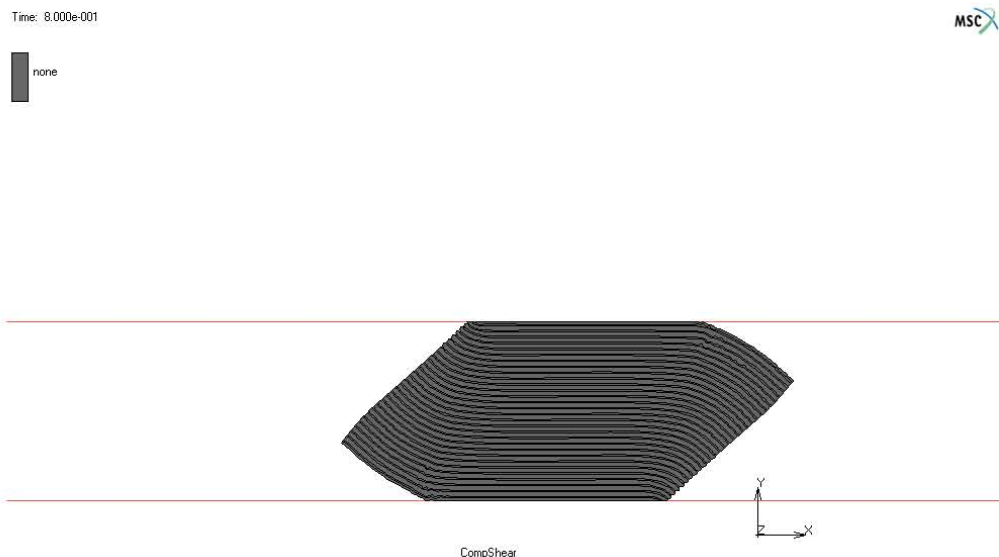


Figure 8.11 RR-FRB (B=240mm) at peak horizontal displacement.

Time: 1.350e+000

MSC

none

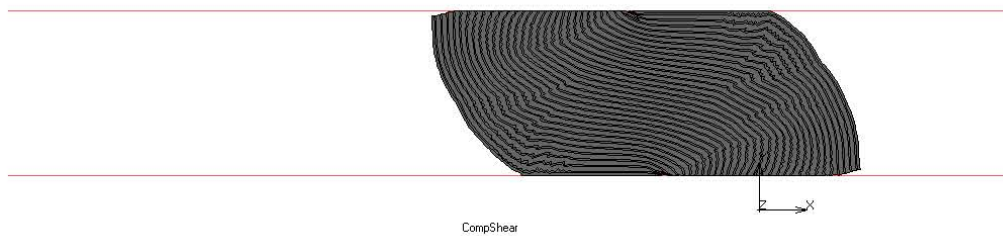


Figure 8.12 RR-FRB (B=240mm) at ultimate horizontal displacement.

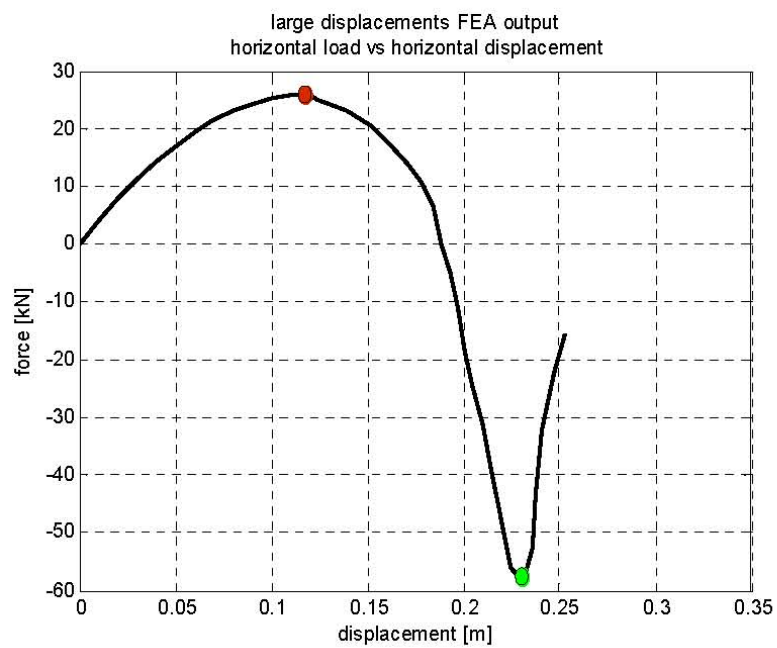


Figure 8.13 RR-FRB (B=240mm) horizontal load vs horizontal displacement. Large displacements analysis.

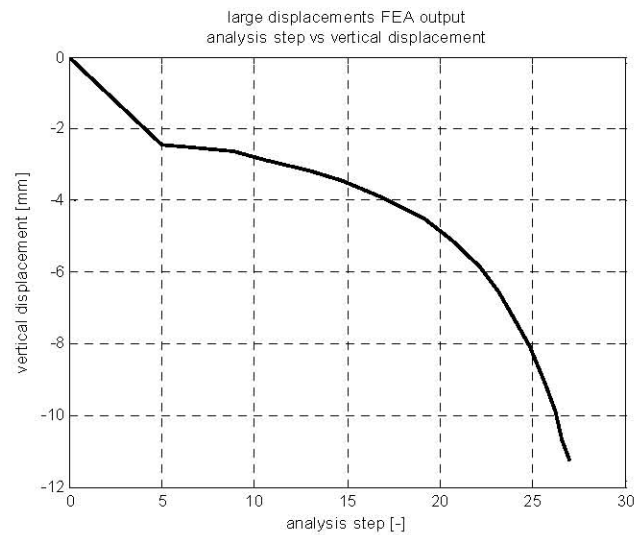


Figure 8.14 RR-FRB (B=240mm) analysis step vs vertical displacement. Large displacements analysis.

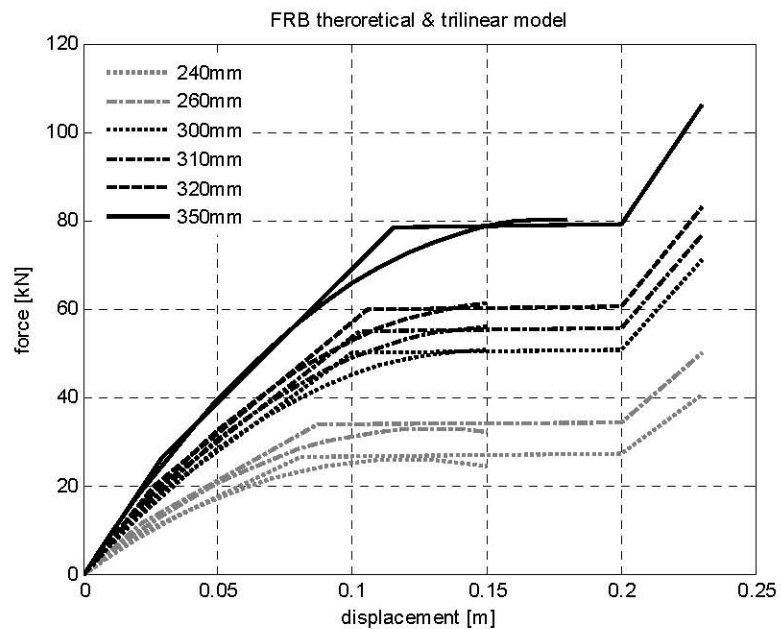


Figure 8.15 FRB trilinear models and results by FEAs.

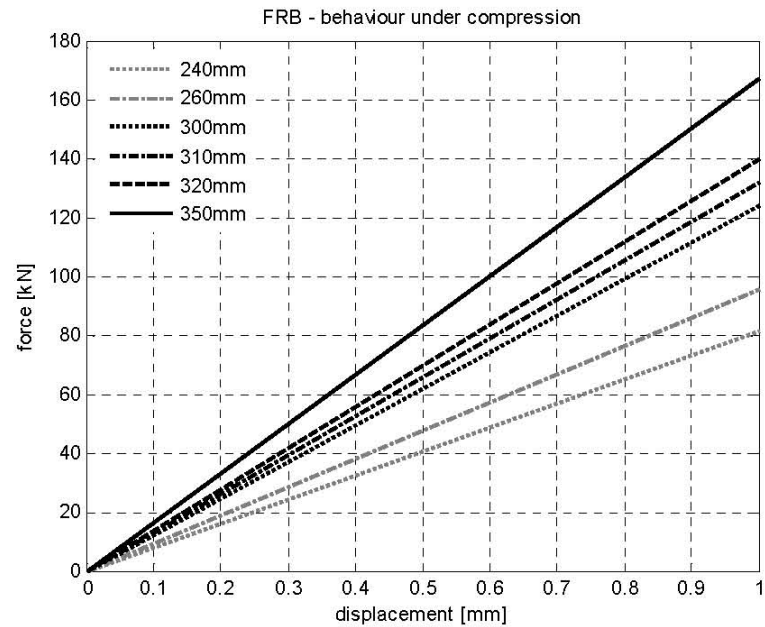


Figure 8.16 Load displacement relation from FEAs.

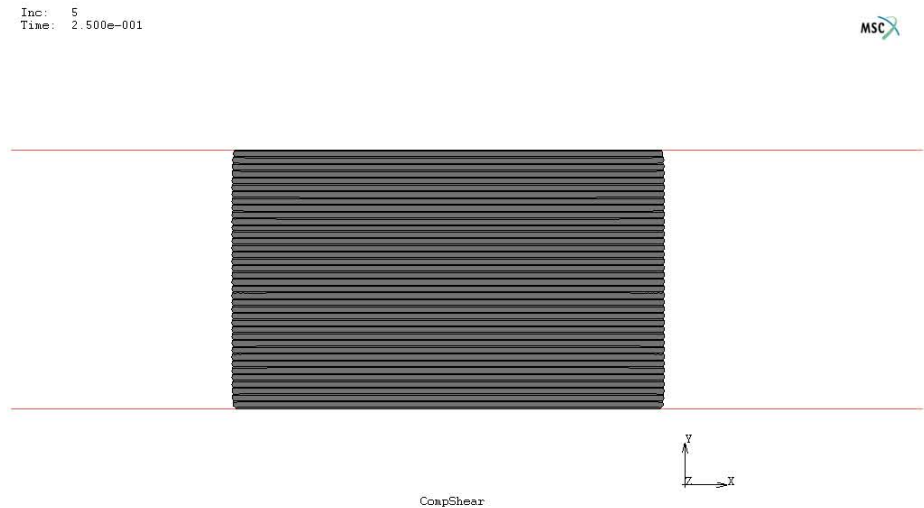


Figure 8.17 Deformed configuration under compression.

Inc: 5
Time: 2.500e-001

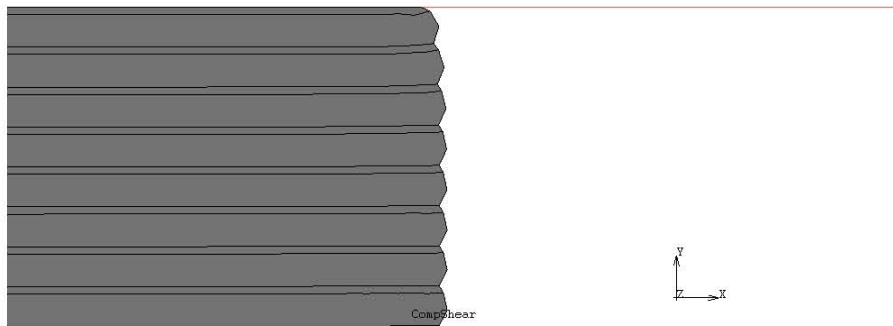


Figure 8.18 Bulging of the rubber and stretching of the fiber layers under compression.

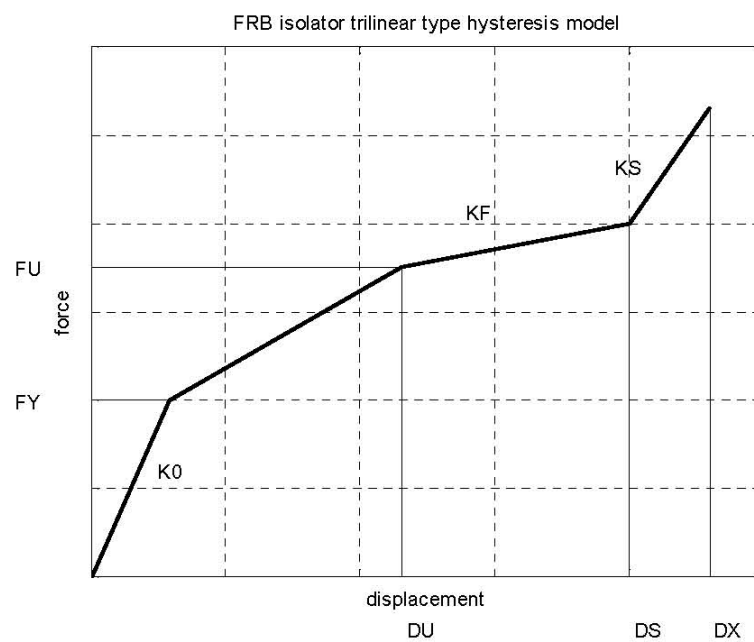


Figure 8.19 Trilinear model for the FRB isolators.

Table 8.3 Properties of RR-FRBs for the analyses.

Base Dimension [cm]		24	26	30	31	32	35
<i>K0</i>	[kN/m]	440.2	515.6	670.6	711.2	753.7	903.5
<i>KF</i>	[kN/m]	4.4	5.2	6.7	7.1	7.5	9.0
<i>DS</i>	[m]	0.20	0.20	0.20	0.20	0.20	0.20
<i>KS</i>	[kN/m]	440.2	515.6	670.6	711.2	753.7	903.5
<i>FY</i>	[kN]	8.9	11.3	16.7	18.2	19.9	26.1
<i>FU</i>	[kN]	26.7	33.8	50.1	54.7	59.7	78.4
<i>DU</i>	[m]	0.08	0.09	0.10	0.10	0.11	0.12
<i>DX</i>	[m]	0.23	0.23	0.23	0.23	0.23	0.23
<i>KC</i>	[kN/m]	81482.8	95445.9	124133.3	131648.6	139522.2	167246.7
<i>KT</i>	[kN/m]	814.8	954.5	1241.3	1316.5	1395.2	1672.5

8.4 TIME-HISTORY ANALYSES

8.4.1 Superstructure Model

Time-history analyses were carried out using a computer program, Perform-3D v5 [Computers and Structures, Inc. 2012]. A full three-dimensional representation of the superstructure (Figure 8.20) with linear elastic behavior is used in the time-history analyses. Columns and beams are modeled using linear beam and columns elements. The floor masses are concentrated to the joints. Diaphragm constraints are used at each floor level above the isolation system. The distribution of the structural elements at each floor is symmetrical in both directions, while the distribution of the mass is slightly asymmetrical in the longitudinal direction: the degree of mass eccentricity is very small - less than 1% of the length of the building. The mass of the structure and the load carried by the building are assumed to be concentrated at the floor levels.

Damping ratio of 0.05 is used for all the superstructure modes. The isolator modes have periods of approximately 2s.

Since the seismic gaps are effective in separating the infills from the structural frames, it is reasonable to exclude the stiffness contribution of the unreinforced masonry walls in the computation of the lateral stiffness of the superstructure. For the fixed base structure, the first period is 0.45s, corresponding to the first mode in the transversal direction. The second period is 0.28s, corresponding to the first mode period in the longitudinal direction.

These periods of the superstructure are well separated from the two-second horizontal period of the isolation system.

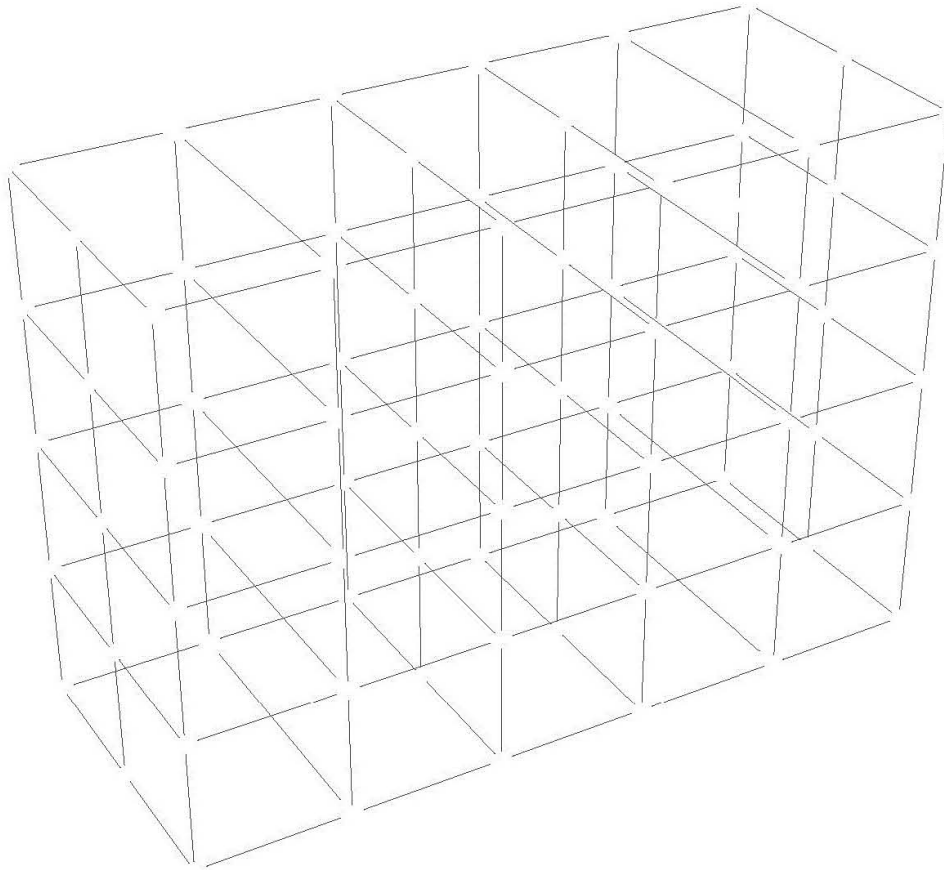


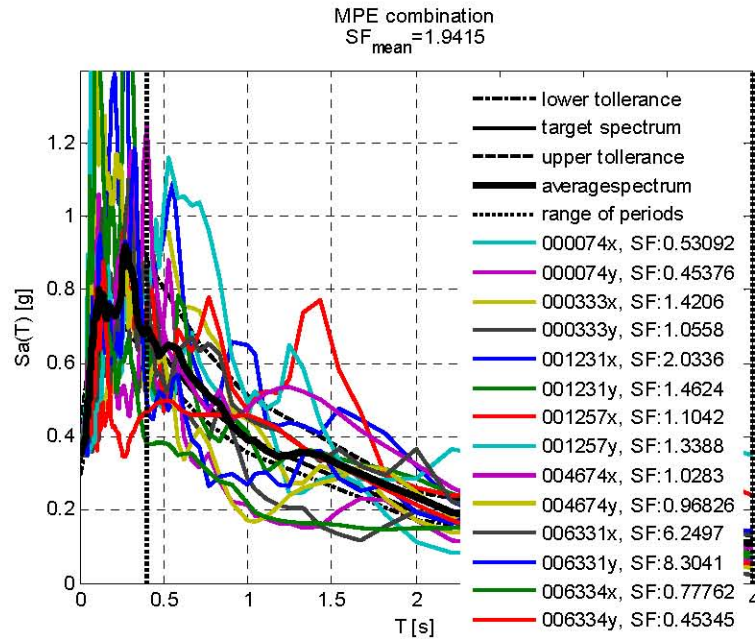
Figure 8.20 Indonesian building-superstructure frame.

8.4.2 Ground Motion Selection

The analytical models are subjected to a series of recorded ground motions that are representative of the site response spectra for the 500yrs return period and MPE seismic risk levels.

The records were selected for the time history analyses using Rexel v 3.4 beta [Iervolino *et al.* 2010]. The main condition for the chosen ground motions sets is that the average elastic spectrum does not underestimate the spectra, with a 10% tolerance, in a wide range of periods 0.4-4s. As for the sets chosen by Taniwangsa and Kelly [1996], are

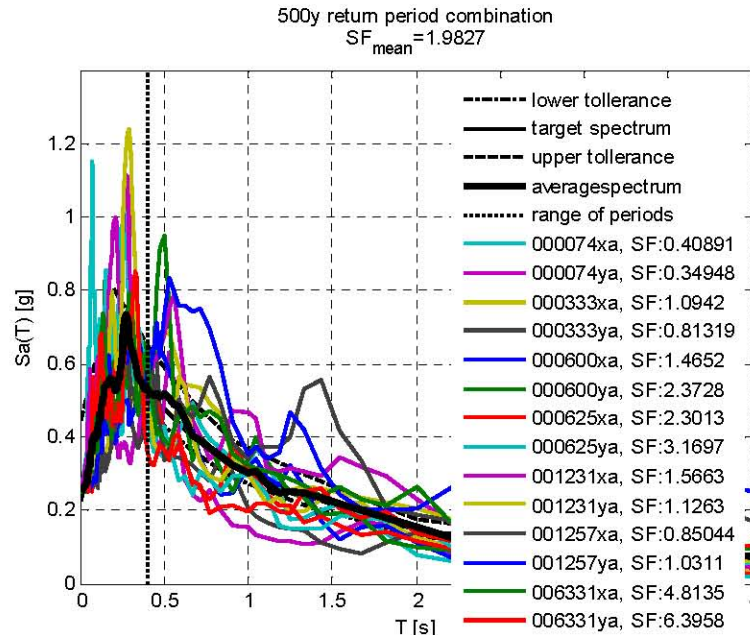
considered accelerograms with $5.5 \leq M \leq 8.1$, R within 0-22km. Figure 8.21 and Figure 8.22 are the MPE and 500yrs return period combination for the site.



Waveform ID	Earthquake ID	Station ID	Earthquake Name	Date	Mw	Fault Mech	E. Dist [km]	PGA_X [m/s ²]	PGA_Y [m/s ²]	PGV_X [m/s]	PGV_Y [m/s]	ID_X	ID_Y	Np_X	Np_Y
6331	2142	ST2486	South Iceland (aftershock)	21/06/2000	6.4	strike slip	22	0.513	0.386	0.057	0.040	6.505	7.101	1.068	0.766
1231	472	ST575	Izmit	17/08/1999	7.6	strike slip	9	1.576	2.192	0.190	0.266	14.585	9.807	0.764	0.995
333	157	ST121	Alkion	24/02/1981	6.6	normal	20	2.257	3.036	0.223	0.226	7.920	7.447	0.759	0.779
74	43	ST27	Gazli	17/05/1976	6.7	thrust	11	6.038	7.065	0.502	0.626	9.813	6.981	1.123	0.570
6334	2142	ST2488	South Iceland (aftershock)		6.4	strike slip	11	4.123	7.070	0.377	0.970	4.507	1.873	0.838	0.945
4674	1635	ST2486	South Iceland	17/06/2000	6.5	strike slip	5	3.118	3.311	0.612	0.238	4.071	9.846	0.795	0.586
1257	472	ST772	Izmit	17/08/1999	7.6	strike slip	20	2.903	2.395	0.525	0.476	6.239	7.859	1.284	0.894
mean:					6.8		14	2.933	3.636	0.355	0.406	7.663	7.273	0.947	0.791

Figure 8.21 MPE combination for the site.

The record are pair of horizontal ground acceleration time histories from different events. The x and y components are applied in the longitudinal and transversal directions of the model, respectively.



Waveform ID	Earthquake ID	Station ID	Earthquake Name	Date	Mw	Fault Mech.	E.Dist.	PGA_X	PGA_Y	PGV_X	PGV_Y	ID_X	ID_Y	Np_X	Np_Y
							[km]	[m/s ²]	[m/s ²]	[m/s]	[m/s]				
6331	2142	ST2486	South Iceland (aftershock)	21/06/2000	6.4	strike slip	22	0.513	0.386	0.057	0.040	6.505	7.101	1.068	0.766
1231	472	ST575	Ismit	17/08/1999	7.6	strike slip	9	1.576	2.192	0.190	0.266	14.585	9.807	0.764	0.995
333	157	ST121	Alkion	24/02/1981	6.6	normal	20	2.257	3.036	0.223	0.226	7.920	7.447	0.759	0.779
74	43	ST27	Gazli	17/05/1976	6.7	thrust	11	6.038	7.065	0.502	0.626	9.813	6.981	1.123	0.570
6334	2142	ST2488	South Iceland (aftershock)		6.4	strike slip	11	4.123	7.070	0.377	0.970	4.507	1.873	0.838	0.945
4674	1635	ST2486	South Iceland	17/06/2000	6.5	strike slip	5	3.118	3.311	0.612	0.238	4.071	9.846	0.795	0.586
1257	472	ST772	Ismit	17/08/1999	7.6	strike slip	20	2.903	2.395	0.525	0.476	6.239	7.859	1.284	0.894
mean:					6.8		14	2.933	3.636	0.355	0.406	7.663	7.273	0.947	0.791

Figure 8.22 500yrs combination for the site.

Acceleration time-histories for the selected ground motions are reported in Appendix D.

8.5 ANALYTICAL PREDICTION OF PERFORMANCE OF THE DEMONSTRATION BUILDING

8.5.1 Time-History Responses

The results of the analyses can be expressed as time-history responses and/or maximum response quantities. Analyses were carried out to show the effects of different isolators properties. In this work are investigated/reported the performances of the building for two sets of ground motions corresponding to 500yrs return period events and 1000yrs return period events. This last set, in accordance with Taniwangsa and Kelly [1996], identifies the Maximum Probable Earthquakes.

The work is oriented to verify the safety margin of FRB isolated buildings under severe events. Modal analysis conducted for the 50yrs return period event showed that the fixed based structure is capable of behaving elastically without exceeding the interstory-drift of 0.005.

The maximum responses in terms of absolute floor accelerations, floor displacements, interstory-drifts are presented for each seismic risk level. In addition, the variation in the column load during the earthquake is computed to verify that the columns remain in compression to enable the bearings to transfer the shear force properly to the superstructure.

Accelerations:

Figures in Appendix E show the response acceleration at the isolation level, and the acceleration response time history at the top level for the FRP, FPS and LRB models. For all the models there is no amplification of the acceleration up to the top of the building. The maximum roof acceleration for the corresponding fixed-base building, considering only the first mode and not accounting for inelastic behavior, for the MPE, is around 0.7g. No amplification of the peak ground acceleration (PGA) in the superstructure occurred. At a roof level, for all the tested technologies, the maximum acceleration was limited in most of the cases to 3.0m/s^2 . This acceleration is considered a limit value for medical facilities, electronic facilities and others [Pan *et al.* 2005].

Displacements:

Large displacements in the bearings occur. Figures in Appendix E show the relative displacement time histories. Figures refer to the displacement in the x-direction, however the maximum isolator displacement is approximately the same in both longitudinal and transverse direction. These maximum displacements occurred at different times. Therefore, the total isolator displacement is not the vectorial sum of the maximum displacement in each direction. The maximum relative displacement at each floor is small compared to the isolator displacement.

The interstory-drift is a very important response parameter in the prediction of the performance of the non-structural elements and building contents.

The maximum interstory-drifts are shown from Figure 8.23 to Figure 8.26. The dashed line in the plots represents the Serviceability Limit State (SLS) as for the Italian building code [NTC 2008].

Since the number of ground motions pairs is seven, the response values used to represent the sets are the mean values of the responses from all ground motions.

The values obtained for the 500yrs and MPE sets for the tested isolation systems are summarized in Table 8.7.

Table 8.4 Average interstory-drift.

[%]								
	500yrs events	MPE events		500yrs events	MPE events		500yrs events	MPE events
FPS	4th floor		LRB	4th floor		RR-FRB	4th floor	
	0.380	0.500		0.134	0.150		0.530	0.660
	1st floor			1st floor			1st floor	
	0.110	0.150		0.035	0.370		0.170	0.220

The isolation systems are not so effective in isolating the building for the 1257 record as they are for other records. This happens because the predominant frequency content of this record is about the frequency of the isolation system.

The displacements of the base isolation layer for the RR-FRB system are generally bigger than LRB and FPS isolated models. LRB devices are effective also against medium-level ground motions with a low input velocity: the damping mechanism begins to work when the velocity is still low. FPS isolated building show a certain degree of response to medium-level ground motions, but the amount of response is relatively small against strong events. This indicates that climbing the slope and exceeding the sliding friction force of an FPS base isolation system requires a certain amount of input. The same behavior has been observed in several experimental campaigns [Hanai *et al.* 2004].

Residual displacements after ground motion excitation are generally small, except for RR-FRBs. For the low-cost bearings there would be the need to perform a zero return after encountering a strong earthquake.

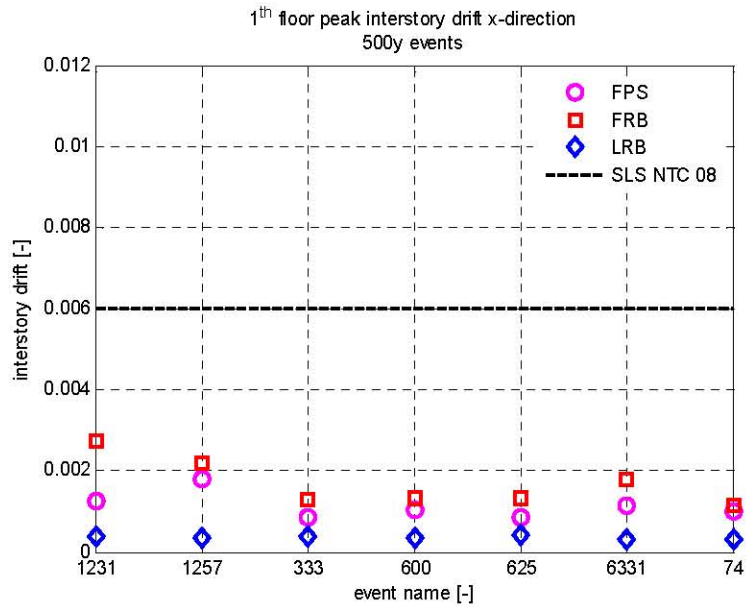


Figure 8.23 1th floor peak interstory-drift (500yrs events).

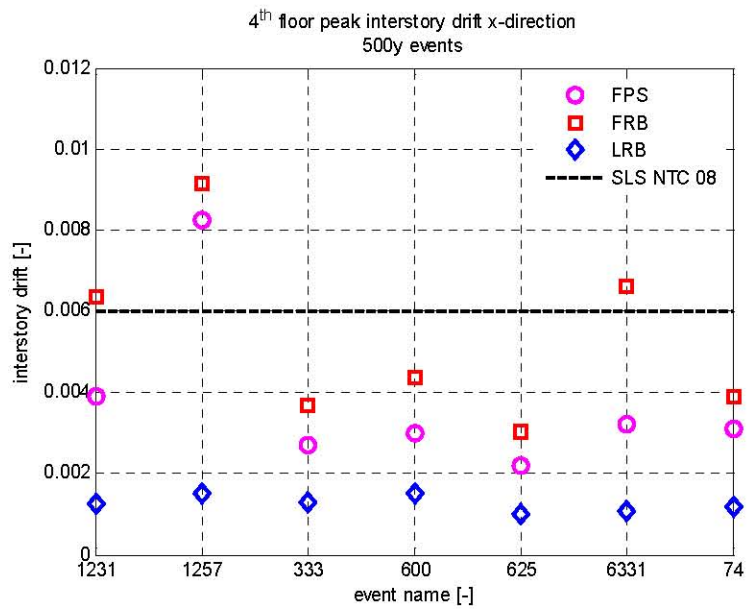


Figure 8.24 4th floor peak interstory-drift (500yrs events).

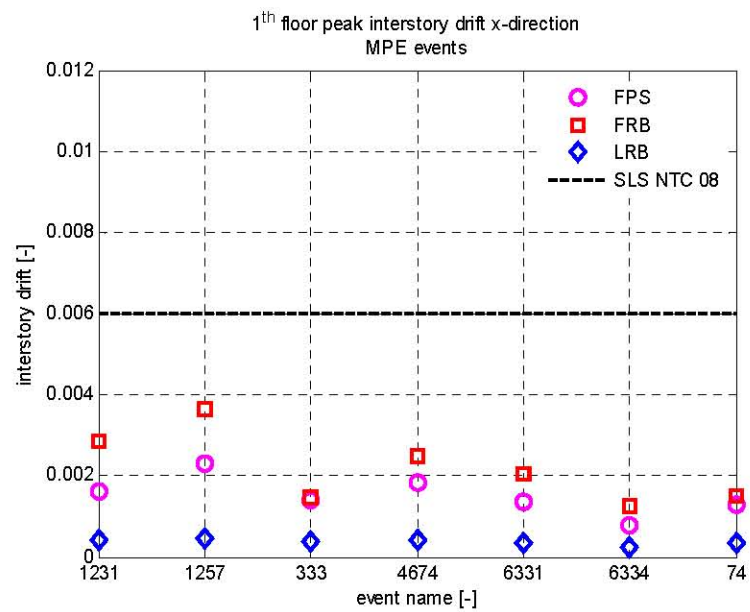


Figure 8.25 1th floor peak interstory-drift (MPE events).

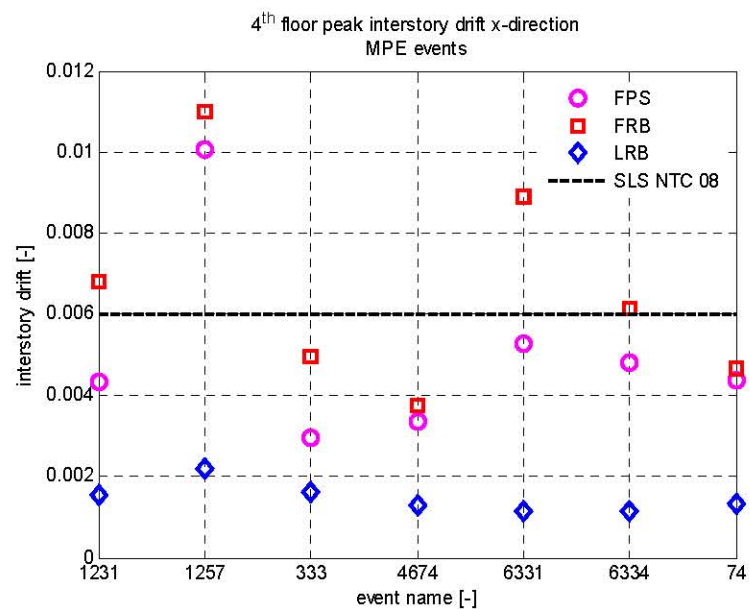


Figure 8.26 4th floor peak interstory-drift (MPE events).

As in the case of study, small interstory-drift imply better performance of the non structural elements and building contents. It was found that the interstory-drift for the base isolated models was very small and the seismic response was significantly better than the one of the non-isolated linear elastic buildings.

During the excitations in which considerable displacement occurred, little torsion was observed regardless of the type of device used.

Shear Forces:

The peak base shear forces for a corner bearing are extracted from the analytical results. Figure 8.27 compares the peak shear force for a corner bearing considering FPS, RR-FRB, LRB isolation systems and fixed base building results. The seismic response of base isolated models compared to non-isolated linear elastic frame is significantly better.

For the MPE combination, the average reduction of base shear with respect to the fixed base structure is 82% for LRB, 70% for FPS and 61% for LRB isolation system.

Axial Load on the Isolation Bearings

FRBs are placed underneath each column. The shear force is transmitted by friction. The contact area between the isolation bearings and the horizontal subgrades is important in maintaining the isolation system configuration. It is important to determine if the column load changes sign during the earthquake, implying column uplift. If the columns are uncompressed, the RR-FRBs under these columns will not participate in carrying the horizontal shear force, and the earthquake force will be redistribute to the other bearings that remain under compression.

FRBs and FPSs, should always be in compression. Because the column loads vary due to the overturning moment during an earthquake, the variation of the axial load in the columns is computed to verify that all the devices are always in compression.

For the cases where only the friction is not sufficient for transmitting the shear forces, recess plates as shear connection for RR-FRBs need to be considered.

Shear connections need also to be used for the cases were the combined vertical and overturning action of ground motions results in complete unloading of the devices

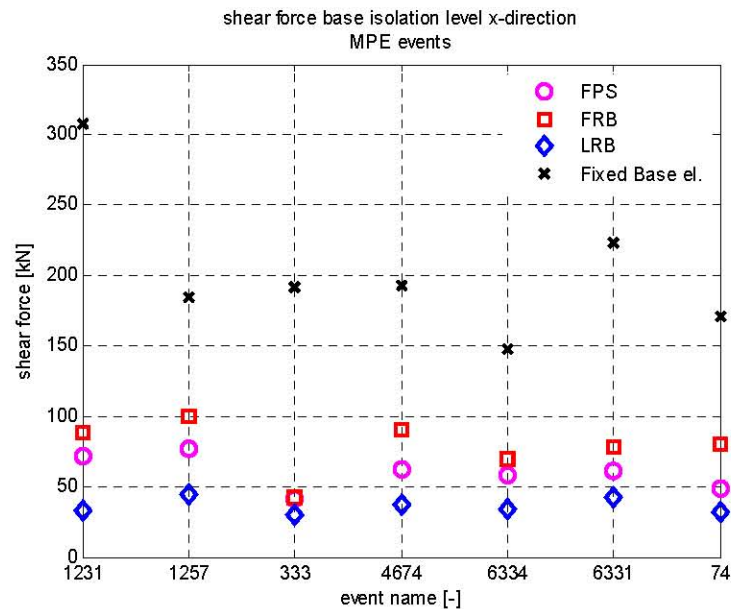


Figure 8.27 Shear force base isolation level (MPE events)

8.6 SUMMARY

Results of the time-history analyses with 14 pairs of recorded ground motions show that the average total isolators displacement is higher for RR-FRBs than FPSs and LRBs. The maximum accelerations transmitted to the superstructure obtained from the different isolation systems are comparable.

The time-history analyses show that all the tested technologies are very effective in isolating the superstructure from the strong ground motions, corresponding to the MPE seismic risk.

This study shows that Recycled Rubber Fiber Reinforced Bearings can be an excellent choice in protecting buildings from strong earthquakes. They are capable to reduce the floor accelerations and interstory-drifts, providing superior performance in terms of building contents, non structural elements and serviceability after major earthquakes. The case study demonstrates that it is possible to develop a cost-effective isolation technology without compromising the performance of the isolated building. The developed bearings are affordable, light and reliable. They represent a valuable solution for common types of buildings and they further encourage the use of base isolation for the seismic protection of structures. The research conducted shows that FRBs have broad application. Their use is not only limited to developing countries, but all countries that are vulnerable to big earthquakes.

The isolators are able to shift the natural period of the building to values beyond the period range of the largest spectral acceleration values, thus significantly reducing the seismic demand. Due to amplitude dependent stiffness and damping of the bearings, the isolated building period, T , and corresponding damping ratio, ξ , are influenced by the level of excitation.

Regardless of the type of device, the response acceleration is lower than the input acceleration. Base isolation layers displacements and the interstory-drift are in the design limit. Thus, all considered devices are effective against the input waves.

Traditional non-isolated buildings are typically designed such that a significant damage to both structural and non-structural components is acceptable. After major earthquakes traditional buildings are expected to be uninhabitable until repaired.

Base isolated buildings are expected to experience little or no damage during a major earthquake and be safely occupied immediately after a seismic event so that when equivalent levels of design performance are compared, an isolated building is always more cost-effective [Kelly 1997]. Results from this study show that a substantial reduction in the peak response acceleration and peak base shear can be achieved by implementing RR-FRB as base isolation system. All of the tested devices are effective as base isolation technologies: the response acceleration is sufficiently low and the interstory-drift is lower than damage level.

9.CONCLUSIONS

9.1 SUMMARY OF WORK

This dissertation has investigated the behavior of innovative bearings, both theoretically and experimentally. The herein proposed Recycled Rubber - Fiber Reinforced Bearings (RR-FRBs) are extremely appealing due to their light-weight and low-cost characteristics, and could be widely employed as an effective seismic risk mitigation strategy for new constructions, as well as for the retrofitting of existing buildings. Developing countries could take advantage of such technology to reduce the earthquake vulnerability of large urban areas.

New closed-form expressions for FRBs under compression are derived for several shapes (infinite strip, rectangular and circular). The formulas allow determining the vertical stiffness, and the stress distribution in the reinforcement, of devices with flexible reinforcements and compressible rubber. It is important to highlight that the derived expressions represent a generalization of existing classical theories (*e.g.*, [Kelly 1999]).

The mechanics of RR-FRBs is also studied with numerical simulations, whose results are reported in Chapter 4. Nonlinear Finite Element Analyses (FEAs) were performed with Marc 2005 [MSC Software, 2004], which is a software package particularly suited to model elastomeric materials. Results from FEAs confirm the outcomes from the analytical study, and provide additional information on large-displacement behavior of the device.

The ultimate displacement of unbounded bearings depends of geometrical and equilibrium considerations. In Chapter 5 these conditions are studied. Design criteria are introduced. The criteria, together with the previous findings, effectively allow a sound theoretical representation of the RR-FRBs.

An extensive testing program has been carried out during this research. Results of the experimental campaigns are reported starting in Chapter 6. Material characterization of recycled rubber compound is obtained with laboratory testing.

Full-scale bearing prototypes, illustrated in Chapter 7, were tested in order to assess the behavior under compression and shear loading. Moreover, the influence of

various configurations in terms of rubber compound, reinforcement typology, and number of layers was also addressed.

A case study describing the application on a benchmark building representative of a low-cost housing typology is presented in Chapter 8. Inelastic Time-History Analyses (ITHAs) were performed considering traditional isolation systems and the performances were compared to the ones obtained with the novel devices. The simulations showed a significant seismic demand reduction in the superstructure when using RR-FRBs. The reduction of interstory-drifts, base shear, and floor accelerations matches what can be obtained with existing, consolidate, bearings. It can therefore be argued that RR-FRBs are extremely advantageous because the same performance is obtained at a lower cost, and with a significantly easier on-site installation.

9.2 SUMMARY OF RESULTS

The research described in this dissertation introduces an original technology with significant advantages for seismic risk reduction. The primary conclusions that can be drawn from this work include:

- a) A low-cost and light-weight rubber isolation system can be produced with recycled rubber compound such, for instance, the one obtained with exhausted tyres or industrial leftovers. These devices are called RR-FRBs.
- b) The most important aspects of these bearings are: no need for thick steel end-plates, no bonding to support surfaces required, very flexible reinforcement provided with Fiber Reinforced Polymers (FRPs).
- c) The use of fiber reinforcement in an unbounded device has the advantage of eliminating the presence of tensile stresses in the bearing. Rolling off from supports can develop without constraints. This eliminates the need for costly vulcanization bonding typical of conventional bearings. Moreover, it gives the possibility of using an elastomeric material with lower mechanical qualities, but also at a lower cost, than the rubber commonly used in seismic isolation.
- d) In the theoretical solution, known as pressure solution, both the compressibility of the rubber and the stretching of the reinforcement are taken into account in order to give closed-form expressions for the determination of the vertical stiffness and the tension in the fiber reinforcements. Two adimensional parameters, α and β are introduced. They are functions, respectively, of the stiffness of the reinforcement and of the compressibility of the rubber. A surprising result of this approach is that the apparently unrelated effects of stretching of the reinforcement and compressibility of the rubber can be described in a similar analytical formulation. In fact the mathematical structure of

the theory is the same. Moreover, the combined solution can be written in a simple form (see demonstrations in Chapter 3).

- e) The developed theoretical models considering flexible reinforcement and compressibility of the rubber are consistent with the “classical solutions” available for steel laminated rubber bearings and incompressible rubber. In fact, when both α and β tend to zero, thus converging on the same hypotheses of rigid reinforcement and incompressible elastomer, the two theoretical models give the same results. Hence, the pressure solution for steel reinforced bearings can be considered a special case of the models proposed herein with more generic assumptions (see Figure 4.6 for the solution of strip type bearings and Figure 4.9 for the solution of circular type devices under compression).
- f) Comparing the theoretical and the FEAs results, it is clear that the pressure solution is an useful tool for the prediction of the vertical stiffness of the bearings, K_v , and the stress distribution in the reinforcing layers, σ_f . As shown in Figure 4.8, the vertical stiffness obtained by the pressure solution is in good agreement with results from FEAs (Figure 4.9). The same result holds for the stress distribution in the reinforcing layers (Figure 4.10). The Figures listed before are examples given for the case of strip-type bearings. Chapter 4 also reports similar considerations for bearings of different materials, geometries, reinforcing configurations and shapes.
- g) FEAs showed that, considering Coulomb friction with $\mu = 0.9$ and a vertical pressure up to $\sigma_v = 3.45 \text{ MPa}$, the external layers of the bearings are in compression (Figure 4.5). For these values of pressure and frictional coefficient, FEAs clarified that the tested bearings are able to displace up to their ultimate horizontal value with no slipping at the contact support. This result is particularly important when designing fiber reinforced bearings. In fact, since they are not bonded at the contact surfaces some amount of friction and vertical load need to be provided in order to have devices capable of deforming in shear without slipping.
- h) For RR-FRBs two limiting horizontal displacements are identified. They set the limit of the horizontal displacement for the overall stability of the bearings and the displacement at which the originally vertical surfaces, while rotating, touch the horizontal plates. Theoretical models are proposed to determine these two limit quantities. The assumptions and the demonstrations of the criteria are discussed in Chapter 5.

Tests on recycled rubber and fiber reinforcement with a polyurethane matrix clarified the behavior of the materials for the production of RR-FRBs:

- i) The mechanical behavior of recycled rubber can be easily modified by changing shape, size and density of the rubber grains of the compound (Figure 6.3 and Figure 6.4).
- j) The ultimate strength and deformation of recycled rubber is proportional to the density of the material (Figure 6.6).
- k) The shape of the rubber grains is fundamental in determining the strength and the ultimate capacity of recycled rubber. The best performances can be obtained using strip shaped rubber grains (Figure 6.7).
- l) The ultimate elongation of recycled rubber specimens is around 1%. The ultimate strength is around 1MPa (Figure 6.6 and Figure 6.7). These values are very low when compared to natural rubber. Anyway, as demonstrated by FEAs, there is no need of using rubber of better quality (and higher cost) for the production of fiber reinforced bearings. In fact, since no bonding to the upper and bottom surfaces is used, the tensile stresses in a shear deformed device are very limited (Figure 4.12). This allows the use of low performances materials. It is again recalled and highlighted that this is indeed one of the main advantages of using a flexible reinforcement in rubber isolators.
- m) Recycled rubber has a shear modulus in the range of 0.4-1.1MPa (Figure 6.9). These values are similar to the ones for natural rubber.
- n) The variability of the shear modulus with the amplitude of imposed lateral displacement, its frequency, and applied vertical load is investigated and described in Chapter 6.
- o) The shear modulus of recycled rubber is also a function of the applied vertical load. As this increases, the voids in the recycled rubber reduce their dimensions thus giving a better interlocking of rubber grains. In turns, such interlocking increases the shear modulus of the material. This characteristic of recycled rubber is extremely significant for seismic isolation. It introduces a proportionality of the horizontal stiffness of the devices to the applied vertical load. Virtually, this could introduce a singularity in seismic isolation with rubber: the capability of producing systems in which the isolation period is unchanged by the changing loads on the structure. In other words, it could be possible to recall with a low-cost rubber bearing a behavior currently only achievable with costly and weather-sensitive Friction Pendulum Bearings (FPBs).
- p) Dissipation properties of recycled rubber are similar to high-damping natural rubber compounds. The equivalent viscous damping is in the range of 10-15%

(Figure 6.11). The variability with displacement amplitudes and frequencies is also investigated, and reported in Chapter 6.

- q) Cyclic shear tests showed no degradation of recycled rubber performances (Appendix A).
- r) Tensile tests on fiber reinforcement with a polyurethane matrix showed that it is possible to substitute the conventional epoxy resin with a polyurethane matrix. In fact, the mechanical characteristics of this new material for the production of RR-FRBs slightly change respect the more diffused fiber reinforced polymers made using epoxy matrices (Figure 6.14). This is advantageous because polyurethane binders are also adopted in recycled-rubber compounds.

Based on the theoretical findings on the behavior of RR-FRBs, and considering the experimentally-obtained properties of component materials, prototype bearings have been designed, manufactured and extensively tested. The experimental campaign on the prototypes showed that:

- s) It is possible to produce RR-FRBs as described in the thesis and the result is a very low-cost technology. The cost of the prototypes for the tests was in the order of the tens of euros per piece. This is very inexpensive when compared to the price of conventional rubber devices that can be in the order of thousands of euros. Moreover, the costs were related to the production of few pieces for the experimental campaign, and they could be realistically reduced for applications on a wider scale.
- t) Compression tests underlined that a carbon reinforcement can be more effective than steel for RR-FRBs (Figura B.5 and Figure B.4). This is mainly due to the fact that the polyurethane binder can flow through the holes of the fiber layers ensuring a better adhesion among the rubber and the reinforcing surfaces.
- u) Glass fiber can also be used as reinforcements for RR-FRBs. However in this case, given the low elastic modulus of G-FRPs, it is particularly important to adopt denser fabric configurations.
- v) The performance of RR-FRBs under shear conditions is very satisfactory. Since no support-bonding is used, they are able to deform freely with no tension generated at the contact surfaces. Successive cycles of loading were applied and no damage was detected.
- w) An unexpected advantage in the use of fiber reinforcement is: the bending of fiber strands in the roll-off portion of the bearing dissipates energy by friction at the different strands interfaces. This energy dissipation is proportional to the roll-off portion of the bearing. In fact, when a fiber reinforced isolator is loaded in

shear, a planar cross section becomes curved. The friction acting between individual fibers in the curved bundles produces frictional damping. This is due to individual fiber strands slipping against each other. Therefore, the energy dissipation in the reinforcement adds to that of the elastomer. The practical advantage of this phenomenon is that it is possible to consider an additional amount of dissipation. Thus, it is not necessary to elaborate any special rubber compound when designing high damping RR-FRBs.

- x) As predicted by FEAs, the experimental campaign demonstrated that it is of fundamental importance, when design RR-FRBs, the investigation of the frictional behavior at the contact surfaces. With low values of vertical load, and/or low friction, the isolators would slip without deforming in shear. The frictional behavior at the interfaces fiber-steel and recycled rubber-steel is therefore derived, and the results are discussed in Chapter 7.

The study of an isolated building (Chapter 8) demonstrates that RR-FRBs can be an excellent choice in protecting buildings from strong earthquakes. They are capable to reduce the base shear (Figure 8.27), the interstory-drifts (Figure 8.23 and Figure 8.26), and the floor accelerations (Appendix E), providing good performances in terms of collapse prevention, damage to non structural elements and serviceability after major earthquakes. The performances of RR-FRBs are generally as good as those of conventional devices.

Anyway, it is important to mention that, as for all rubber seismic devices, possible periods of isolation and maximum allowed displacements are strictly connected to the applied vertical load. In RR-FRBs, since the bearings are not bonded, the geometry of each device is fixed by the friction coefficient at the interface with the upper and lower structure and by the stability criteria under a given vertical load and horizontal displacement. This causes the principal drawback of the FRBs technology. In fact, a minimum vertical load value has to be provided to the devices otherwise the bearing will slip without deforming in shear. Very light structures could not obtain a significant benefit from FRBs isolation.

This dissertation gives a large amount of information for the design of RR-FRBs as seismic isolators. Performances, limits of applicability, and design criteria are widely investigated. It is deemed that this research effort is a significant contribution for the real application of this low-cost technology on a large scale. The obtained results are of great significance, not only for developing countries, but also for all historic Italian downtowns mainly characterized by masonry buildings. Some of these structures can be highly

vulnerable even in case of a moderate seismic event. It is a hope of the author that massacres as that of the Italian cities of Polla (near Salerno) or L'Aquila (Figure 9.1), which have shown conditions unchanged for centuries, could be significantly contained by applications of a robust and low-cost technology.



a) *Polla, Italy, after the Great Neapolitan earthquake, (Lithograph, London, Mallet R 1862)*



b) *Aerial view of collapsed buildings around L'Aquila, Italy April 6, 2009*

Figure 9.1 Collapses of old buildings after two major Italian earthquakes.

9.3 RECOMMENDATIONS FOR FUTURE RESEARCH

The thesis is part of a wider investigation, and further research is already planned to provide more insight into the subject. Other topics that could be addressed are reported in the following.

- a) Cyclic tests herein performed (Appendix A) were not failure oriented. Degradation and long term performances of these materials have to be investigated with an appropriate experimental campaign. This aspect is of fundamental importance. In fact, seismic isolation devices are designed for a life at least of fifty years, and must remain functional over a broad range of ambient temperatures and weather conditions.

- b) Constitutive models for the recycled elastomers could be developed and compared to laboratory results.
- c) The response under bidirectional excitation of bearings of different shapes needs to be evaluated.
- d) The response to near-fault ground motions (pulse effects and high vertical component content) deserves consideration.
- e) Shake Table studies on building prototypes isolated with RR-FRBs could provide empirical evidence of their effectiveness, as well as allowing the study of additional phenomena at a larger scale.
- f) A special effort should be done to frame the use of RR-FRBs in current seismic codes. For instance, in the Italian seismic code [NTC 2008] the use of recycled elastomers for seismic isolators is not specifically neglected, but a technical bulletin [UNI 6065 2001] for structural bearings does not allow their use. One of the possible solutions for this problem would be to consider RR-FRBs as bearings “for the collapse prevention” thus dividing the seismic devices in different capacity ranges. Realistically, with more studies conducted on these devices, it is possible to fully address this issue. Such effort would be justified, as the proposed isolators seem a promising and low-cost technology for seismic risk prevention.

9.4 CURRENT DEVELOPMENTS

Currently, further research development is in progress together with other institutions. Several hybrid simulations on RR-FRBs are planned and are going to be performed in collaboration with Dr. Salvatore Strano from the Department of Mechanical Engineering of the University of Naples Federico II. The first hybrid simulation results have been presented [Calabrese *et al.* 2013] and other test are scheduled in the near future. Another aspect that is currently studied is the fire resistance of RR-FRBs bearings. Dr. Alan Muhr at TARRC is conducting this research as fire performances are crucial for seismic isolators, and rubber bearings deserve a particular consideration. A RELUIS research project (ReLUIIS-DFC 2009-2012 TASK 2.3.2) will investigate the behavior of scaled prototype buildings isolated with RR-FRBs. Shake Table tests of two-story models are being programmed at this time. It is therefore envisaged that these programs will contribute to a broader description of the system and will help to its larger acceptance in the society and in the construction industry.

REFERENCES

- Almazan JL, De la Llera JC, Inaudi JA (1998). Modeling aspects of structures isolated with the friction pendulum system, *Earthquake Engineering & Structural Dynamics*, Vol. 27, No. 8, 845–867.
- ASTM D412 (2006). Standard test methods for vulcanized rubber and thermoplastic elastomers — tension, ASTM International, West Conshohocken, PA, USA.
- Becker TC, Mahin SA (2012). Experimental and analytical study of the bi-directional behavior of the triple friction pendulum isolator, *Earthquake Engineering & Structural Dynamics*, Vol. 41, No. 3, 355–373.
- Brown R (2006). *Physical testing of rubber*, 4th ed., Springer–Verlag, London.
- Caltrans (1994). *The Caltrans guidelines bridge memo to designers*, Sacramento, CA, USA.
- Calabrese A, Kelly JM, Onorii C, Serino G (2011). Theoretical and experimental analysis of recycled rubber bearings with a flexible reinforcement for developing countries, 7th World Congress on Joints, Bearings and Seismic Systems for Concrete Structures, Las Vegas, Nevada, USA.
- Calabrese A, Serino G, Strano S, Terzo M (2013). Investigation of the seismic performances of an FRBs base isolated steel frame through hybrid testing, The 2013 International Conference of Mechanical Engineering, London, UK.
- Chalhoub MS, Kelly JM (1986). Reduction of the stiffness of rubber bearings due to compressibility, Rept. No. UCB/SESM–1986–06, Department of Civil Engineering, University of California, Berkeley, CA, USA.
- Chalhoub MS, Kelly JM (1990). Effect of bulk compressibility on the stiffness of cylindrical base isolation bearings, *International Journal of Solids and Structures*, Vol. 26, No. 7, 743–760.
- Christopoulos C, Filiatrault A (2006). *Principles of Passive Supplemental Damping and Seismic Isolation*, IUSS Press, Milan, Italy.

- Computers and Structures, Inc. (2012). Perform-3D v5. Nonlinear analysis and performance assessment of 3D structures, Computers and Structures, Inc. Berkeley, CA, USA.
- Constantinou MC (2004). Friction Pendulum Double Concave Bearing, Technical Report, State University of New York Buffalo, Buffalo, NY, USA.
- Dao ND, Ryan KL, Sato E, Sasaki T (2013) Predicting the displacement of triple pendulum™ bearings in a full-scale shaking experiment using a three-dimensional element, *Earthquake Engineering and Structural Dynamics*, Online Version of Record published before inclusion in an issue.
- ETRMA (2011). End of life tyres – A valuable resource with growing potential, European Tyre & Rubber Manufacturers' Association, Brussels, Belgium.
- Freyssinet, E. (1954). "Dispositif de liaison élastique à un ou plusieurs degrés de liberté", French patent No.1.110.285 Classification F06 d 25/5/54, Ministry of Industry and Commerce, France.
- Gent AN (2001). *Engineering with rubber: how to design rubber components* 2nd edition, HanserGardner Publications Inc., Cincinnati, OH, USA.
- Gent AN, Lindley PB (1959). Compression of bounded rubber blocks, *Proceedings, Institution of Mechanical Engineers*, Vol. 173, No. 1, 111–122.
- Gent AN, Meinecke EA (1970). Compression, bending and shear of bonded rubber blocks, *Polymer Engineering & Science*, Vol. 10, No 1, 48–53.
- Grant DN, Fenves GL, Auricchio F (2005). Modelling and analysis of high-damping rubber bearings for the seismic protection of bridges, *Research Report Rose 2005/01*, IUSS Press, Milan, Italy.
- Hanai T, Nakata S, Kiriya S, Fukuwa N (2004). Comparison of seismic performance of base-isolated house with various devices, *13th World Conference on Earthquake Engineering*, Vancouver, B.C., Canada.
- Herrmann LR (1965). Elasticity equations for nearly incompressible materials by a variational theorem, *The American Institute of Aeronautics and Astronautics Journal*, Vol. 3, 1896–1900.
- Iervolino I, Galasso C, Cosenza E (2010). REXEL: computer aided record selection for code-based seismic structural analysis, *Bulletin of Earthquake Engineering*, Vol. 8, No. 2, 399–362.

- Jerrams S, Sanders K, Goo KB (2001). Realistic modelling of earthquake-isolation bearings, *Journal of Materials Processing Technology*, Vol. 118, 158–164.
- Kelly JM (1991). Dynamic and failure characteristics of Bridgestone bearings, Report No. UCB/EERC–1991–04, Earthquake Engineering Research Center, University of California, Berkeley, CA, USA.
- Kelly JM (1997). *Earthquake-resistant design with rubber*, 2nd ed., Springer-Verlag, London, UK.
- Kelly JM (1999). Analysis of fiber-reinforced elastomeric isolator, *Journal of Seismology and Earthquake Engineering*, Vol. 2, No. 1, 19–34.
- Kelly JM (1999). The role of damping in seismic isolation, *Earthquake Engineering & Structural Dynamics*, Vol. 28, No. 1, 3–20.
- Kelly JM (2008). Analysis of the run-in effect in fiber-reinforced isolators under vertical load, *Journal of Mechanics of Materials and Structures*, Vol. 3, No. 7, 1383–1401.
- Kelly JM, Calabrese A (2012). *Mechanics of Fiber Reinforced Bearings*, Report No. PEER 2012-101, Pacific Earthquake Engineering Research Center, University of California, Berkeley, CA, USA.
- Kelly JM, Calabrese A, Serino G (2012). Design criteria for fiber reinforced rubber bearings, 15th World Conference on Earthquake Engineering, Lisbon, Portugal.
- Kelly JM, Konstantinidis D (2011). *Mechanics of rubber bearings for seismic and vibration isolation*, John Wiley & Sons Ltd., Chichester, UK.
- Kelly JM, Quiroz E (1990). Testing and evaluation of CEGB isolation system, UCB/EERC–1990–04, Earthquake Engineering Research Center, University of California, Berkeley, CA, USA.
- Kelly JM, Takhirov SM (2002). Analytical and experimental study of fiber-reinforced bearings, Report No. UCB/PEERC–2002–11, Pacific Earthquake Engineering Research Center, University of California, Berkeley, CA, USA.
- Koh CG, Kelly JM (1989). Compression stiffness of bonded square layers of nearly incompressible material, *Engineering Structures*. Vol. 11, No. 1, 9–15.
- Konstantinidis D, Kelly JM, Makris N (2008). Experimental investigations on the seismic response of bridge bearings, Report No. UCB/PEERC–2008–02, Department of Civil Engineering, University of California, Berkeley, CA, USA.
- Lake GJ, Lindley PB (1967) *Ozone Attack and Fatigue Life of Rubber, Use of Rubber in Engineering*, Maclaren & Sons Ltd., London, UK.

- Makarov VM, Drozdovski VF (1991). Reprocessing of tyres and rubber wastes. Recycling from the rubber products industry, Ellis Horwood, Chichester, UK.
- Mallet R (1862). Great Neapolitan earthquake of 1857, the first principles of observational seismology as developed in the report to the Royal Society of London. 2 vols., Chapman & Hall, London, UK.
- Micelli F, Nanni A (2003). Tensile characterization of FRP rods for reinforced concrete structures, *Mechanics of Composite Materials*, Vol. 39, No. 4, 293–304.
- Mosqueda G, Withtaker AS, Fenves GL (2004). Characterization and modeling of friction pendulum bearings subjected to multiple components of excitation, *Journal of Structural Engineering*, Vol. 130, No. 3, 433–442.
- MSC Software (2000). Nonlinear finite element analysis of elastomers, Withe Paper, MSC Software Corporation, Santa Ana, CA, USA.
- MSC Software (2004). MSC Marc 2005 and MSC Marc Mentat 2005, MSC Software Corporation, Santa Ana, CA, USA.
- Naeim F, Kelly JM (1999). Design of seismic isolated structures. From theory to practice, John Wiley & Sons Inc., New York, NY, USA.
- NTC (2008). Nuove norme tecniche per le costruzioni, DM 14 gennaio 2008, *Gazzetta Ufficiale* n. 29 del 4 febbraio 2008 – Supplemento Ordinario n. 30.
- Pan P, Zamfirescu D, Nakashima N (2005). Base-isolation design practice in Japan: introduction to the post-Kobe approach, *Journal of Earthquake Engineering*, Vol. 9, No. 1, 147–171.
- Persson BNJ (2001). Theory of rubber friction and contact mechanics, *Journal of Chemical Physics*, Vol. 115, No. 8, 3830–3861.
- Robert AD (1988). Natural rubber science and technology, Oxford University Press, Oxford, UK.
- Robinson WH (1977). A lead-rubber shear damper, *Bulletin of the New Zealand National Society for Earthquake Engineering*, No. 3, 93–101.
- Robinson WH (1982). Lead-rubber hysteretic bearings suitable for protecting structures during earthquakes. *Earthquake Engineering & Structural Dynamics*. No.10, 593–604.
- Rocard Y (1973). Note sur le calcul des proprietes elastique des supports en caoutchouc adherent, *Journal de Physique et Le Radium*, Vol. 8, No. 5, 197–203.

-
- Russo G, Pauletta M. (2013). Sliding instability of fiber-reinforced elastomeric isolators in unbonded applications, *Engineering Structures*, Vol. 48, 70–80.
- Seky W, Fukahori Y, Iseda Y, Matsunaga T (1987). A large deformation finite element analysis for multilayer elastomeric bearings, *Rubber Chemistry and Technology*, Vol. 60, No. 5, 856–869.
- Simo JC, Kelly JM (1984). Finite element analysis of the stability of multilayer elastomeric bearings, *Engineering Structures*, Vol. 6, No 3, 162–174.
- Takayama M, Tada H, Tanaka R (1994). Finite element analysis of laminated rubber bearings used in base-isolation system, *Rubber Chemistry and Technology*, Vol. 65, No. 1, 46–62.
- Taniwangsa W, Kelly JM (1996). Experimental and Analytical studies of base isolation applications for low-cost housing, Report No. UCB/PEERC–1996–04, Pacific Earthquake Engineering Research Center, University of California, Berkeley, CA, USA.
- Toopchi-Nezhad H, Tait MJ, Drysdale RG (2009). Parametric study on the response of stable unbonded-fiber reinforced elastomeric isolators (SU-FREIs), *Journal of Composite Materials*, Vol. 43, No. 15, 1569-1587.
- Tsai HC, Kelly JM (2001). Stiffness analysis of fiber reinforced elastomeric isolators, Report No. UCB/PEERC–2001–05, Pacific Earthquake Engineering Research Center, University of California, Berkeley, CA, USA.
- UNI 6065 (2001) Elastomeri – Prove su gomma vulcanizzata e termoplastica – Prova di trazione.
- Zayas V, Low S, Mahin SA (1987). The FPS earthquake resisting system, Report No. UCB/EERC–1987–01, Department of Civil Engineering, University of California, Berkeley, CA, USA.

Appendix A: SHEAR TESTS ON RECYCLED RUBBER

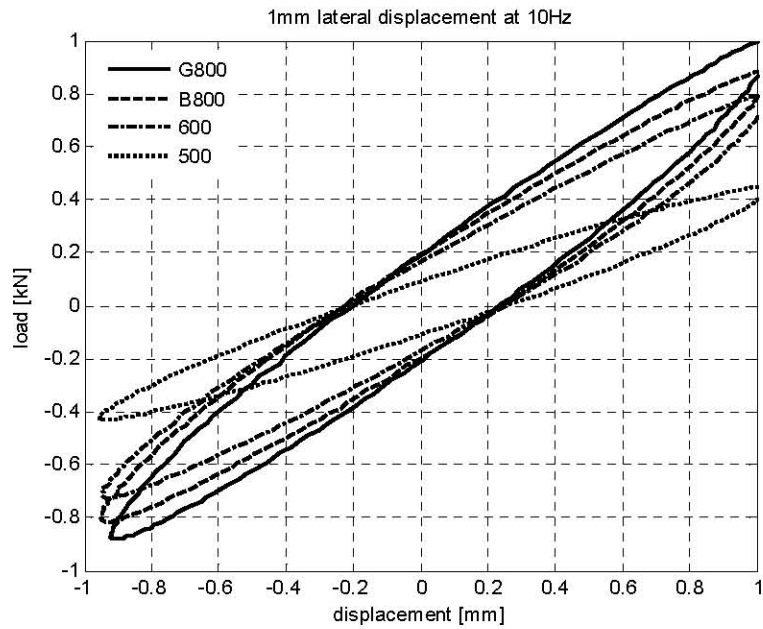


Figure A.1 Dynamic shear tests 1mm lateral displacement (10Hz).

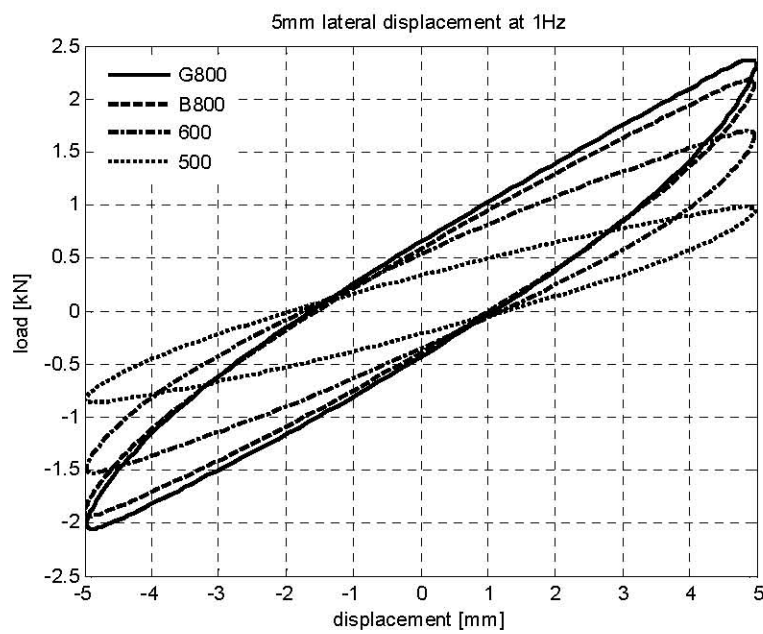


Figure A.2 Dynamic shear tests 5mm lateral displacement (1Hz).

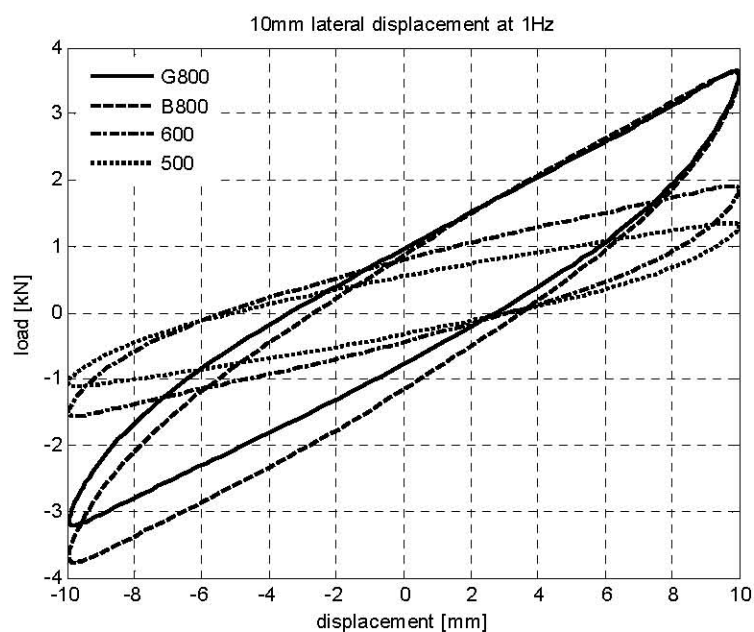


Figure A.3 Dynamic shear tests 10mm lateral displacement (1Hz).

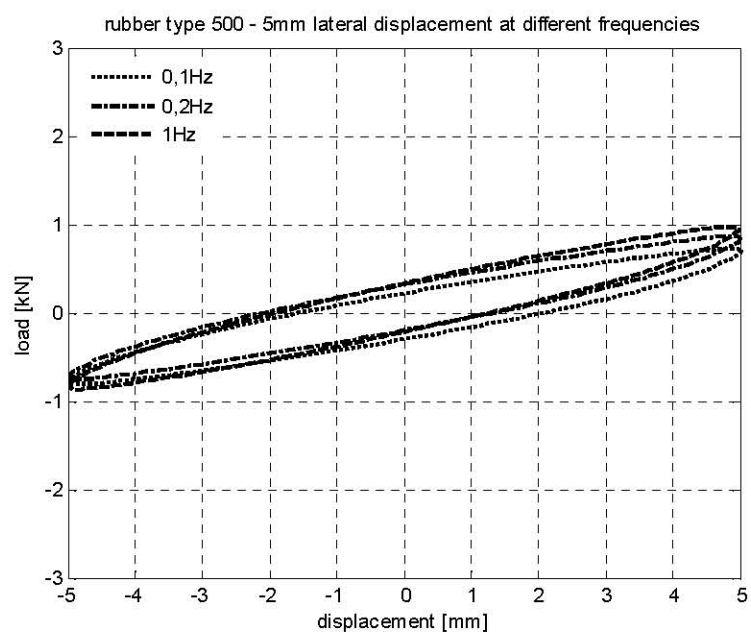


Figure A.4 Rubber type 500 – dynamic shear test results (5mm lateral displacement).

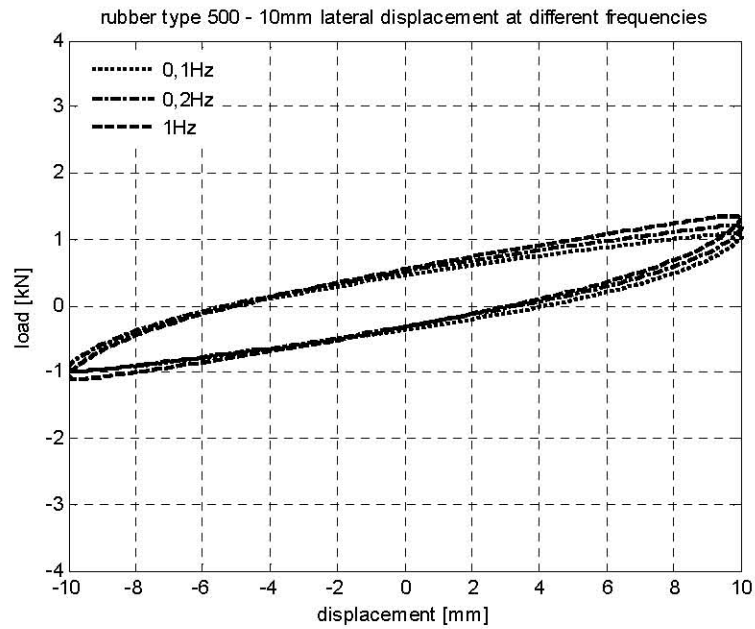


Figure A.5 Rubber type 500 – dynamic shear test results (10mm lateral displacement).

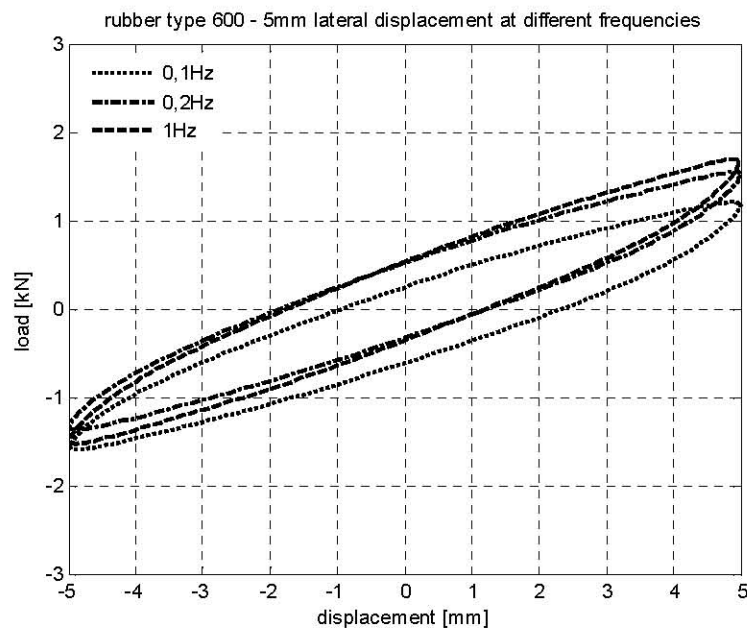


Figure A.6 Rubber type 600 – dynamic shear test results (5mm lateral displacement).

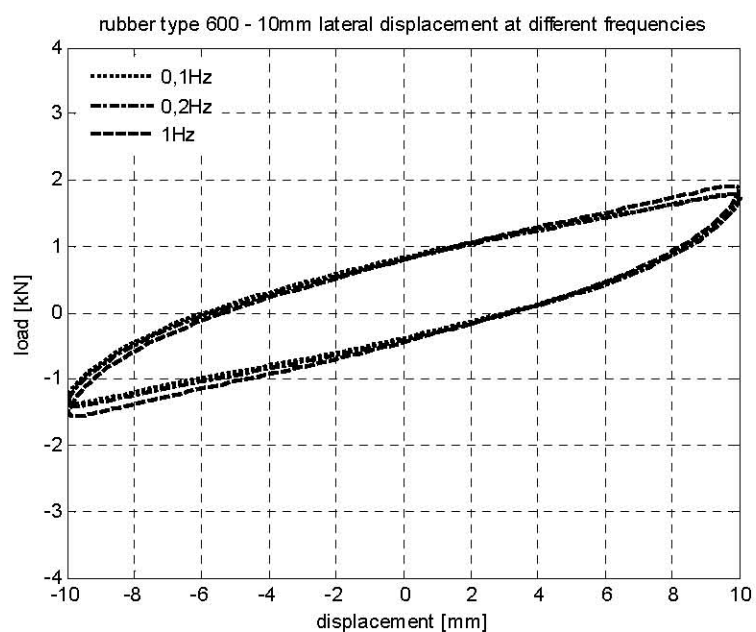


Figure A.7 Rubber type 600 – dynamic shear test results (10mm lateral displacement).

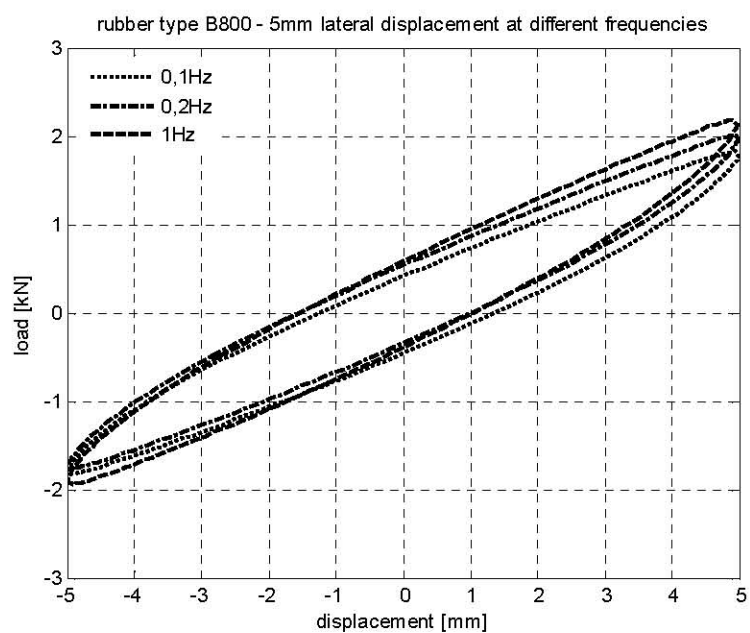


Figure A.8 Rubber type B800 – dynamic shear test results (5mm lateral displacement).

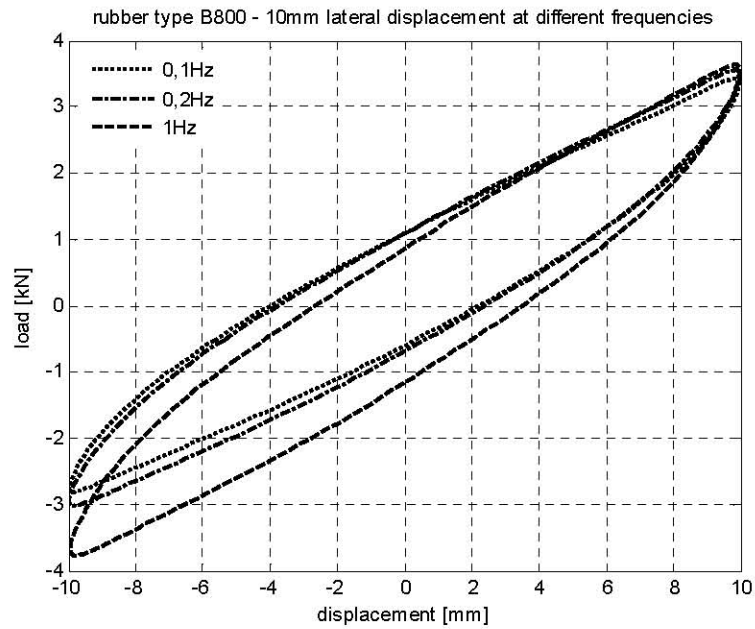


Figure A.9 Rubber type B800 – dynamic shear test results (10mm lateral displacement).

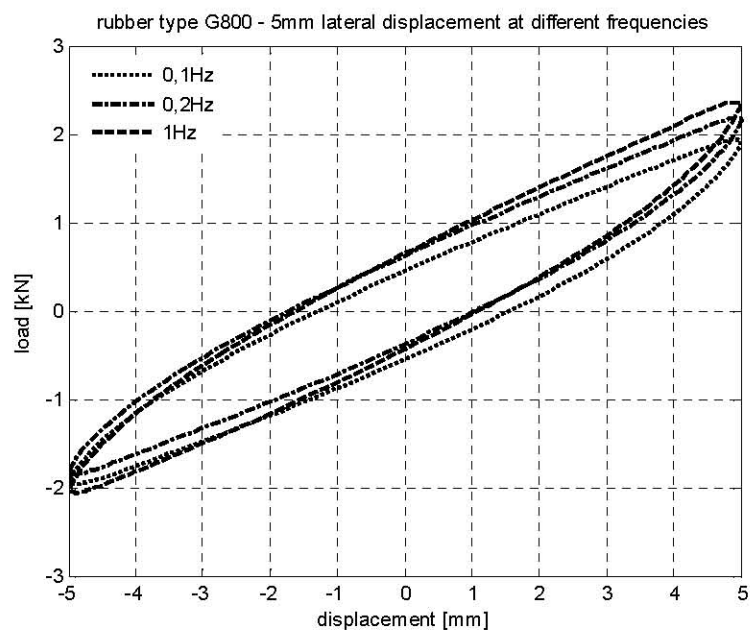


Figure A.10 Rubber type G800 – dynamic shear test results (5mm lateral displacement).

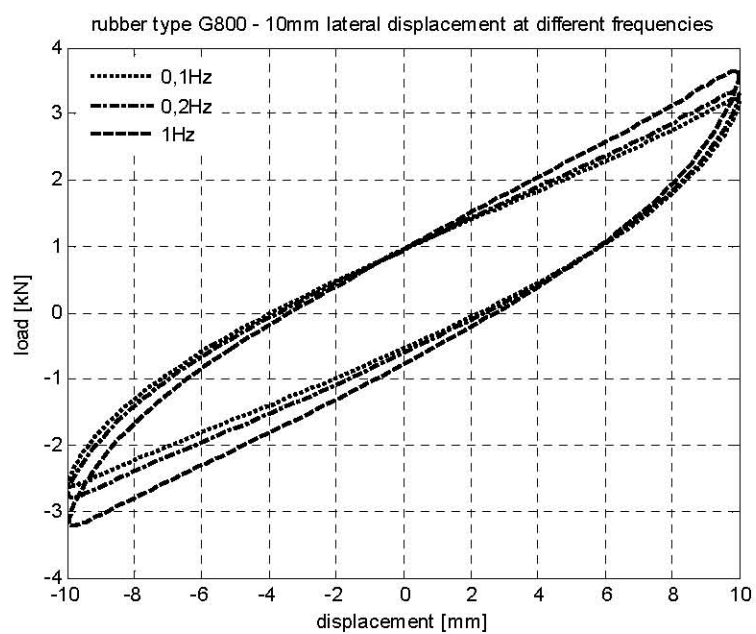


Figure A.11 Rubber type G800 – dynamic shear test results (10mm lateral displacement).

Appendix B: COMPRESSION TESTS ON RR-FRBs

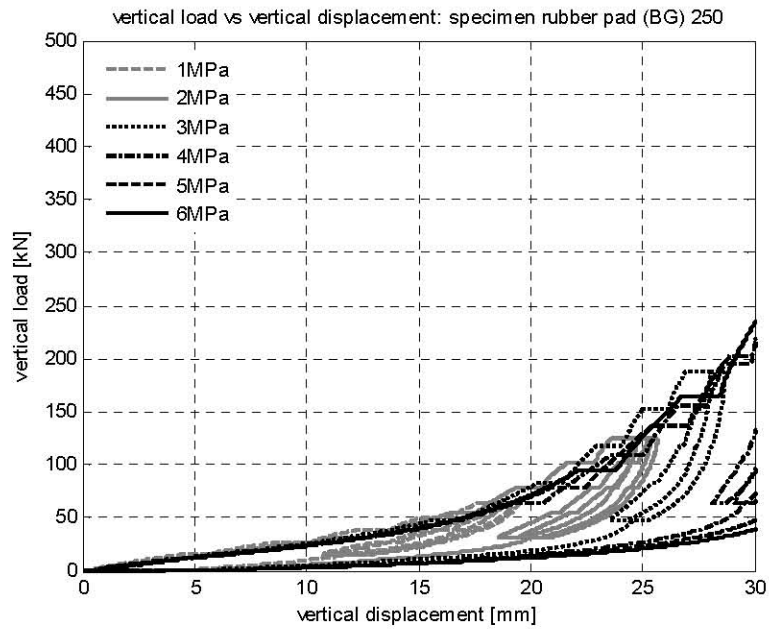


Figure B.1 Vertical test results for rpad(BG)250.

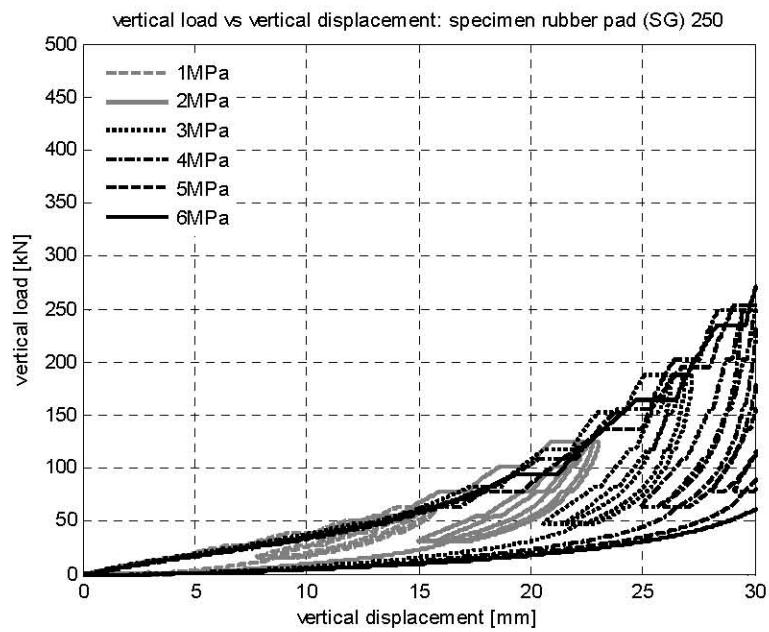


Figure B.2 Vertical test results for rpad(SG)250.

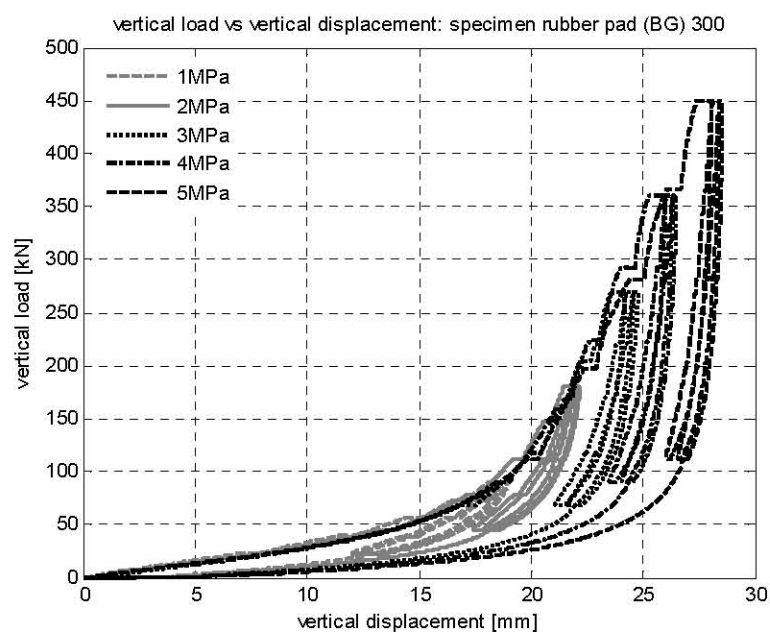


Figure B.3 Vertical test results for rpad(BG)300.

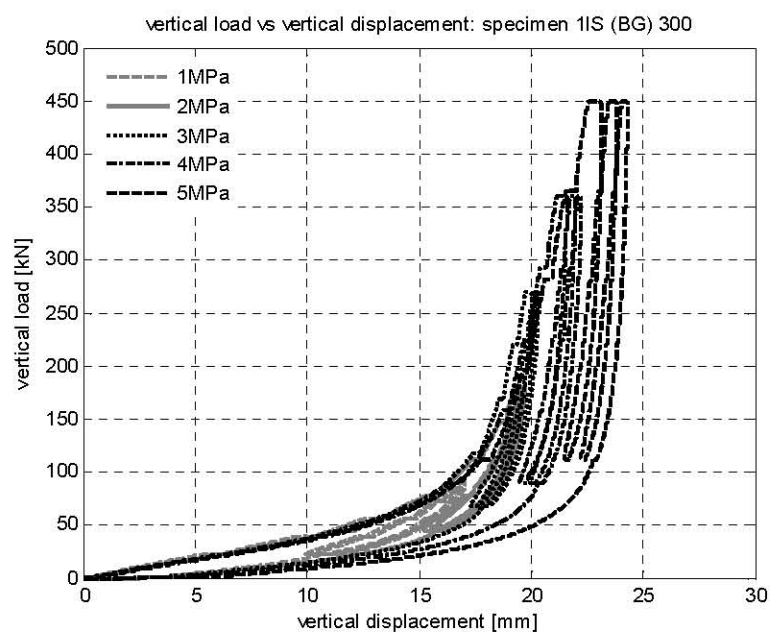


Figure B.4 Vertical test results for 1LS(BG)300.

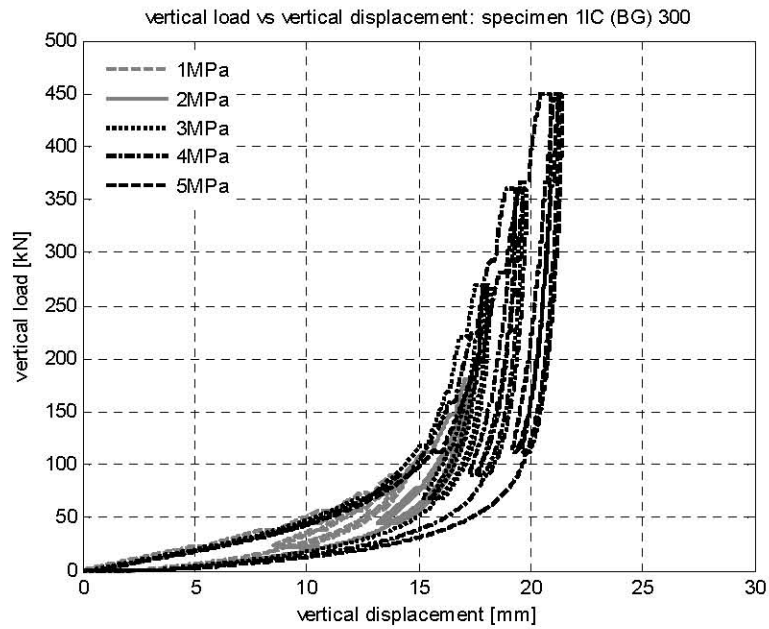


Figure B.5 Vertical test results for 1LC(BG)300.

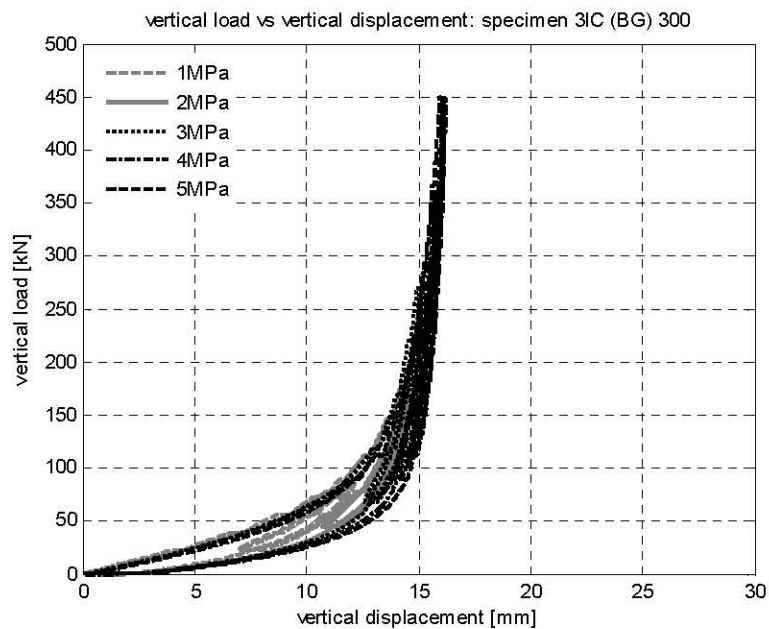


Figure B.6 Vertical test results for 3LC(BG)300.

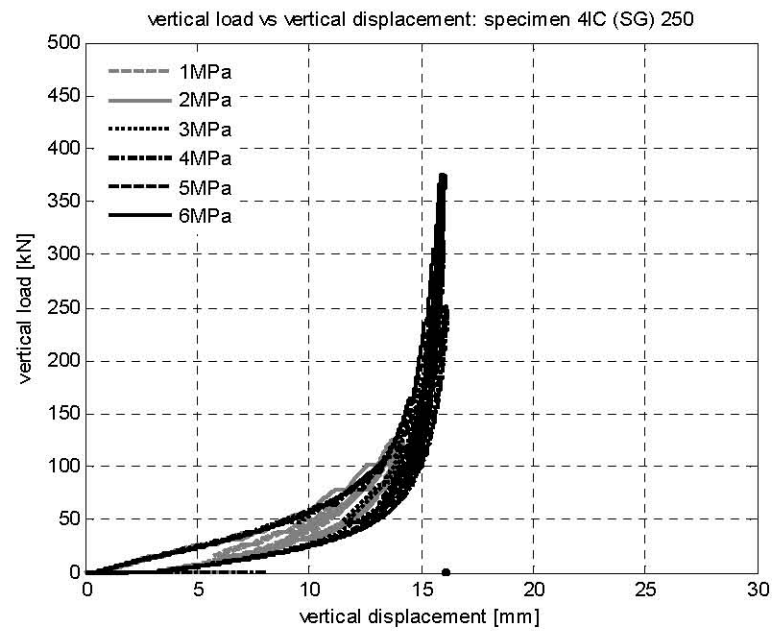


Figure B.7 Vertical test results for 4LC(SG)250.

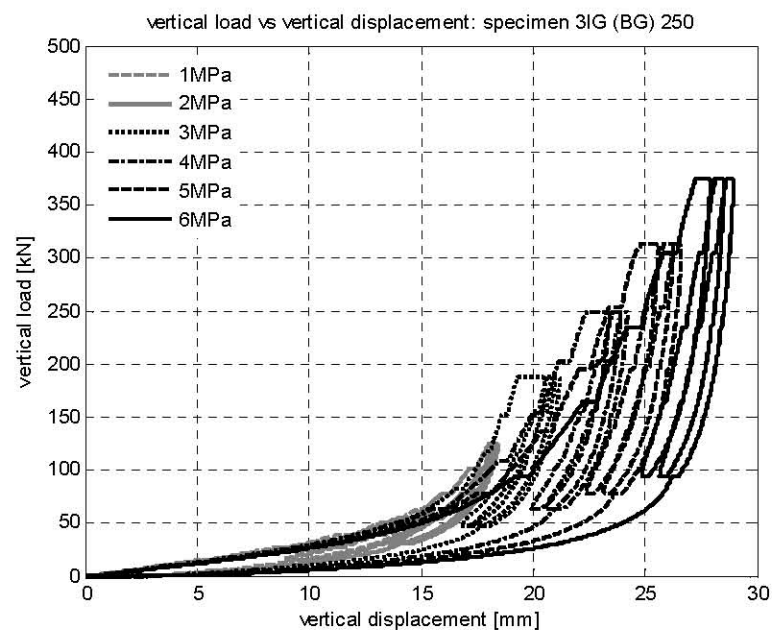


Figure B.8 Vertical test results for 3LG(BG)250.

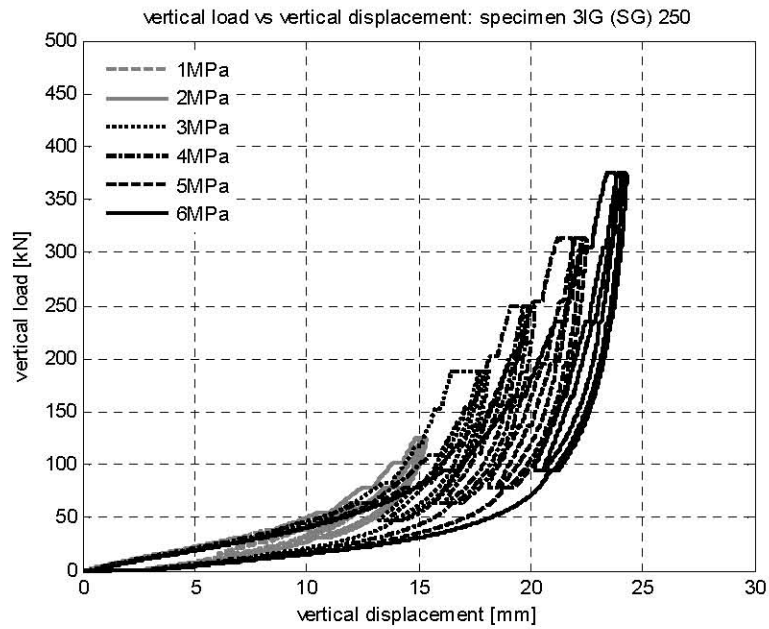


Figure B.9 Vertical test results for 3LG(SG)250.

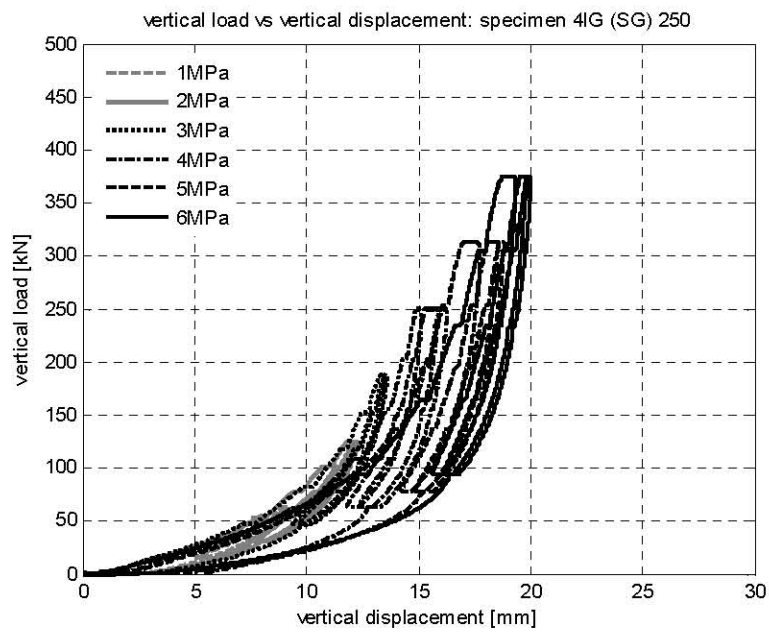


Figure B.10 Vertical test results for 4LG(SG)250.

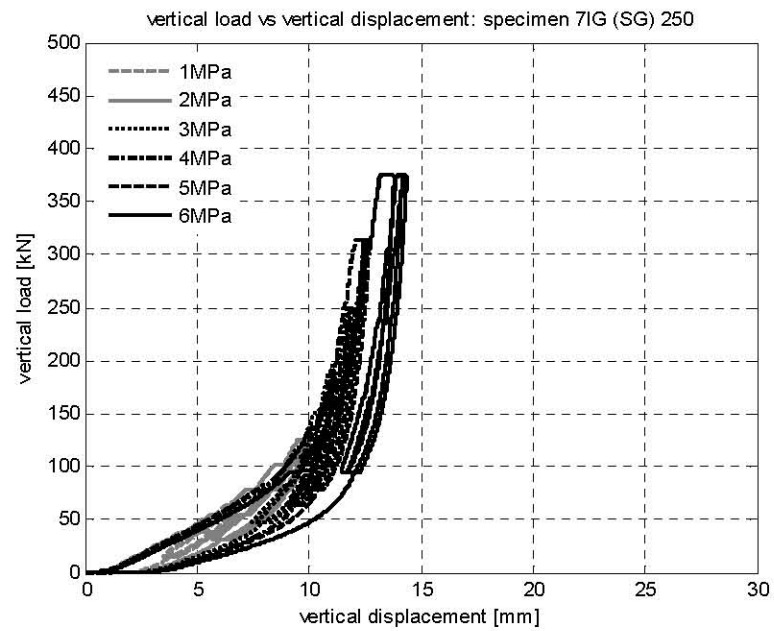


Figure B.11 Vertical test results for 7LG(SG)250.

Appendix C: SHEAR TESTS ON RR-FRBs

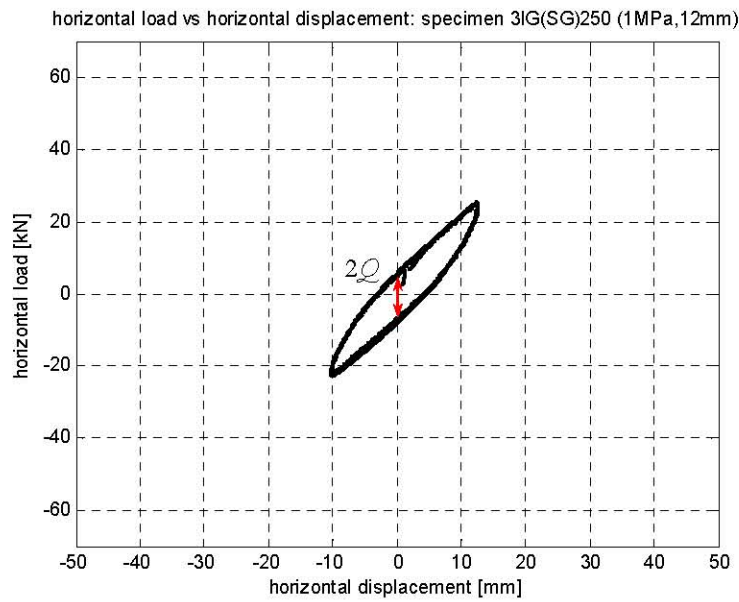


Figure C.1 Horizontal test results for 3LG(SG)250 with 1MPa vertical pressure (1st displacement sequence-12mm).

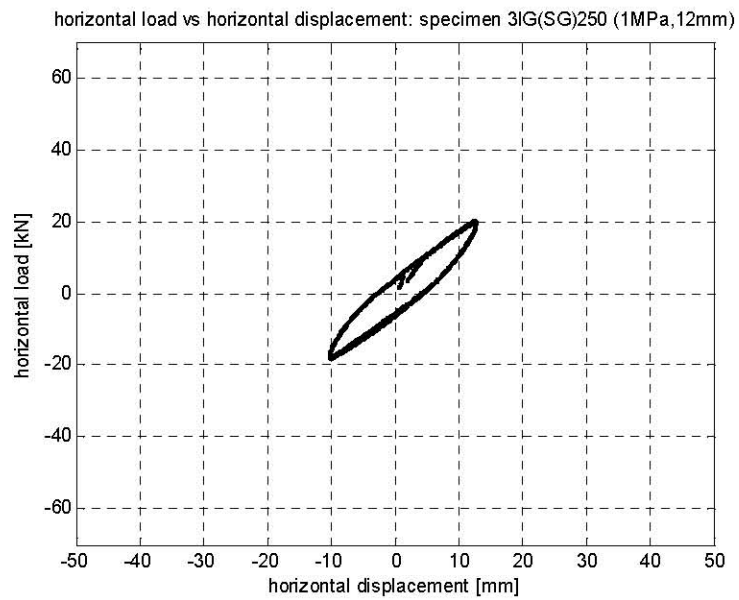


Figure C.2 Horizontal test results for 3LG(SG)250 with 1MPa vertical pressure (2nd displacement sequence-12mm).

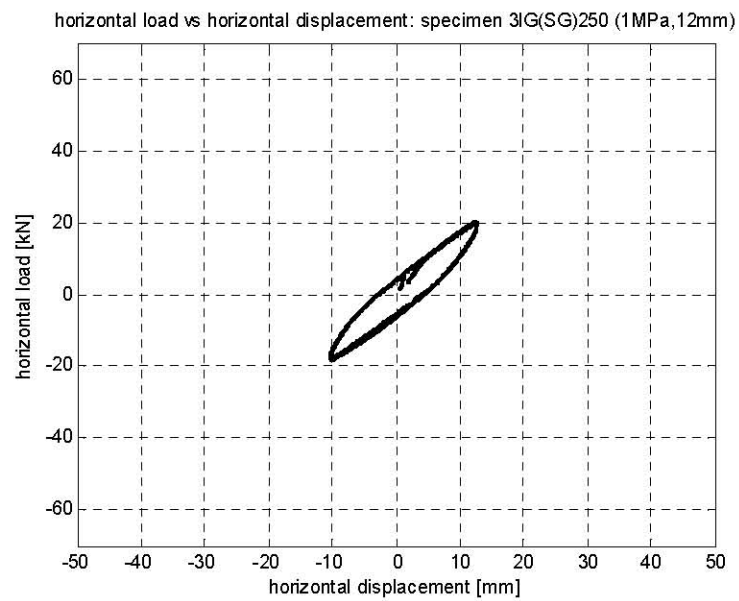


Figure C.3 Horizontal test results for 3LG(SG)250 with 1MPa vertical pressure (3rd displacement sequence-12mm).

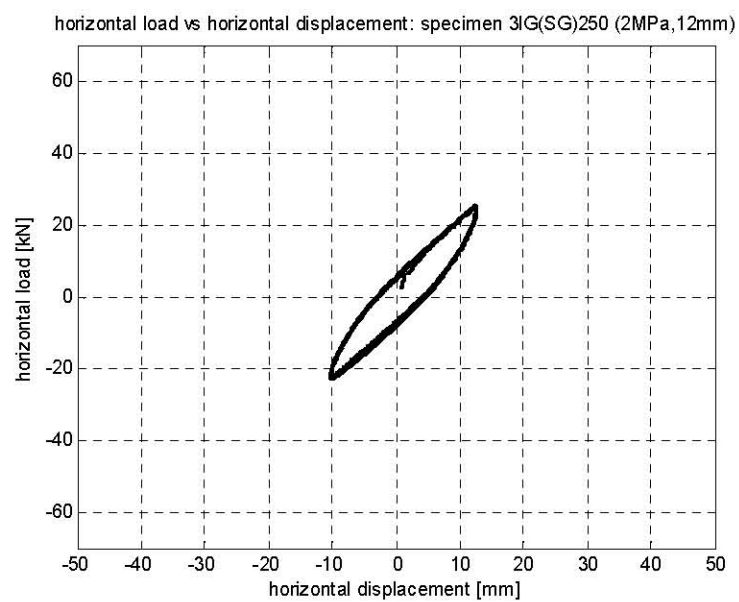


Figure C.4 Horizontal test results for 3LG(SG)250 with 2MPa vertical pressure (12mm horizontal displacement).

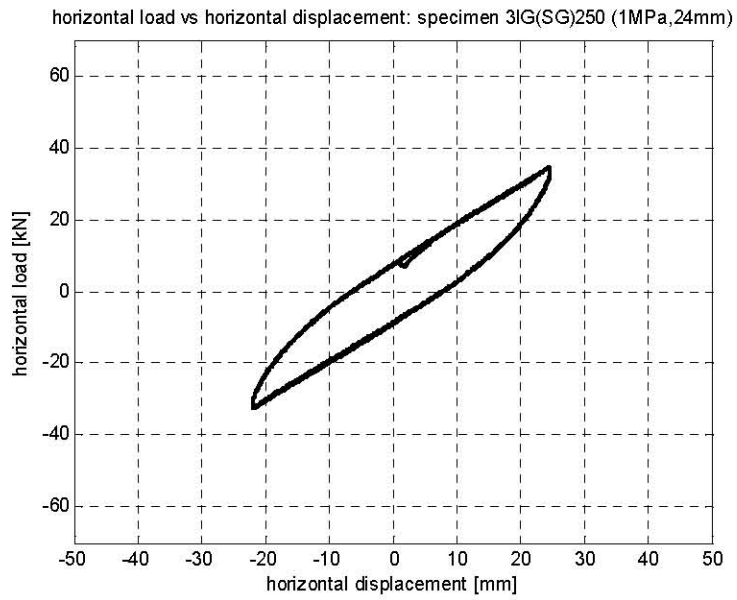


Figure C.5 Horizontal test results for 3LG(SG)250 with 1MPa vertical pressure (24mm horizontal displacement).

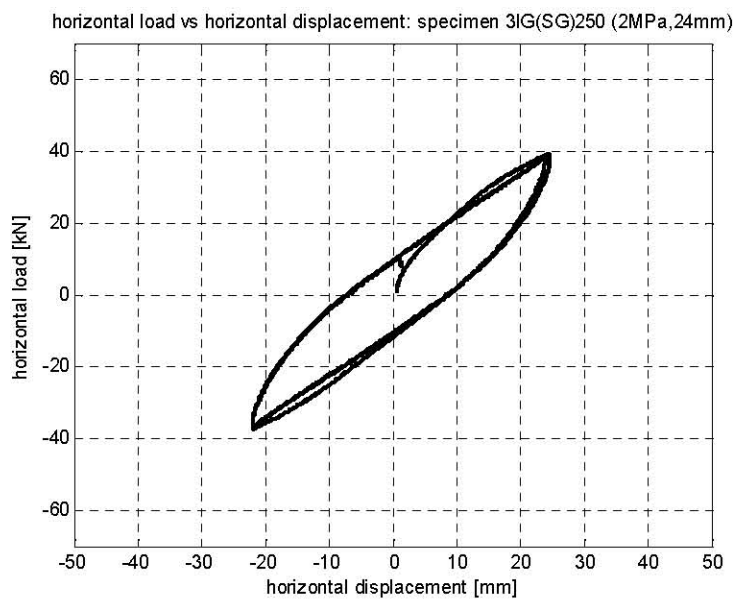


Figure C.6 Horizontal test results for 3LG(SG)250 with 2MPa vertical pressure (24mm horizontal displacement).

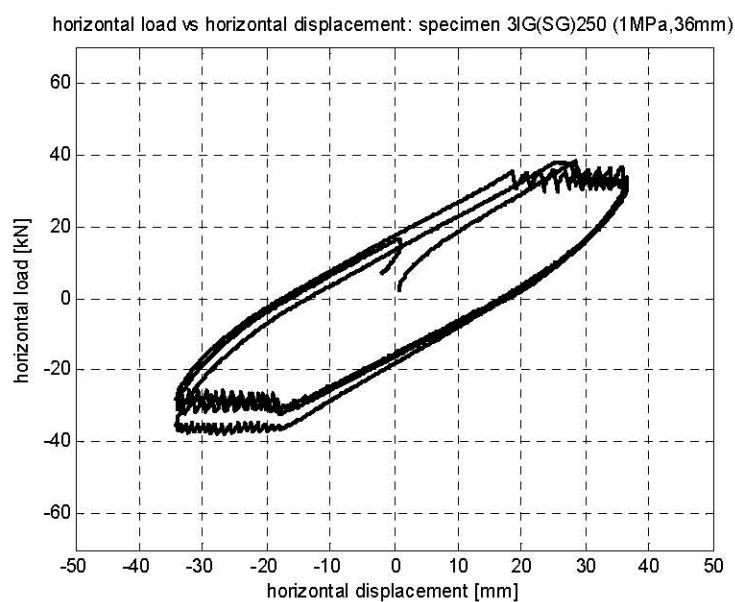


Figure C.7 Horizontal test results for 3LG(SG)250 with 1MPa vertical pressure (36mm horizontal displacement).

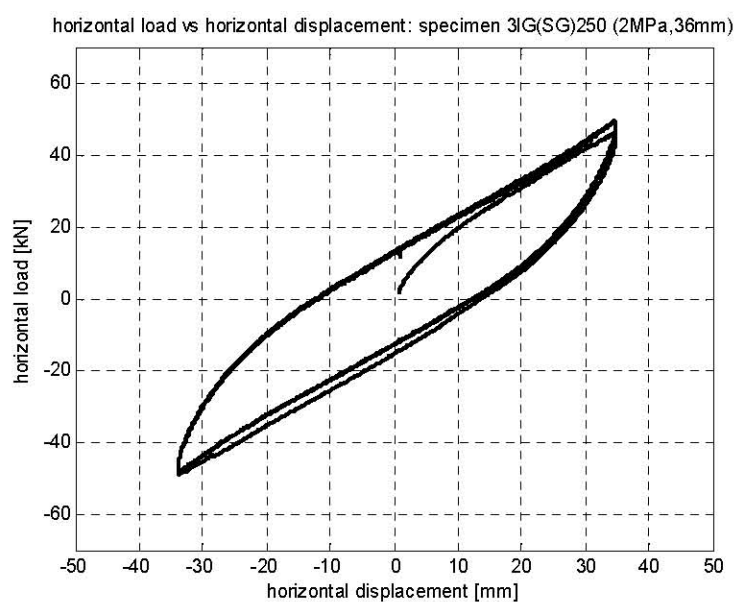


Figure C.8 Horizontal test results for 3LG(SG)250 with 2MPa vertical pressure (36mm horizontal displacement).

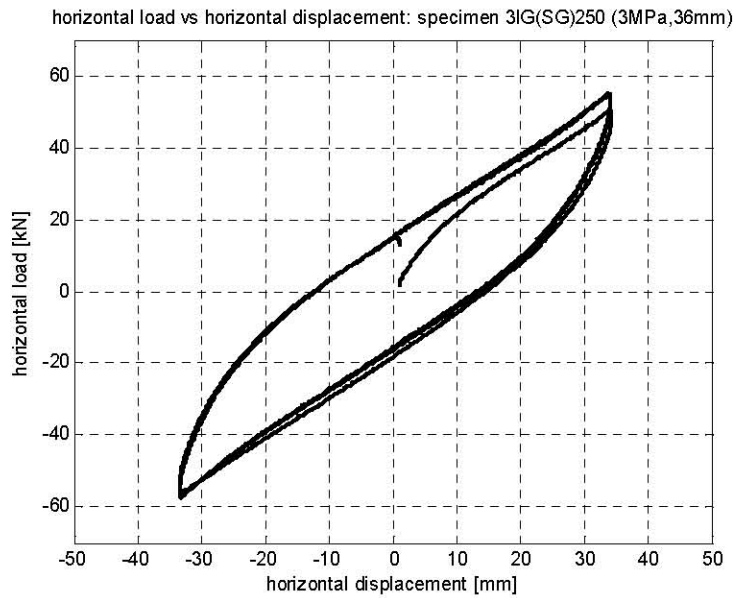


Figure C.9 Horizontal test results for 3LG(SG)250 with 3MPa vertical pressure (36mm horizontal displacement).

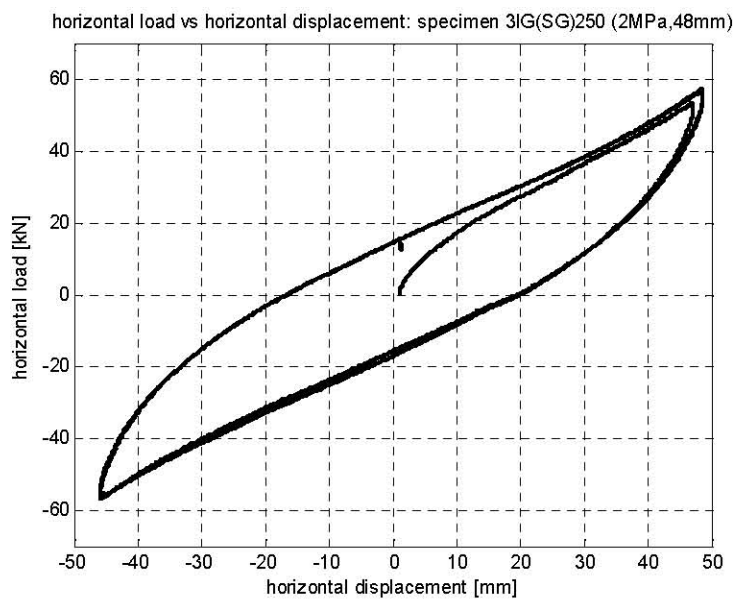


Figure C.10 Horizontal test results for 3LG(SG)250 with 2MPa vertical pressure (48mm horizontal displacement).

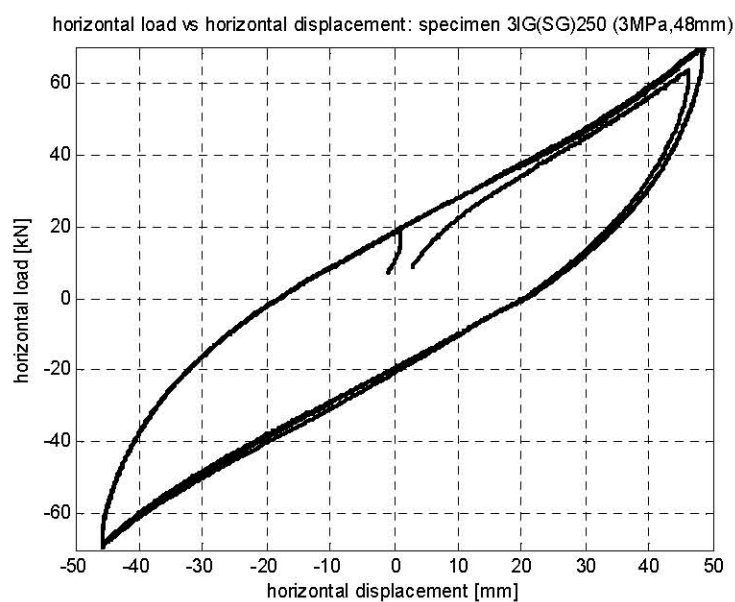


Figure C.11 Horizontal test results for 3LG(SG)250 with 3MPa vertical pressure (48mm horizontal displacement).

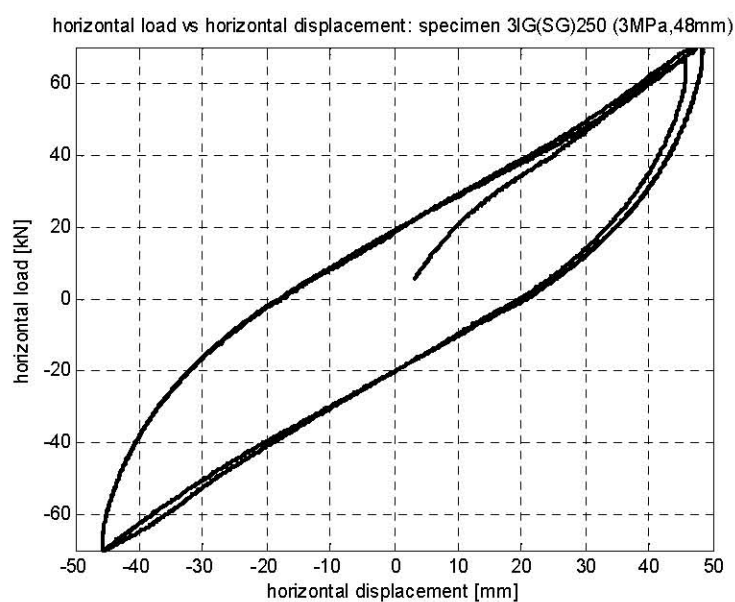


Figure C.12 Horizontal test results for 3LG(SG)250 with 3MPa vertical pressure (48mm horizontal displacement).

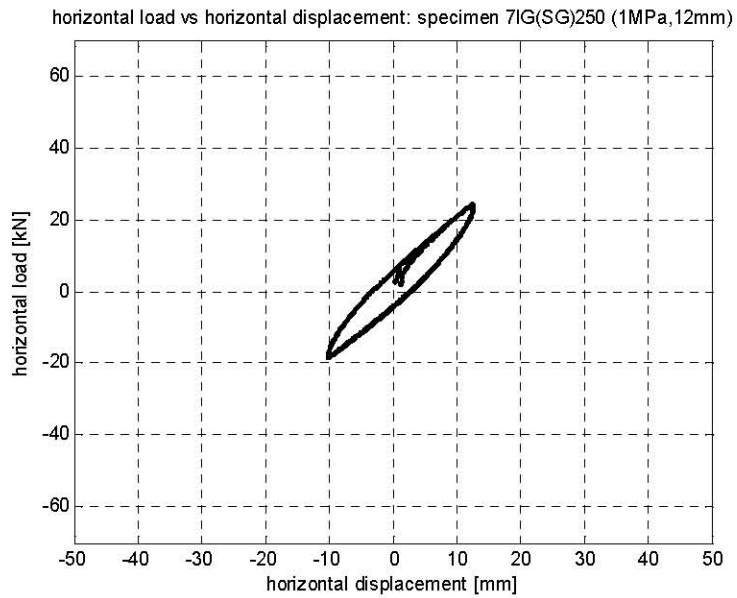


Figure C.13 Horizontal test results for 7LG(SG)250 with 1MPa vertical pressure (12mm horizontal displacement).

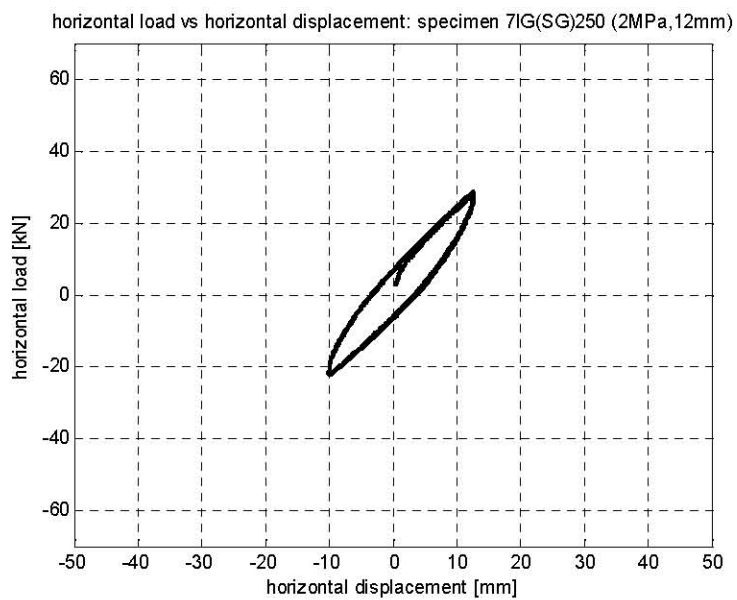


Figure C.14 Horizontal test results for 7LG(SG)250 with 2MPa vertical pressure (12mm horizontal displacement).

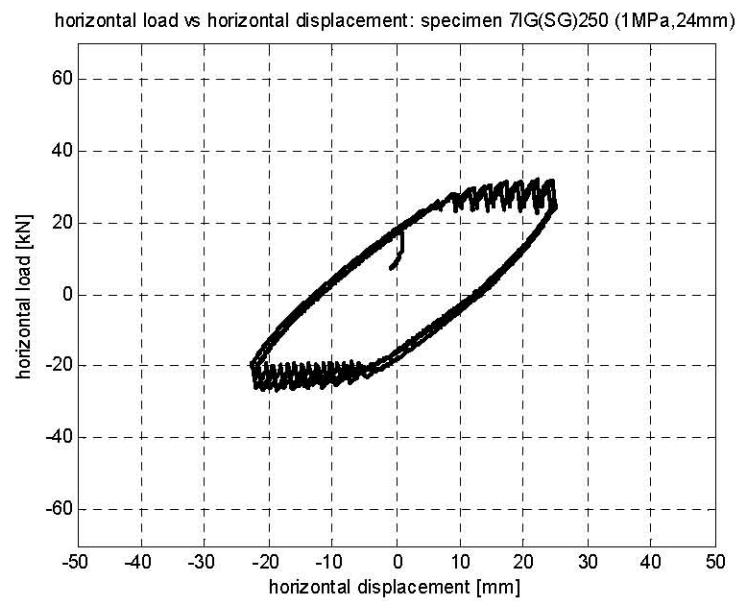


Figure C.15 Horizontal test results for 7LG(SG)250 with 1MPa vertical pressure (24mm horizontal displacement).

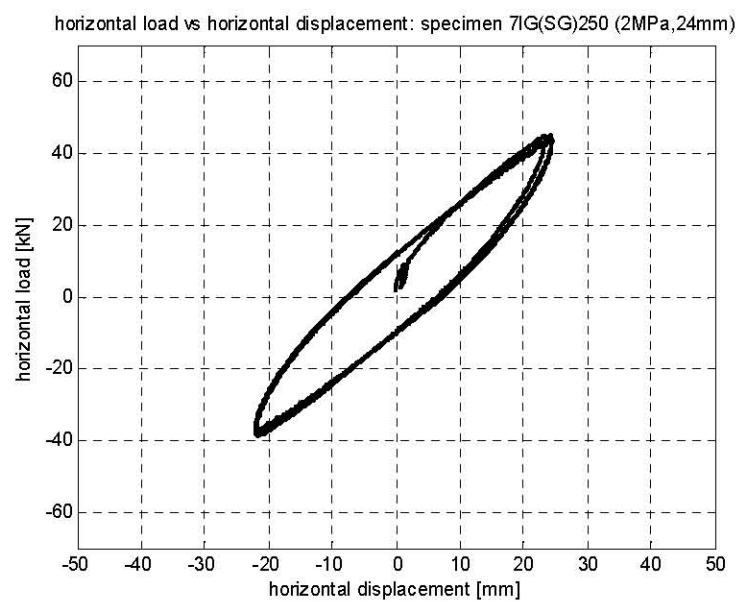


Figure C.16 Horizontal test results for 7LG(SG)250 with 2MPa vertical pressure (24mm horizontal displacement).

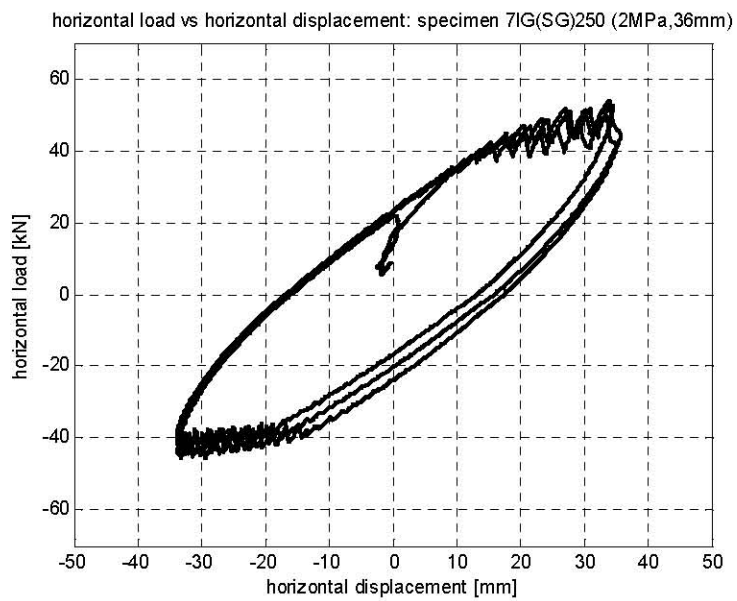


Figure C.17 Horizontal test results for 7LG(SG)250 with 2MPa vertical pressure (36mm horizontal displacement).

Appendix D: INPUT GROUND MOTIONS FOR THE ANALYSES

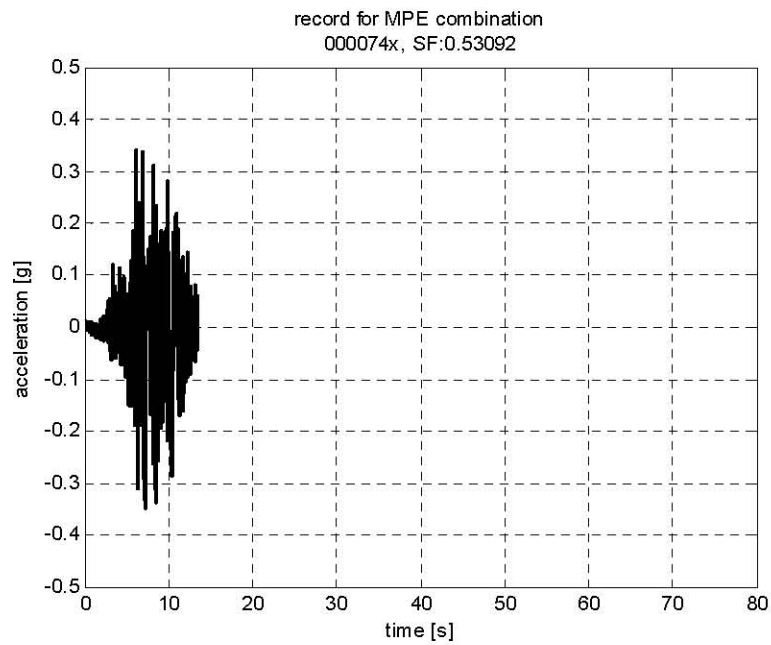


Figure D.1 MPE combination – record 000074xa, SF:0.53092

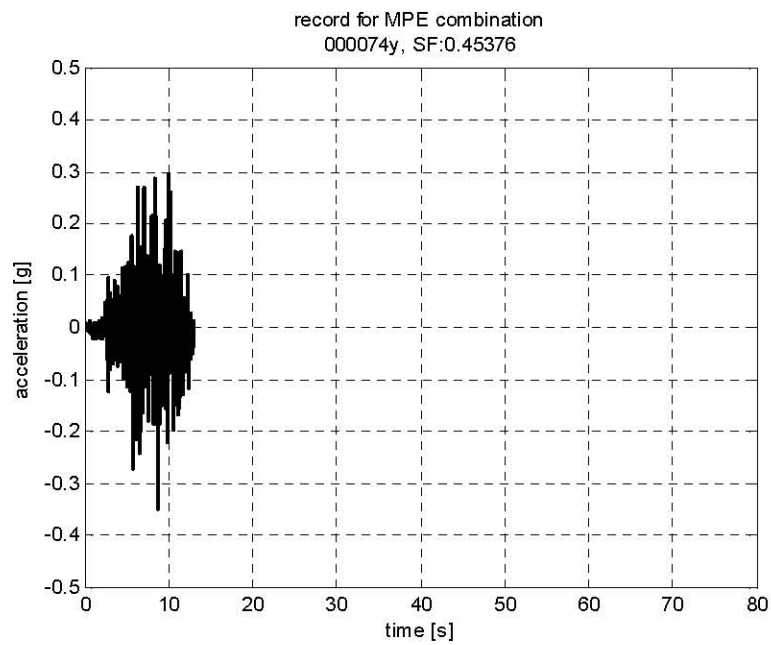


Figure D.2 MPE combination – record 000074ya, SF:0.45376

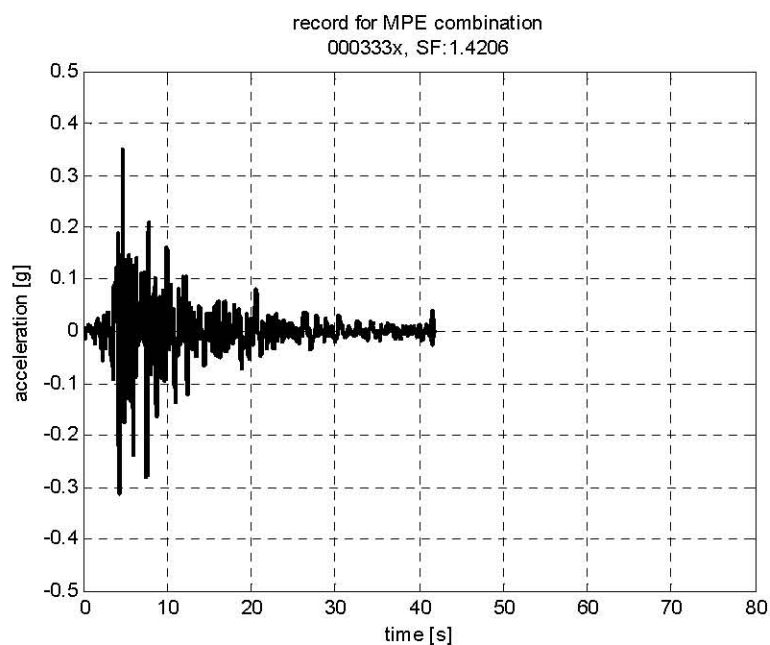


Figure D.3 MPE combination – record 000333xa, SF:1.4206

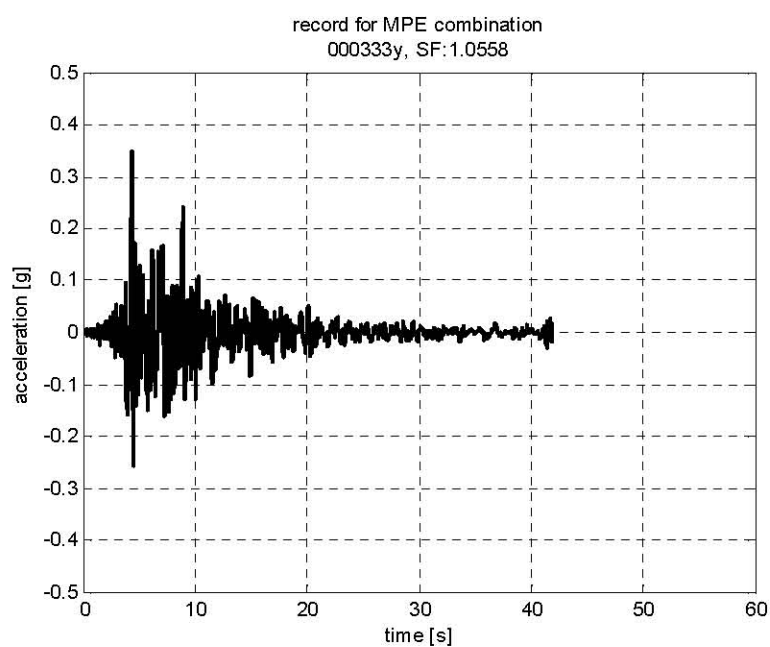


Figure D.4 MPE combination – record 000333ya, SF:1.0558

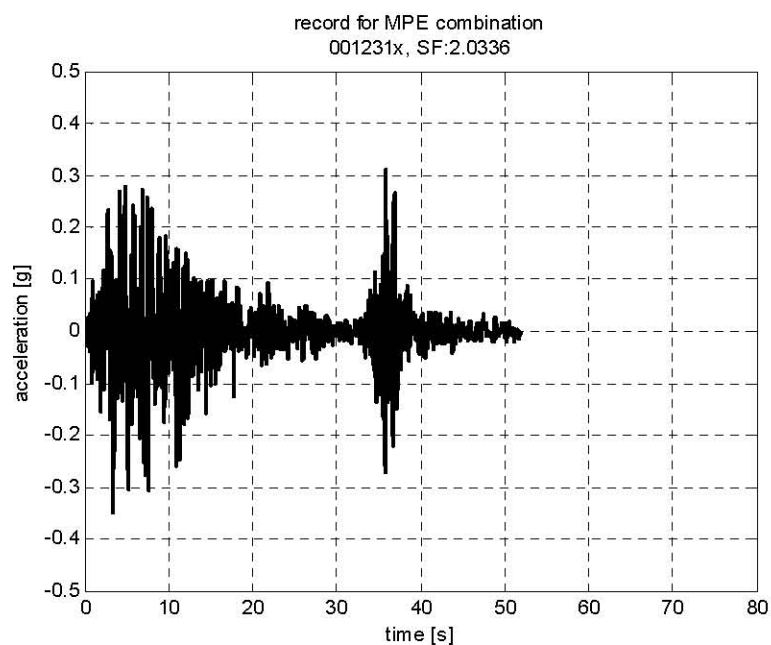


Figure D.5 MPE combination – record 001231xa, SF:2.0336

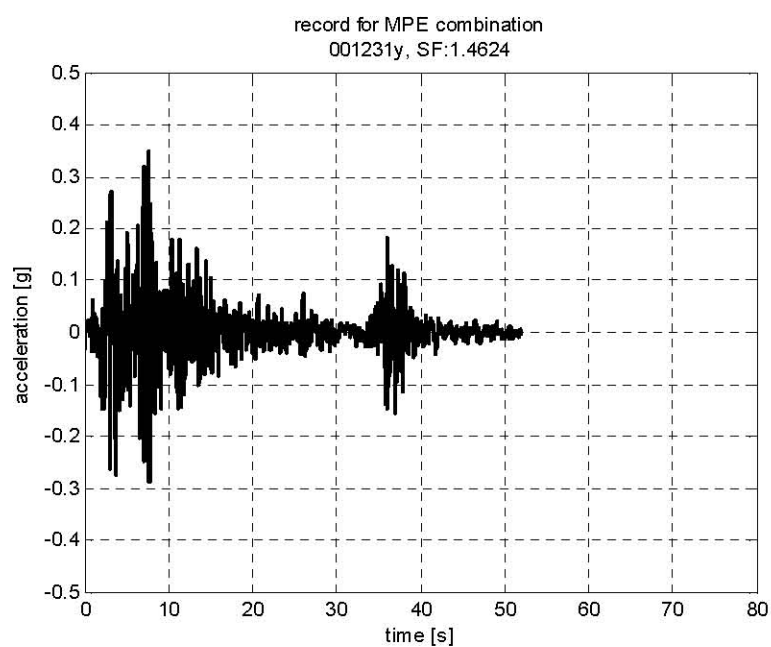


Figure D.6 MPE combination – record 001231ya, SF:1.4624

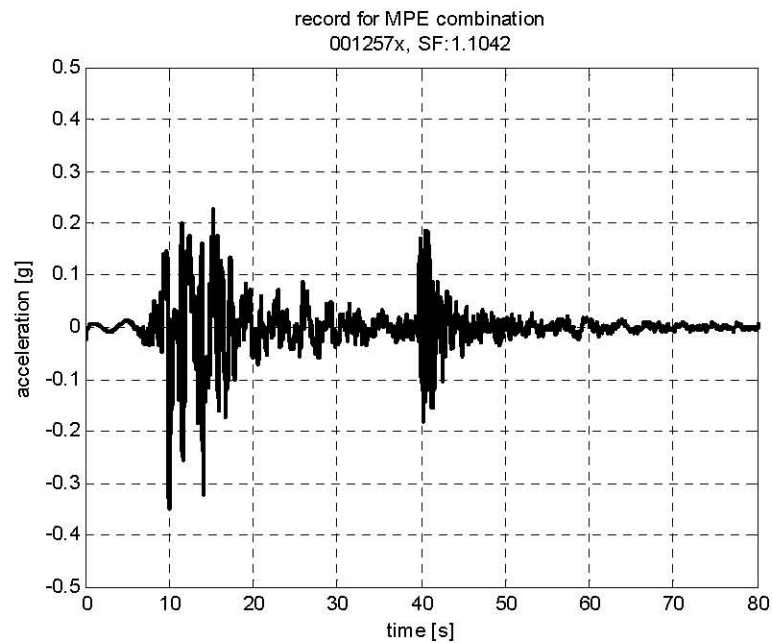


Figure D.7 MPE combination – record 001257xa, SF:1.1042

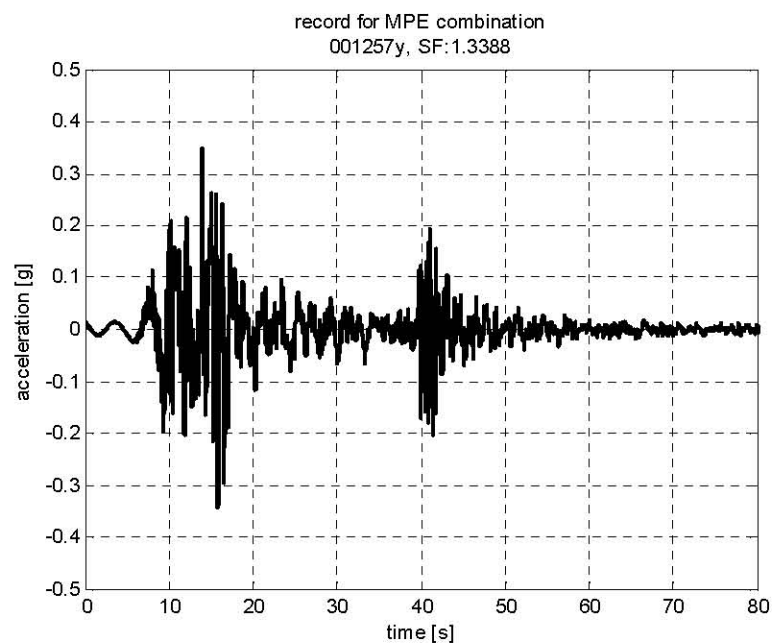


Figure D.8 MPE combination – record 001257ya, SF:1.3388

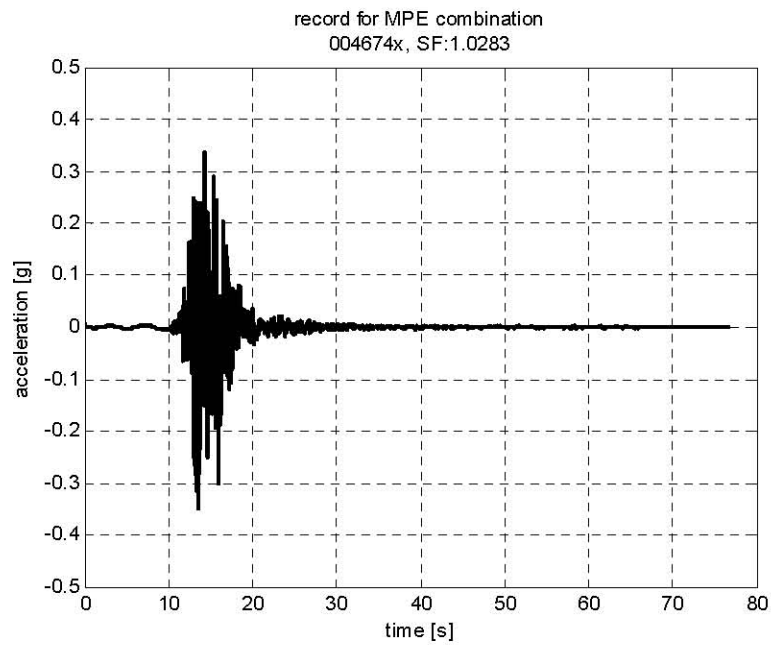


Figure D.9 MPE combination – record 004674xa, SF:1.0283

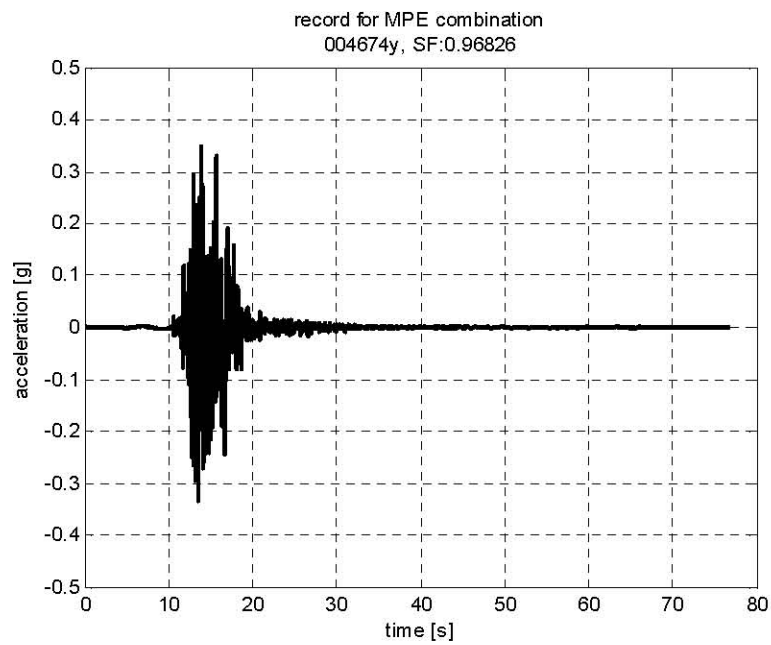


Figure D.10 MPE combination – record 004674ya, SF:0.96826

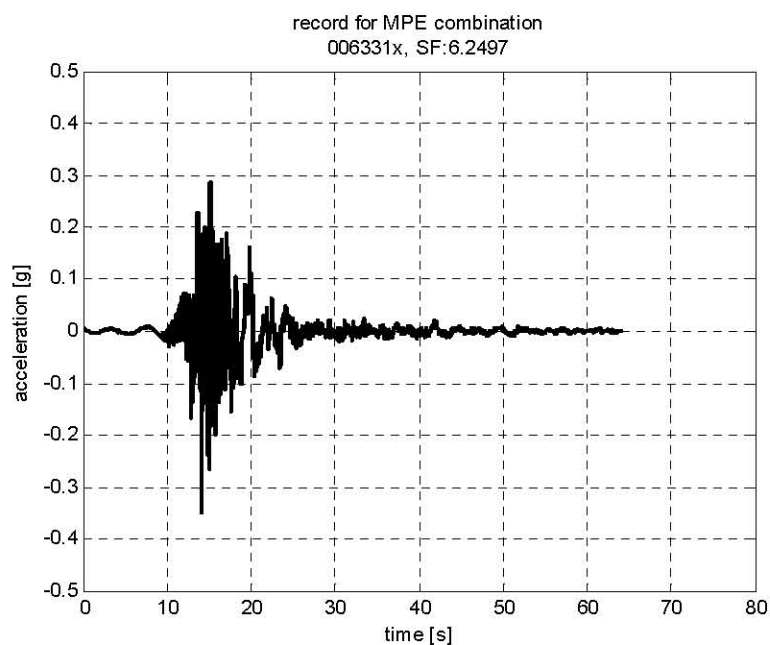


Figure D.11 MPE combination – record 006331xa, SF:6.2497

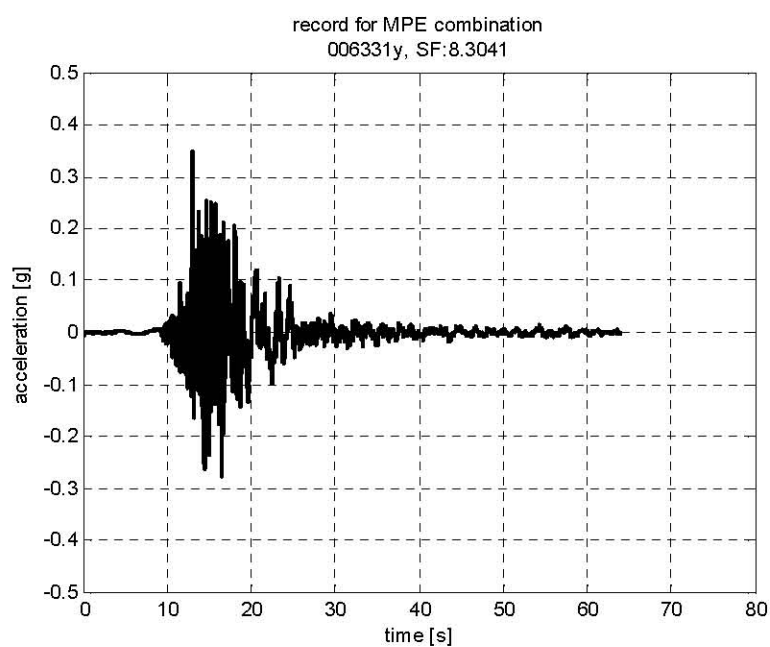


Figure D.12 MPE combination – record 006331ya, SF:8.3041

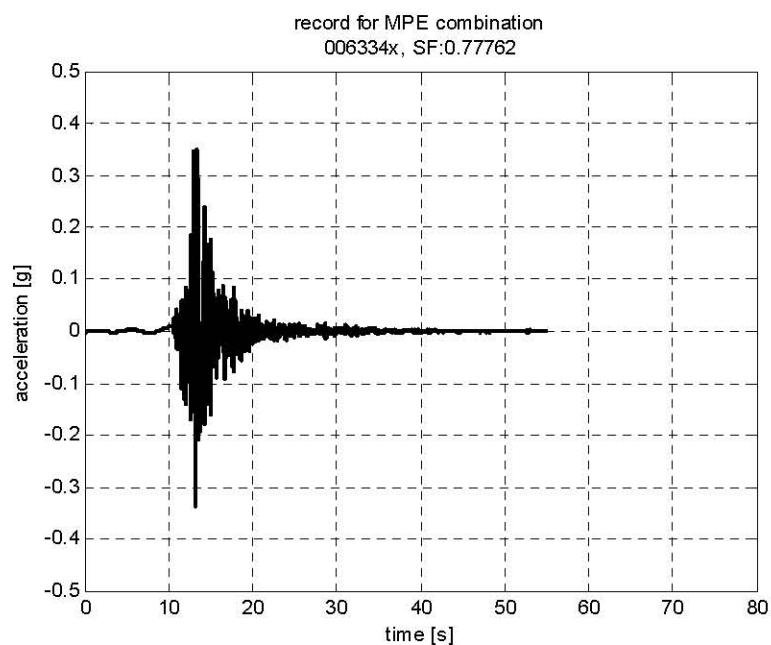


Figure D.13 MPE combination – record 006334xa, SF:0.77762

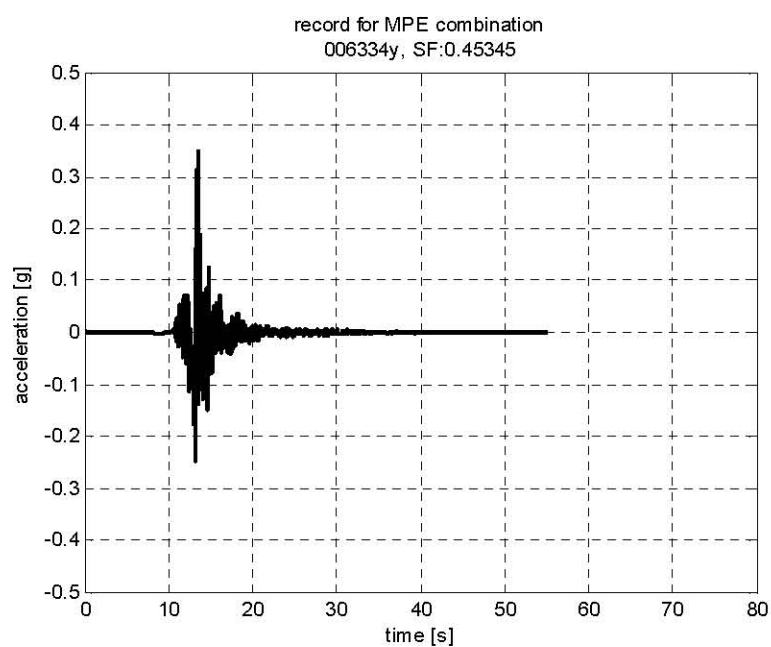


Figure D.14 MPE combination – record 006334ya, SF:0.45345

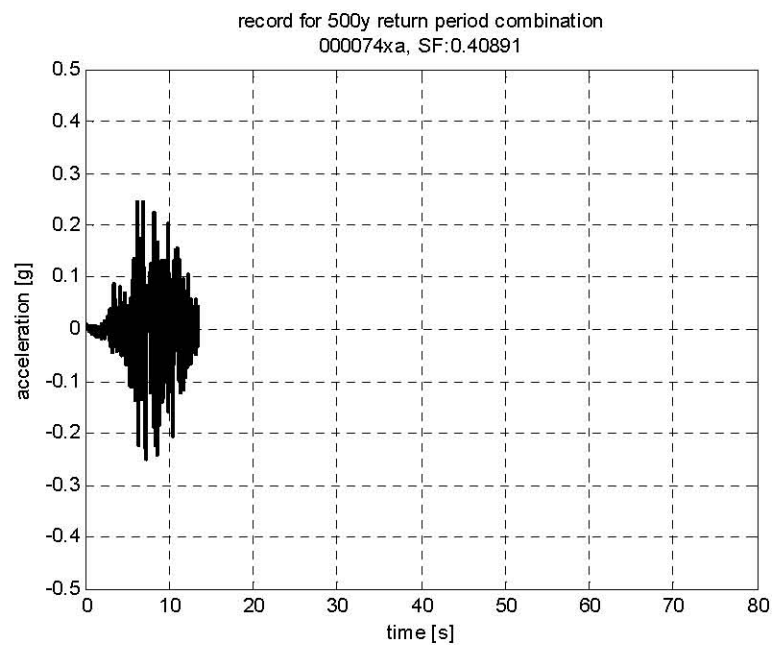


Figure D.15 500yrs combination – record 000074xa, SF:0.40891

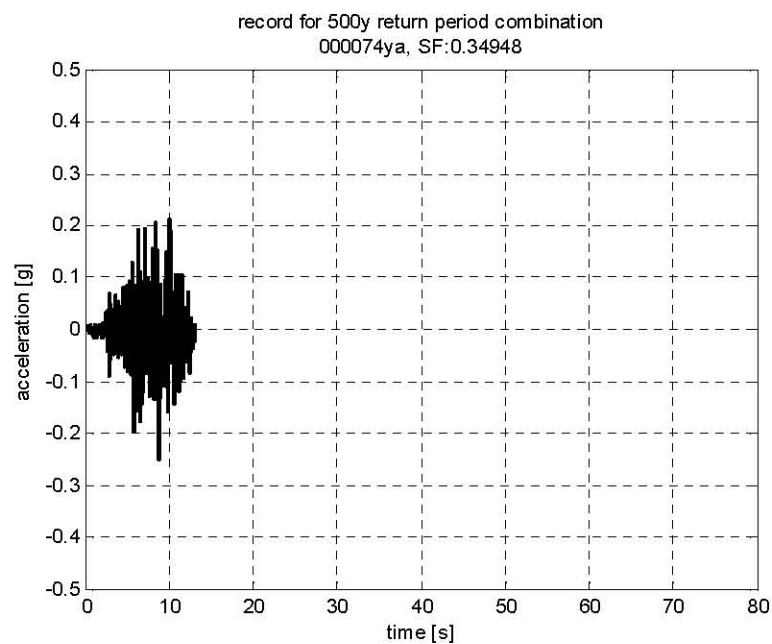


Figure D.16 500yrs combination – record 000074ya, SF:0.34948

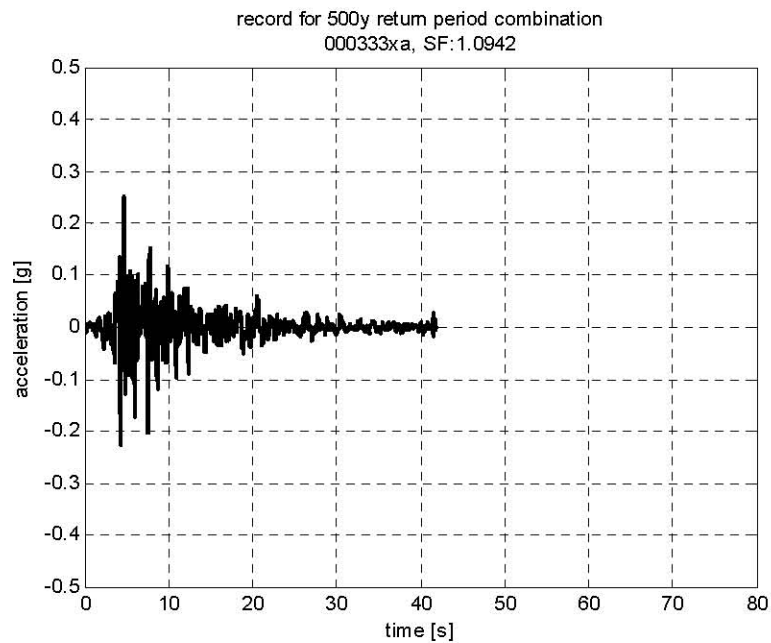


Figure D.17 500yrs combination – record 000333xa, SF:1.0942

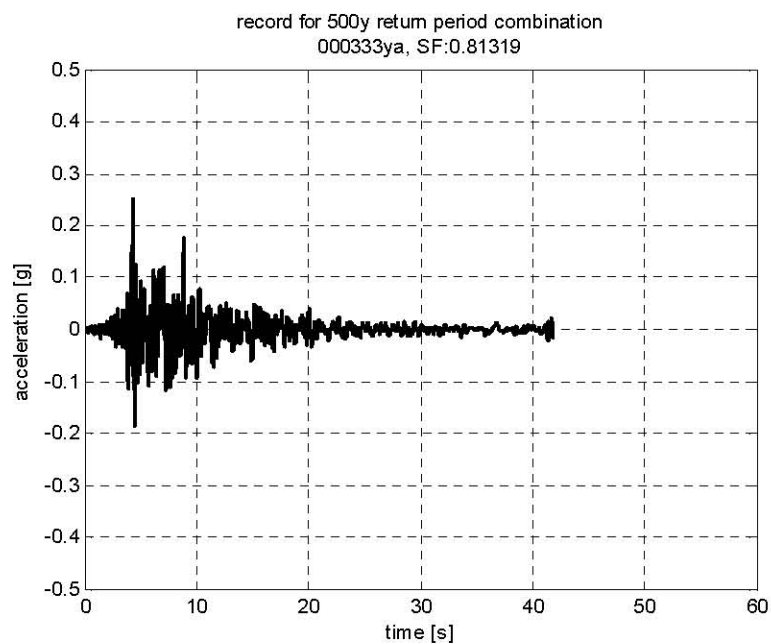


Figure D.18 500yrs combination – record 000333ya, SF:0.81319

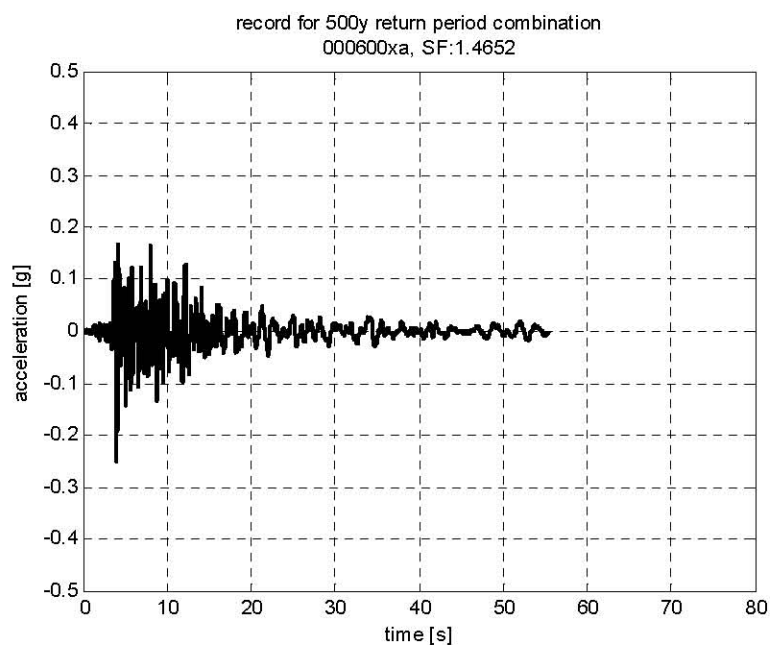


Figure D.19 500yrs combination – record 000600xa, SF:1.4652

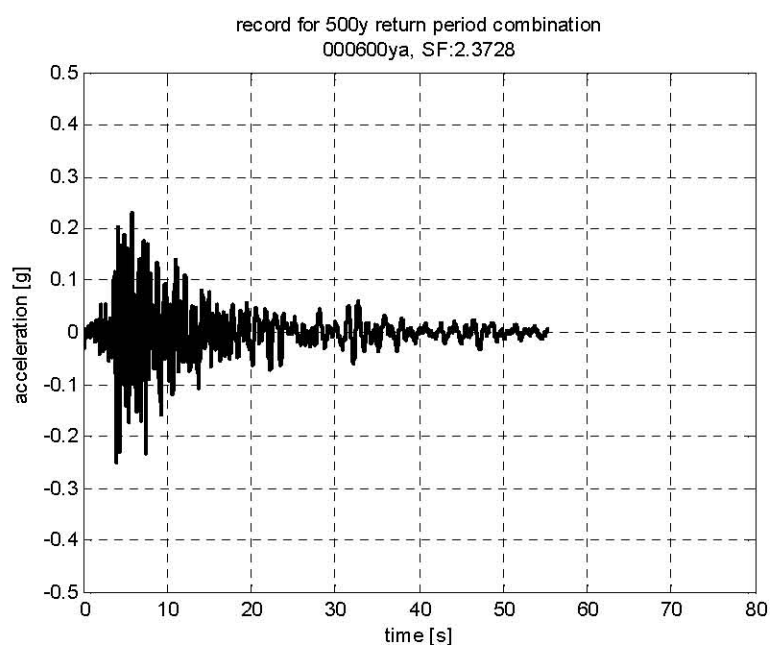


Figure D.20 500yrs combination – record 000600ya, SF:2.3728

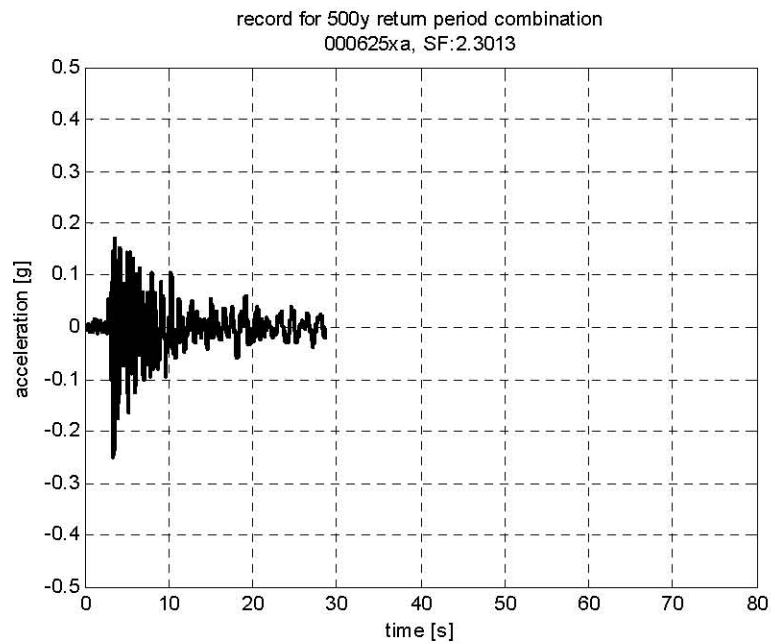


Figure D.21 500yrs combination – record 000625xa, SF:2.3013

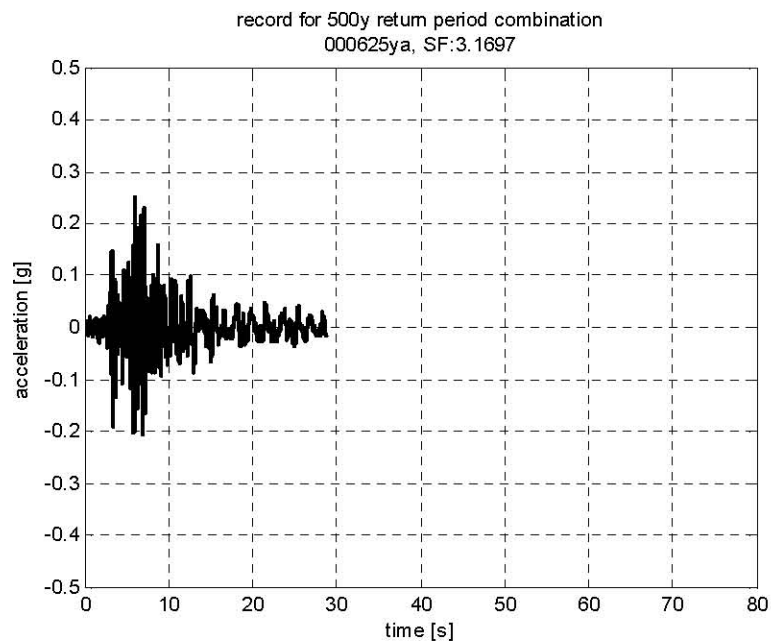


Figure D.22 500yrs combination – record 000625ya, SF:3.1697

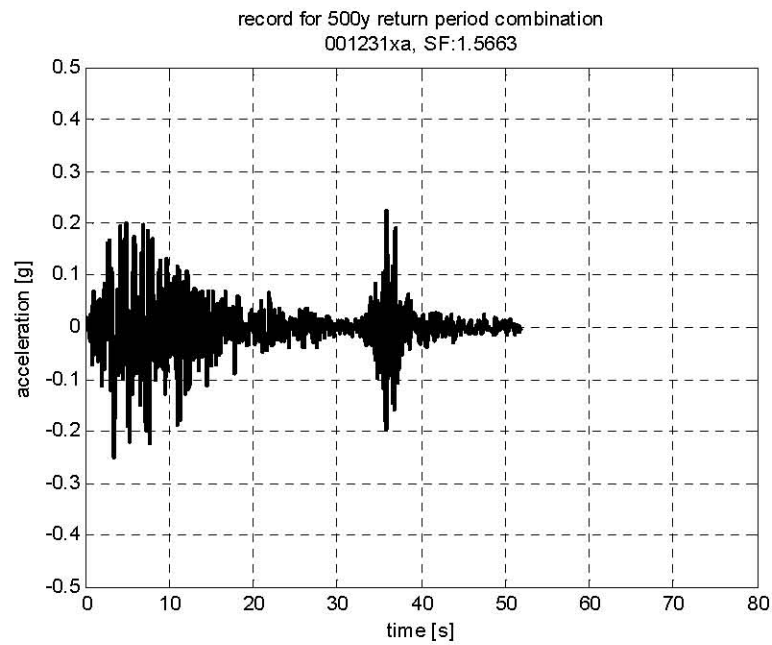


Figure D.23 500yrs combination – record 001231xa, SF:1.5663

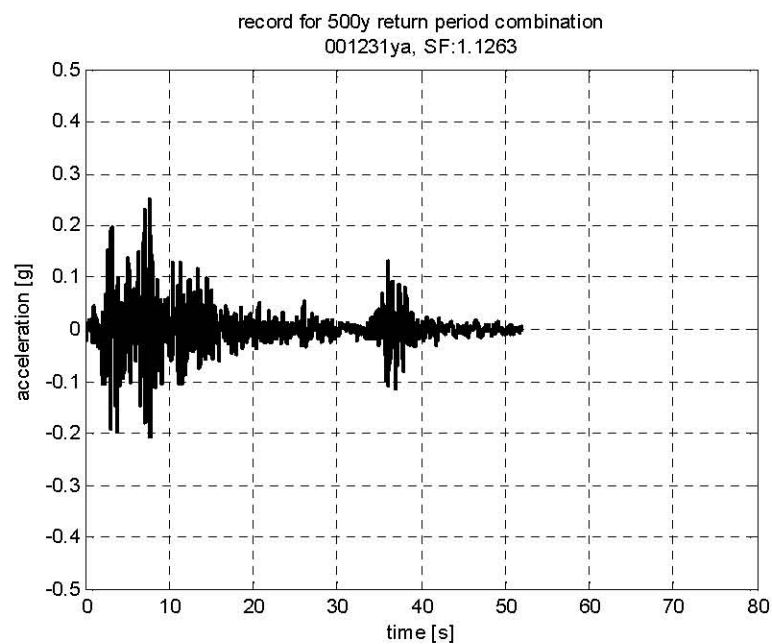


Figure D.24 500yrs combination – record 001231ya, SF:1.1263

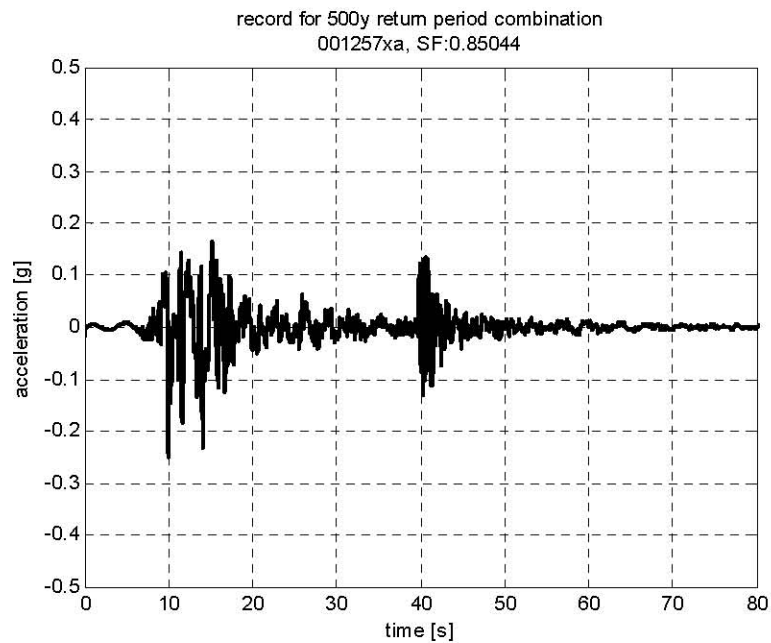


Figure D.25 500yrs combination – record 001257xa, SF:0.85044

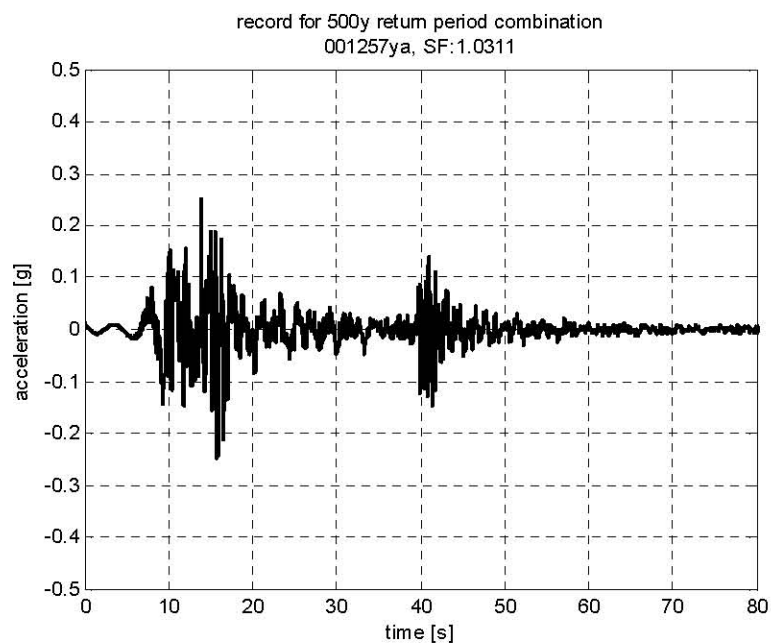


Figure D.26 500yrs combination – record 001257ya, SF:1.0311

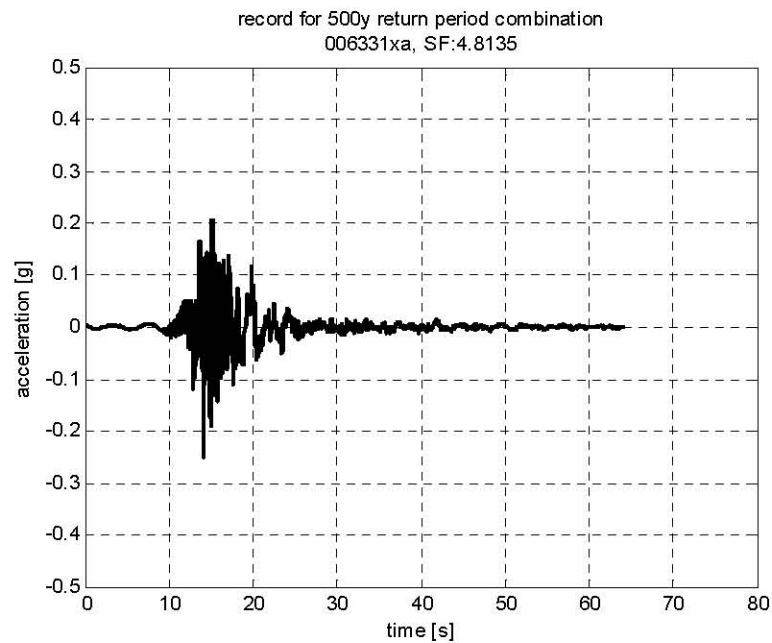


Figure D.27 500yrs combination – record 006331xa, SF:4.8135

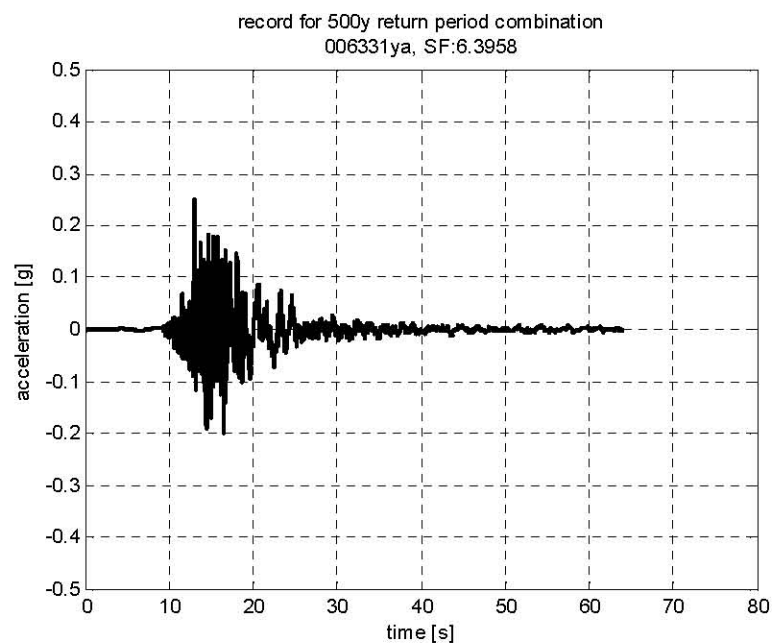


Figure D.28 500yrs combination – record 006331ya, SF:6.3958

Appendix E: TIME HISTORY ANALYSIS RESULTS

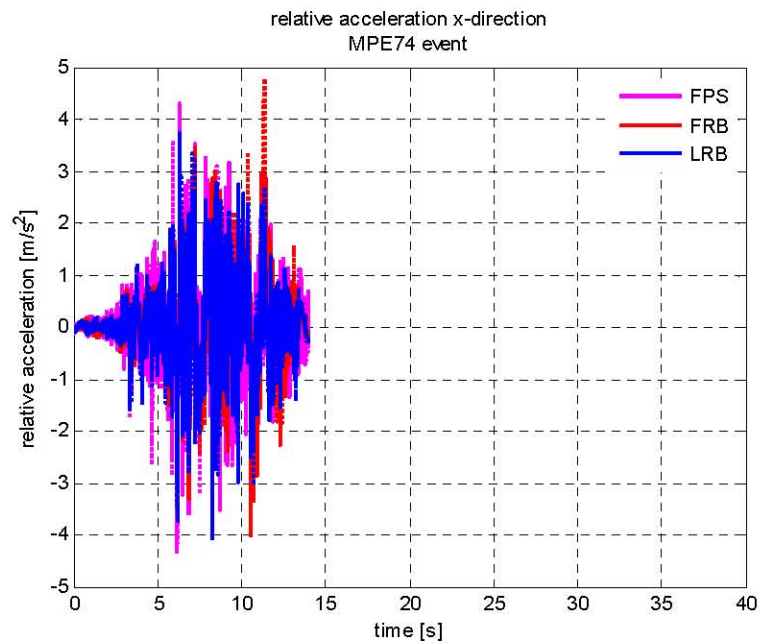


Figure E.1 Relative acceleration x-direction – event 74 MPE combination.

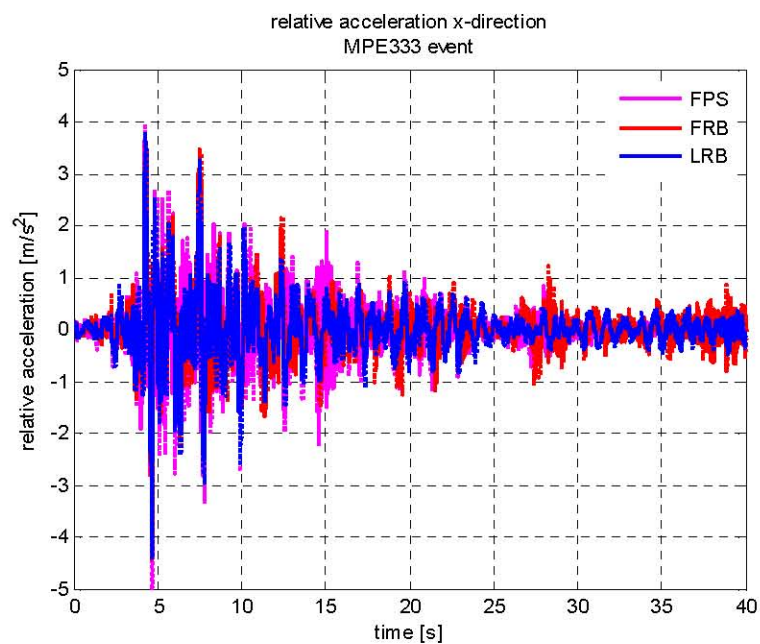


Figure E.2 Relative acceleration x-direction – event 333 MPE combination.

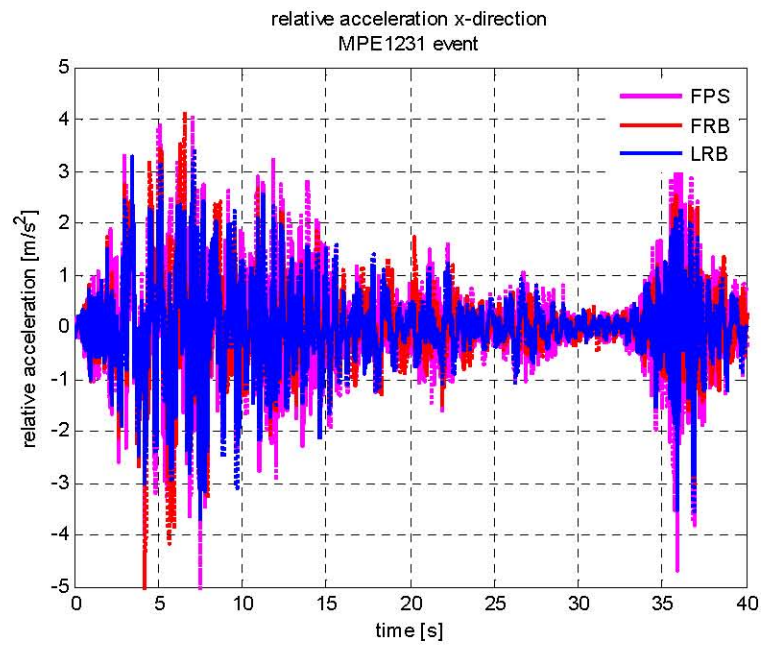


Figure E.3 Relative acceleration x-direction – event 1231 MPE combination.

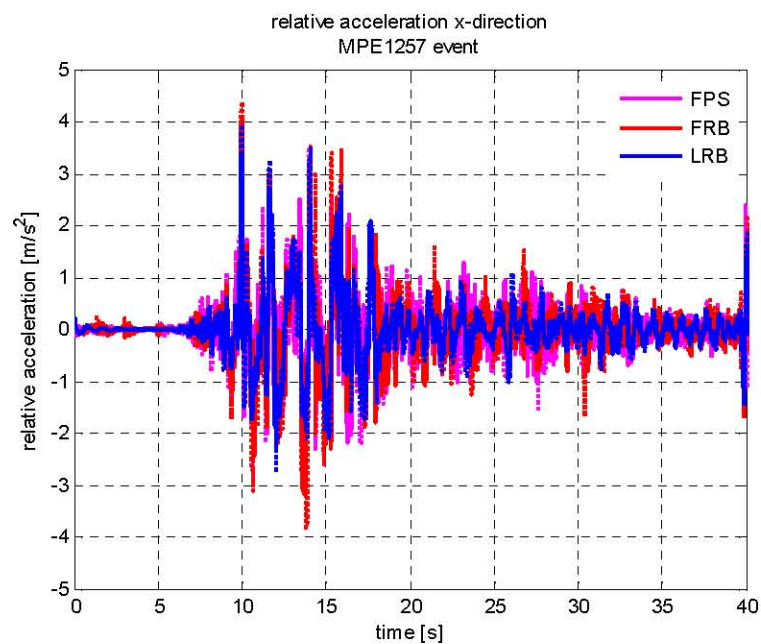


Figure E.4 Relative acceleration x-direction – event 1257 MPE combination.

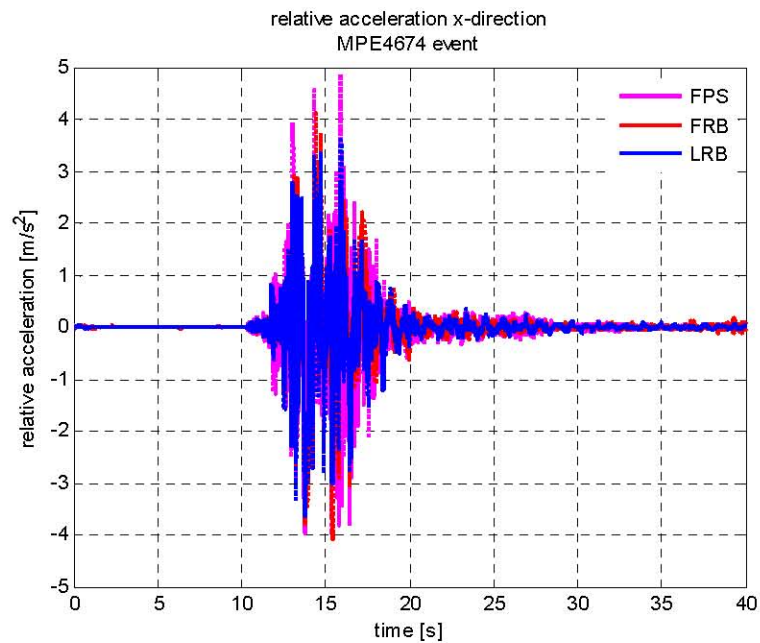


Figure E.5 Relative acceleration x-direction – event 4674 MPE combination.

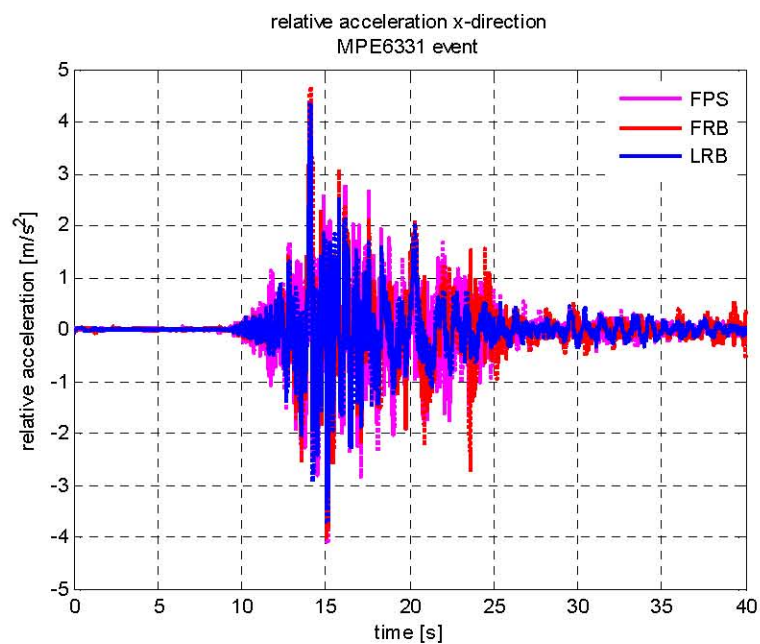


Figure E.6 Relative acceleration x-direction – event 6331 MPE combination.

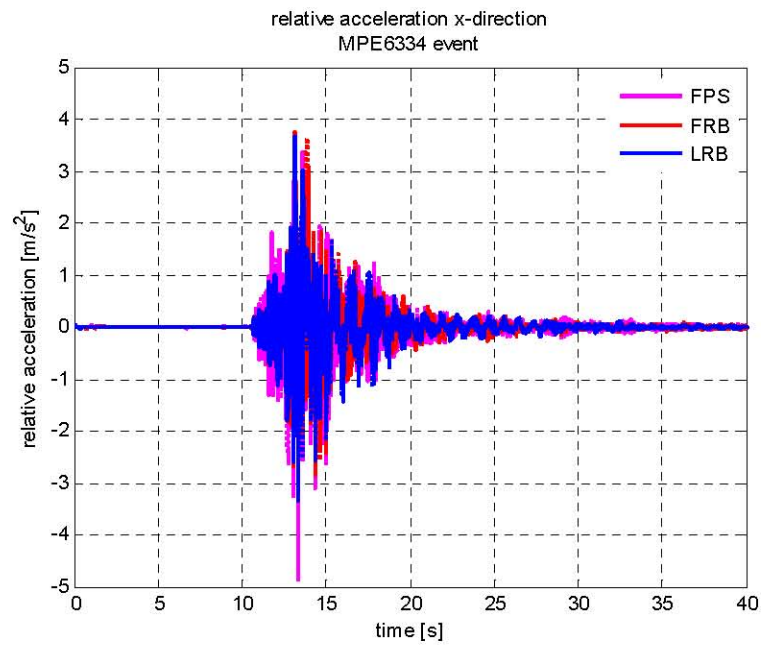


Figure E.7 Relative acceleration x-direction – event 6334 MPE combination.

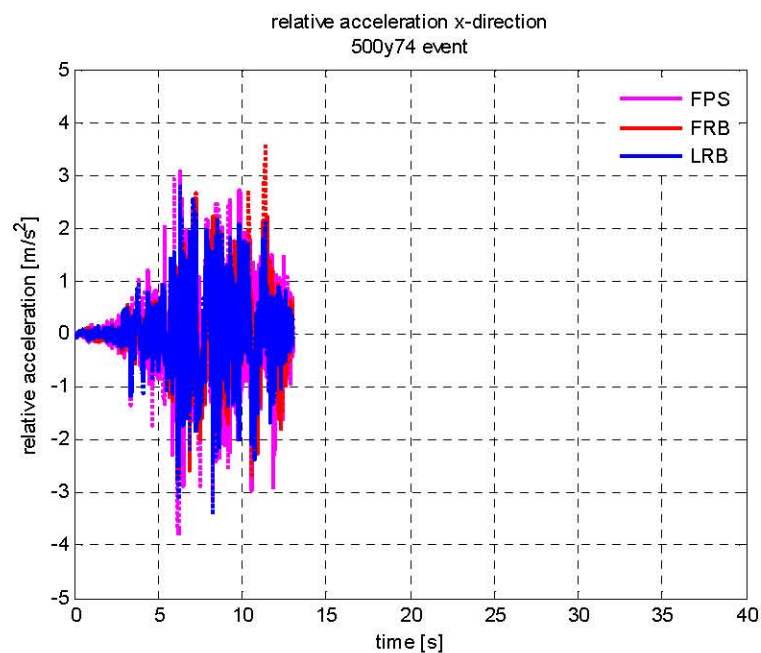


Figure E.8 Relative acceleration x-direction – event 74 500yrs combination.

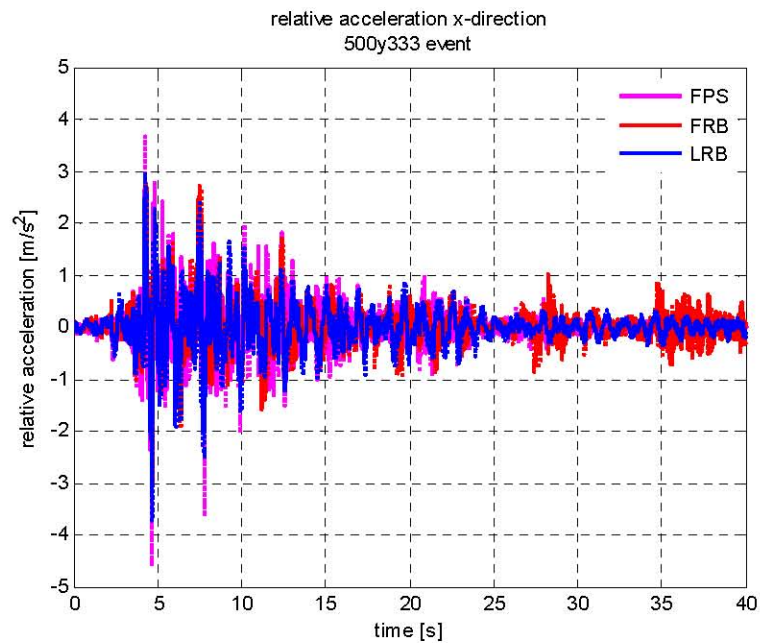


Figure E.9 Relative acceleration x-direction – event 333 500yrs combination.

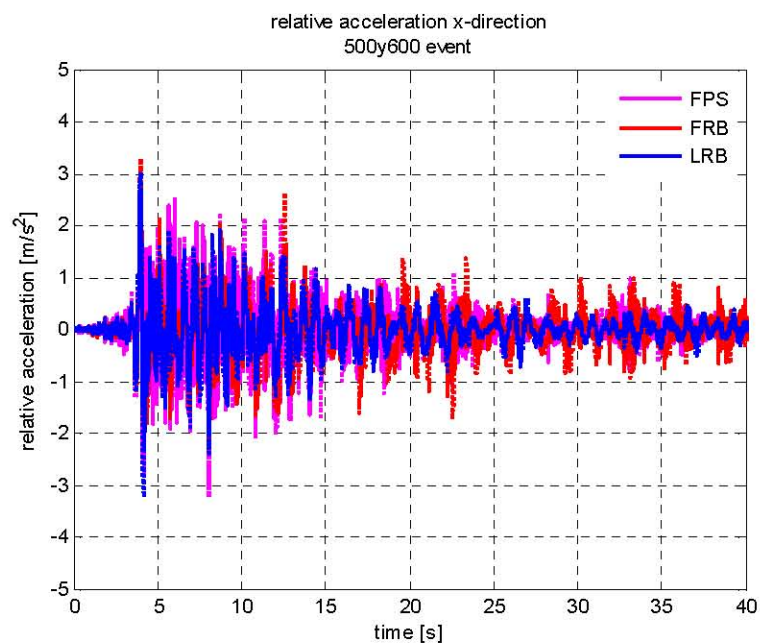


Figure E.10 Relative acceleration x-direction – event 600 500yrs combination.

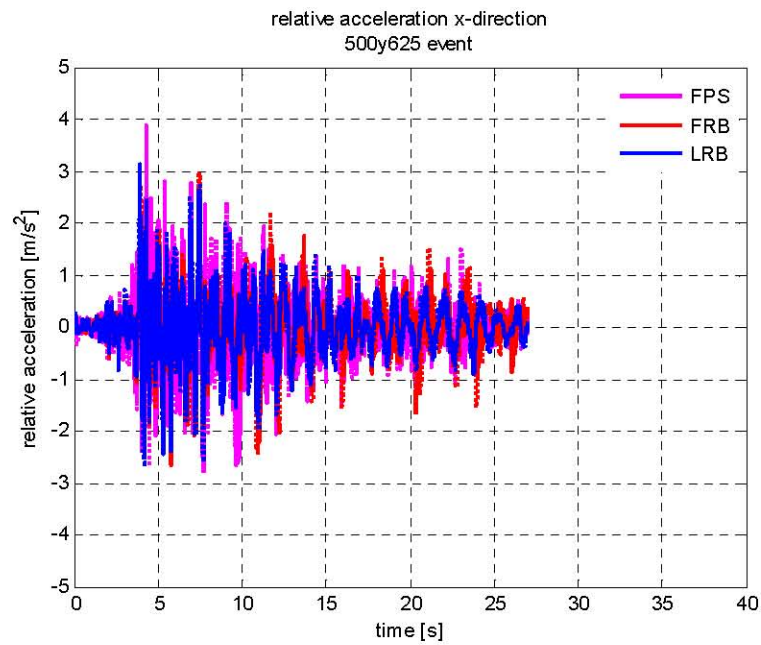


Figure E.11 Relative acceleration x-direction – event 625 500yrs combination.

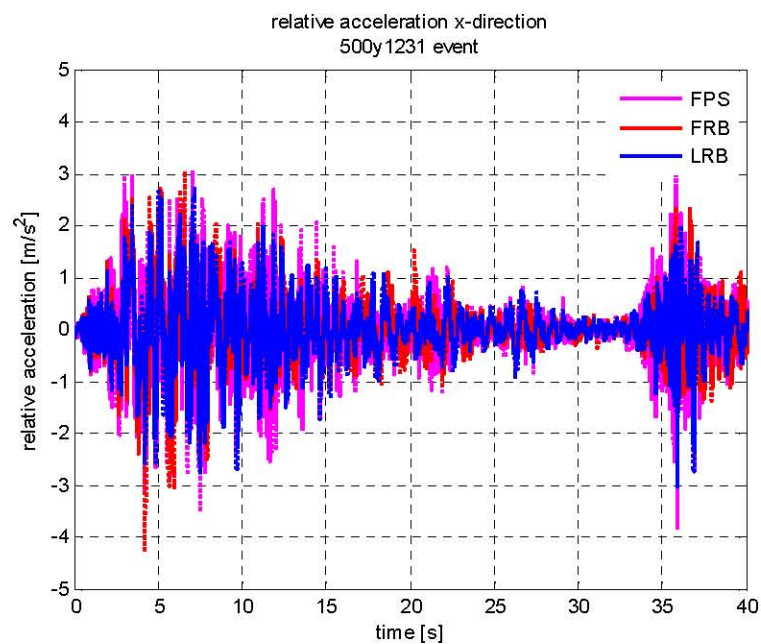


Figure E.12 Relative acceleration x-direction – event 1231 500yrs combination.

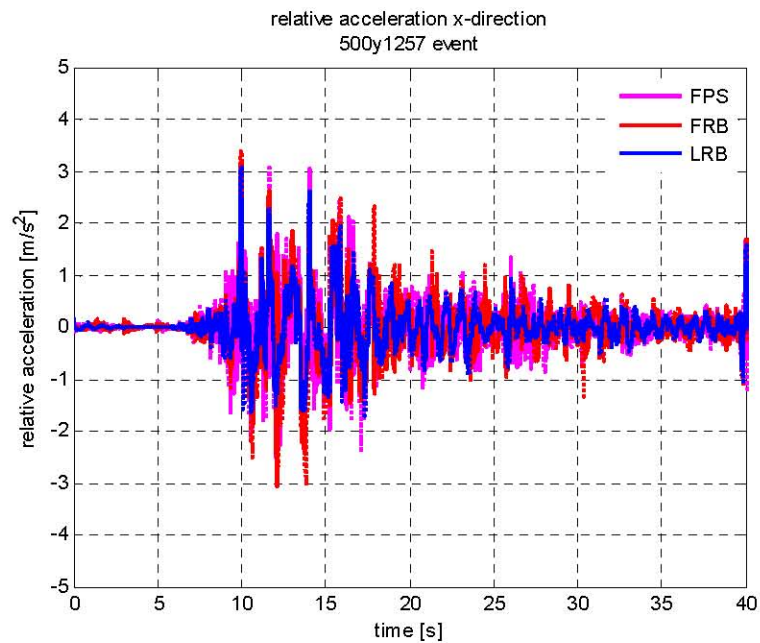


Figure E.13 Relative acceleration x-direction – event 1257 500yrs combination.

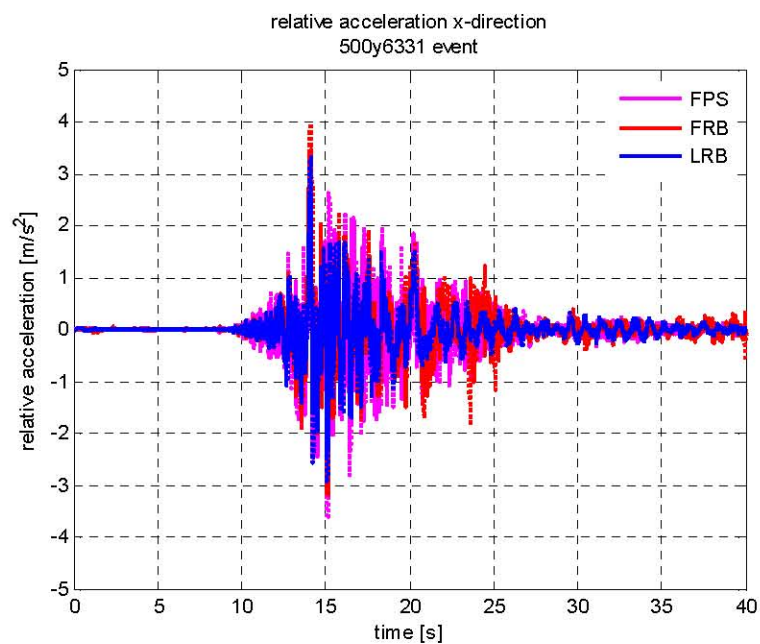


Figure E.14 Relative acceleration x-direction – event 6331 500yrs combination.

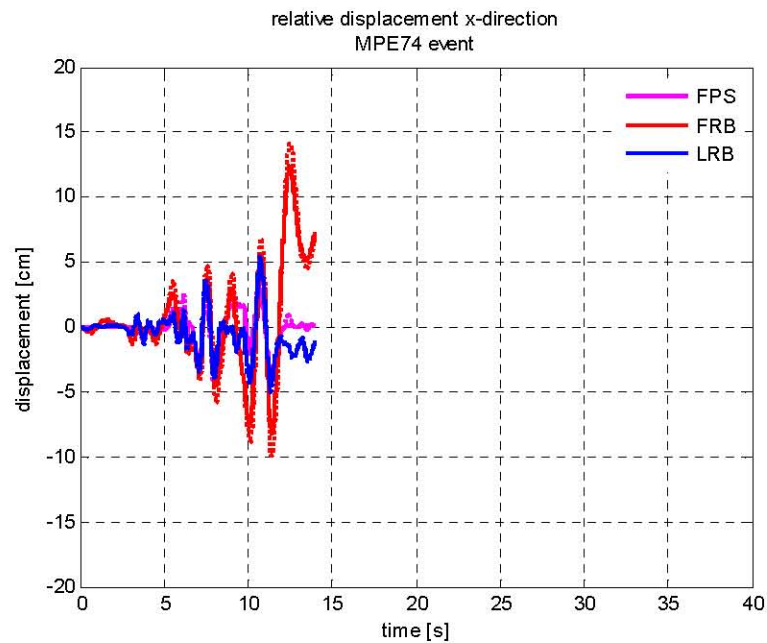


Figure E.15 Relative acceleration x-direction – event 74 MPE combination.

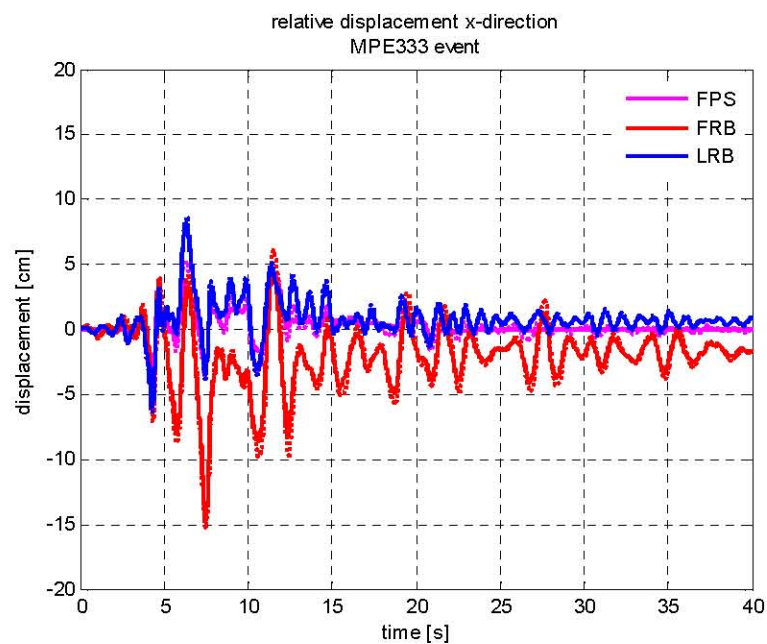


Figure E.16 Relative acceleration x-direction – event 333 MPE combination.

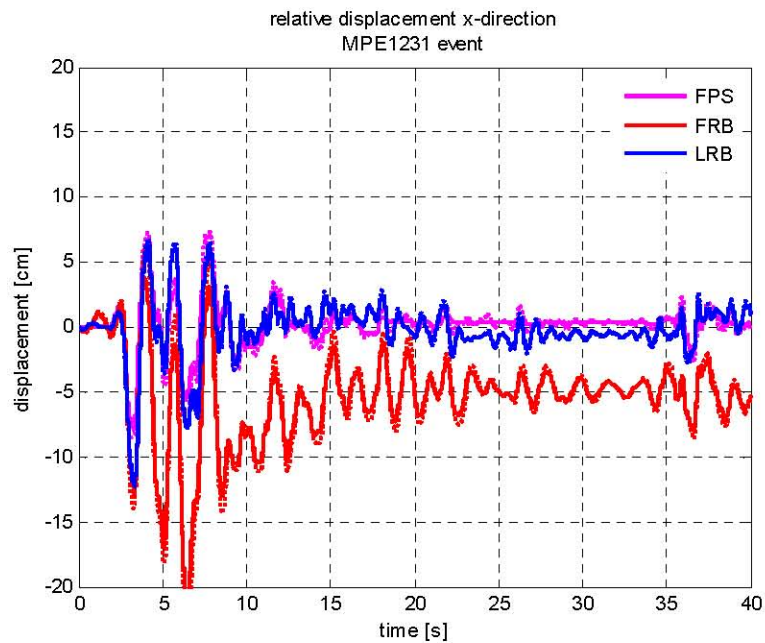


Figure E.17 Relative acceleration x-direction – event 1231 MPE combination.

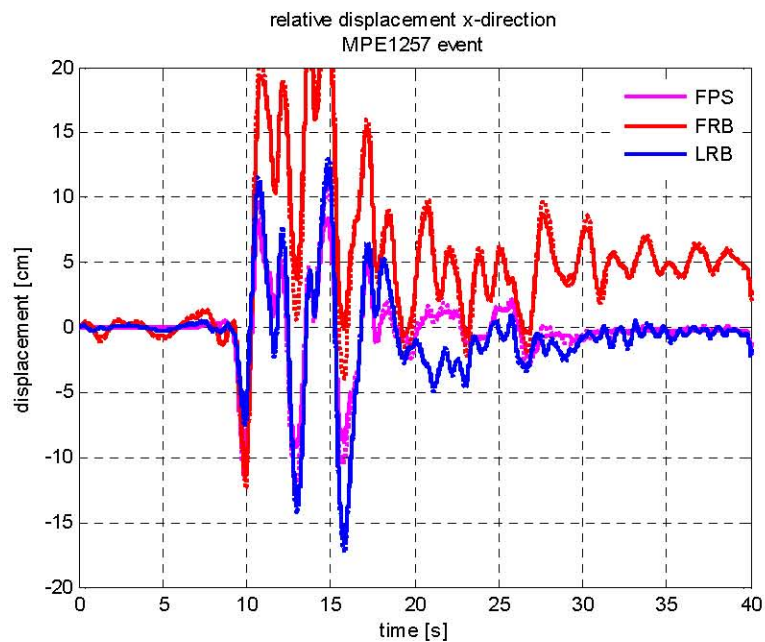


Figure E.18 Relative acceleration x-direction – event 1257 MPE combination.

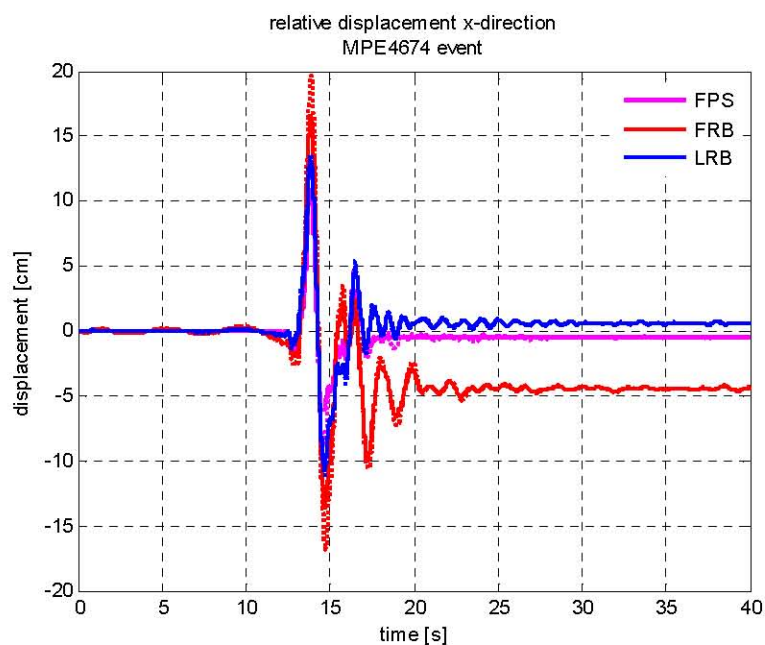


Figure E.19 Relative acceleration x-direction – event 4674 MPE combination.

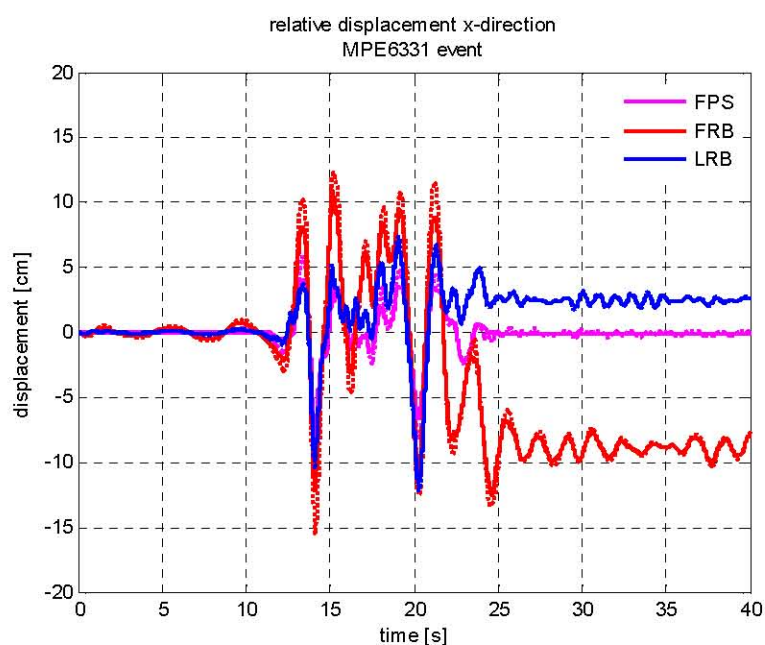


Figure E.20 Relative displacement x-direction – event 6331 MPE combination.

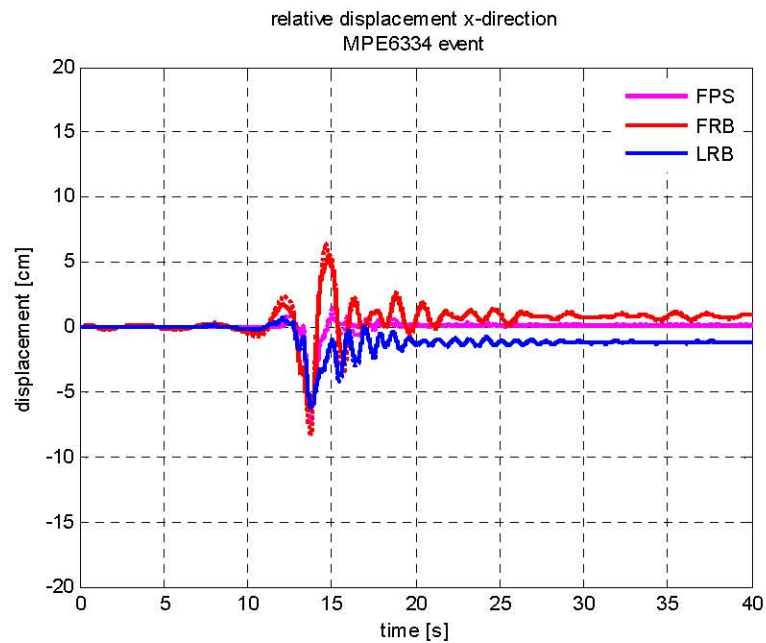


Figure E.21 Relative acceleration x-direction – event 6334 MPE combination.

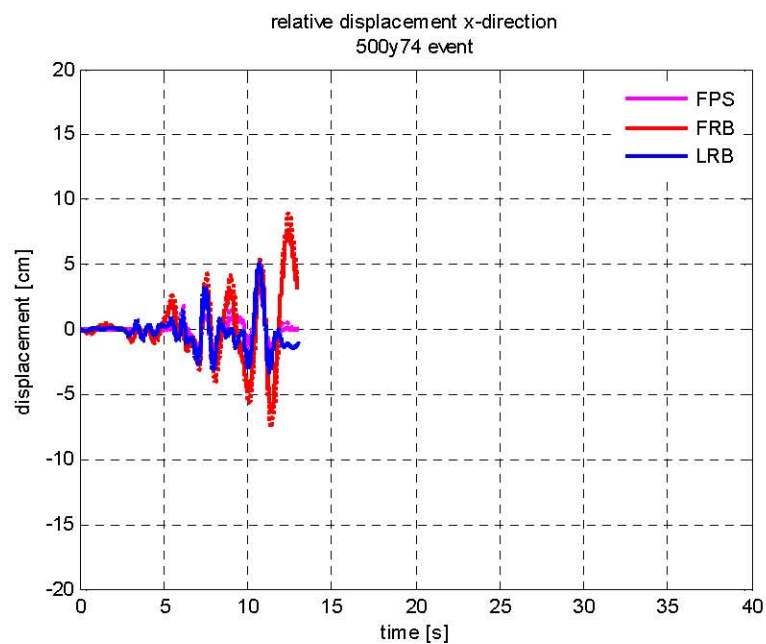


Figure E.22 Relative acceleration x-direction – event 74 500yrs combination.

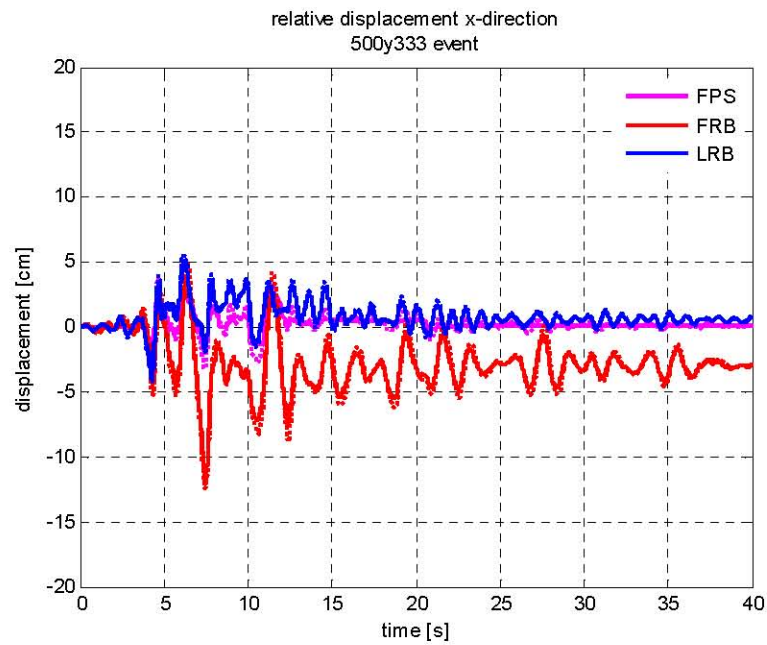


Figure E.23 Relative acceleration x-direction – event 333 500yrs combination.

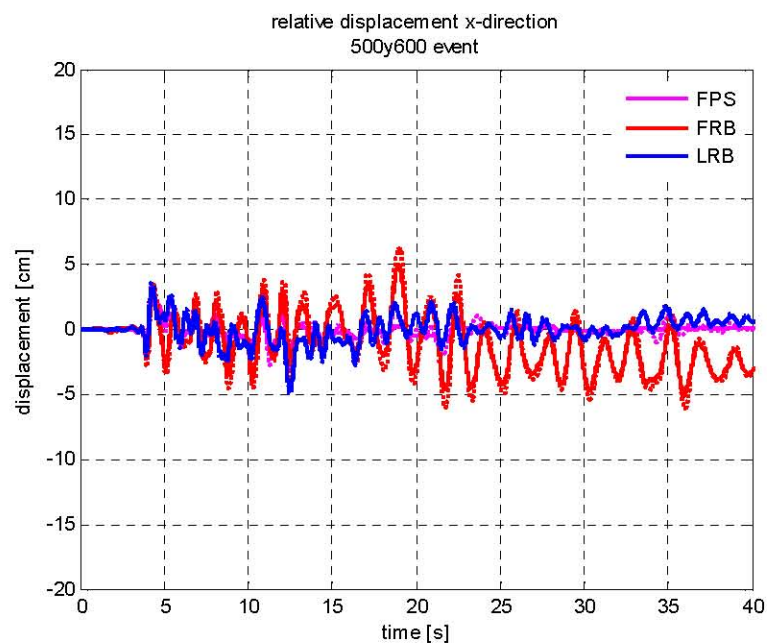


Figure E.24 Relative acceleration x-direction – event 600 500yrs combination.

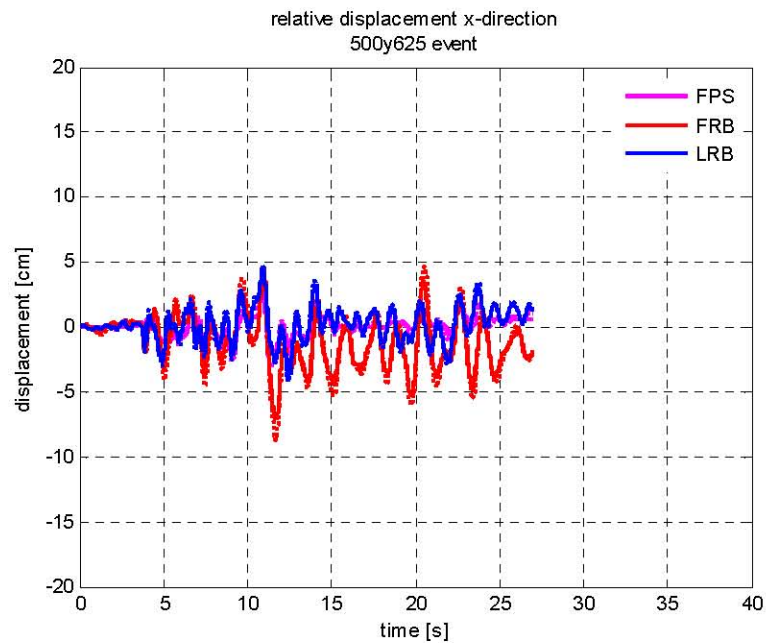


Figure E.25 Relative acceleration x-direction – event 625 500yrs combination.

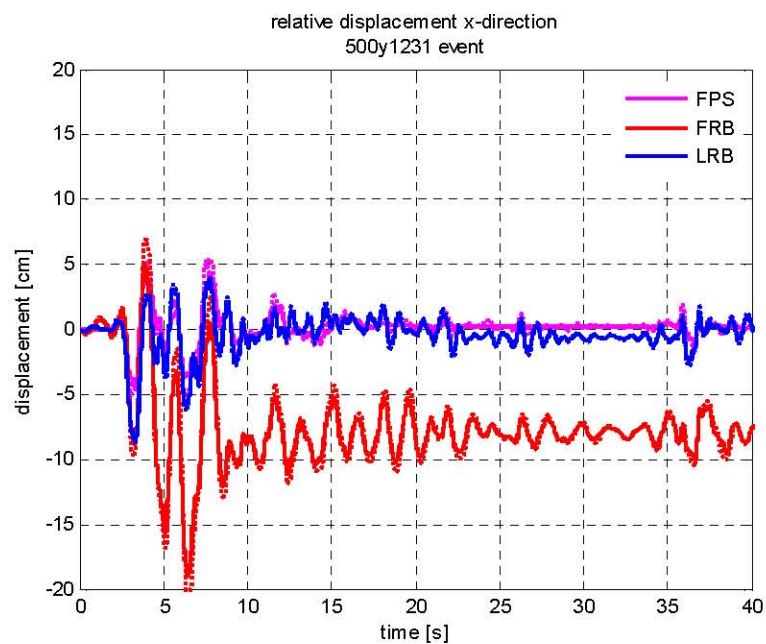


Figure E.26 Relative acceleration x-direction – event 1231 500yrs combination.

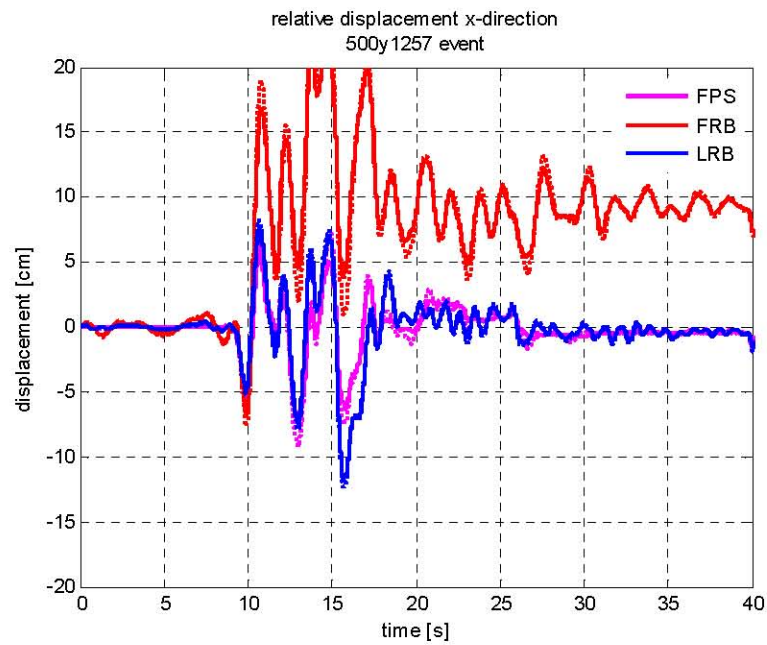


Figure E.27 Relative acceleration x-direction – event 1257 500yrs combination.

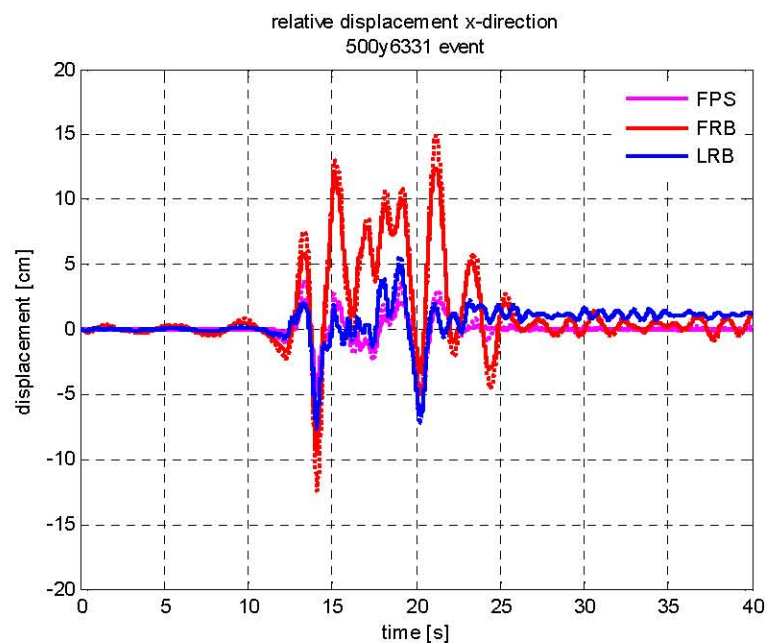


Figure E.28 Relative acceleration x-direction – event 6331 500yrs combination.